SELF-ASSEMBLY AND TEMPLATE-DIRECTED SYNTHESIS IN MULTI-STRAND PORPHYRIN ARRAYS

A thesis submitted to the board of the Faculty of Physical Sciences in partial fulfilment of the requirements for the degree of

Doctor of Philosophy of the University of Oxford

By

Nuntaporn Kamonsutthipaijit

The Chemistry Research Laboratory and Keble College, Oxford

Trinity Term 2016

SELF-ASSEMBLY AND TEMPLATE-DIRECTED SYNTHESIS IN MULTI-STRAND PORPHYRIN ARRAYS

D.Phil Thesis, Trinity Term 2016

Nuntaporn Kamonsutthipaijit, Keble College, University of Oxford

Abstract

This thesis describes the use of supramolecular chemistry in self-assembling systems based on pyridyl porphyrins and porphyrin nanorings. Pyridine substituted porphyrins are used as ligands to bind to Zn porphyrin nanorings in systems reminiscent of the light harvesting complexes in nature. The study of energy transfer in such complexes gives insight into the efficiency of the natural systems. This thesis also illustrates the scope of classical and Vernier templating as an alternative tool for the synthesis of linear porphyrin oligomers.

Chapter 1 gives a general overview of porphyrins and fully conjugated porphyrin oligomers, and then introduces supramolecular self-assemblies based upon pyridyl porphyrin ligand interactions. It also covers energy transfer processes in the selected synthetic porphyrin arrays, and includes a short review of template-directed synthesis of cyclic, linear and Vernier porphyrin oligomers.

Chapter 2 presents the syntheses and energy transfer studies of double- and triple-strand complexes based on porphyrin nanorings. The arrangement of the porphyrin units in the double-strand nanoring complex mimics the LH2 structure of purple bacteria in natural light harvesting systems. The presence of a second nanoring in the triple-strand structure should fix the conformation of the complex, enhancing the conjugation around the nanorings.

Chapter 3 introduces a synthetic antenna-nanoring system based on a series of conjugated porphyrin arrays. By varying the size of the acceptor nanoring, the effects of binding, local strain and energy transfer between antenna and nanoring are investigated. Binding of the antenna unit induces a local strain in the nanoring, and this strain is determined as a function of the size of the nanoring, providing information on the flexibility of the system. The rates of energy transfer in these systems were found to be surprisingly insensitive to the size of the nanoring.

Chapter 4 presents the classical template-directed synthesis of linear porphyrin oligomers. The stabilities and cooperativities of related ladder complexes are investigated. Two concepts of Vernier and Vernier-reciprocal templates for the synthesis of non-commensurate length oligomer products from two simple components are also introduced and investigated in detail. This study gives another approach for the supramolecular synthesis of nanoscale materials.

Acknowledgements

First of all, I would like to thank my supervisor, Prof. Harry L. Anderson FRS, for giving me the opportunity to explore in many different areas in my research. His patience, motivation and guidance during almost four years of my DPhil time has been invaluable, and the large amount of time he devoted to this project is greatly appreciated. My experience working with Harry will be fundamental for my future research.

This research would not have been completed without the contributions of numerous collaborators. Thank you to Dr. Tim Claridge, Dr. Barbara Odell, Tina Jackson and Mrs. Maria Marshall (Oxford Chemistry) for the NMR training, discussion and recording NMR spectra, Mr. Colin Sparrow (Oxford Chemistry) for training me to use the MS instrument, EPSRC mass spectrometry service (Swansea) for mass measurements of the high molecular weight porphyrins, Dr. Mark Malfois (Diamond Light Source) for help with SAXS experiments. Very special thanks go to very bright collaborators who I was very lucky to work with: Dr. Patrick Parkinson and Prof. Laura M. Herz (Oxford Physics) for help and discussion in the photoluminescence measurements and energy transfer studies. I would like to thank the Royal Thai Government scholarship for financially supporting my study.

My experience in Oxford will be memorable because of the special people I have met here. Thank you to Dr. Sophie Rousseaux, Dr. Christiane Knappke and Dr. Kanokkorn Sirithip for being good friends and teaching me many things at my starting DPhil stage; to Dr. Cecile Roche, Dr. Arjen Cnossen, Renee Haver and Isabell Gruebner for proofreading parts of my thesis and being incredible friends; to all HLA members: Dima, Pengpeng, Qianfu, Di, Jane (Yaoyao), Patrik, Ludovic, Martin, René, Pablo, Karolina, Igor, Wojciech, Levon, Julien, Ibo, James, Giulia, Hiroshi, Dominik, Izzy, Johannes, Dan, Sabine, Jonathan, Andreas, Yutaka, Takayuki, Anjul, Tom and many others for making my time in HLA group enjoyable and making the lab like another home for me.

Thanks to all my good Thai friends outside of the lab: Bee, Pop, Korn, Art, Kate, Valentine, Sary, Plum and Nodd for creating warm environment even in the place far from Thailand.

Last but not least, I would like to dedicate this work to my parents who always support me whenever I needed. Thanks to my fiancé, Chanan Euaruksakul, who never gives up believing in me, and is always by my side to encorage me to finish this degree.

Table of Contents

Abbreviations

A	Acceptor (in energy transfer)	DPM	Dipyrromethane
A	Absorbance	EM	Effective molarity
Ar	Aryl	Et	Ethyl
ATP	Adenosine triphosphate	GPC	Gel permeation chromatography
B band	Soret band, porphyrin S_0-S_2 absorption band	HOMO	Highest occupied molecular orbital
BChl	Bacteriochlorophyll	*i*	Iso
BiPy	Bipyridine	IC	Internal conversion
BQ	Benzoquinone	ISC	Intersystem crossing
Bu	Butyl	LH	Light harvesting system
COSY	Correlation spectroscopy	LUMO	Lowest unoccupied molecular orbital
CPDIPS	(3-cyanopropyl) diisopropylsilyl	m	Multiplet (in NMR)
D	Donor (in energy transfer)	*m*	Meta
d	Doublet (in NMR)	MALDI	Matrix-assisted laser desorption ionisation
Da	Dalton	Me	Methyl
DABCO	1,4-Diazabicyclo[2.2.2]-octane	MM	Molecular mechanics
dba	Dibenzylideneacetone	MS	Mass spectroscopy
DCM	Dichloromethane	MW	Molecular weight
DCTB	*trans*-2-[3-(4-*tert*-Butylphenyl)-2-methyl-2-propenylidene]malononitrile	NBS	*N*-Bromosuccinimide
DDQ	2,3-Dichloro-5,6-dicyano-*para*-benzoquinone	NIR	Near-infrared
DNA	Desoxyribonucleic acid	NOE	Nuclear Overhauser effect
DOSY	Diffusion-ordered NMR spectroscopy	NOESY	Nuclear Overhauser effect spectroscopy

o	Ortho
p	Para
PDF	Pair distribution function
Ph	Phenyl
PL	Photoluminescence
Py	Pyridine
Q band	Porphyrin S_0-S_1 absorption band
RC	Reaction centre
rt	Room temperature
s	Singlet (in NMR)
SAXS	Small angle X-ray scattering
SEC	Size exclusion chromatography
STM	Scanning tunneling microscopy
t	Triplet (in NMR)
t	Tertiary carbon
TBAF	Tetra-*n*-butylammonium fluoride
TFA	Trifluoroacetic acid
THF	Tetrahydrofuran
THS	Trihexylsilyl
TLC	Thin layer chromatography
TMEDA	Tetramethylethylenediamine
TOF	Time of flight
UV	Ultra-violet
vis	Visible

Chapter 1

Introduction

This chapter provides an introduction to the basic concepts of porphyrins and their vital role in the natural light harvesting system, before outlining the optical properties and synthesis of linear porphyrin oligomers with butadiyne linkages. Next, self-assembly processes based on the interactions of pyridyl porphyrin ligands and metalloporphyrins are discussed. A short review of energy transfer in selected synthetic porphyrin systems is presented, as well as a summary of developments in the field of template-directed synthesis of cyclic and linear porphyrin oligomers.

1.1 Porphyrin in the natural light harvesting system

Porphyrins are a family of heterocyclic macrocycles consisting of four pyrrole units linked by unsaturated =CH- groups called methine bridges through their α-positions. Porphin is the simplest porphyrin, in which hydrogen atoms substitute all positions on the periphery of the macrocycle. Structural modification of the porphyrin core can easily be achieved through substitution at the four methine carbon atoms, termed *meso*-substitution, and at the eight β-pyrrole positions, termed β-substitution (**Figure 1.1a**). The name "porphyrin" is derived from the Greek word *porphura*, meaning the colour purple.[1] Their intense colour originates from delocalisation of their total 26 π-electrons over the macrocycle. Porphyrins are aromatics due to following Hückel's rule, 18 out of their 26 π-electrons provide a cyclic conjugation path (**Figure 1.1b**). Due to an aromatic ring current, the N-H internal protons are shielded and the external protons are deshielded, as observed in ^{1}H NMR (**Figure 1.1b**).

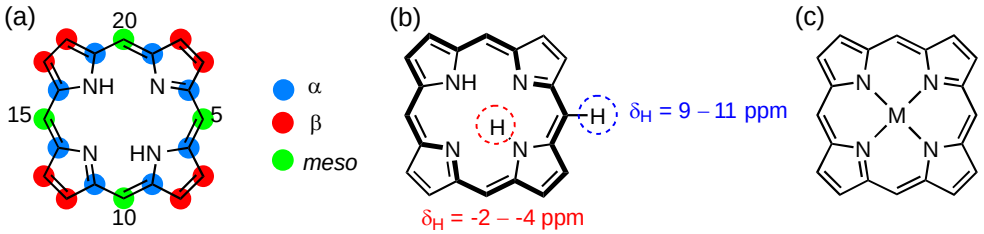

Figure 1.1 (a) Structure of free-base porphin illustrating the nomenclature and numbering for the macrocycle. (b) The bold bonds mark the 18 π-electron delocalisation pathway responsible for aromaticity in porphyrins and the resulting chemical shifts of inner (red) and outer (blue) protons. (c) Structure of metalloporphyrin.

The four inward-pointing nitrogen donors in a deprotonated free-base porphyrin structure are an excellent chelating ligand for various metals, providing a diversity of metalloporphyrins. Zn atoms can be located into the cavity of porphyrins, resulting in a strong complex which can further bind to a fifth axial ligand. This property can be used for self-assembly of porphyrins through metal-ligand coordination and will be discussed in more detail throughout this thesis. Binding of pyridine to the zinc centre can be used to prevent aggregation of the planar porphyrin π-system.

Macromolecules consisting of porphyrins are found in nature. Metalloporphyrin derivatives play crucial roles in biochemical processes. The well-known examples are hemes featuring

iron-porphyrin complexes in hemoglobin and myoglobin responsible for transporting oxygen through the body or storing oxygen in muscle tissue. The structure of vitamin B_{12} contains a cobalt porphyrinoid that is important for maintaining a healthy nervous system. Factor F430 is a nickel porphyrinoid which is part of the enzyme methyl coenzyme M reductase in methanogenic bacteria that catalyses the release of methane. Another important metalloporphyrinoid is chlorophyll featuring bound magnesium metal, which is involved in light harvesting systems in plant and bacteria.

Natural photosynthetic light-harvesting systems are highly evolved for efficient energy collection and their photophysics have been thoroughly investigated, particularly for systems from photosynthetic bacteria.[2] Many of the critical properties of these molecular assemblies have been attributed to the geometric structure of their key light-harvesting (LH) complexes.[3–6] The light harvesting system is a gigantic complex (**Figure 1.2**) found inside the cell membrane of photosynthetic bacteria, consisting of two cyclic LH complexes called LH1 and LH2, and a reaction centre (RC) which is embedded inside LH1 (**Figure 1.2c**). The LH complexes contains bacteriochlophyll *a* (BChl *a*) units (**Figure 1.2a**), which are magnesium porphyrinoids, and serve as the predominant light absorbing pigments in LH1 and LH2. The BChl *a* units are held precisely in three different environments by a protein scaffold, resulting in absorption maxima at different wavelengths as shown by the number in their name: the B875 ring found in LH1 and the B850 and B800 rings, both found in LH2. B800 ring comprises of 9 porphyrin units lying in the same plane, parallel to a second cyclic array, B850, consisting of 18 porphyrin units (**Figure 1.2b**). LH1 contains B875 which is a large single ring consisting of 30-32 units. The electronic coupling in the LH2 and LH1 systems is based on their pigment-pigment distances – the shorter the distance the stronger the electronic coupling. The centre-centre distances within the LH complex increase as follows: 9 Å (B850-B850 in LH2) < 18 Å (B800-B800 and B800-B850 in LH2) < 30 Å (B850-B875 between LH2 and LH1) < 45 Å (B875 from LH1 to RC).[7] Photosynthesis starts from the absorption of a photon by LH1 or LH2, after which the energy is transferred to RC where it is used to drive transmembrane charge separation (**Figure 1.2d**). The LH apparatus acts as antenna to funnel the solar energy to the RC, where it can be concentrated and transduced into useful

chemical energy in the form of ATP. LH complexes perform highly efficient photon capture followed by ultrafast energy transfer between multiple chromophores. In LH2, the transfer of excitons from B800 to B850 takes place within 1 ps; transfer between B850 rings in two neighboring LH2 complexes as well as the transfer from a LH2 to a nearby LH1 typically occurs within 5–10 ps; the transfer from the LH1 ring to the RC happens within 30–50 ps.[8]

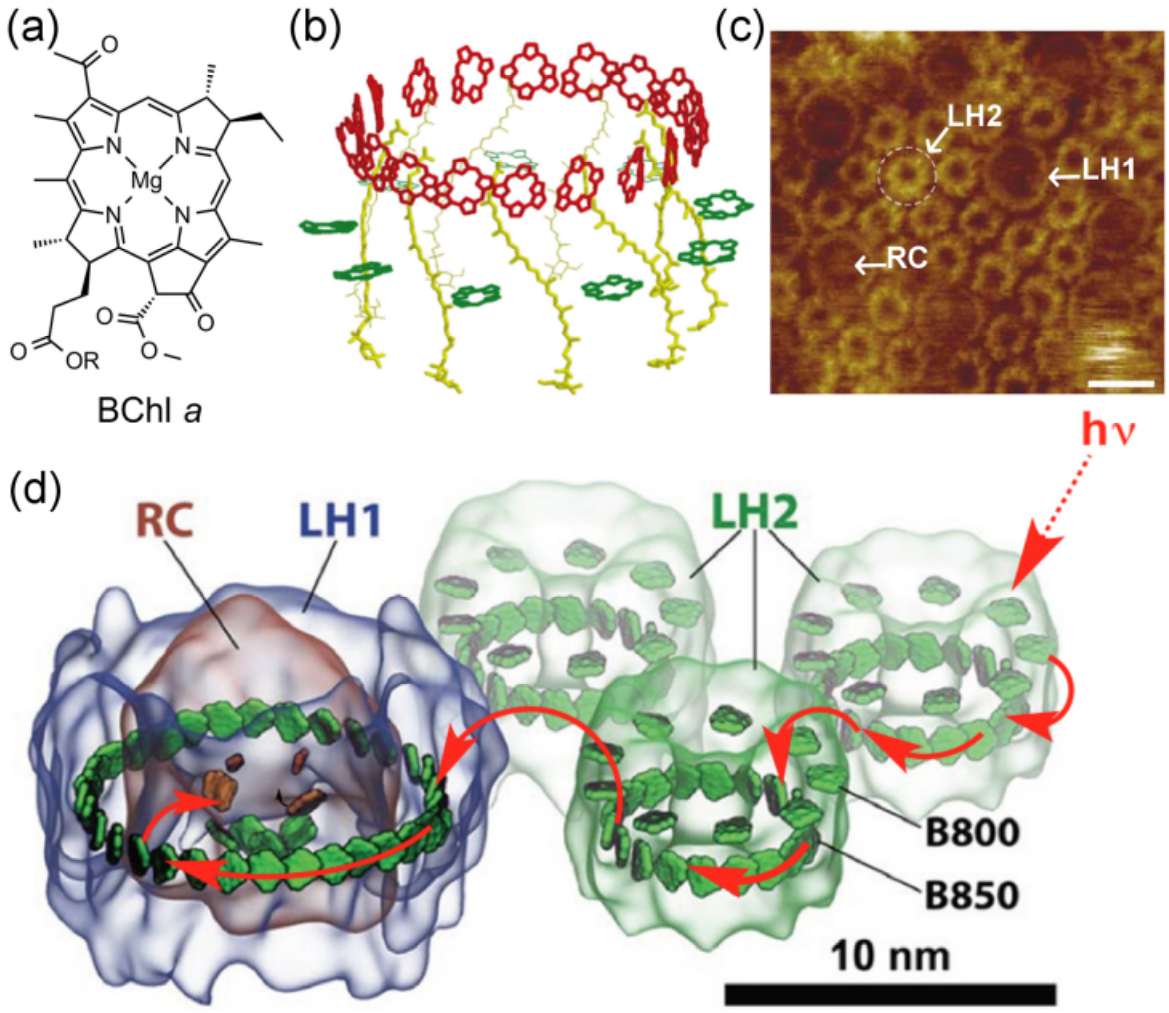

Figure 1.2 Light harvesting system of purple bacteria. (a) Structure of bacteriochlorophyll (b) Side view of the LH2 of purple bacteria. Model reprinted from *http://www.chemphys.lu.se/old/kfresearch/den-antennas.html*. (c) AFM image of a native membrane of Rs. photometricum (scale bar = 10 nm).[9] Adapted with permission from ref. 9. Copyright 2016 American Association for the Advancement of Science. (d) A model of a LH1-RC complex with LH2 complexes nearby. The red arrows indicate the flow of energy from absorption to charge-separation.[10] Adapted with permission from ref. 10. Copyright 2016 American Chemical Society.

Much research has been motivated by the desire to elucidate the range of physical processes that lead to robustness and high efficiency of the energy transfer mechanism.[11–13] The aim of such studies is to understand any potential roles of molecular structure and quantum mechanics in

biological systems in order to design synthetic (biomimetic) light-harvesting devices.[14–16] Studies on such chromophore systems have revealed the importance of symmetry,[17] and energy funnelling for photosynthetic efficiency.[18] However, active control over natural systems has not yet been achieved to test the relative importance of such factors. This topic is discussed in more detail in **Chapter 2** and **3**.

1.2 Exciton coupling

A chromophore can be excited from its ground electronic state to an excited electronic state by a photon with a wavelength that matches the energy gap between these states. The interaction of a molecule with light involves a transitory redistribution of electron density, termed the electric transition dipole moment (μ). It is described by a vector with an orientation corresponding to the direction of electron displacement and a magnitude that is proportional to the intensity of the transition. When multiple chromophores come into close proximity, their transition dipole moments will start interacting. This phenomenon is called *exciton coupling* and it can be explained by the simple point-dipole exciton coupling theory, developed by Kasha.[19] The original excited states of an assembly of chromophores are coupled to one another to give resultant excitonic states, which are not equal to the localised excitation of individual species of the assembly.

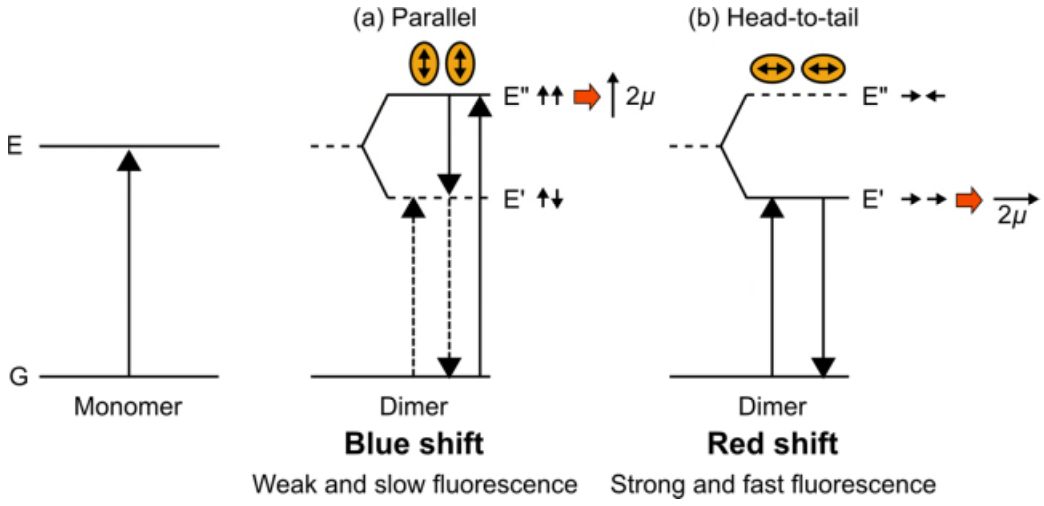

Figure 1.3 Exciton coupling of a pair of spatially proximate chromophores. (a) Parallel transition dipole moments. (b) Head-to-tail transition dipole moments. Vertical arrows indicate allowed transitions and dash arrows indicate forbidden transitions.

The simplest example of exciton coupling is the interaction of a pair of degenerate chromophores. When the two dipoles are brought to close proximity side by side, their orientations will cause the splitting in the energy of individual molecules, E into two new states, E' and E". Two chromophores orientations which have parallel and head-to-tail transition dipoles are depicted in **Figure 1.3**. For parallel arrangement (**Figure 1.3a**), the dipoles are repulsive to each other and get to higher energy, while the antiparallel dipoles has a zero net transition dipole hence transitions to this state are forbidden. The net effect of exciton coupling on electronic absorption spectrum in this case is a blue shift. The fluorescence is weak and slow because the lower electronic state is forbidden. In contrast, for head-to-tail arrangement (**Figure 1.3b**), the head-to-tail coupling of transition dipole vectors has a nonzero magnitude and excitation to the lower energy exciton state is allowed. The net effect is a red shift of the absorption compared to uncoupled chromophores and strong and fast fluorescence.

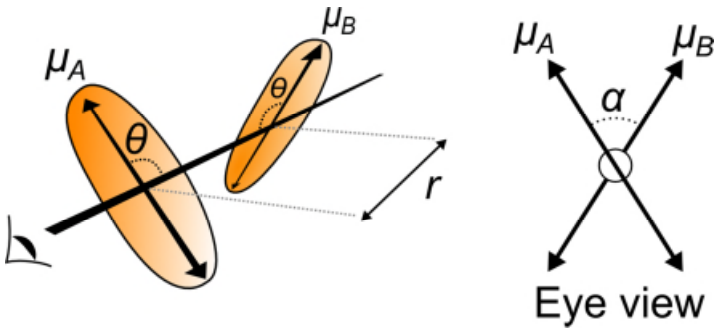

Figure 1.4 Model for the coupling of two transition dipole moments.

In general cases, the exciton splitting energy, ΔE, of two adjacent transition dipole moments μ_A and μ_B is described by the equation:

$$\Delta E = E'' - E' = \frac{2|\mu_A \mu_B|}{r^3}(\cos\alpha + 3\cos^2\theta) \qquad \textbf{(eq. 1.1)}$$

where μ_A and μ_B are the transition dipole moments for the singlet-singlet transitions of monomers, r is the centre-to-centre distance, α is the torsional angle between two molecular planes of the chromophores and θ is the angle between polarisation axes and the centre-to-centre line assuming the same angles for both dipoles for simplicity (**Figure 1.4**).[19] From the equation above, it is important that the chromophores must be close in space as the energy gap between the excitonic

states is proportional to $1/r^3$. Note that the maximum exciton coupling is achieved when two chromophores are planarised (α = 0°, cos α = 1) and their dipoles are oriented along the centre-to-centre line (θ = 0°, cos θ = 1).

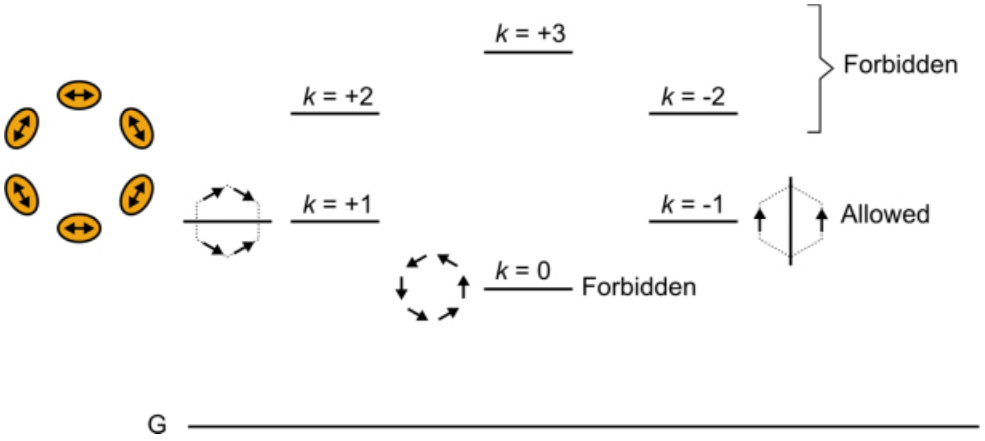

Figure 1.5 Exciton coupling of six chromophores which are arranged as a ring.

The formalism given above for a pair of chromophores can easily be extended to ring systems. When six chromophores are arranged as a ring, the six dipoles will interact and split the energy of the individual chromophores. The splitting of the energy levels of the ring systems can be structured through the simple Hückel theory which can be described using the symmetry of molecular orbitals in benzene. This method provides two non-degenerate (k = 0 and k = 3) and two pairwise degenerate (k = ±1 and k = ±2) excitonic states (**Figure 1.5**). However, only the two degenerate k = ±1 states are allowed while the transitions to the lowest k = 0 state are forbidden due to the dipole contributions summing to zero. Therefore, once the molecule has relaxed into its lowest state, the fluorescence will be strongly retarded allowing effective competition from non-radiative decay processes. This approach can be applied for the larger rings such as the LH complexes and it explains why rings of chromophores tend to have weak absorption and emission to the first excited state.[18]

1.3 Linear porphyrin oligomers with butadiyne linkages

Synthesis of models for natural light harvesting systems is of great interest in the broader context of organic electronic materials. In order to design synthetic chromophore arrays with strong electronic coupling reminiscent of that in the natural light harvesting complexes, chemists

link chromophores covalently, either directly or by conjugated bridges, leading to the concept of π-conjugated oligomers and polymers.[20,21] The delocalisation of excited states and charge transport in these structures[22,23] gives a basis for application of light harvesting systems in photovoltaic devices.[24,25] Porphyrins are well known as a good candidate for such applications. The choice of linkers between porphyrin units is flexible with different degrees of electronic coupling; selected linker examples include C–C single bonds,[26] ethyne bonds,[27] butadiyne bonds,[22] and phenylene (*ortho*-,[28] *meta*-[29,30] and *para*-[31]) groups as shown in **Figure 1.6**. All work presented in this thesis is based on butadiyne-bridged porphyrin oligomers; thus, the rest of this section will focus on the chemistry of these oligomers.

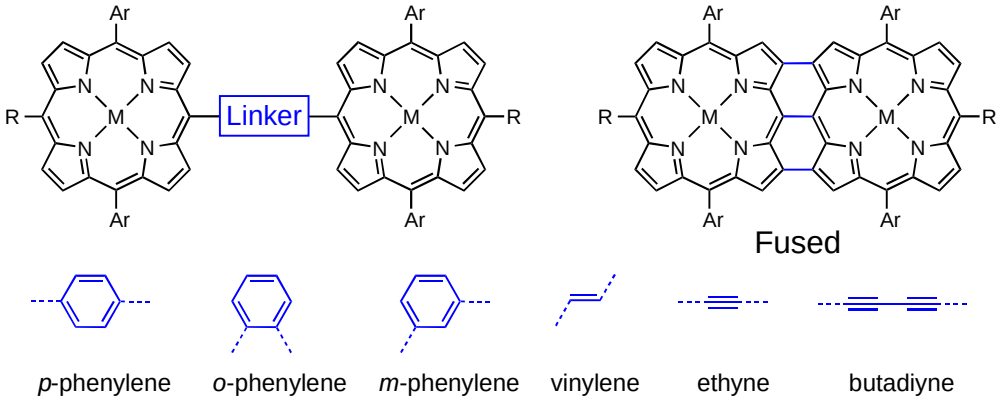

Figure 1.6 Selected porphyrin dimer linkers include phenylene, vinylene, ethyne, butadiyne groups and C-C single bonds (fused).

1.3.1 Optoelectronic properties

All porphyrins are highly coloured due to their strong π-π* electronic absorption bands. The two lowest transitions in the absorption spectrum of an ordinary porphyrin monomer are a strong transition to the second excited state ($S_0 \rightarrow S_2$) at about 400 nm (the Soret or B band) and a relatively weak transition to the first excited state ($S_0 \rightarrow S_1$) at about 550 nm (the Q band). Internal conversion from S_2 to S_1 is rapid, resulting in detection of fluorescence only from S_1.[22] The origin of these $\pi \rightarrow \pi^*$ transitions in the B and Q bands can be described using the four orbital model proposed by Gouterman (**Figure 1.7a**).[22,32] The four frontier orbitals in D_{4h} symmetric porphyrins are two π orbitals: a_{1u} and a_{2u}, and a degenerate pair of π* orbitals: $e_{g\,x}$ and $e_{g\,y}$. The two highest occupied π orbitals a_{1u} and a_{2u} have almost the same energy. Both transitions from $a_{1u} \rightarrow e_g$ and

$a_{2u} \rightarrow e_g$ would be expected to have coincident absorption bands. However, a process known as configurational interaction causes the split of these two transitions, resulting in significantly different intensities and energies: the more intense B band ($S_0 \rightarrow S_2$), and the less intense Q band ($S_0 \rightarrow S_1$) (**Figure 1.7b** and **c**). Structural modification of the porphyrin core at the *meso*-positions influences its electronic properties more than modification at the β positions due to the higher frontier orbital coefficients at the former sites. Many synthetic porphyrins have *meso*-aryl substituents which would be expected to influence the electronic structure of the porphyrin core. However, a large dihedral angles between aryl and porphyrin leads to a minimal π conjugation.

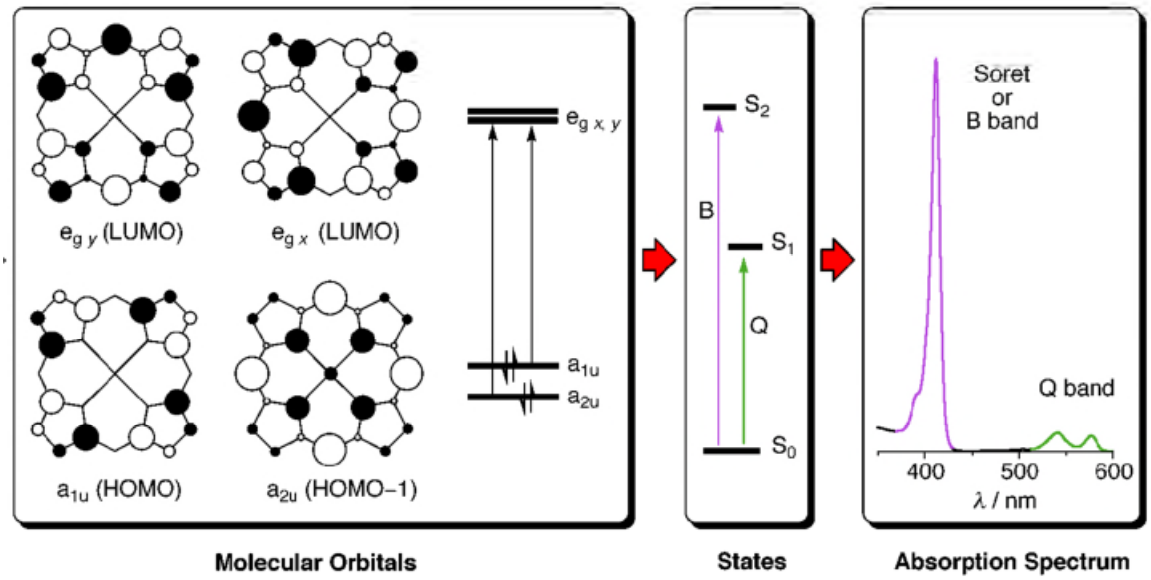

Figure 1.7 (Left) The four Gouterman molecular orbitals of a typical D_{4h} symmetrical porphyrin monomer and configurational interaction between $a_{1u} \rightarrow e_{g\,y}$ and $a_{2u} \rightarrow e_{g\,x}$ results in (middle and right) two absorption bands of different intensities.[22] Adapted with permission from ref. 22, Copyright 2016 Royal Society of Chemistry.

For the butadiyne-linked porphyrin oligomers, the *meso–meso* butadiyne link allows strong inter-porphyrin electronic coupling and the extension of conjugation upon oligomerisation results in a progressively intensified and red-shifted Q-band (**Figure 1.8**).[33] However, the butadiyne link also allows a continuous range of torsion angles (θ) between the porphyrin units.[34] The length of the butadiyne bridge is sufficient to avoid any steric clash between the opposing β hydrogens of the porphyrins and gives the lowest energy conformer as planar (θ = 0°). The energy difference between two conformers (planar and perpendicular) leads to different resonance stabilisation

between porphyrin units via butadiyne-bridge. Increasing length of a porphyrin oligomer causes the diversity of possible configurations of torsional angles between the porphyrin units, resulting in the increasing width of Q band absorption (**Figure 1.8**). Torsion angle-dependence can also be seen in the B band, despite the presence of several overlapping transitions.

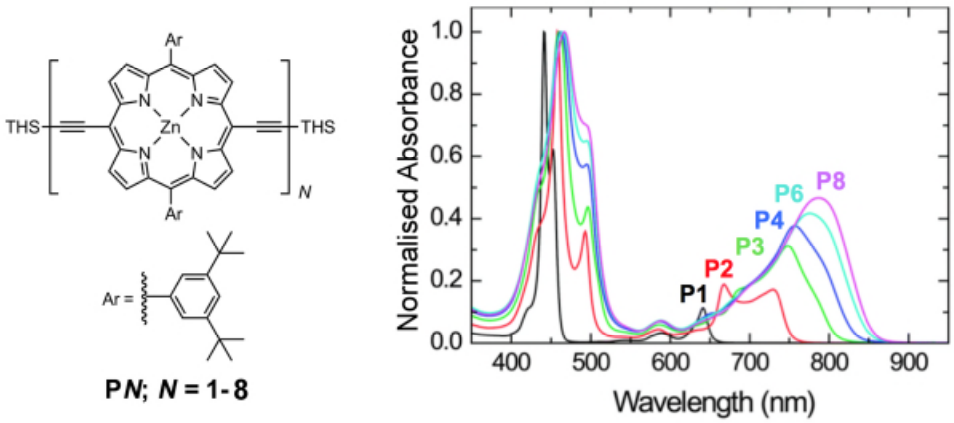

Figure 1.8 Normalised absorption spectra of **P1** (black), **P2** (red), **P3** (green), **P4** (blue), **P6** (blue sky) and **P8** (magenta).[33] Adapted with permission from Ref 33, Copyright 2016 The Royal Society of Chemistry.

In order to enhance π-conjugation between porphyrin units, the torsion angle can be locked in a coplanar arrangement using the tools of supramolecular chemistry. By forming ladder complexes with bidentate ligands such as DABCO or 4,4'-bipyridine,[35] or 1 : 1 complexes between oligomers and designed templates such as **T2** (**Figure. 1.9b**),[36] a planar conformation can be promoted. This leads to the expected red shift and sharpening of the Q band (**Figure. 1.9a** at θ = 0°).

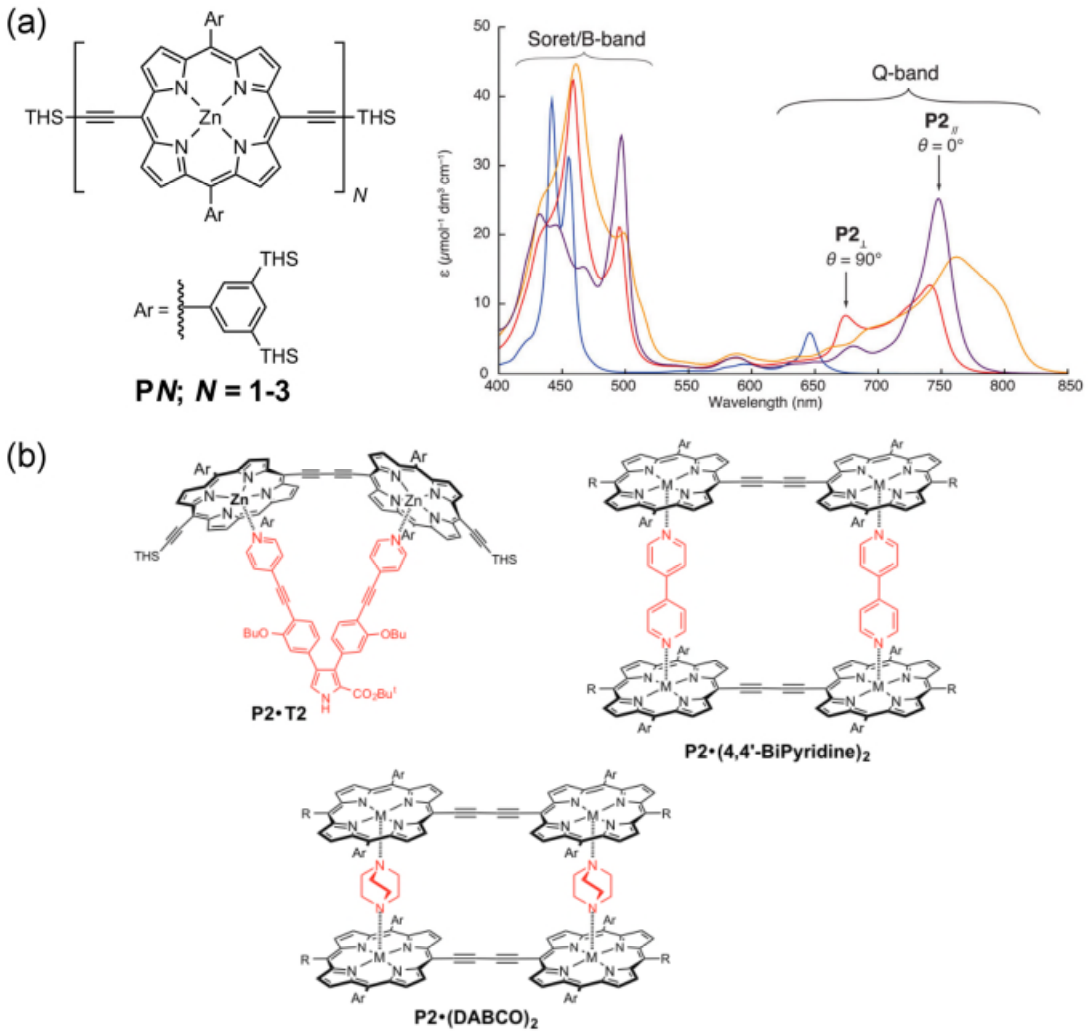

Figure 1.9 (a) Absorption spectra of linear oligomers: monomer **P1** (blue), dimer **P2** (red), trimer **P3** (yellow) and planar dimer complex **P2•T2** (purple). (Solvent: CH_2Cl_2/THF/pyridine 10:10:1, except **P2•T2**:CH_2Cl_2. THS = trihexylsilyl).[34] Adapted from Ref 34 with permission of the PCCP Owner Societies. (b) Different strategies applied to restrict the torsion angle in porphyrin dimer **P2**.

1.3.2 Synthesis of butadiyne-linked porphyrin oligomers

Apart from modification of electronic properties, one of the reasons to synthesise a variety of butadiyne-linked porphyrin oligomers has been to achieve control over the solubility and self-assembly or aggregation. The first generation of butadiyne-linked porphyrin dimers was introduced by Arnold[37] and Anderson[38] using β-alkyl solubilising groups in order to obtain good solubility. However, aggregates still form in the absence of an axial ligand such as pyridine (**Figure 1.10a**). The second generation of porphyrin dimers and longer oligomers was modified at the *meso*-positions instead of the β-positions, with aryl substituents instead of alkyl groups (**Figure 1.10b**), introduced by Anderson[39] and Ogawa.[40] These solubilising groups improve the solubility of

porphyrin oligomers and also reduce aggregation, since the aryl side group lies almost perpendicular to the porphyrin plane. In the Anderson group, the most commonly used aryl substituents are, in the order of increasing solubility, 3,5-bis-*tert*-butyl phenyl (*t*-Bu), 3,5-bis-*n*-octyloxy phenyl (C8) and 3,5-bis-trihexylsilyl phenyl (THS) groups. The synthesis of oligomer series with THS side groups (***l*-P*N*$_{THS}$**) and with C8 side groups (***l*-P*N*$_{C8}$**) is detailed here as these derivatives were used throughout this thesis.

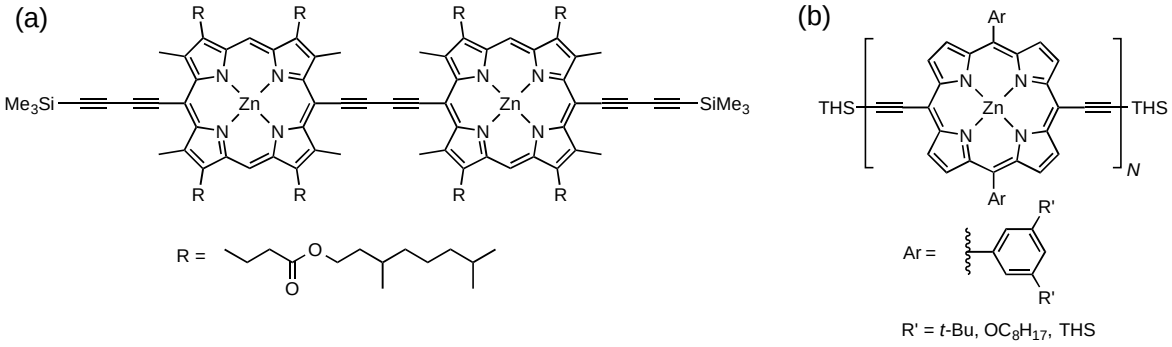

Figure 1.10 (a) The structure of the first generation of butadiyne-linked porphyrin dimer in the Anderson group.[38] (b) The structure of linear butadiyne-linked porphyrin oligomers commonly used in the recent years.

A well-established synthesis of porphyrins with identical substituents on opposing *meso*-positions was presented by Lindsey.[41] This method is based on the condensation of a functionalised aldehyde with dipyrromethane (DPM) to initially form a porphyrinogen that is subsequently oxidized to a free-base porphyrin (**Scheme 1.1**). The preparation of porphyrin monomer (***l*-P1**) using DPM **1**[42] and benzaldehyde derivatives **2a**[43] or **2b**[44] is feasible on a multi-gram scale. Free-base porphyrins **3a/b** are quantitatively metallated to zinc porphyrins **4a/b** by treating with $Zn(OAc)_2 \bullet 2H_2O$. The electrophilic bromination at the two available *meso*-positions with *N*-bromosuccinimide (NBS) is selective due to the higher HOMO coefficients at the *meso* compared to the β-positions (**Section 1.3.1**) and gives excellent yields. Then, Sonogashira coupling between dibromoporphyrins **5a/b** and trihexylsilyl-protected acetylene provides porphyrin monomers ***l*-P1$_{THS}$(THS,THS)/*l*-P1$_{C8}$(THS,THS)**, which can be used as a building block in the synthesis of porphyrin oligomers.

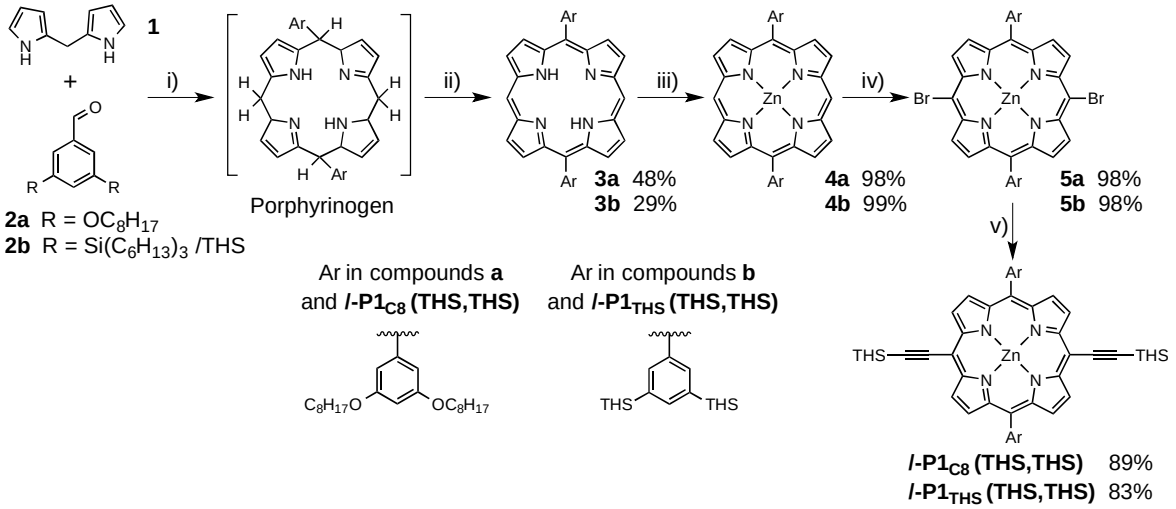

Scheme 1.1 Synthesis of the porphyrin monomer building block. THS = trihexylsilyl. Reagents and conditions: i) TFA; ii) DDQ; iii) $Zn(OAc)_2 \bullet 2H_2O$; iv) NBS; v) (trihexylsilyl)acetylene, THS-acetylene, $Pd_2(dba)_3$, PPh_3, CuI, *i*-Pr_2NH.

Porphyrin oligomers are synthesised by an iterative method using the partial deprotection of ***l*-P*N*(THS,THS)**. The THS groups on porphyrins can statistically be removed with tetra-*n*-butylammonium fluoride (TBAF), producing the desired mono-deprotected product ***l*-P*N*(H,THS)** as well as fully-deprotected product ***l*-P*N*(H,H)** and remain starting material which can be separated by column chromatography. Subsequent oxidative homo-coupling of ***l*-P*N*(H,THS)** gives a *bis*-trihexylsilyl acetylene substituted oligomer ***l*-P2*N*(THS,THS)** with a double length of the starting material in high yield (**Scheme 1.2**).[45]

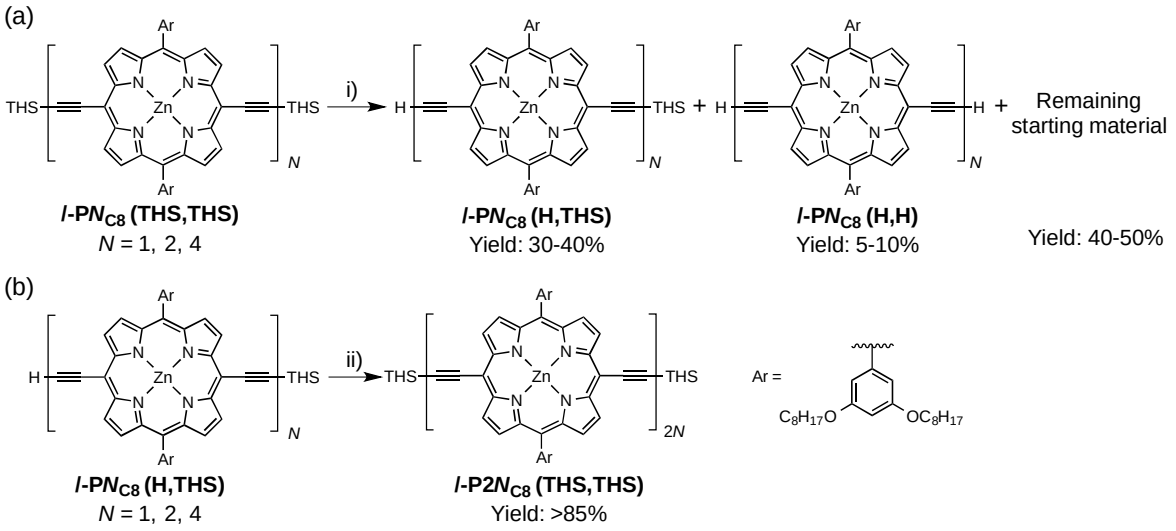

Scheme 1.2 (a) Statistical deprotection of porphyrin oligomers.[45] (b) Oxidative homo-coupling of mono-deprotected porphyrin oligomers to double the chain length. i) TBAF; ii) $Pd(PPh_3)_2Cl_2$, CuI, 1,4-benzoquinone, *i*-Pr_2NH.

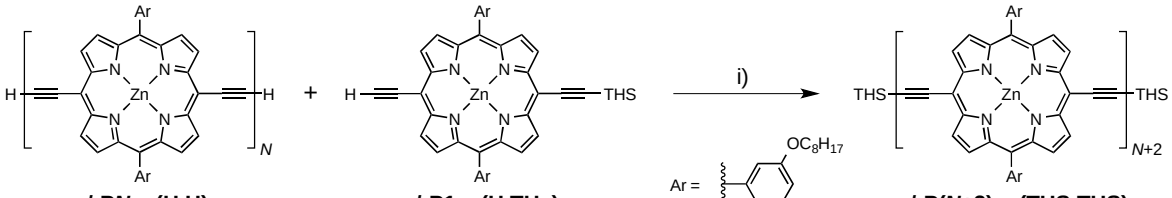

***l*-P*N*$_{C8}$ (H,H)**
1 equiv.
N = 1, 3, 8

***l*-P1$_{C8}$ (H,THS)**
4 equiv. for *N* = 1
5 equiv. for *N* = 3
28 equiv. for *N* = 8

***l*-P(*N*+2)$_{C8}$ (THS,THS)**
27% for *N* = 1
29% for *N* = 3
79% for *N* = 8

Scheme 1.3 Synthesis of linear porphyrin oligomers by "capping" strategy.[46] i) $Pd(PPh_3)_2Cl_2$, CuI, 1,4-benzoquinone, *i*-Pr_2NH.

The syntheses of oligomers that cannot be reached simply by doubling the number of porphyrin units such as trimers require a "capping" strategy (**Scheme 1.3**).[46] Oxidative coupling of fully deprotected porphyrin oligomers ***l*-P*N*(H,H)**, with large excess of ***l*-P1(H,THS)** (the "cap") produces the desired product ***l*-P(*N*+2)(THS,THS)** as well as a major fraction of ***l*-P2(THS,THS)** from homo-coupling. The excess of the "cap" prevents the polymerisation by homo-coupling of ***l*-P*N*(H,H)**, making the product mixture less complicated and also minimising wasting of precious material. For the synthesis of long oligomers, the strong aggregation due to π-π stacking should be taken into account. This could cause a low reactivity of the coupling reaction; the addition of pyridine to the reaction mixture will inhibit aggregation and enhance the formation of the desired product.

1.4 Self-assembly of porphyrins

Self-assembly has been defined by Whitesides as "*the autonomous organisation of components into patterns or structures without human intervention*".[47] Self-assembly is characterised by reversibility. The binding between Zn(II) and an amine is one of the commonly used metal-ligand combinations for porphyrin assemblies. Zn porphyrins can be five-coordinate and can rapidly and reversibly bind an axial nitrogen-based ligand (**Figure 1.11**). A sixth coordination in Zn porphyrins is rare but can sometimes be seen in the solid state[48] or in solution under particular conditions such as high concentration as a consequence of a chelate effect.[49]

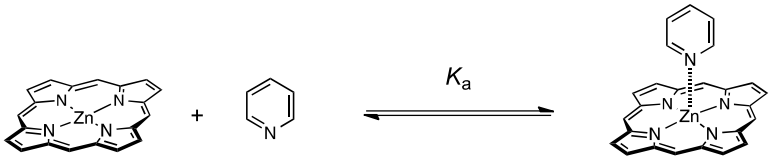

Figure 1.11 Binding of Zn porphyrin monomer with axial pyridine.

1.4.1 Thermodynamic stability of axial coordination

Prior to trying to construct a supramolecular assembly, it is important to understand the thermodynamic stability of axial coordination compounds. If the condition of coordination is badly chosen, the system will be unstable and dissociate to the individual building blocks.

For binding of nitrogen-based ligands to Zn-porphyrins, the association constants K_a can range widely from 10 to 10^9 M^{-1}, and the higher the binding constant the greater stability of the arrays that are constructed. At the lower binding constants, systems are dynamic and mixtures of associated and dissociated species can be observed by spectroscopic analysis. On the other hand, systems at the higher binding constants strongly bind together, resulting in mostly coordinated assemblies.

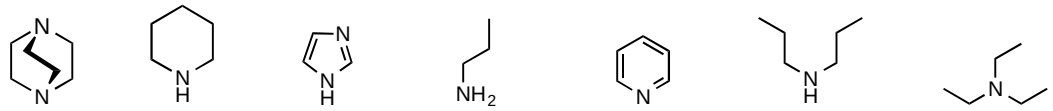

	DABCO	Piperidine	Imidazole	Propylamine	Pyridine	Dipropylamine	Triethylamine
log K_a	5.2	4.8	4.7	4.3	3.8	3.1	1.1

Figure 1.12 The order of binding constants (log K_a) of nitrogen-based ligands to Zn 5,10,15,20-tetraphenyl porphyrin (**ZnTPP**) in toluene at 298 K.[50–52]

The association constants of porphyrin-nitrogen-based ligand systems are correlated with basicity and steric hindrance of the ligands. The order of binding affinity of a selection of the nitrogen-based ligands to Zn porphyrin monomer is shown in **Figure 1.12**.[50–52] The steric hindrance increases from primary to secondary to tertiary amines, resulting in a decreasing binding affinity from propylamine to dipropylamine and then to triethylamine. Similarly, when the steric hindrance of cyclic secondary and tertiary amines is reduced, their binding constants increase as seen when comparing DABCO and triethylamine. When the differences in steric interferences become insignificant, among the aromatic ligands, the relationship between the stability constant

and the basicity increases. This is evident for the more basic imidazole which has a binding constant 10 times greater than that of pyridine.

Solvent and temperature also play an important role in binding affinities. The binding constants of Zn porphyrin monomer with pyridine in various solvents at 25 ºC are reported in the order of decreasing binding constants as follows: cyclohexane > dichloromethane ≈ toluene > chloroform.[53] Increasing the temperature reduces the binding constant.

1.4.2 Pyridyl porphyrin as ligands

Substituted pyridines are the most extensively studied classes of ligands for Zn porphyrins. Functionalised pyridyl substituents can be directly incorporated during porphyrin syntheses in order to design porphyrins as axial ligands. The *meso*-pyridine substituted porphyrins are mostly used in multi-porphyrin arrays in any possible combination of stoichiometries (mono- to tetra-pyridyl porphyrin) and substitution patterns (for example, 5,10- or 5,15-di–pyridyl porphyrin) as shown in **Figure 1.13**, which shows how the different substitution patterns of the pyridyl porphyrin (arrowed square) reflect the overall geometry of the array as linear, angular, T-shape or cruciform complexes.

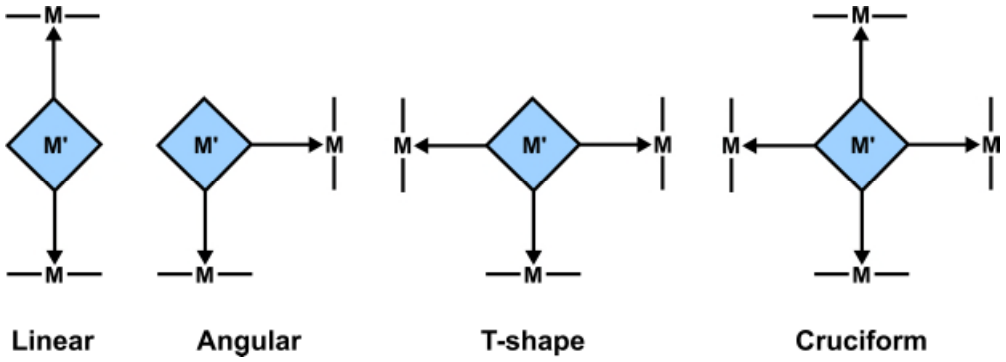

Figure 1.13 The representation of the porphyrin-as-ligand complexation.

Pyridyl porphyrins are commonly used as free-base porphyrins in the coordination to Zn porphyrins[54] in order to avoid the self-assembly of the pyridyl porphyrins among themselves. However, zinc metallated porphyrins with pyridyl substituents are also found in self-sorting assemblies.[55]

As described in **Section 1.3.1**, butadiyne-linked porphyrins have a distribution of torsional angles between the porphyrin planes.[34] However, the formation of a triple-strand porphyrin array (**Figure 1.14a**) leads to a stable system in which the porphyrin planes are restricted to a co-planar arrangement.[56] This is apparent from the increased red shift of the Q bands in UV-vis absorption spectrum of the complex compared to the individual components (**Figure 1.14b**). The design of the pyridyl porphyrin structures that are being used throughout this thesis is based on the one in the triple strand array. Similarly, the studies can be extended to more complex structures like tritopic porphyrin and hexatopic pyridyl porphyrins binding into the cavities of cyclic porphyrin hexamers as reported by Gossauer (**Figure 1.14c**).[57] The binding constants of such complexes are in the range of 10^9-10^{10} M^{-1}, due to the additive effect of the individual Zn-pyridine binding events. The hexameric wheels can act as an antenna and about 43% energy transfer from the Zn porphyrin wheel to the free-base pyridyl porphyrin was observed by fluorescence spectroscopy.[58]

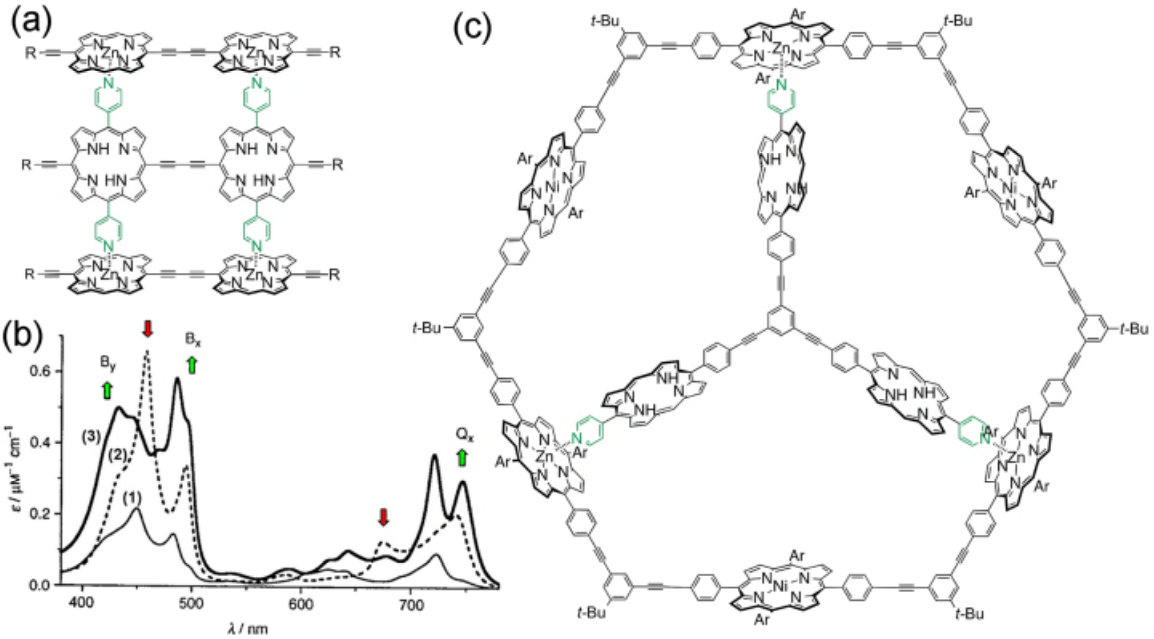

Figure 1.14 (a) Triple-strand porphyrin array. (b) The UV-vis absorption spectra of (1) the free-base dimer, (2) the Zn-dimer-$(pyridine)_2$ complex (3) triple strand complex in DCM. The scale of (2) is multiplied by two to facilitate comparison with (3). Arrows highlight regions of increased (green) or decreased (red) absorption in the complex (3). Adapted from Ref 56 with permission of The Royal Society of Chemistry. (c) Tritopic pyridyl porphyrin complexed with a cyclic Zn-porphyrin hexamer.

In another example, pyridyl porphyrins are used in self-sorting processes. In this case, pyridyl porphyrins are metallated with Zn, which allows them to bind to themselves. The dimensionality of

the porphyrin arrays may increase from porphyrin monomers to oligomers as seen in the following example. *meso*-Pyridine-substituted porphyrin monomer forms a supramolecular square (**Figure 1.15a**),[55] but the corresponding *meso*-dimer self-assembles into a box (**Figure 1.15b**)[55] with interesting homochiral self-sorting assembly of *R* and *S* enantiomers.

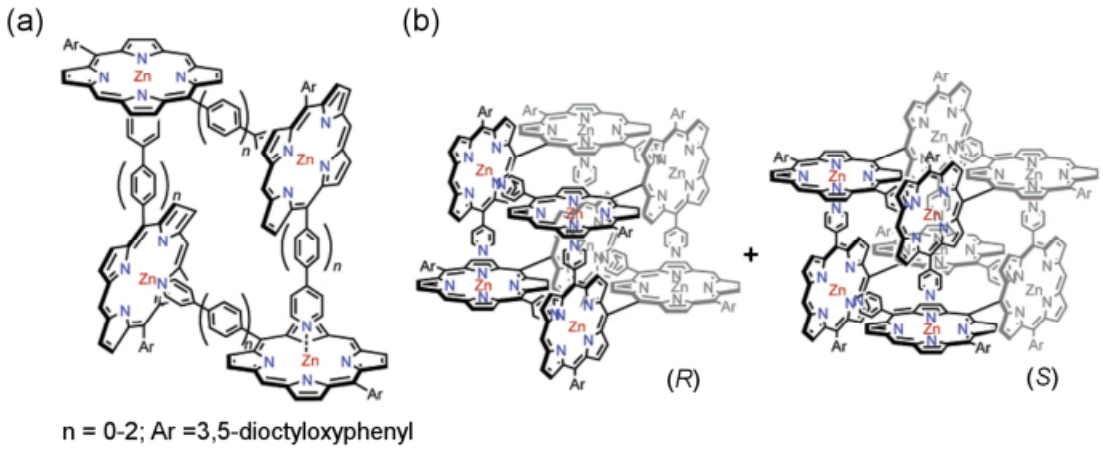

Figure 1.15 Self-sorting assemblies of pyridyl Zn porphyrins. (a) Formation of two-dimensional porphyrin squares from pyridyl porphyrin monomers. (b) Formation of three-dimensional porphyrin boxes from pyridyl porphyrin dimers. Homochiral self-sorting results in the formation of enantiomers. Adapted with permission from Ref 55. Copyright 2016 American Chemical Society.

1.5 Energy transfer in synthetic porphyrins

1.5.1 Photophysical processes – the Jablonski diagram

Absorption and emission pathways in molecules after electronic excitation can be explained by means of a Jablonski diagram. Photoexcitation starts when a molecule in the ground state (S_0) absorbs a photon. One electron is excited to a higher orbital level (S_1, S_2, S_3...) depending on photon's energy. The higher excited singlet states will rapidly relax non-radiatively by internal conversion (IC) to S_1. This excited state can then relax to S_0 either via IC, or the process called fluorescence, which emits a photon as shown in **Figure 1.16**.

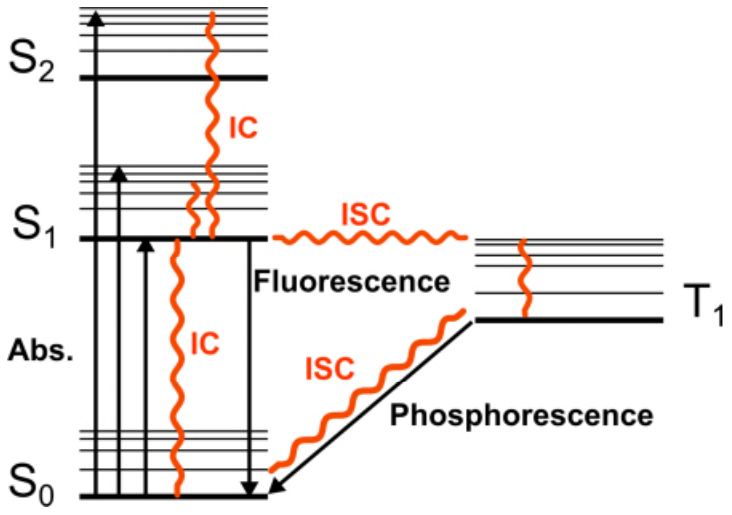

Figure 1.16 Jablonski diagram. Straight arrows indicate radiative pathways and curly lines indicate non-radiative pathways. Thin lines indicate vibrational levels.

Alternatively, the S_1 excited state can undergo spin inversion by (non-radiative) intersystem crossing (ISC) and generate a different excited state, a triplet state (T_1). This triplet state can relax to the ground state S_0 by either ISC or photon-emitting phosphorescence (**Figure 1.16**). As opposed to fluorescence, this process implies a change of electronic spin, which is forbidden by spin selection rules, making phosphorescence (radiative decay from T_1 to S_0) much slower than fluorescence (radiative decay from S_1 to S_0). Therefore, triplet states have lifetimes ranging from microseconds to seconds while singlet state lifetimes are on nanosecond timescales.[59] The singlet and triplet excited states can be deactivated by electron or energy transfer to other chromophores. Energy transfer is a non-radiative process in which the excited molecule relaxes to the ground state and another molecule is then elevated to an excited state.

1.5.2 The mechanism of excitation-energy transfer in photosynthetic systems

Energy transfer in supramolecular systems is considered as a non-radiative transition between two "localised" electronically excited states: the originally excited molecule, the donor (D) and the finally excited molecule, the acceptor (A). The electronic coupling between the two excited states interconverted by the energy transfer process involves the HOMOs and LUMOs of the energy-donor and energy–acceptor components. This coupling can be split into two terms called an *exchange* term and a *Coulombic* term. The two terms differ greatly in their dependence on spin of

ground and excited states, donor-acceptor distance, etc. **Figure 1.17** represents the exchange and Coulombic mechanisms.[60]

The exchange (also called Dexter-type[61]) mechanism is closely related to electron transfer. It is allowed even if the energy transfer involves forbidden states on D and A, such as in the case of triplet excitation transfer, and it requires orbital overlap between D and A, which typically requires short distances, ≤ 0.5 nm.[61] Its rate constant exponentially decreases with increasing distance. The energy transfer rate, k_{dexter} is given by

$$k_{\text{dexter}} = KJ\exp\left(\frac{-2R_{\text{DA}}}{L}\right) \qquad \textbf{(eq. 1.2)}$$

in which J is the normalised absorption and emission spectral overlap integral, K is an experimental factor, R_{DA} is the distance between D and A, and L is the effective orbital radius.

The exchange interaction can be considered (**Figure 1.17**) as a double electron transfer process; one electron moving from the LUMO of the excited donor (D*) to the LUMO of the excited acceptor (A*), and the other from the acceptor HOMO to the donor HOMO.

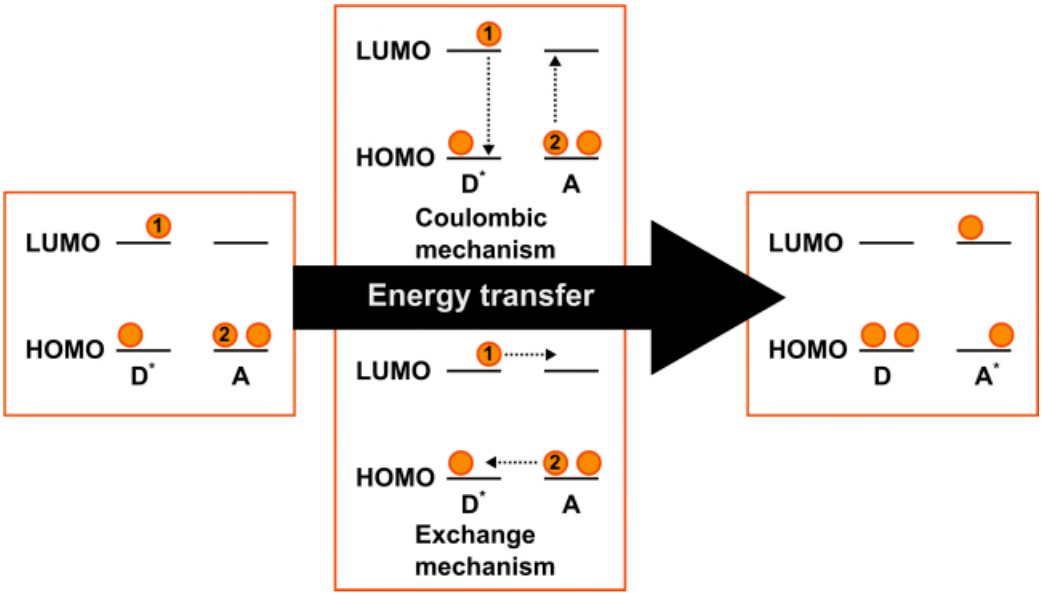

Figure 1.17 The exchange (Dexter) and coulombic (Förster) mechanisms.

The Coulombic (also called Förster-type[62]) mechanism is effective over larger distances (up to ~3 nm) and does not require physical contact between D and A. The most important term within the Coulombic interaction is the dipole–dipole term, following the same selection rules as the corresponding dipole transitions of the two partners (D*→D and A→A*, **Figure 1.17**). Thus,

systems in which each partner has a high probability of transition by photon absorption and emission (i.e. high oscillator strength) are likely to have efficient Coulombic energy transfer. The rate constant for the dipole–dipole Coulombic energy transfer can be approximated by the expression as shown below:[60]

$$k_{\text{Förster}} = 8.8 \times 10^{-25} \frac{K^2 \Phi}{n^4 R_{DA}^6 \tau} J_{\text{F}} \qquad \textbf{(eq. 1.3)},$$

where K is an orientation factor which accounts for the directional nature of the dipole–dipole interaction (it can take values from 0 for a perpendicular arrangement to 4 for a parallel arrangement), Φ and τ are the luminescence quantum yield and lifetime of the donor respectively, n is the solvent refractive index, R_{DA} is the distance (in Å) between donor and acceptor, and J_{F} is the Förster overlap integral between the luminescence spectrum of the donor and the absorption spectrum of the acceptor on an energy scale (cm^{-1}).

1.5.3 Synthetic light harvesting molecules

As described in **Section 1.1**, the energy transfer in photosynthetic organisms is extremely efficient (> 90%) due to optimal relative positioning of the chromophores. To mimic the structure and function of the LH antenna complexes of natural systems, cyclic porphyrin arrays have been developed over the last couple of decades. These cyclic porphyrin arrays can be classified into two types: closed-ring and dendritic structures.[63,64] Arrays with closed ring architecture are accessible by means of covalent bonding and supramolecular self-assembling. The covalent-linked porphyrin arrays have an advantage in structural robustness while the advantage of self-assembly of cyclic structures is the relatively easy synthetic accessibility. For the latter, the designed building units automatically arrange themselves into cyclic structures based on complementary coordination. However, non-covalently assembled arrays are usually sensitive to their environment. For instance, dissociation of array occurs in coordinating solvents or in the presence of competing coordination species like pyridine. Alternatively, dendritic architectures can be used to form petal-like cyclic structures which benefit from the large number of porphyrin units in three-dimensional space to provide high absorptivity and also high quantum efficiency of energy transfer as a consequence of

multiple energy migration pathways. **Figure 1.18** shows some selected examples of synthetic cyclic arrays with closed-ring (including covalent bonding, fully conjugated covalent bonding and self-assembling) and with dendritic structures.[64]

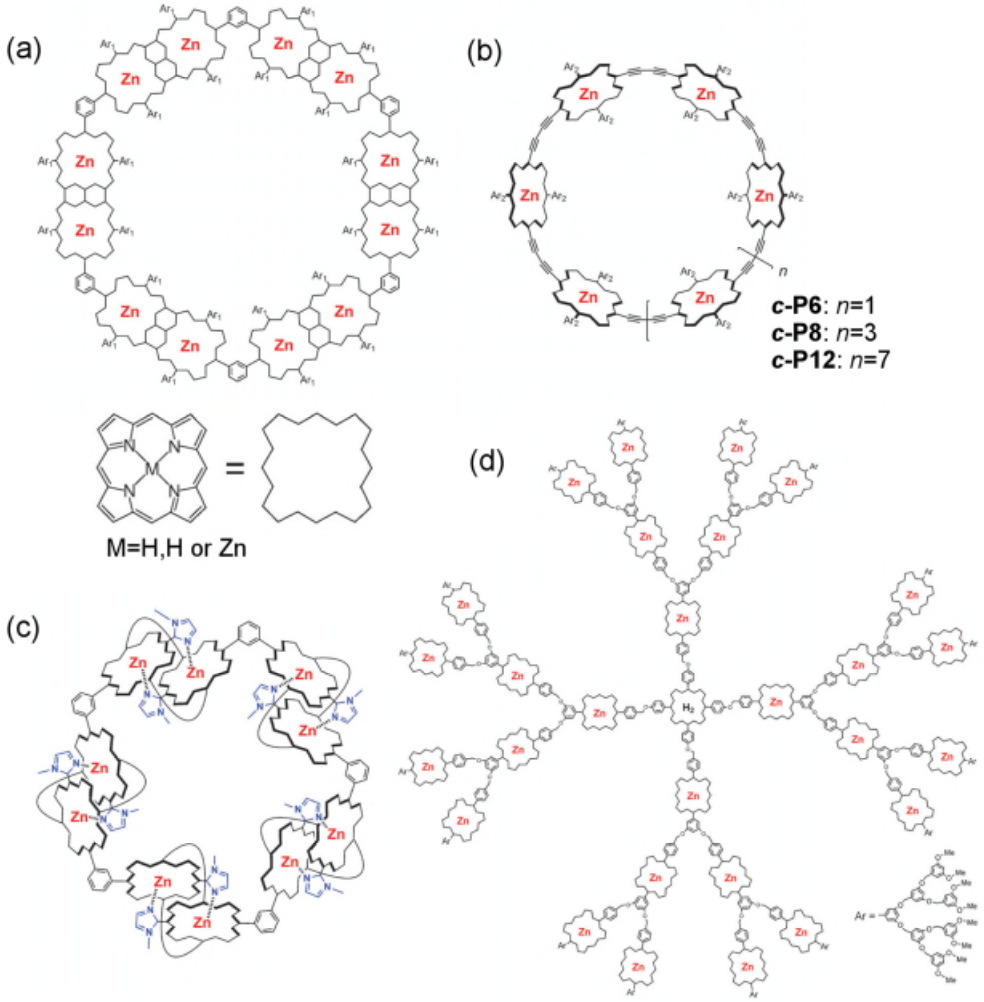

Figure 1.18 Selected examples of synthetic cyclic porphyrin arrays with closed ring including (a) covalent bonding, (b) fully conjugated covalent bonding and (c) self-assembling, and with (d) dendritic structures. Adapted from Ref 64 with permission of The Royal Society of Chemistry.

Fully conjugated cyclic porphyrin arrays (**Figure 1.18b**) were first introduced by Anderson and can be prepared by template-directed synthesis, with sizes up to 50 porphyrin units.[65] The absorption of these porphyrin rings reaches the NIR region due to the delocalisation of the π system over the entire or at least most of the molecular frameworks (**Figure 1.19a**). The extent of π-conjugation also depends on their ring size, and the absorption and fluorescence spectra are correlated with their electronic structures. For example, for the most symmetric compound ***c*-P6•T6**, 6-ring (***c*-P6**) with wheel-like template (**T6**) inside, the energy-level structure can be

described by the simple Hückel molecular orbital method of cyclic π-conjugated molecule mimicking the symmetry of benzene (**Figure 1.19b**). The absorption spectrum of ***c*-P6•T6** is dominated by the strongly allowed, two degenerate (k = ±1) states of orthogonal polarisation. The lowest (k = 0) transition state is essentially forbidden due to the high symmetry of ***c*-P6•T6** in a hexagonal arrangement causing dipole contributions summing to zero.[66,67] Thus, when the molecule has relaxed back to its lowest (k = 0) state, emission is expected to be strongly suppressed. However, the emission in the NIR region can be observed. This forbidden transition becomes allowed by the combination of vibrational and electronic states which creates the new symmetry, i.e. Herzberg-Teller coupling (**Figure 1.19c**).[67] Therefore, when ***c*-P6•T6** absorbs light through the degenerate (k = ±1) states that are orthogonally polarised, which is followed by a relaxation to the k = 0 state, the forbidden emission from this state takes place via the weak Herzberg-Teller coupling. The low fluorescence quantum yield and small radiative constant of this complex are observed as a consequence of a fully delocalised lowest excited state over all six porphyrin units.[66]

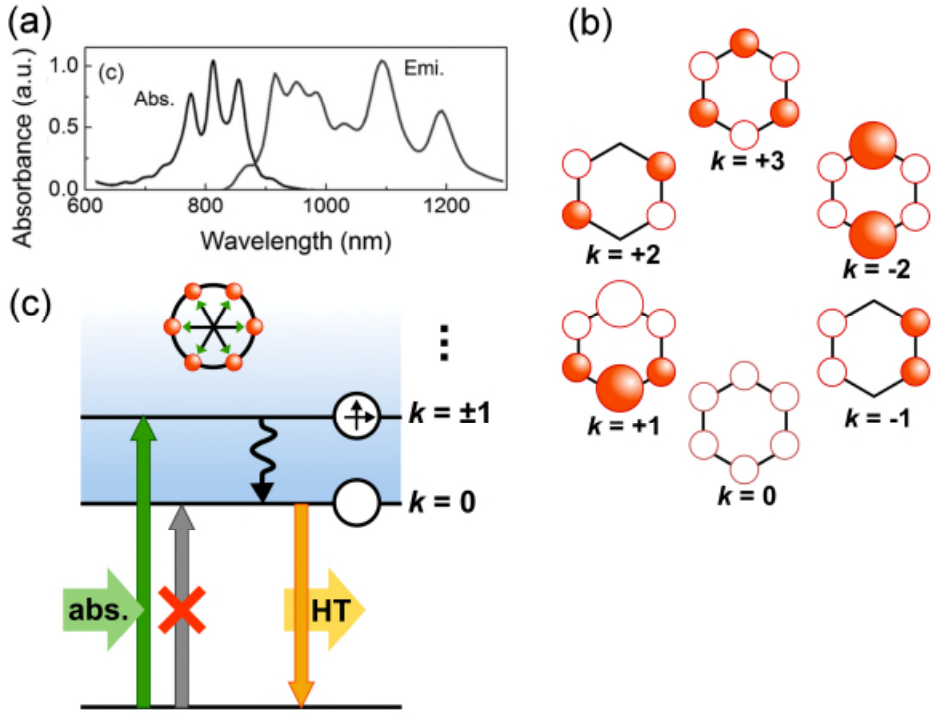

Figure 1.19 (a) Steady-state absorption and emission spectra of ***c*-P6•T6**. Adapted from Ref 66 with permission of The Royal Society of Chemistry. (b) The Hückel molecular orbital of benzene. (c) Schematic diagram showing Herzberg-Teller activating transitions from the k = 0 state to ground state.

Studies of energy transfer from antenna chromophores to a synthetic nanoring have been limited by the ability to create such a system. In **Chapter 2**, we present the synthesis and energy transfer dynamics of two supramolecular antenna-nanoring complexes of a 12-porphyrin ring with two different free-base porphyrin dimers whose architectures resemble the LH2 complexes in nature.

1.6 Template-directed synthesis

What is a template? In the context of organic synthesis, Busch gave a definition as *"A chemical template organizes an assembly of atoms with respect to one or more geometric loci, in order to achieve a particular linking of atoms."*[68] This is a general definition to highlight the features of a template as an instruction to form a single product from a substrate or substrates which otherwise tend to assemble and react in uncontrollable ways.

1.6.1 Cyclic and linear templated reactions of functionalised porphyrins

Templates can be classified by their topology as cyclisation, linear and interweaving (**Figure 1.20**).[69] The porphyrins in this thesis are prepared by using templates in the first two categories. Metal coordination allows organic ligands to be used as templates in porphyrin synthesis due to the fact that metalloporphyrins can bind axial ligands such as pyridine.

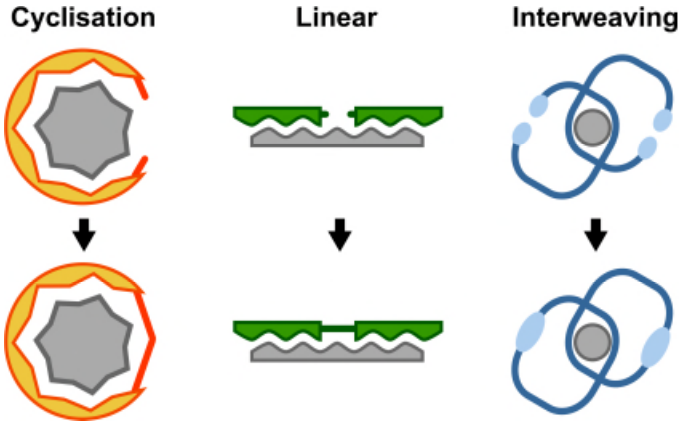

Figure 1.20 Classification of templates according to their topology of operation.

Cyclisation templates. A wheel-like template is one of the most widely used shapes to direct the porphyrin substrates into a conformation in which cyclisation is favoured. The first cyclic

porphyrin trimer was prepared by Sanders and Anderson in 1989 using Glaser coupling,[70] by oxidatively coupling two terminal acetylenes to give a butadiyne bridge. Synthesis of the cyclic porphyrin trimer ***c*-P3** was effectively templated by tripyridyltriazine **T3** (**Scheme 1.4**). Using efficient template-directed reactions, Sanders has been successful in preparing a number of cyclic porphyrin arrays comprised of 2-4 porphyrins linked by aryl or alkynyl units.[71]

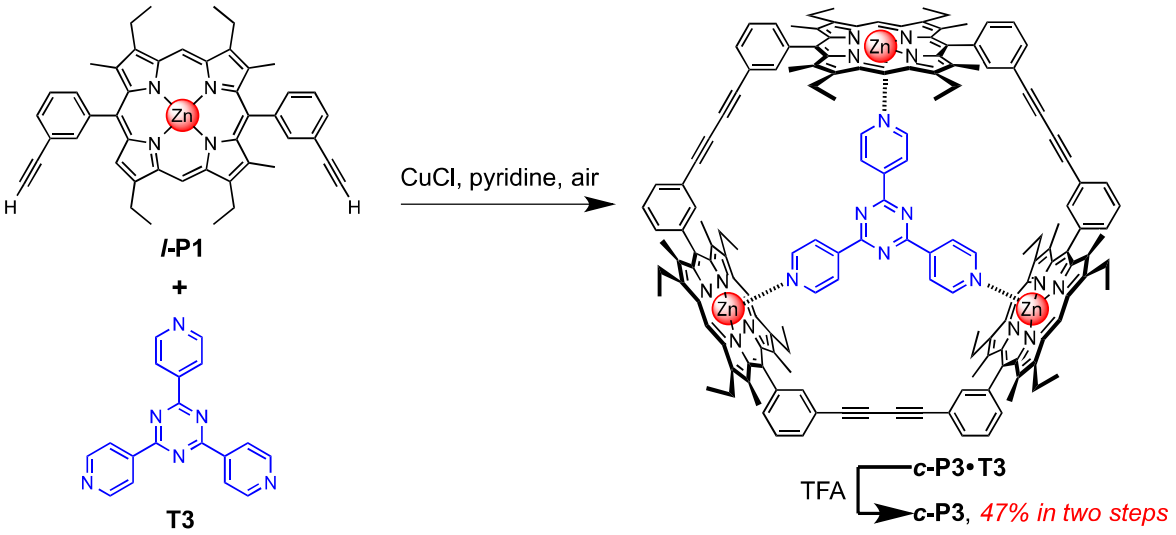

Scheme 1.4 Synthesis of cyclic porphyrin trimer ***c*-P3** was effectively templated by tripyridyltriazine **T3**. TFA = trifluoroacetic acid.

Likewise, Anderson has used a variety of radial templates to direct formation of fully conjugated cyclic porphyrin oligomers comprised of 6, 8 or 12 porphyrin units. The interaction of Zn-porphyrin subunits with pyridine residues helps to arrange linear porphyrin building blocks around a circular template before their terminal acetylene ends are oxidatively coupled to yield a nanoring-template complex. Upon treatment with competing ligands, such as pyridine or DABCO, the complex can liberate the template resulting in the corresponding metal-free porphyrin nanoring. Cyclic porphyrin octamer (***c*-P8**) was first synthesised by coupling linear porphyrin octamer (***l*-P8**) at 60 ºC in the presence of a complementary octadentate template **T8** in 14% yield, followed by efficient removal of **T8** by treatment with excess pyridine (**Scheme 1.5**).[72] By using a radial hexadentate template **T6** instead, cyclic porphyrin hexamer ***c*-P6** can be synthesised in a similar approach from linear porphyrin dimer ***l*-P2**, giving the desired product (***c*-P6•T6**) in 33% yield (**Scheme 1.6**).[73] Replacing the dimer ***l*-P2** substrate with monomer ***l*-P1** under the same conditions

gave only a 5% yield of ***c*-P6•T6**, but further optimisation by replacing iodine with 1,4-benzoquinone[74] and lowering the temperature from 60 ºC to 20 ºC gave ***c*-P6•T6** in 21% yield.[66] The increased efficiency of this synthesis is partly a consequence of the stronger interaction of the zinc porphyrin units with the template at lower temperature.

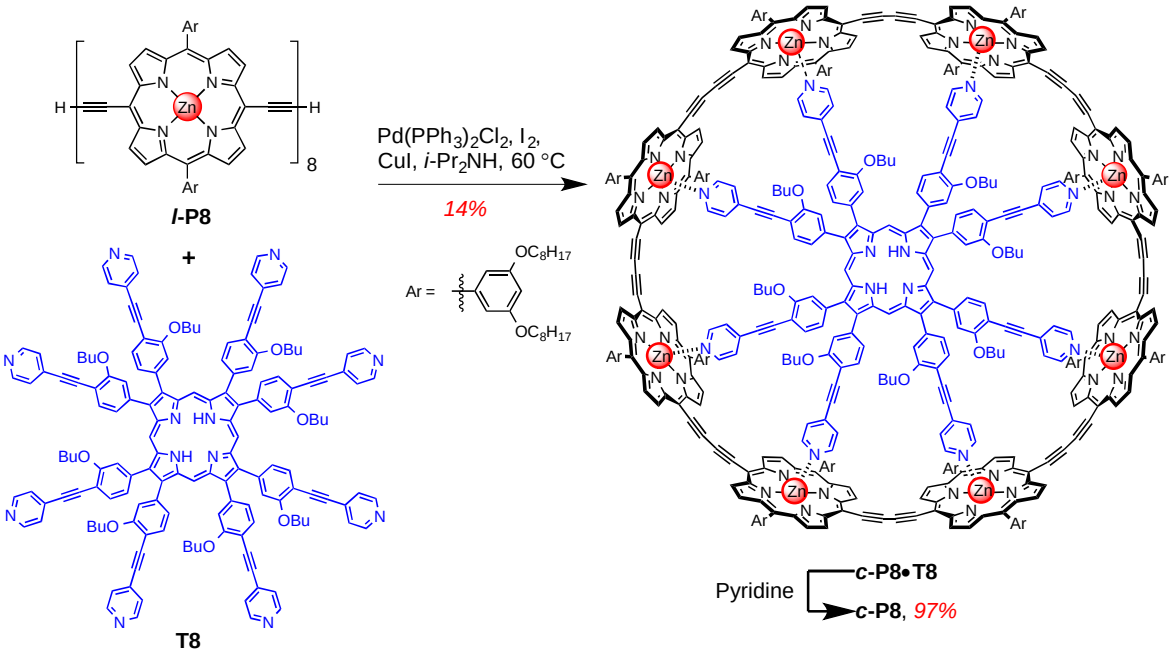

Scheme 1.5 Template-directed synthesis of cyclic porphyrin octamer ***c*-P8** from linear octamer ***l*-P8**.

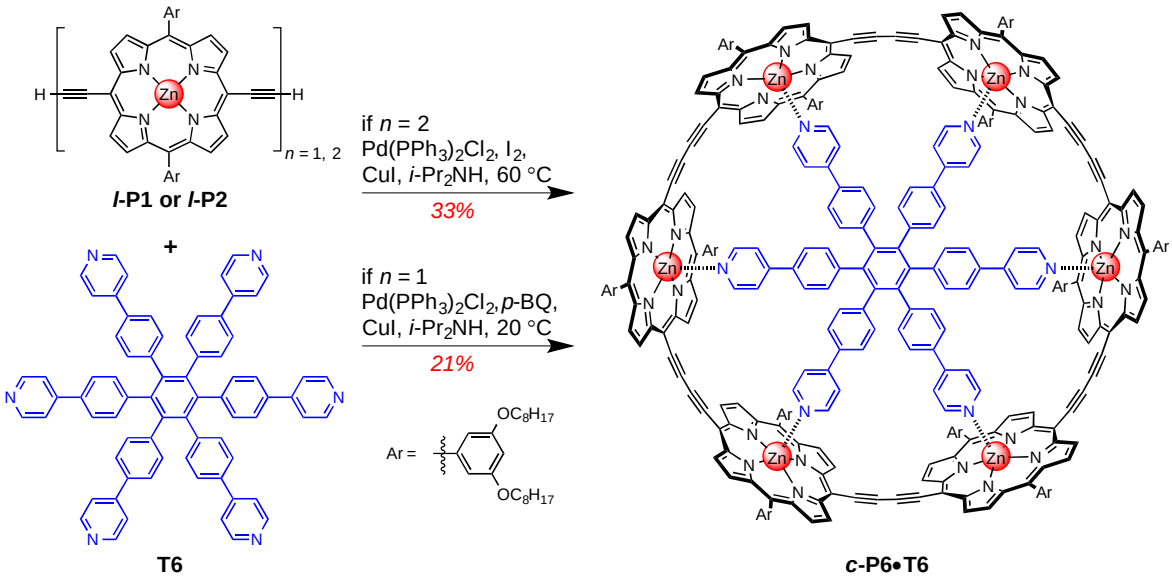

Scheme 1.6 Template-directed synthesis of cyclic porphyrin hexamer ***c*-P6** from various linear porphyrin precursors such as dimer ***l*-P2** and monomer ***l*-P1**. *p*-BQ = *p*-benzoquinone.

Linear templates. DNA replication is a supreme example of linear template-assisted synthesis that is believed to have played an essential role in the origin of life. Owing to its robust mechanism in which the duplex can separate into two strands and each individual strand can then act as a template for the formation of two new duplexes, the synthesis and amplification of any types of DNA sequence are very efficient.[75] Recently, a template-directed synthesis reminiscent of the DNA system was developed as a powerful strategy in the synthesis of nano-scale 2D or 3D structures of either organic[69,76–84] or bio-macromolecules.[85–88] The template-driven process for the construction of a wide range of such supramolecular assemblies requires mutual complementarity of the components to hold them together.

In the synthesis of linear porphyrin oligomers, the simplest strategy is dimerization of partially deprotected material, but this reaction can be carried out efficiently only in the absence of fully deprotected molecules to avoid the oligomerisation between themselves together with the partially deprotected material. Column chromatography is needed to separate the fully deprotected molecules before coupling but this becomes more difficult with increasing the number of porphyrin units. As shown in **Figure 1.21**, the use of templates as *scavengers* can overcome this problem since the template induces molecules with two reactive ends to cyclise and mono-deprotected molecules are left to couple with each other.[79] After coupling, the separation is much easier because the desired linear compound is twice the size of either the starting material or the cyclic by-product. This approach was successfully used to synthesise linear porphyrin oligomers such as octamer (***l*-P8**). The statistical mixture of mono-deprotected, fully deprotected tetramer and the remaining starting material from the statistical deprotection of tetramer (***l*-P4**) can be directly used to oxidatively couple in the presence of the four-legged template (**H2-Py4P**). As expected, this templated reaction produced the desired linear octamer (***l*-P8**) in 50% analytical yield while the cyclised tetramer (***c*-P4**) and the unreacted starting material were provided in 25% analytical yield each.

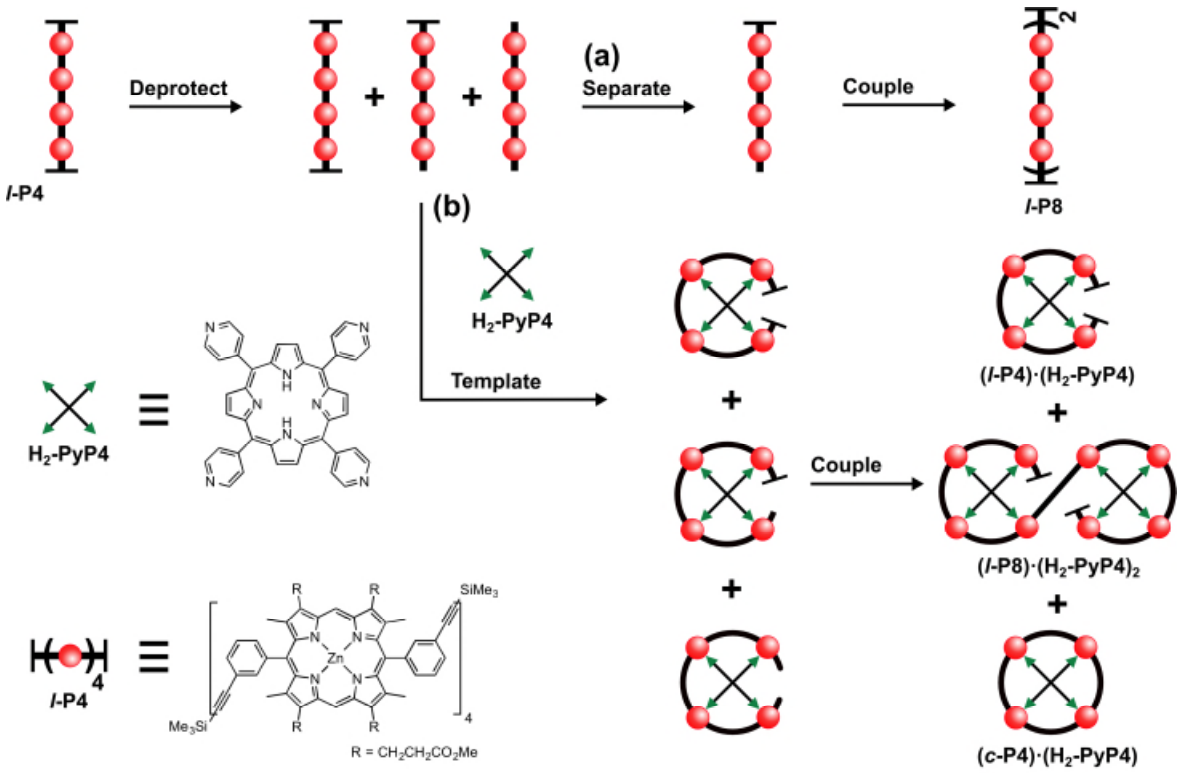

Figure 1.21 (a) A general strategy for the formation of a linear octamer ***l*-P8** from a symmetrically protected tetramer ***l*-P4**. (b) A scavenger template induces molecules with two reactive ends to cyclise, thus allowing efficient coupling of mono-deprotected material. Capping lines represent protecting groups.

The work of Anderson, Anderson and Sanders has shown how the metal-ligand coordination between metalloporphyrins and axial amine ligands can be used to form different supramolecular architectures.[79] **Chapter 4** describes the attempts to utilise the principles of self-assembly to synthesise linear conjugated porphyrin oligomers by linear template-directed reactions.

1.6.2 Vernier assemblies and Vernier templated reactions

The use of the Vernier principle in chemical self-assembly was first proposed in 1991; it exploits the mismatch between binding sites of two complementary components to bind each other until all binding sites are occupied.[89] The total number of binding sites in a Vernier assembly is the lowest common multiple of the number of binding sites in its components. In 1998, Kelly reported the first example of a 3+2 molecular Vernier complex using H-bonding between two molecules of triguanidium **A** and three molecules of dicarboxylate **B**.[90] The binding groups in the respective monomers **A** and **B** were held at a fixed distance by a rigid aromatic backbone. The Vernier

complex is simply obtained in quantitative yield by mixing **A** and **B** in the stoichiometry of 2:3 (**Scheme 1.7**).

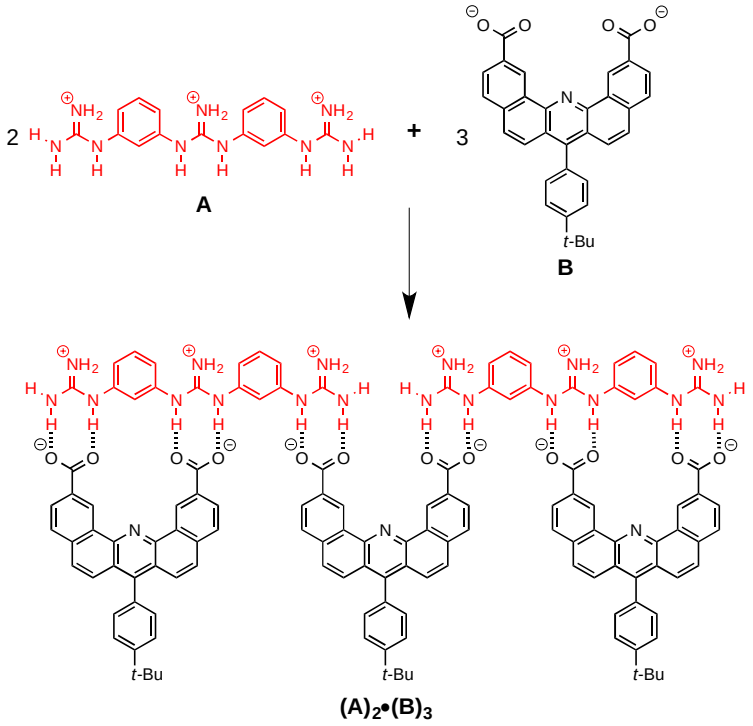

Scheme 1.7 The first example of a 3+2 molecular Vernier complex using two molecules of a triguanidium **A** and three molecules of dicarboxylate **B**.

Later, Hunter revealed that the stability of a Vernier complex could be limited by the weakest link in the chain.[91] A triple stranded Vernier approach was proposed as the solution, since the weakest link now has cooperative interactions to two interstrand bindings, making the whole Vernier system more stable (**Figure 1.22**). This approach utilised two types of linear porphyrin oligomers as the scaffold with identical spacings between monomer binding sites that are complementary to each other. A tin porphyrin dimer was treated with isonicotinic acid, giving the complex **Sn2L$_4$**, and a zinc porphyrin trimer **Zn3** was used as a complementary binding unit to form a three stranded Vernier assembly (**Figure 1.23**). The results from fluorescence titration and size exclusion chromatography (SEC) confirmed formation of the 4:3 Vernier complex, but the method was highly sensitive to variations in concentration and the relative stoichiometry of two types of porphyrins.

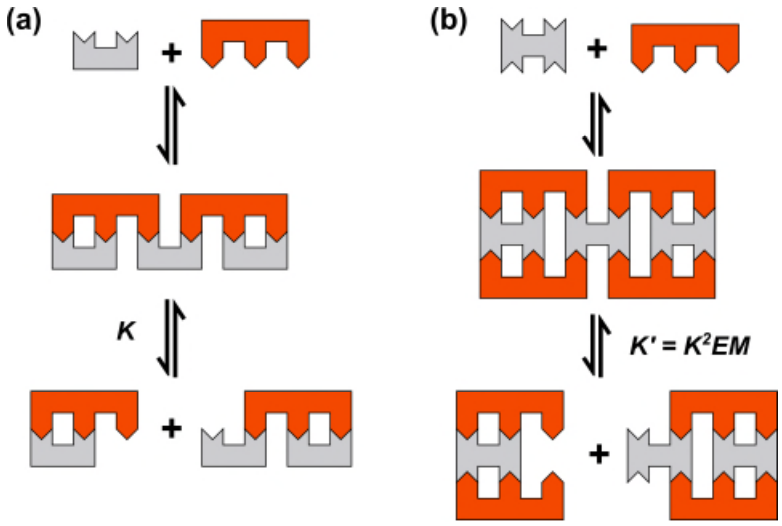

Figure 1.22 (a) The stability of double-strand Vernier assembly is limited by a weakest link (monodentate link) with binding constant (*K*). (b) A triple-strand Vernier assembly is more stable than a simple double-strand Vernier assembly as in (a) due to stronger cooperativity. *EM* is the effective of molarity of the second intramolecular interaction and statistical factors are ignored for simplicity.

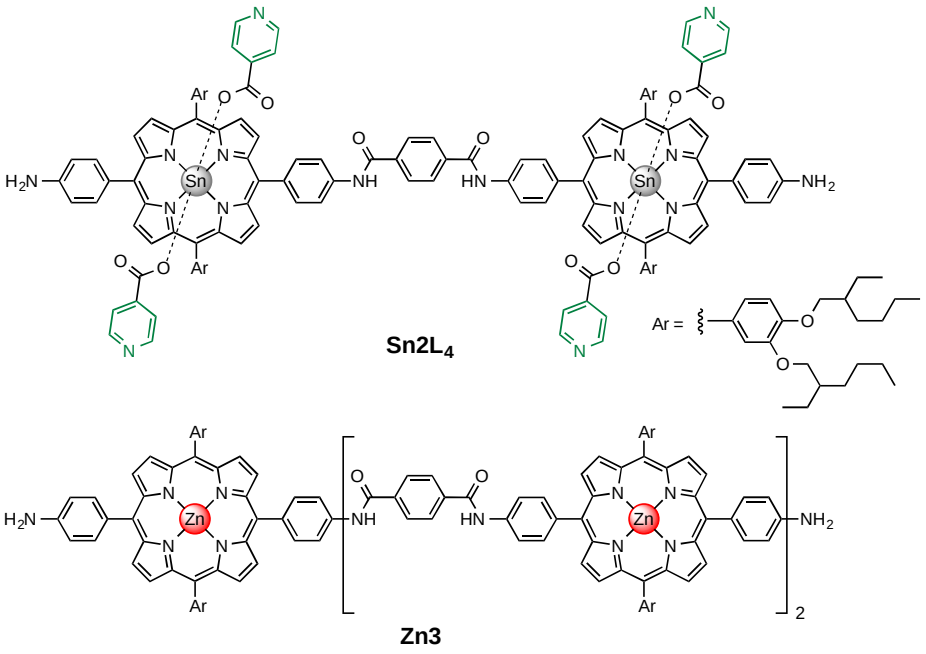

Figure 1.23 Tetraisonicotinate tin porphyrin dimer **Sn2L$_4$** and zinc porphyrin trimer **Zn3** were used in the formation of Hunter's triple-strand 3+2 Vernier complex.

Anderson showed the novel concept of Vernier template-directed synthesis using subsequent ligation to connect arranged components of a Vernier assembly into a covalent strand in Vernier architectures. Recently, we exhibited efficient cyclic Vernier templating using the stoichiometric combination of a radial hexadentate ligand template **T6** and a zinc porphyrin tetramer (***l*-P4**) to produce a 12-unit porphyrin nanoring ***c*-P12** in 39% isolated yield (**Figure 1.24**).[92,93] The structure

of the Vernier product ***c*-P12•(T6)$_2$** was confirmed by small-angle X-ray scattering (SAXS) and X-ray crystallography. With the same approach, larger porphyrin nanorings can be synthesised with the sizes from 30 to 50 units (**Figure 1.25a**).[65] The STM images of these nanorings revealed their topology as shown in **Figure 1.25b**,**c**. Inspired by the efficient Vernier template effect in the synthesis of cyclic porphyrins, we attempted to adapt the approach to synthesise linear Vernier porphyrin oligomers using the same number of binding sites as in the cyclic Vernier templating; this research is described in **Chapter 4**.

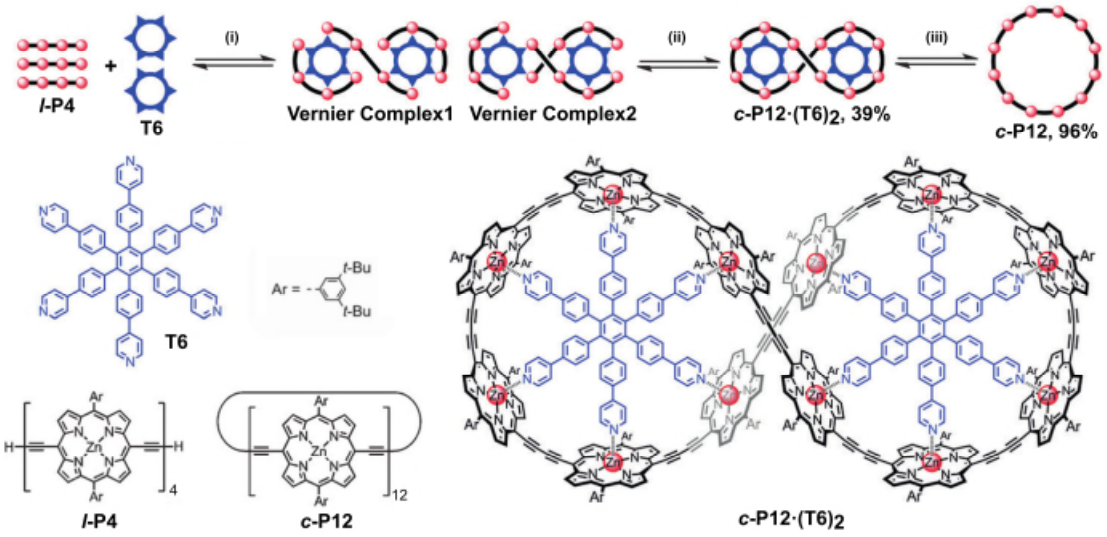

Figure 1.24 Vernier template-directed synthesis of cyclic porphyrin dodecamer ***c*-P12** from linear porphyrin tetramers ***l*-P4** and hexapyridyl ligand template **T6**. i) Self-assembly; ii) $Pd(PPh_3)_2Cl_2$, CuI, 1,4-benzoquinone, *i*-Pr_2NH; iii) Pyridine. Adapted with permission from ref. 92, Copyright 2016 John Wiley and Sons.

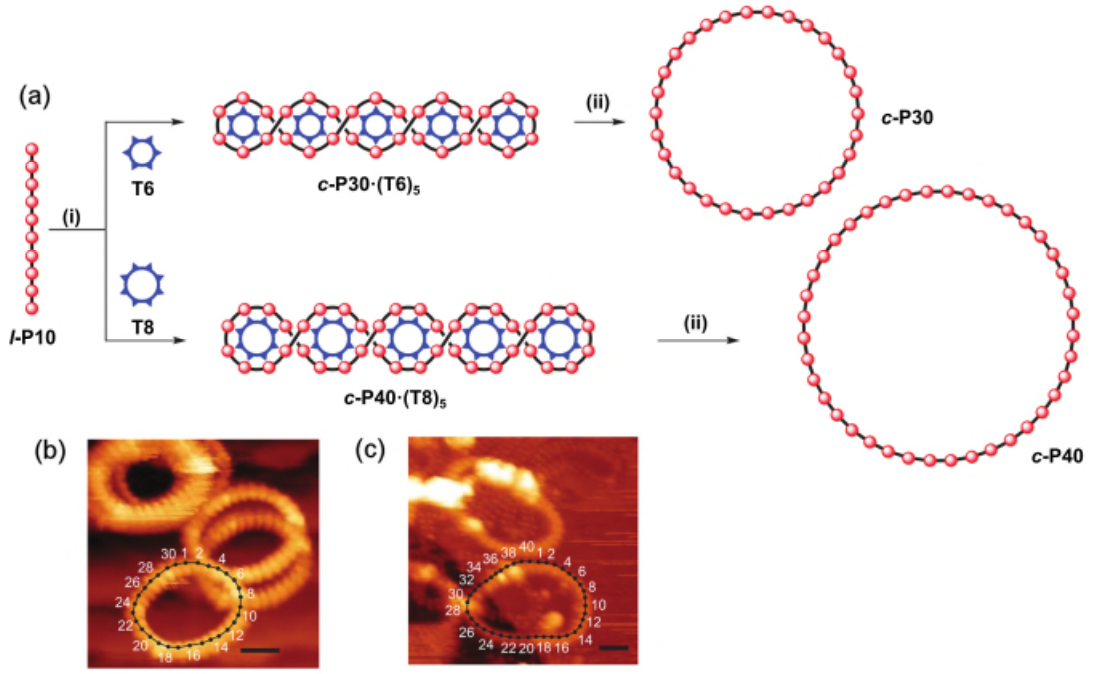

Figure 1.25 (a) Vernier-template-directed syntheses of large cyclic porphyrin nanorings: ***c*-P30** (from ***l*-P10** and **T6**) and ***c*-P40** (from ***l*-P10** and **T8**). i) $Pd(PPh_3)_2Cl_2$, CuI, 1,4-benzoquinone, *i*-Pr_2NH; ii) Pyridine. STM images of (b) ***c*-P30** and (c) ***c*-P40.** All scale bars are 5 nm. Adapted by permission from Macmillan Publishers Ltd: Nature Chemistry (ref. 65), copyright 2016.

1.7 References

(1) Milgrom, L. R. *The Colours of Life: An Introduction to the Chemistry of Porphyrins and Related Compounds*; Oxford University Press: Oxford, United Kingdom, **1997**.

(2) van Grondelle, R.; Dekker, J. P.; Gillbro, T.; Sundstrom, V. *Biochim. Biophys. Acta* **1994**, *1187*, 1–65.

(3) McDermott, G.; Prince, S. M.; Freer, A. A.; Hawthornthwaite-Lawless, A. M.; Papiz, M. Z.; Cogdell, R. J.; Isaacs, N. W. *Nature* **1995**, *374*, 517–521.

(4) Cogdell, R. J.; Fyfe, P. K.; Barrett, S. J.; Prince, S. M.; Freer, A. A.; Isaacs, N. W.; McGlynn, P.; Hunter, C. N. *Photosynth. Res.* **1996**, *48*, 55–63.

(5) Jimenez, R.; Dikshit, S. N.; Bradforth, S. E.; Fleming, G. R. *J. Phys. Chem.* **1996**, *100*, 6825–6834.

(6) Scholes, G. D.; Fleming, G. R. *J. Phys. Chem. B* **2000**, *104*, 1854–1868.

(7) Pullerits, T.; Sundström, V. *Acc. Chem. Res.* **1996**, *29*, 381–389.

(8) Sener, M.; Strümpfer, J.; Hsin, J.; Chandler, D.; Scheuring, S.; Hunter, C. N.; Schulten, K. *Chem. Phys. Chem.* **2011**, *12*, 518–531.

(9) Scheuring, S.; Sturgis, J. N. *Science.* **2005**, *309*, 484–488.

(10) Strümpfer, J.; Sener, M.; Schulten, K. *J. Phys. Chem. Lett.* **2012**, *3*, 536–542.

(11) Engel, G. S.; Calhoun, T. R.; Read, E. L.; Ahn, T.-K.; Mancal, T.; Cheng, Y.-C.;

Blankenship, R. E.; Fleming, G. R. *Nature* **2007**, *446*, 782–786.

(12) Collini, E.; Wong, C. Y.; Wilk, K. E.; Curmi, P. M. G.; Brumer, P.; Scholes, G. D. *Nature* **2010**, *463*, 644–647.

(13) Novelli, F.; Nazir, A.; Richards, G. H.; Roozbeh, A.; Wilk, K. E.; Curmi, P. M. G.; Davis, J. A. *J. Phys. Chem. Lett.* **2015**, *6*, 4573–4580.

(14) Wasielewski, M. R. *Acc. Chem. Res.* **2009**, *42*, 1910–1921.

(15) Aratani, N.; Kim, D.; Osuka, A. *Acc. Chem. Res.* **2009**, *42*, 1922–1934.

(16) Yoneda, Y.; Noji, T.; Katayama, T.; Mizutani, N.; Komori, D.; Nango, M.; Miyasaka, H.; Itoh, S.; Nagasawa, Y.; Dewa, T. *J. Am. Chem. Soc.* **2015**, *137*, 13121–13129.

(17) Matsushita, M.; Ketelaars, M.; van Oijen, A. M.; Köhler, J.; Aartsma, T. J.; Schmidt, J. *Biophys. J.* **2001**, *80*, 1604–1614.

(18) Cogdell, R. J.; Gall, A.; Köhler, J. *Q. Rev. Biophys.* **2006**, *39*, 227–324.

(19) Kasha, M.; Rawls, H. R.; Ashraf El-Bayoumi, M. *Pure Appl. Chem.* **1965**, *11*, 371–392.

(20) Martin, R. E.; Diederich, F. *Angew. Chem.-Int. Ed.* **1999**, *38*, 1350–1377.

(21) Tour, J. M. *Chem. Rev.* **1996**, *96*, 537–554.

(22) Anderson, H. L. *Chem. Commun.* **1999**, 2323–2330.

(23) Holten, D.; Bocian, D. F.; Lindsey, J. S. *Acc. Chem. Res.* **2002**, *35*, 57–69.

(24) Günes, S.; Neugebauer, H.; Sariciftci, N. S. *Chem. Rev.* **2007**, *107*, 1324–1338.

(25) Hagfeldt, A.; Boschloo, G.; Sun, L.; Kloo, L.; Pettersson, H. *Chem. Rev.* **2010**, *110*, 6595–6663.

(26) Tsuda, A.; Osuka, A. *Science.* **2001**, *293*, 79–82.

(27) Lin, V. S.; DiMagno, S. G.; Therien, M. J. *Science.* **1994**, *264*, 1105–1111.

(28) Osuka, A.; Je Satoshi Nakajima; Maruyama, K.; Mataga, N.; Asahi, T.; Yamazaki, I.; Nishimura, Y.; Ohno, T.; Nozaki, K. *J. Am. Chem. Soc.* **1993**, *115*, 4577–4589.

(29) Anderson, S.; Anderson, H. L.; Sanders, J. K. M. *J. Chem. Soc. Perkin Trans. 1* **1995**, *18*, 2255–2267.

(30) Maeda, C.; Taniguchi, T.; Ogawa, K.; Ema, T. *Angew. Chem.-Int. Ed.* **2015**, *54*, 134–138.

(31) Pawlicki, M.; Morisue, M.; Davis, N. K. S.; Mclean, D. G.; Haley, J. E.; Beuerman, E.; Drobizhev, M.; Rebane, A.; Thompson, A. L.; Pascu, S. I.; Accorsi, G.; Anderson, H. L. *Chem. Sci.* **2012**, *3*, 1541–1547.

(32) Gouterman, M. *J. Mol. Spectrosc.* **1961**, *6*, 138–163.

(33) Albinsson, B. *Chem. Soc. Rev.* **2015**, *44*, 845–862.

(34) Peeks, M. D.; Neuhaus, P.; Anderson, H. L. *Phys. Chem. Chem. Phys.* **2016**, *18*, 5264–5274.

(35) Taylor, P. N.; Anderson, H. L. *J. Am. Chem. Soc.* **1999**, *121*, 11538–11545.

(36) Winters, M. U.; Karnbratt, J.; Eng, M.; Wilson, C. J.; Anderson, H. L.; Albinsson, B. *J. Phys. Chem. C* **2007**, *111*, 7192–7199.

(37) Arnold, D. P.; Johnson, A. W.; Mahendran, M. *J. Chem. Soc. Perkin Trans. 1* **1978**, 366–370.

(38) Anderson, H. L. *Inorg. Chem.* **1994**, *33*, 972–981.

(39) Taylor, P. N.; Huuskonen, J.; Rumbles, G.; Aplin, R. T.; Williams, E.; Anderson, H. L. *Chem. Commun.* **1998**, 909–910.

(40) Kawao, M.; Ozawa, H.; Tanaka, H.; Ogawa, T. *Thin Solid Films* **2006**, *499*, 23–28.

(41) Lindsey, J. S. *Acc. Chem. Res.* **2010**, *43*, 300–311.

(42) Littler, B. J.; Miller, M. A.; Hung, C.-H.; Wagner, R. W.; O'Shea, D. F.; Boyle, P. D.; Lindsey, J. S.; Carolina, N. *J. Org. Chem.* **1999**, *64*, 1391–1396.

(43) Aratani, N.; Takagi, A.; Yanagawa, Y.; Matsumoto, T.; Kawai, T.; Yoon, Z. S.; Kim, D.; Osuka, A. *Chem. Eur. J.* **2005**, *11*, 3389–3404.

(44) Grozema, F. C.; Houarner-Rassin, C.; Prins, P.; Siebbeles, L. D. A.; Anderson, H. L. *J. Am. Chem. Soc.* **2007**, *129*, 13370–13371.

(45) Wilson, C. J. *Large Porphyrin-Based π-Systems*, D.Phil thesis, University of Oxford, Oxford, **2006**.

(46) Kondratiuk, D. V. *Synthesis and Properties of Giant Porphyrin Nanorings*, D.Phil thesis, University of Oxford, Oxford, **2013**.

(47) Whitesides, G. M.; Grzybowski, B. *Science.* **2002**, *295*, 2418–2421.

(48) Samanta, S. K.; Samanta, D.; Bats, J. W.; Schmittel, M. *J. Org. Chem.* **2011**, *76*, 7466–7473.

(49) Favereau, L.; Cnossen, A.; Kelber, J. B.; Gong, J. Q.; Oetterli, R. M.; Cremers, J.; Herz, L. M.; Anderson, H. L. *J. Am. Chem. Soc.* **2015**, *137*, 14256–14259.

(50) Sakuragi, M.; Ichimura, K.; Sakuragi, H. *Bull. Chem. Soc. Jpn.* **1992**, *65*, 1944–1949.

(51) Imai, H.; Nakagawa, S.; Kyuno, E. *J. Am. Chem. Soc.* **1992**, *114*, 6719–6723.

(52) Bhyrappa, P.; Krishnan, V.; Nethaji, M. *J. Chem. Soc. Dalt. Trans* **1993**, 1901–1906.

(53) Ercolani, G. *Thermodynamics of Metal-Mediated Assemblies of Porphyrins In Struct. Bond.*, Vol 121.; Springer-Verlag: Berlin Heidelberg, **2006**.

(54) Beletskaya, I.; Tyurin, V. S.; Tsivadze, A. Y.; Guilard, R.; Stern, C. *Chem. Rev.* **2009**, *109*, 1659–1713.

(55) Hwang, I. W.; Kamada, T.; Tae, K. A.; Dah, M. K.; Nakamura, T.; Tsuda, A.; Osuka, A.; Kim, D. *J. Am. Chem. Soc.* **2004**, *126*, 16187–16198.

(56) Wilson, S. G.; Anderson, H. L. *Chem. Commun.* **1999**, 1539–1540.

(57) Rucareanu, S.; Mongin, O.; Schuwey, A.; Hoyler, N.; Gossauer, A. *J. Org. Chem.* **2001**, *66*, 4973–4988.

(58) Bouamaied, I.; Coskun, T.; Stulz, E. *Axial coordination to metalloporphyrins leading to multinuclear assemblies*, Vol 121.; Springer-Verlag: Berlin Heidelberg, **2006**.

(59) Wayne, C. E.; Wayne, R. P. *Photochemistry*, 1st ed.; Oxford University Press: Oxford,

United Kingdom, **1996**.

(60) Balzani, V.; Bergamini, G.; Sebastiano, C.; Puntoriero, F. *Photochemistry and Photophysics of Coordination Compounds : Overview and General Concepts*; Springer-Verlag: Berlin Heidelberg, **2007**.

(61) Dexter, D. L. *J. Chem. Phys.* **1953**, *21*, 836–850.

(62) Förster, T. *Ann. Phys.* **1948**, *2*, 55–75.

(63) Nakamura, Y.; Aratani, N.; Osuka, A. *Chem. Soc. Rev.* **2007**, *36*, 831–845.

(64) Yang, J.; Yoon, M.; Yoo, H.; Kim, P.; Kim, D. *Chem. Soc. Rev.* **2012**, *41*, 4808–4826.

(65) Kondratuk, D. V; Perdigão, L. M. A.; Esmail, A. M. S.; O'Shea, J. N.; Beton, P. H.; Anderson, H. L. *Nat. Chem.* **2015**, *7*, 317–322.

(66) Sprafke, J. K.; Kondratuk, D. V; Wykes, M.; Thompson, A. L.; Ho, M.; Drevinskas, R.; Chen, W.; Yong, C. K.; Joakim, K.; Bullock, J. E.; Malfois, M.; Wasielewski, M. R.; Albinsson, B.; Herz, L. M.; Zigmantas, D.; Beljonne, D.; Anderson, H. L. *J. Am. Chem. Soc.* **2011**, *133*, 17262–17273.

(67) Gong, J. Q.; Favereau, L.; Anderson, H. L.; Herz, L. M. *J. Phys. Chem. Lett.* **2016**, *7*, 332–338.

(68) Busch, D. H. *J. Incl. Phenom.* **1992**, *12*, 389–395.

(69) Anderson, S.; Anderson, H. L.; Sanders, J. K. M. *Acc. Chem. Res.* **1993**, *26*, 469–475.

(70) Anderson, H. L.; Sanders, J. K. M. *J. Chem. Soc., Chem. Commun.* **1989**, 1714–1715.

(71) McCallien, D. W. J.; Sanders, J. K. M. *J. Am. Chem. Soc.* **1995**, *117*, 6611–6612.

(72) Hoffmann, M.; Wilson, C. J.; Odell, B.; Anderson, H. L. *Angew. Chem.- Int. Ed.* **2007**, *46*, 3122–3125.

(73) Hoffmann, M.; Kärnbratt, J.; Chang, M.; Herz, L. M.; Albinsson, B.; Anderson, H. L. *Angew. Chem.- Int. Ed.* **2008**, *120*, 5071–5074.

(74) Williams, V. E.; Swager, T. M. *J. Polym. Sci., Polym. Chem.* **2000**, *38*, 4669–4676.

(75) Watson, J.; Crick, F. H. F. *Nature* **1953**, *171*, 737–738.

(76) Kelly, T. R.; Zhao, C.; Bridger, G. J. *J. Am. Chem. Soc.* **1989**, *111*, 3744–3745.

(77) Kelly, T. R.; Bridger, G. J.; Zhao, C. *J. Am. Chem. Soc.* **1990**, *112*, 8024–8034.

(78) Wintner, E. A.; Conn, M. M.; Rebek, Jr., J. *Acc. Chem. Res.* **1994**, *27*, 198–203.

(79) Anderson, S.; Anderson, H. L.; Sanders, J. K. M. *J. Chem. Soc. Perkin Trans. 1* **1995**, *18*, 2247–2254.

(80) Wintner, E. A.; Rebek, Jr., J. *Acta Chem. Scand.* **1996**, *50*, 469–485.

(81) MacGillivray, L. R.; Reid, J. L.; Ripmeester, J. A. *J. Am. Chem. Soc.* **2000**, *122*, 7817–7818.

(82) Diederich, F.; Stang, P. J. *Templated Organic Synthesis*; Wiley-VCH Verlag GmbH, **2000**.

(83) Stross, A. E.; Iadevaia, G.; Hunter, C. A. *Chem. Sci.* **2015**, *7*, 94–101.

(84) Wei, T.; Jung, J. H.; Scott, T. F. *J. Am. Chem. Soc.* **2015**, *137*, 16196–16202.

(85) Steinhauer, C.; Jungmann, R.; Sobey, T. L.; Simmel, F. C.; Tinnefeld, P. *Angew. Chem - Int. Ed.* **2009**, *48*, 8870–8873.

(86) Rothemund, P. W. K. *Nature* **2006**, *440*, 297–302.

(87) Andersen, E. S.; Dong, M.; Nielsen, M. M.; Jahn, K.; Subramani, R.; Mamdouh, W.; Golas, M. M.; Sander, B.; Stark, H.; Oliveira, C. L. P.; Pedersen, J. S.; Birkedal, V.; Besenbacher, F.; Gothelf, K. V; Kjems, J. *Nature* **2009**, *459*, 73–76.

(88) Hung, A. M.; Micheel, C. M.; Bozano, L. D.; Osterbur, L. W.; Wallraff, G. M.; Cha, J. N. *Nat. Nanotechnol.* **2010**, *5*, 121–126.

(89) Lindsey, J. S. *New J. Chem* **1991**, *15*, 153–180.

(90) Kelly, T. R.; Xie, R. L.; Weinreb, C. K.; Bregant, T. *Tetrahedron Lett.* **1998**, *39*, 3675–3678.

(91) Hunter, C. A.; Tomas, S. *J. Am. Chem. Soc.* **2006**, *128*, 8975–8979.

(92) Kondratuk, D. V; Sprafke, J. K.; O'Sullivan, M. C.; Perdigao, L. M. A.; Saywell, A.; Malfois, M.; O'Shea, J. N.; Beton, P. H.; Thompson, A. L.; Anderson, H. L. *Chem. Eur. J.* **2014**, *20*, 12826–12834.

(93) O'Sullivan, M. C.; Sprafke, J. K.; Kondratuk, D. V; Rinfray, C.; Claridge, T. D. W.; Saywell, A.; Blunt, M. O.; O'Shea, J. N.; Beton, P. H.; Malfois, M.; Anderson, H. L. *Nature* **2011**, *469*, 72–75.

Chapter 2

Biomimetic Multistrand Nanorings

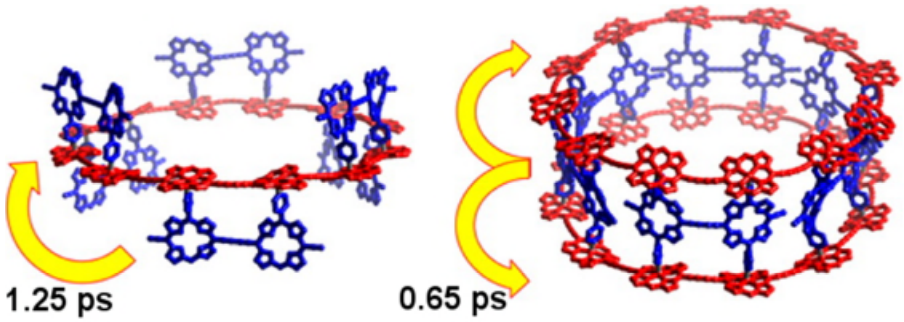

This chapter reports the synthesis of LH2-like supramolecular double- and triple-strand complexes based upon porphyrin nanorings. Energy transfer from the antenna dimers to the π-conjugated nanoring occurs on a sub-picosecond timescale, rivalling transfer rates in natural light harvesting systems. The presence of a second nanoring acceptor doubles the transfer rate, providing strong evidence for multi-directional energy funnelling. These complexes are versatile synthetic models for natural light harvesting systems. Additionally, the double-strand complexes were used to investigate a new approach to porphyrin nanoring template-directed synthesis: using one ring to template a new complementary ring.

Parts of the results in this chapter have been published in the following article:

Ultrafast Energy Transfer in Biomimetic Multistrand Nanorings
Parkinson, P.; Knappke, C. E. I.; Kamonsutthipaijit, N.; Sirithip, K.; Matichak, J. D.; Anderson, H. L.; Herz, L. M. *J. Am. Chem. Soc.* **2014**, *136*, 8217–8220.

2.1 Background information

The architecture and function of natural light-harvesting systems have been thoroughly investigated, particularly in purple bacteria,[1] revealing the geometric structure of such molecular self-assemblies (known as LH1 and LH2) as the key factor to the critical properties of their light-harvesting processes.[2–5] Synthetic biomimics have become a topic of intense research in order to understand, utilise and possibly surpass the efficiency of the natural system.[6,7] A variety of approaches have been explored;[8–11] most recently, investigation of porphyrin nanorings has provided an insight into fully conjugated macromolecules with analogous properties to the B850 ring-structures in natural LH2, which exhibit electronic delocalisation around curved surfaces.[12,13] Research on both natural and synthetic B850-like acceptor nanorings has revealed the importance of properties such as static and dynamic disorder-induced symmetry breaking.[14,15] However, studies of energy transfer from antenna chromophores to a synthetic nanoring have been limited by the challenges in creating such systems. Investigating energy dynamics in synthetic LH2-like complexes may give important insights into the working mechanisms of both natural and synthetic light-harvesting systems. In this study, we describe the synthesis and energy transfer dynamics for two supramolecular antenna-nanoring complexes of a 12-porphyrin nanoring ***c*-P12$_{THS}$** with two different free-base porphyrin dimers, **P2py2** and **P2py4**.[18-21]

Moreover, the development of synthetic LH2-like complexes was further extended to the following question: is it possible to use a nanoring as a template to make a new complementary nanoring via double- and triple-strand architectures? The answer of this question was investigated as shown in the last section in this chapter.

The photophysical measurements discussed in this chapter were carried out by Dr. Patrick Parkinson and Dr. Laura Herz (Department of Physics, University of Oxford) and the synthesis of the double-strand dimer-nanoring complex and the ring-ring templating synthesis of the palladium-12-ring were contributed by Dr. Christiane Knappke (Department of Chemistry, University of Oxford), in close collaboration with me.

2.2 Molecular design of double and triple strand nanoring complexes

Coordination of the pyridyl substituents to the zinc metal centres drives the self-assembly of the complexes, as shown in **Figure 2.1**. The ring-dimer complex ***c*-P12$_{THS}$·(P2py2)$_6$** (**Figure 2.1-top**) consists of a porphyrin nanoring and six **P2py2** dimers; these free-base porphyrin dimers have one *meso*-4-pyridyl substituent on each porphyrin unit to coordinate to the zinc centres of the nanoring. The 3,5-bis(trihexylsilyl)phenyl substituents on both components provide solubility and avoid aggregation. The ring-dimer-ring complex **(*c*-P12$_{THS}$)$_2$·(P2py4)$_6$** (**Figure 2.1-bottom**) features analogous porphyrin dimers with four 4-pyridyl substituents allowing the coordination to two nanorings forming a barrel-shaped architecture. To enhance the solubility of the dimers, dodecyloxy-substituents are attached to the 3 and 5-position of the pyridyl-moiety. During the work presented in this chapter, we used two types of ***c*-P12**, with trihexylsilyl (THS) and OC_8H_{17} (C8) side chains on the aromatic substituents. Both these 12-porphyrin nanorings were synthesised by Vernier templating.[20] Most of the studies were carried out using 12-ring with THS side chains ***c*-P12$_{THS}$** but the characterisation of the triple-strand complex; ring-dimer-ring complex by mass spectrometry used12-ring with OC_8H_{17} side chains ***c*-P12$_{C8}$** because in this case it gave superior solubility. The synthesis and full characterisation of these compounds are given in **Experimental section 2.7**.

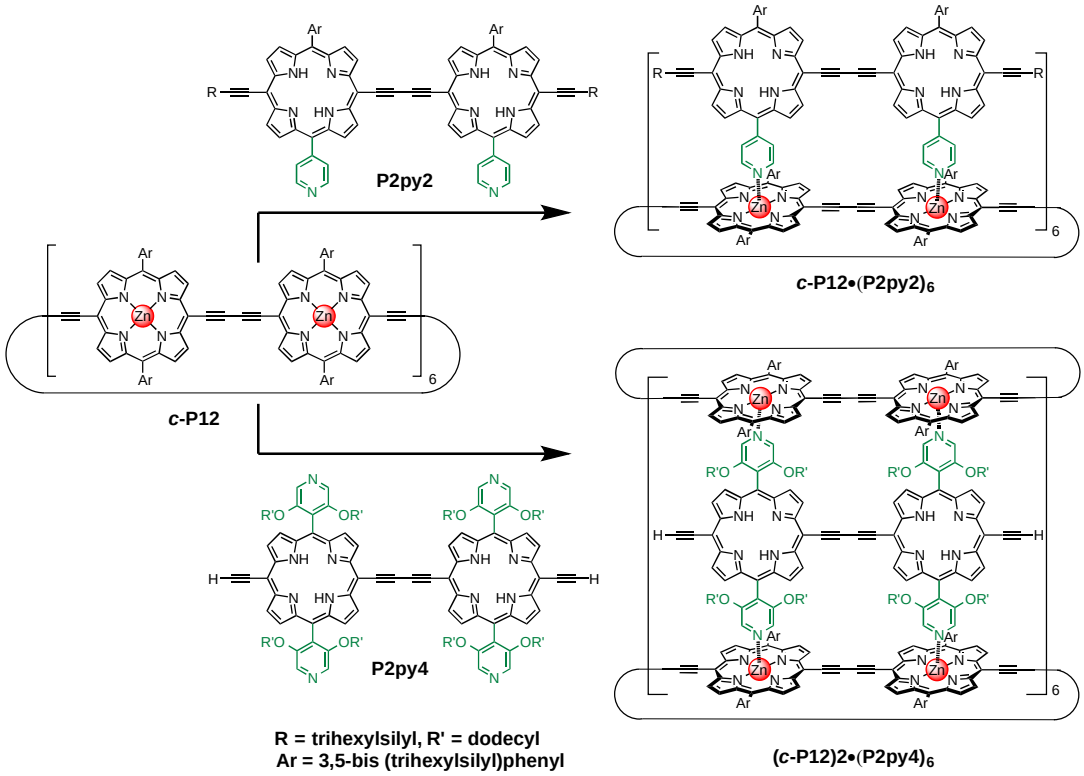

Figure 2.1 Assemblies of the ring-dimer complex ***c*-P12$_{THS}$·(P2py2)$_6$** (top), and the ring-dimer-ring complex **(*c*-P12$_{THS}$)$_2$·(P2py4)$_6$** (bottom). Ar = 3,5-bis(trihexylsilyl)phenyl, R = trihexylsilyl, R' = dodecyl.

2.3 Characterisations of the complexes

The formation of the complexes can be monitored using fluorescence, UV-vis and ^{1}H NMR titrations, ^{1}H NMR diffusion (DOSY) and MALDI-ToF mass technique. The geometry of the pyridine-zinc porphyrin interaction was assumed from published structures in Cambridge Structural Database (CSD).

2.3.1 Fluorescence titrations

The absorption spectra of the complexes and their components are plotted in **Figure 2.2e,f** (plotted as molar absorption coefficient, scaled for the number of components). The complexes show notable shifts when compared with the components; in particular, a sharpening and redshift in nanoring absorption for the ring-dimer-ring complex, which is attributed to planarisation of the nanoring.[21] The absorption spectrum of the nanoring undergoes less change when it forms the ***c*-P12$_{THS}$·(P2py2)$_6$** ring−dimer complex, reflecting the greater conformational heterogeneity of this complex compared with the more rigid ring−dimer−ring complex.

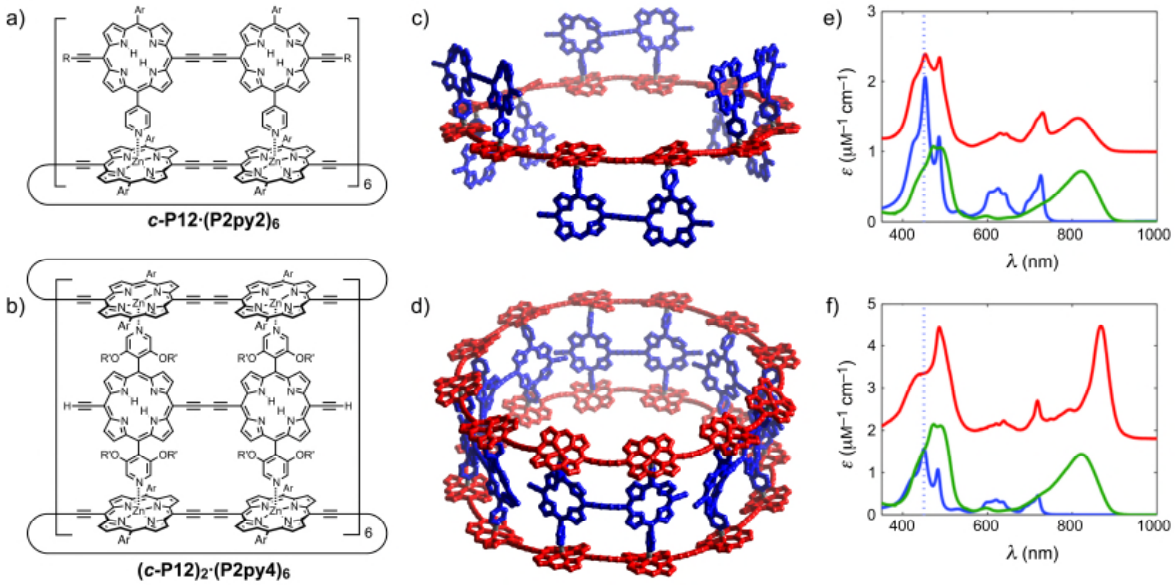

Figure 2.2(a,b) Chemical structure and (c,d) structural models of the ring-dimer complex ***c*-P12$_{THS}$·(P2py2)$_6$** (top), and the ring-dimer-ring complex (***c*-P12$_{THS}$)$_2$·(P2py4)$_6$** (bottom). Ar = 3,5-bis(trihexylsilyl)phenyl, R = trihexylsilyl, R' = dodecyl. (e,f) The molar absorption coefficients of the components in toluene/1% pyridine (dimer in blue, ***c*-P12$_{THS}$** nanoring in green), scaled for their relative number within the complex. The absorption spectra of the two complexes in toluene (solid red line) are also shown (offset for clarity). The excitation wavelength used for photoluminescence measurements is indicated as a dashed vertical blue line at 450 nm. The models (c,d) are energy-minimised geometries, calculated using the mm+ forcefield in HyperChem.

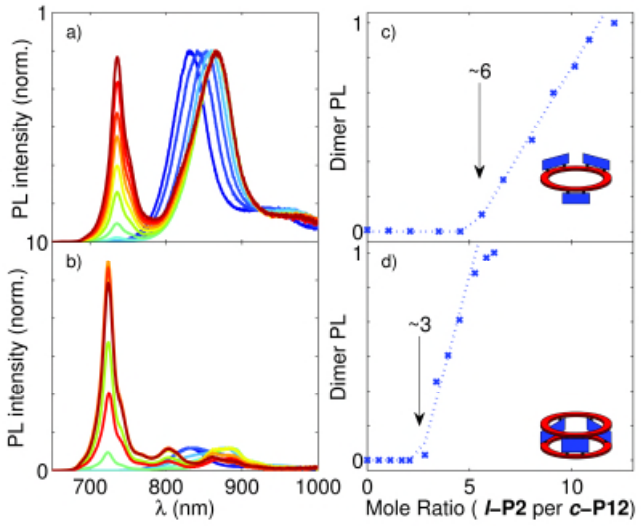

Figure 2.3 PL titrations (excitation: 450 nm) of ***c*-P12$_{THS}$** with (a,c) **P2py2** and with (b,d) **P2py4**; normalised to the nanoring emission peak in (a) and (b). The endpoints are indicated by black arrows at approximately 6 equiv. of **P2py2** (c) and 3 equiv. of **P2py4** (d) per ***c*-P12$_{THS}$** respectively.

Photoluminescence (PL) titrations were performed and analysed by Dr. Patrick Parkinson and Dr. Laura Herz (Department of Physics, University of Oxford). All fluorescence spectra were recorded at concentrations of around 0.1 mM in toluene; under these conditions the dimer is > 99% bound as described later in binding study. We found that the complexes exhibit efficient energy

transfer from dimer antennae to the nanoring (**Figure 2.3a,b**). When complexes are assembled without additional free dimer in solution, the fluorescence (photoluminescence, PL) spectra are dominated by the emission from the nanoring acceptors (800–900 nm) due to energy transfer from the dimer to nanoring, followed by emission. In these measurements, components are excited at a wavelength of 450 nm which gives approximately 2:1 (1:1) selectivity for dimer excitation in the ring-dimer (ring-dimer-ring) complex (see dashed blue line in the absorption spectra, **Figure 2.2e,f**). The effective quenching of the dimer PL (710–730 nm) therefore qualitatively demonstrates the occurrence of efficient energy transfer to the nanoring acceptor. **Figure 2.3** shows that an increase of the ratio of dimer to nanoring results in an abrupt onset of dimer emission at the endpoint of the titration, revealing the presence of unbound dimer in the solution. We are therefore able to utilise the PL measurements as a sensitive tool for determining the association state of the complexes. As expected, close to 6 dimers per ***c*-P12$_{THS}$** nanoring for the ring-dimer complex and close to 3 dimers for the ring-dimer-ring complex were required (**Figure 2.3c,d**).

2.3.2 Binding study

The binding constant of the dimer **P2Py2** to the nanoring ***c*-P12$_{THS}$** was determined by UV-vis titration performed by Dr Christiane Knappke (for similar experiments on ***c*-P12** with OC_8H_{17} side chains see **Chapter 3**). The dimer was added to the 12-ring and the concentration of the 12-ring was kept constant during the titration (**Figure 2.4**). The data (**Figure 2.5**) were analysed by global fitting with the software SPECFIT assuming a 1:1 binding situation, i. e. the dimer molecules behave independently in their binding to the 12-ring and the 12-ring is treated as 6 dimer sites. If this assumption were fully fulfilled in the actual system, isosbestic behaviour would be expected. The actual titration shows slight deviation from isosbestic behaviour, which may be due to slight initial aggregation of the 12-ring. Nevertheless, using the described 1:1 model an acceptable fit (**Figure 2.5**) is obtained and a binding constant of log K = 6.7 results. This binding constant compares well with the binding constant (log K = 8.7) measured for a dimer-dimer system (detail of dimer system as described in **Chapter 4**); as expected the binding to the curved system is slightly weaker than that of a linear one.

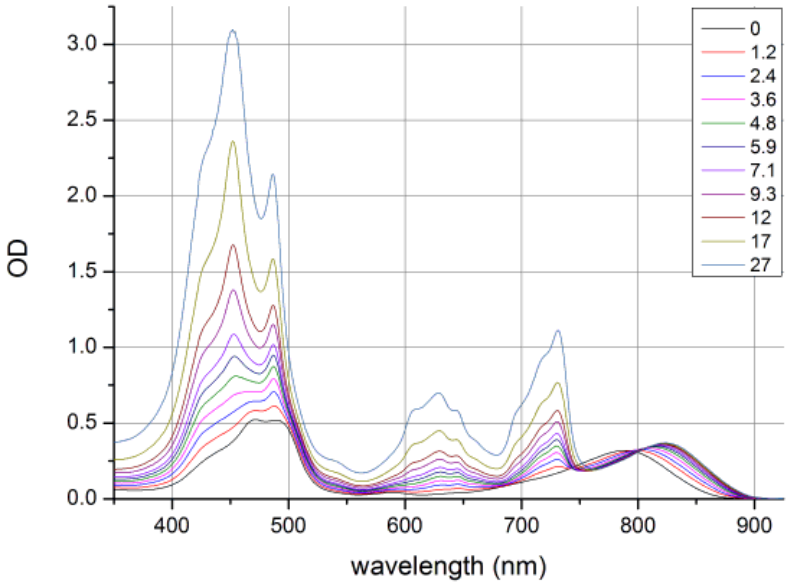

Figure 2.4 UV-vis titration of ***c*-P12$_{THS}$** with **P2py2**. The concentration of ***c*-P12$_{THS}$** is kept constant during the titration (4.26×10^{-7} mol/L). Values in the legend indicate the molar ratio of **P2py2** to ***c*-P12$_{THS}$**.

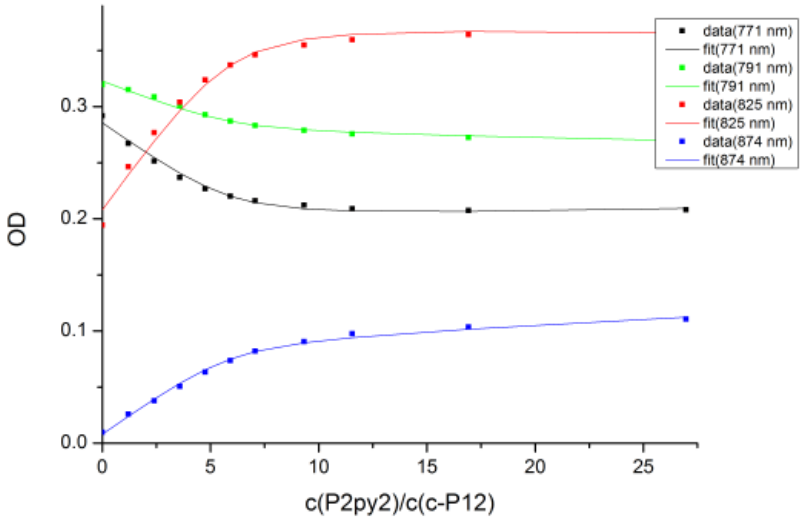

Figure 2.5 Plot of the molar concentration ratio of dimer **P2py2** to 12-ring ***c*-P12$_{THS}$** against optical density at various wavelengths. Data are from the UV-vis titration shown in **Figure 2.4**. Fittings were at various wavelengths, obtained by global analysis with SPECFIT using a 1:1 model.

2.3.3 ^{1}H NMR titrations

^{1}H NMR titration analysis was performed to confirm the self-assembly of the complexes. Upon adding dimer **P2py2** to 12-ring **c-P12$_{THS}$**, the appearance of new species was observed (**Figure**

2.6). **Figure 2.7** shows the comparison between ^{1}H NMR spectra of free ***c*-P12$_{THS}$**, free **P2py2** and bound **P2py2** to ***c*-P12$_{THS}$**. The α- and β-protons of the pyridyl substituents of the bound free-base dimer **P2py2** display tremendous high-field shifts: $\Delta\delta$ = 5.11 and = 1.55, compared to the resonances at 7.66 and 8.91 ppm of the corresponding protons in the unbound dimer. This shift is consistent with the coordination of the pyridyl groups to the Zn centres of the porphyrin. The porphyrin system possesses a strong ring-current that leads to the high field shift of the bound pyridyl-protons.

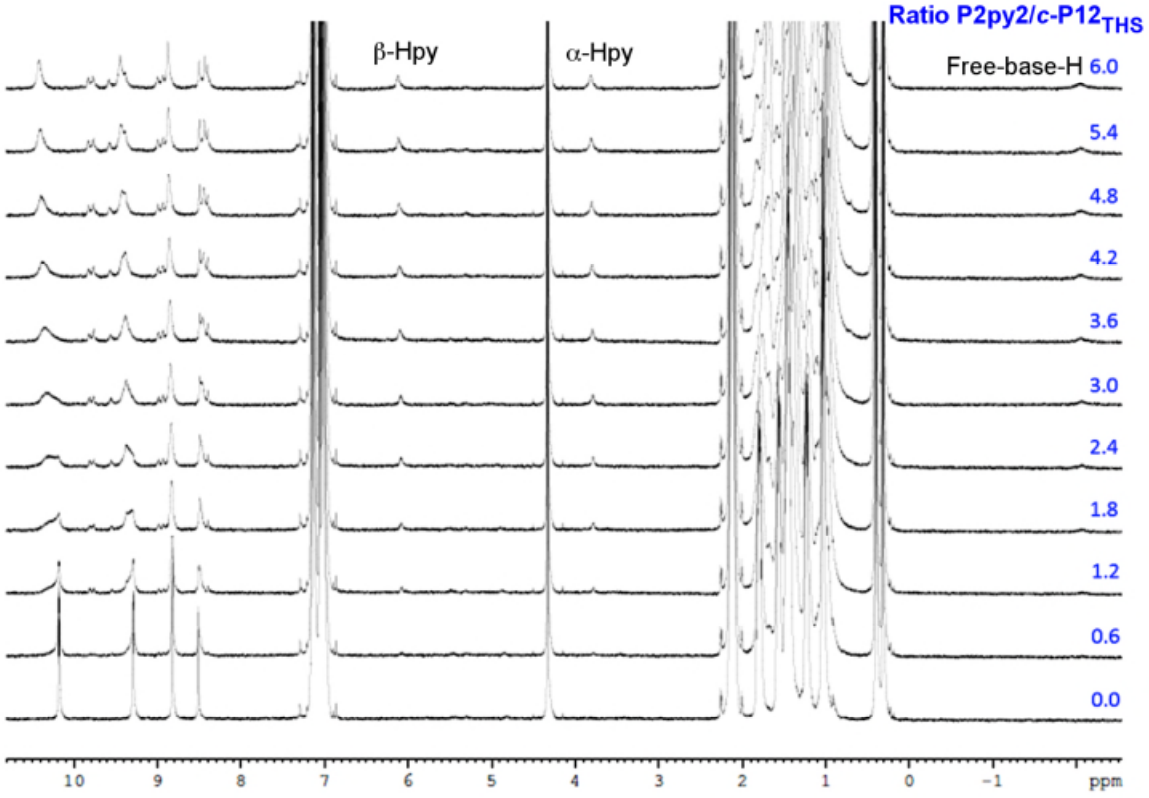

Figure 2.6 ^{1}H-NMR formation titration of ***c*-P12$_{THS}$** with **P2py2** (toluene-*d8*, 298 K, 500 MHz, [***c*-P12$_{THS}$**] = 0.08 mM) and assignment of ratio of **P2py2/*c*-P12$_{THS}$**

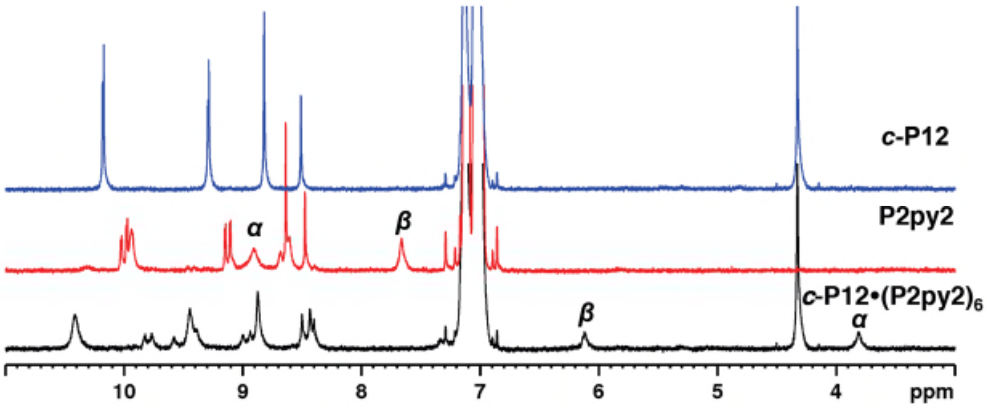

Figure 2.7 Comparison between ^{1}H NMR spectra (toluene-*d8*, 298 K, 500 MHz) of free ***c*-P12$_{THS}$**, free **P2py2** and bound **P2py2** to ***c*-P12$_{THS}$**. α- and β-protons of the pyridyl substituents of the free-base dimer **P2py2** display tremendous high-field shifts: $\Delta\delta$ = 5.11 and = 1.55, respectively.

2.3.4 ^{1}H NMR DOSY spectra of *c*-P12$_{THS}$•(P2py2)$_6$, *c*-P12$_{THS}$ and P2py2

Diffusion-ordered spectroscopy (DOSY) is used to separate the NMR signals of different species according to their diffusion coefficient. The DOSY plot of ***c*-P12$_{THS}$·(P2py2)$_6$** demonstrates that all protons corresponding to the complex diffuse at the same rate in comparison to the diffusion of toluene-*d8* as the reference, implying all proton-diffusion signals come from the same object. The diffusion coefficients of the double-ring complex show that the complex diffuses less rapidly than either ***c*-P12$_{THS}$** or **P2py2**, implying that the hydrodynamic radius for the complex is larger than its components, as expected.

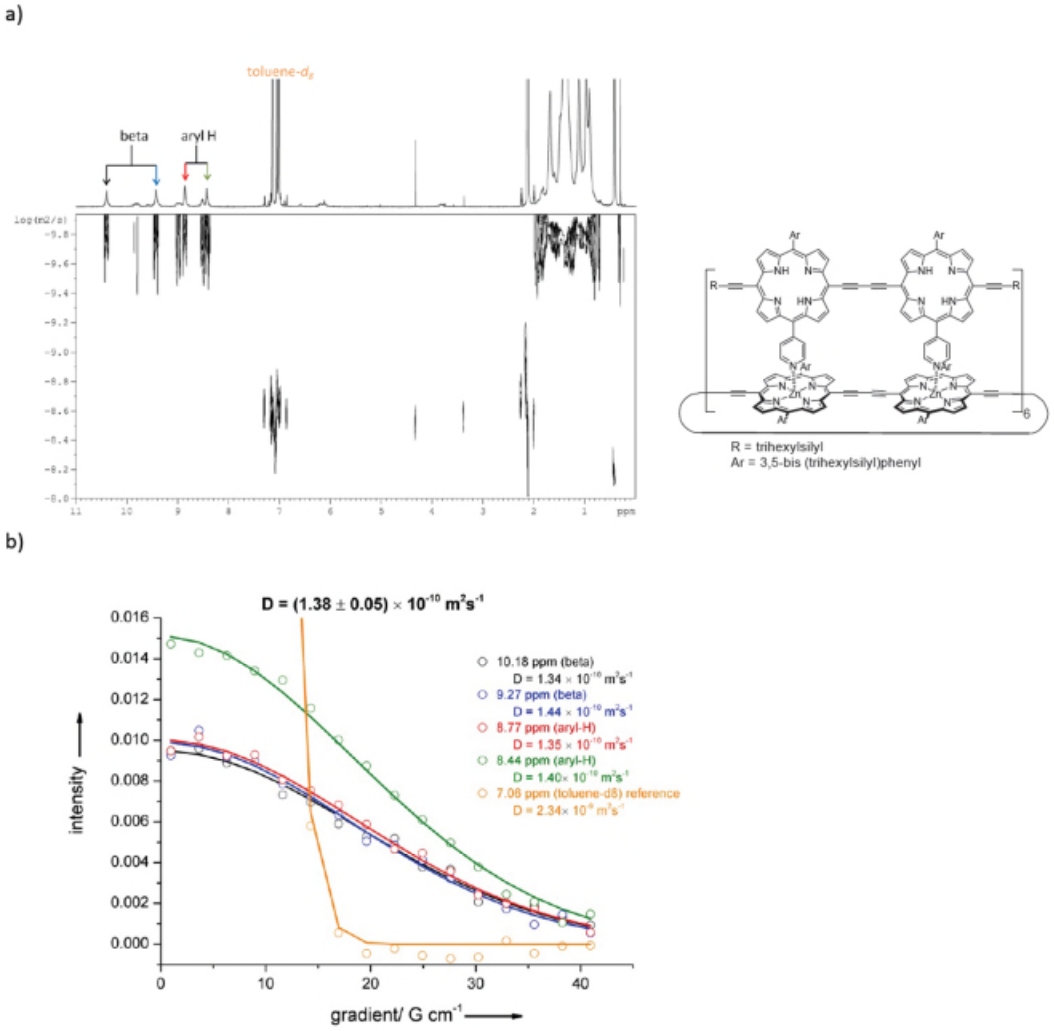

Figure 2.8 ^{1}H DOSY of ***c*-P12$_{THS}$·(P2py2)$_6$** in toluene-d8 at 298 K measured at 500 MHz with Δ = 100 ms, δ = 4 ms and g = 0.96-41 G cm^{-1}. a) DOSY plot (made by TOPSPIN software version 2.1) b) Fitted diffusion decay curves and resulting diffusion coefficients. Only diffusion coefficients from four proton resonances at the core of the molecule (two porphyrin-beta and two aryl of ***c*-P12$_{THS}$**) were used to calculate the diffusion coefficient.

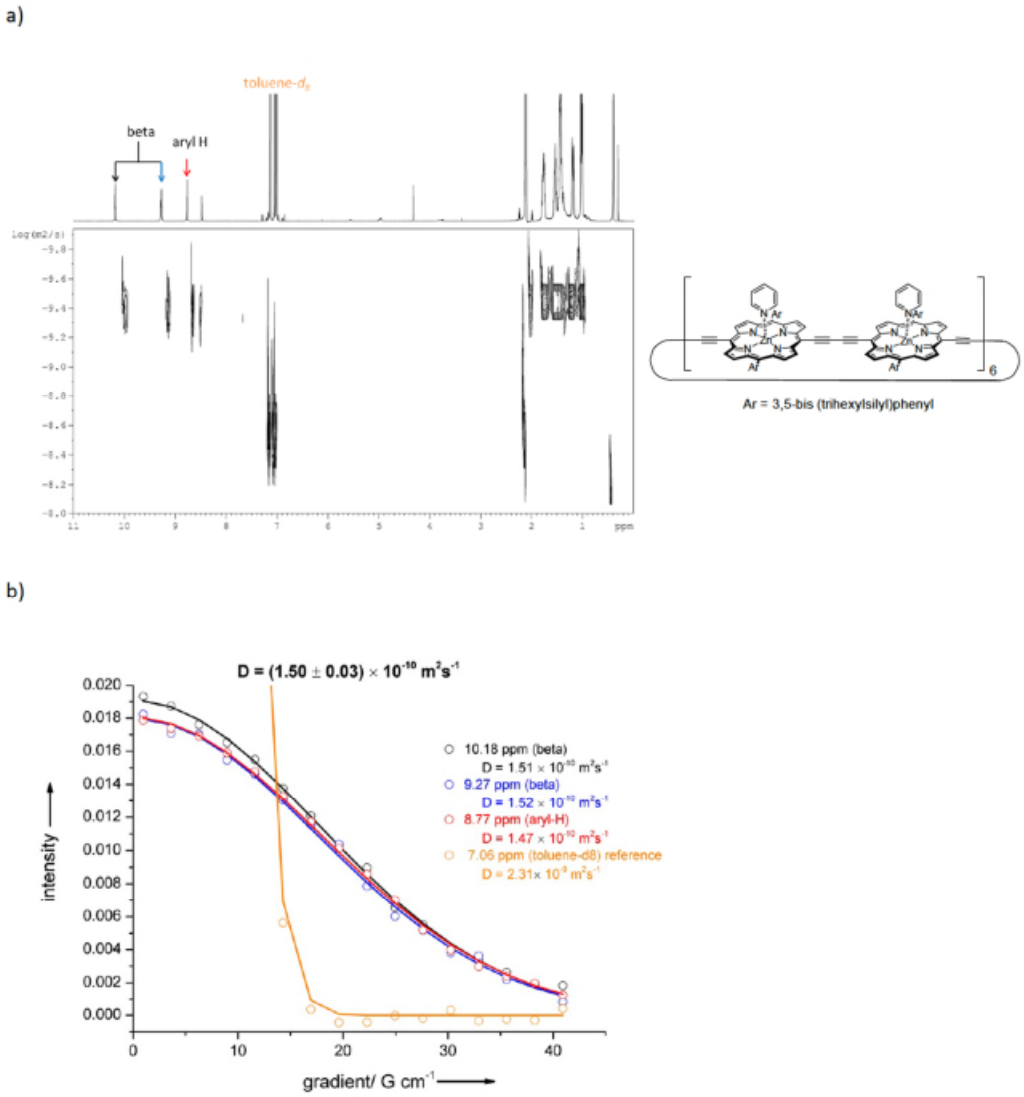

Figure 2.9 ^{1}H DOSY of ***c*-P12$_{THS}$** in toluene-d8 at 298 K measured at 500 MHz with Δ = 100 ms, δ = 4 ms and g = 0.96-41 G cm^{-1}. a) DOSY plot was made by TOPSPIN software version 2.1 b) Fitted diffusion decay curves and resulting diffusion coefficients. Only diffusion coefficients from four proton resonances at the core of the molecule (two porphyrin-beta and aryl) were used to calculate the diffusion coefficient.

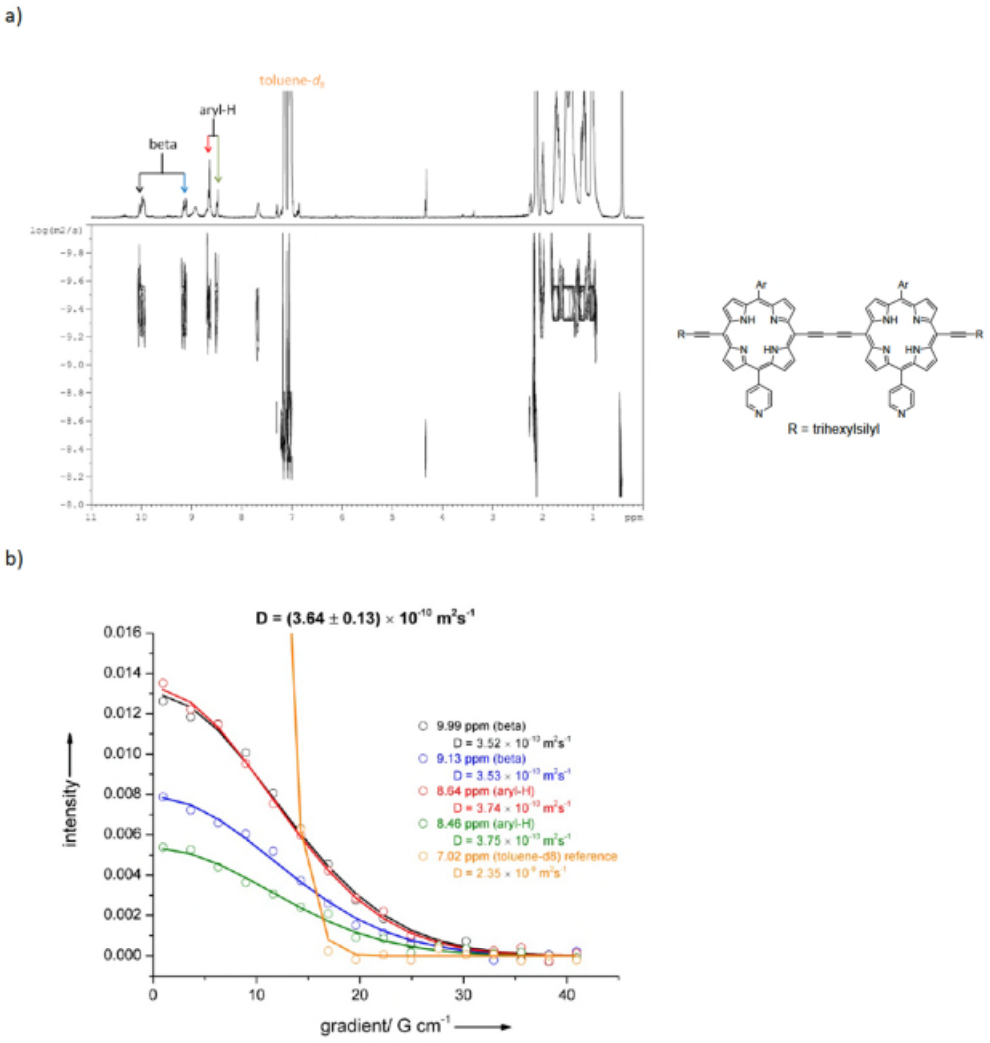

Figure 2.10 ^{1}H DOSY of **P2py2** in toluene-*d8* at 298 K measured at 500 MHz with Δ = 100 ms, δ = 4 ms and g = 0.96-41 G cm^{-1}. a) DOSY plot was made by TOPSPIN software version 2.1 b) Fitted diffusion decay curves and resulting diffusion coefficients. Only diffusion coefficients from four proton resonances at the core of the molecule (two porphyrin-beta and two aryl) were used to calculate the diffusion coefficient.

2.3.5 MALDI-ToF of the ring-dimer-ring (*c*-P12$_{C8}$)$_2$•(P2py4)$_6$ complex

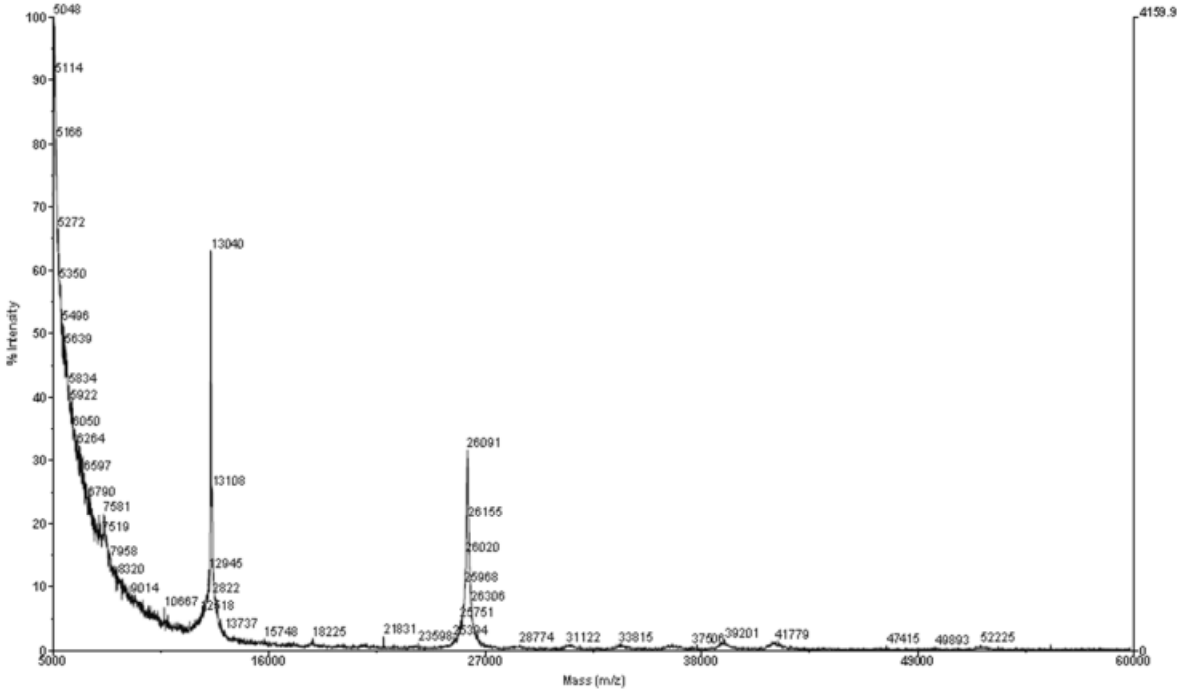

Figure 2.11 MALDI-ToF analysis of the (***c*-P12$_{C8}$)$_2$·(P2py4)$_6$** complex; full range (spectrum acquired by the EPSRC National Mass Spectrometry Center at Swansea University).

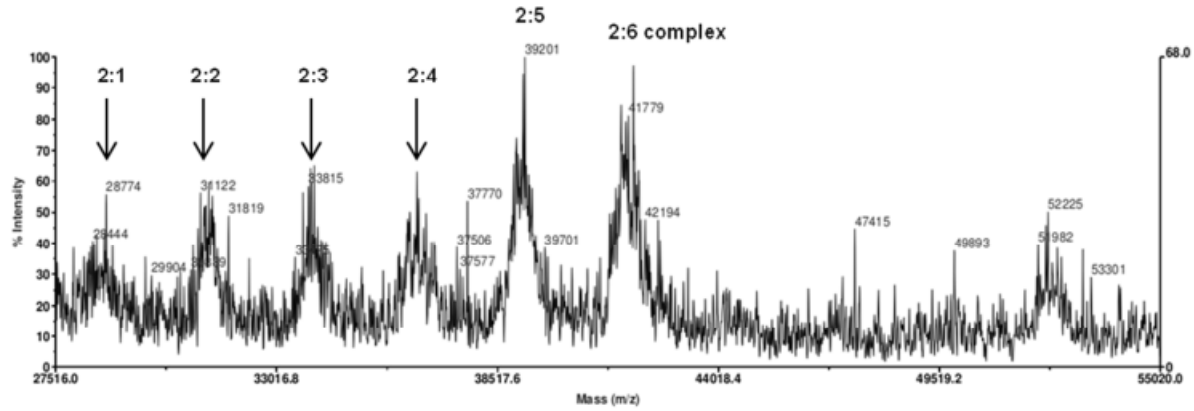

Figure 2.12 MALDI-ToF analysis of the (***c*-P12$_{C8}$)$_2$·(P2py4)$_6$** complex; zoom in (spectrum acquired by EPSRC National Mass Spectrometry Center at Swansea University).

The self-assembly between the 12-ring ***c*-P12$_{C8}$**, which was synthesised from the linear tetramer by Vernier templating according to the published procedure, and **P2py4** was analysed by MALDI-ToF mass technique. The two major peaks correspond to ***c*-P12$_{C8}$** (*m/z* 13,040, expected 13,018) and **(*c*-P12$_{C8}$)$_2$** aggregate (*m/z* 26,091, expected 26,036). Interestingly, when looking at the magnified spectrum, six minor peaks were found, corresponding to the expected mass for

(*c*-P12$_{C8}$)$_2$·(P2Py4)$_6$ (*m/z* 41,779, expected 41,024), **(*c*-P12$_{C8}$)$_2$·(P2Py4)$_5$** (*m/z* 39,201, expected 38,526), **(*c*-P12$_{C8}$)$_2$·(P2Py4)$_4$** (*m/z* 36,508, expected 36,028), **(*c*-P12$_{C8}$)$_2$·(P2Py4)$_3$** (*m/z* 33,815, expected 33,530), **(*c*-P12$_{C8}$)$_2$·(P2Py4)$_2$** (*m/z* 31,122, expected 31,032) and **(*c*-P12$_{C8}$)$_2$·(P2Py4)** (*m/z* 28,444, expected 28,534), respectively. This mass result confirms the presence of the triple ring complex.

2.3.6 Geometry of associated complexes

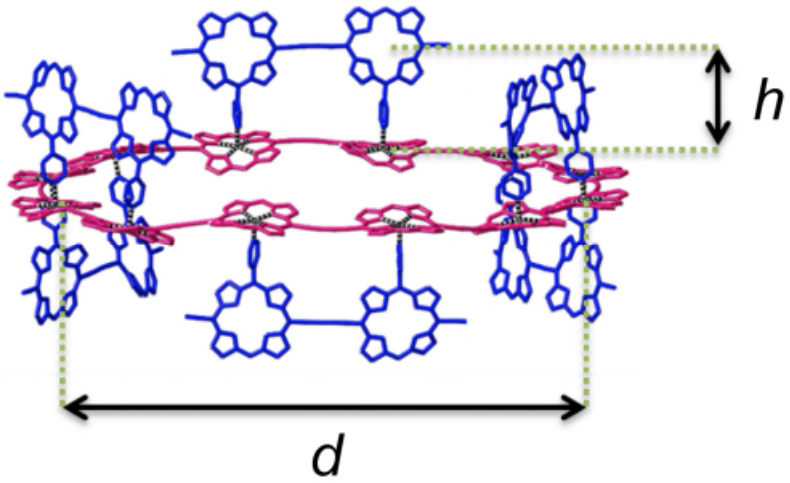

Figure 2.13 Dimensions of ring-dimer complex, ***c*-P12$_{THS}$·(P2Py2)$_6$** where *h* is the dimer-nanoring distance and *d* is the nanoring diameter.

Calculations of energy transfer rates within the Förster formalism are extremely sensitive to length scales (because of the R^{-6} factor). The critical dimensions of the complex are the distance from the center of the dimer porphyrin to the mean plane of the ***c*-P12$_{THS}$** nanoring porphyrin (indicated by *h* in **Figure 2.13**) and the diameter of the nanoring (indicated by *d*). The diameter of the nanoring has been previously measured to be 47 Å using small-angle X-ray scattering (SAXS) and STM imaging.[20,22] The distance *h* between the donor dimer porphyrin center and the adjacent ***c*-P12$_{THS}$** acceptor porphyrin center was estimated by analyzing several related crystal structures. A search in the Cambridge Structural Database (CSD) resulted in 7 structures that fulfilled the requirement that a free-base porphyrin with a 4-pyridyl-substituent in the meso-position is bound to a zinc-porphyrin (**Figure 2.14**). **Table 2.1** shows the distance *h* between the centroid A calculated from the coordinates of the four nitrogen atoms of the free-base porphyrin and the

centroid B of the four nitrogen atoms of the zinc-porphyrin unit (using the program Mercury). Structures no. 1 and no. 5 were not taken into consideration since the angle formed between the centroid A, the pyridyl-nitrogen atom and centroid B is strongly deviating from 180°. Taking the remaining structures into account gives an arithmetic mean of h = 10.16 Å (standard deviation = 0.09 Å).

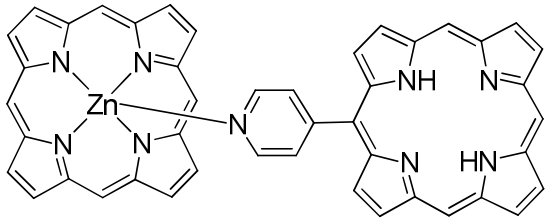

Figure 2.14 Crystal structures that contained this motif were used for the determination of *h*.

Table 2.1 Data used to obtain a value for *h*. (Structure no. 2 contains the motif shown in **Figure 2.14** twice, each with different parameters.)

Structure No.	***h*** **(centroid A-centroid B)**	**angle (centroid A-N-centroid B)**	**Reference**
1	9.84 Å	141°	D. V. Konarev, A. L. Litvinov, I. S. Neretin, N. V. Drichko, Y. L. Slovokhotov, R. N. Lyubovskaya, J. A. K. Howard, D. S. Yufit, *Cryst. Growth Des.* **2004**, *4*, 643.
2	10.06 Å 10.07 Å	175° 173°	E. Iengo, E. Zangrando, R. Minatel, E. Alessio; *J. Am. Chem. Soc.* **2002**, *124*, 1003.
3	10.12 Å	173°	E. Iengo, E. Zangrando, E. Alessio, J.-C. Chambron, V. Heitz, L. Flamigni, J.-P. Sauvage, *Chem. Eur. J.* **2003**, *9*, 5879.
4	10.33 Å	175°	A. K. Burrell, B. M. Jones, S. B. Hall, D. L. Officer, D. C. W. Reid, K. Y. Wild, *J. Inclusion Phenom. Macrocyclic Chem.* **1999**, *35*, 185.
5	9.71 Å	143°	R. K. Kumar, I. Goldberg, *Angew. Chem. Int. Ed.* **1998**, *37*, 3027.
6	10.20 Å	177°	M. Beyler, V. Heitz, J.-P. Sauvage, B. Ventura, L. Flamigni, K. Rissanen, *Inorg. Chem.* **2009**, *48*, 8263.
7	10.18 Å	177°	S. Anderson, H. L. Anderson, A. Bashall, M. McPartlin, J. K. M. Sanders, *Angew. Chem. Int. Ed.* **1995**, *34*, 1096.

2.4 Ultrafast Photophysics

The work presented in this section was performed and analysed in collaboration with Dr. Patrick Parkinson and Dr. Laura Herz (Department of Physics, University of Oxford). I prepared the samples and Dr. Parkinson did most of the measurements.

The addition of an excess of a competing ligand such as pyridine (1% by volume) effectively dissociates ring-dimer ***c*-P12$_{THS}$·(P2py2)$_6$** and ring-dimer-ring **(*c*-P12$_{THS}$)$_2$·(P2py4)$_6$** complexes. In this way, we are able to control the association state of the complexes, allowing for unambiguous isolation of electronic effects leading to energy transfer from dimers to nanorings. **Figure 2.15a** and **b** show the steady-state photoluminescence (PL) spectra for the complexes in their associated state (blue line) and dissociated state (red line) following addition of excess pyridine. A vertical dashed red line indicates the dimer PL emission wavelength at 731 nm (716 nm) for the ring-dimer (ring-dimer-ring) complex, respectively. A qualitative comparison of the PL from the assembled and disassembled states shows the expected quenching of dimer emission for associated states. In addition, the effect of decreased planarisation for the ring-dimer complex can be observed through changes in both spectral position and intensity of the nanoring emission.[12,13]

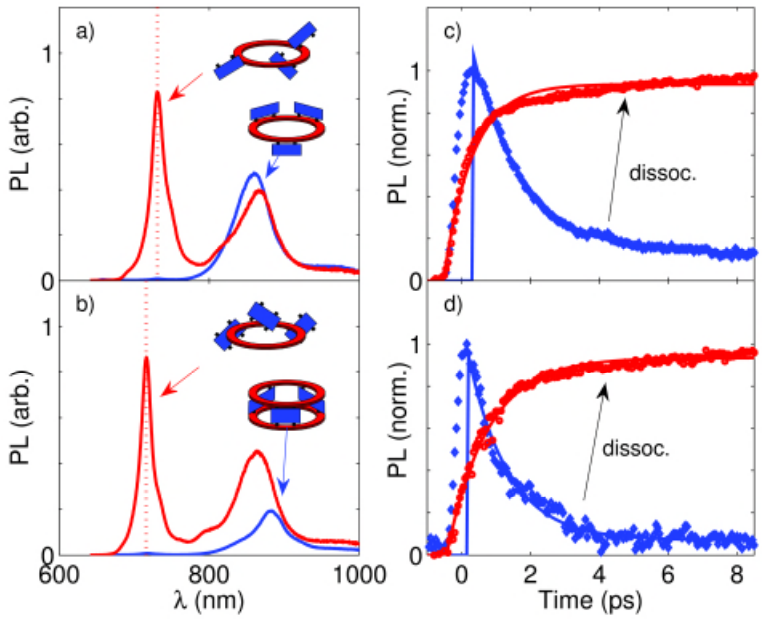

Figure 2.15 (a,b) Steady-state PL spectra for the (a) ring-dimer and (b) ring-dimer complexes in the associated (blue line) and dissociated (red line) state. The dimer emission is indicated with a vertical dashed red line. (c,d) Time-resolved PL dynamics for dimer emission for the (c) ring-dimer and (d) ring-dimer-ring structure are shown for each association state.

To explore the rates at which energy is transferred in these complexes, we employed ultrafast time-resolved PL spectroscopy. We experimentally assessed the dimer-to-nanoring energy transfer process by comparing the dynamics[23] of dimer emission in the associated state with that of the free dimer after breaking the complex by adding excess pyridine. These measurements reveal that in the supramolecular complex, energy transfer to the nanoring provides an additional and dominant decay channel, leading to rapid PL quenching. **Figure 2.15c** and **2.15d** show that energy transfer in the dimer-nanoring complexes is remarkably fast: the dimer PL emission for the associated state (blue points and line) drops rapidly in comparison to that for the dissociated state (red points and line). By modelling the ratio of the dimer emission for the assembled and disassembled states, we are able to determine an energy transfer rate of $(1.25\ \text{ps})^{-1}$ and $(0.65\ \text{ps})^{-1}$ for ring-dimer ***c*-P12$_{THS}$·(P2py2)$_6$** and ring-dimer-ring **(*c*-P12$_{THS}$)$_2$·(P2py4)$_6$** complexes, respectively. The effective doubling of the energy transfer rate upon addition of the second nanoring is a striking demonstration of the effects of adding a second, acceptor deactivation channel. These synthetic ring assemblies therefore demonstrate the feasibility of both uni- and bi-directional energy funnelling.

Any excess of unbound dimer contributes a constant offset to the PL intensity (**Figure 2.16**); this contribution does not however change the energy transfer rate observed for the dimer emission from associated complexes. We titrated the donor dimer **P2Py2** into a solution of the acceptor nanoring ***c*-P12$_{THS}$** to reach the stoichiometric ratio in the 6:1 complex. However, due to the strength of the association constant, at thermodynamic equilibrium it is expected that a sub-population of unbound dimers will exist in the solution even at the stoichiometric 6:1 mole ratio. The influence of this population on the energy transfer dynamics was measured using stoichiometric and super-stoichiometric (excess dimer) mixtures of the ring-dimer complex. **Figure 2.16** demonstrates the effect of changing this ratio; in both cases, identical energy transfer constants are observed, with a variable baseline depending upon the free-dimer concentration.

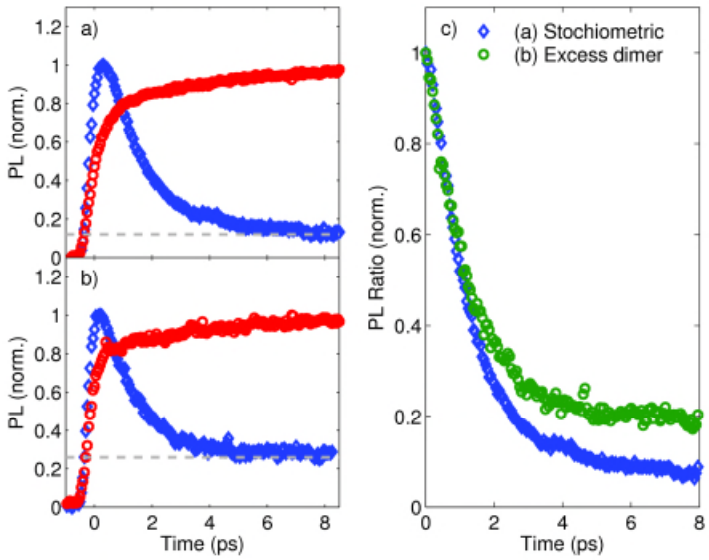

Figure 2.16 Dimer photoluminescence dynamics for (a) stoichiometric ***c*-P12$_{THS}$·(P2py2)$_6$** and (b) super-stoichiometric mixtures of the ring-dimer complex, which excess **P2py2**. Dynamics for both associated complex (blue diamonds) and dissociated states formed by adding pyridine (red circles) are shown; the baseline is indicated by a dashed grey line. (c) The ratio of photoluminescence emission (indicating energy transfer from dimer to nanoring) is shown for both cases. Excitation wavelength: 450 nm; emission wavelength: 735 nm

Interesting results have been observed by comparing the energy transfer rates of these synthetic nanoring assemblies to those of their natural counterparts. We found that energy transfer rates in the synthetic system is similar to those found in LH2 complexes of purple bacteria in which an energy transfer rate of $(0.9\ ps)^{-1}$ has been established between B800 antenna chromophores and B850 acceptor chromophores.[24] This suggests the possibility for gaining further insight into the natural light harvesting systems through modelling energy transfer in the presented complexes in the further research.

2.5 Ring-ring template-directed synthesis

After we illustrated successful formation and photophysical properties of double- and triple-strand complexes (dimer-ring and ring-dimer-ring complexes) in the previous section, our attention was drawn to the question whether it is possible to use a nanoring as a template to make another complementary nanoring with the commensurate size via double- and triple-strand architectures (**Figure 2.17**). The use of an existing nanoring as a template for a new nanoring could open an avenue for self-replication of such systems.

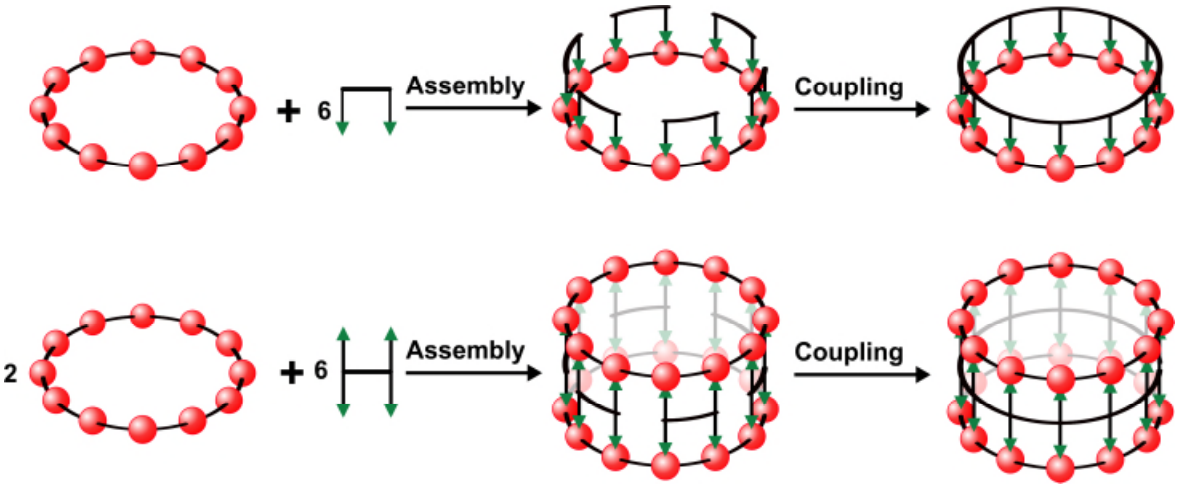

Figure 2.17 Synthesis of porphyrin nanoring. (Top) New approaches using an existing nanoring as a template for the synthesis of a new ring of the same size via a double-strand complex and (Bottom) via a triple-strand complex.

While the syntheses of the ring-ring templating via double-strand complexes proved successful (details provided in the subsequent section), the formation of triple-strand architectures concentration exhibited solubility problems at micromolar. We decided that it was not worth investing a considerable amount of time and precursors into the synthesis of a triple-strand ring complex that was likely to be extremely difficult to purify and characterise, and instead focused only on the double-strand synthesis. While I was working on the ring-ring templating synthesis of free-base nanoring ***c*-H$_2$P12py12** from 12-ring template and free-base porphyrin dimer **P2py2** substrate, Dr. Christiane Knappke investigated a similar reaction but used palladium porphyrin tetramer **PdP4py4** as a substrate instead to synthesise the palladium nanoring ***c*-PdP12py12**. I worked with her to characterise this ring-ring complex. Preliminary results of ring-ring templating reactions of ***c*-PdP12py12** and free-base nanoring ***c*-H$_2$P12py12** are shown as follows.

2.5.1 The synthesis of *c*-PdP12py12 from Pd porphyrin tetramer and 12-porphyrin ring

Initially we attempted the synthesis of the ring-ring complex ***c*-P12$_{THS}$·*c*-PdP12py12** using the 12-nanoring bearing 3,5-bis(trihexylsilyl)phenyl (THS) substituents ***c*-P12$_{THS}$** as a template and the deprotected tetramer **FD-PdP4py4** as a substrate. Unfortunately, after the coupling reaction no ring-ring complex was observed by UV-vis and GPC analyses. This result indicates that the ***c*-P12$_{THS}$** ring is not a suitable template for the synthesis of the ring-ring complex, which might be

due to steric interactions by the large THS-substituents. It appears that there may be some unfavourable interaction between the THS-groups of neighbouring porphyrin units, when the ***c*-P12$_{THS}$** ring is forced into a planar conformation.

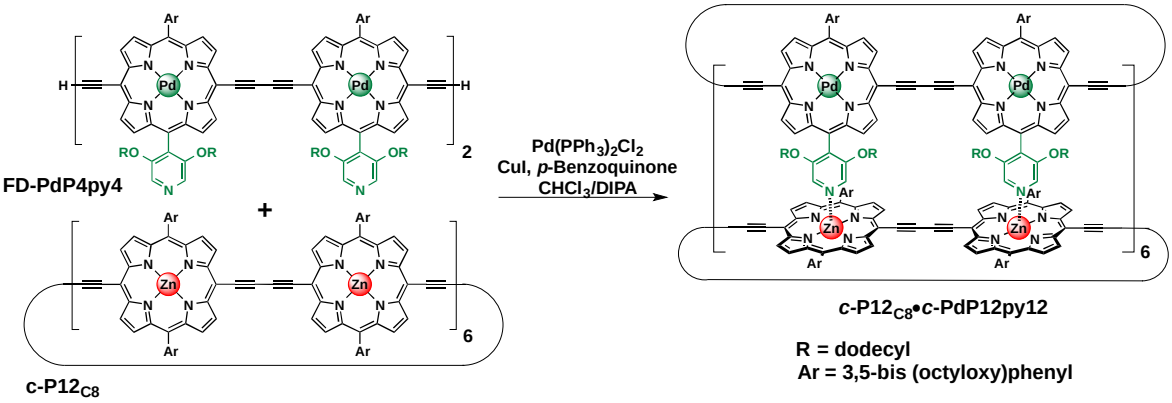

Figure 2.18 The ring-ring templating synthesis of the ring-ring complex ***c*-P12$_{C8}$·*c*-PdP12py12**.

Since the use of ***c*-P12$_{THS}$** proved to be unfruitful, the 12-ring bearing octyloxy aryl substituents ***c*-P12$_{C8}$**, which are smaller than the THS side groups, was considered. The reaction was performed under the usual palladium-catalysed coupling conditions (**Figure 2.18**) and was monitored by UV-vis-NIR spectroscopy (**Figure 2.19**). After the first catalyst addition, both Q-bands from the zinc-porphyrin 12-ring ***c*-P12$_{C8}$** (from 840 to 870 nm) and from the palladium porphyrin tetramer **FD-PdP4py4** (from 710 to 730 nm) are red shifted. After the second catalyst addition and heating to 50 °C for 2 h, the Q-band of ***c*-P12$_{C8}$** band further red shifts and becomes more structured. After the third catalyst addition and stirring overnight the structure of the far-red band further changed, which might be attributed to the disappearance of the initially observed band around 870 nm. The red shift of the Q-bands is attributed to the formation of a bigger oligomer in the case of the palladium porphyrins, and the planarisation and therefore enhancement of the effective conjugation length of the zinc-porphyrin 12-ring ***c*-P12$_{C8}$**.

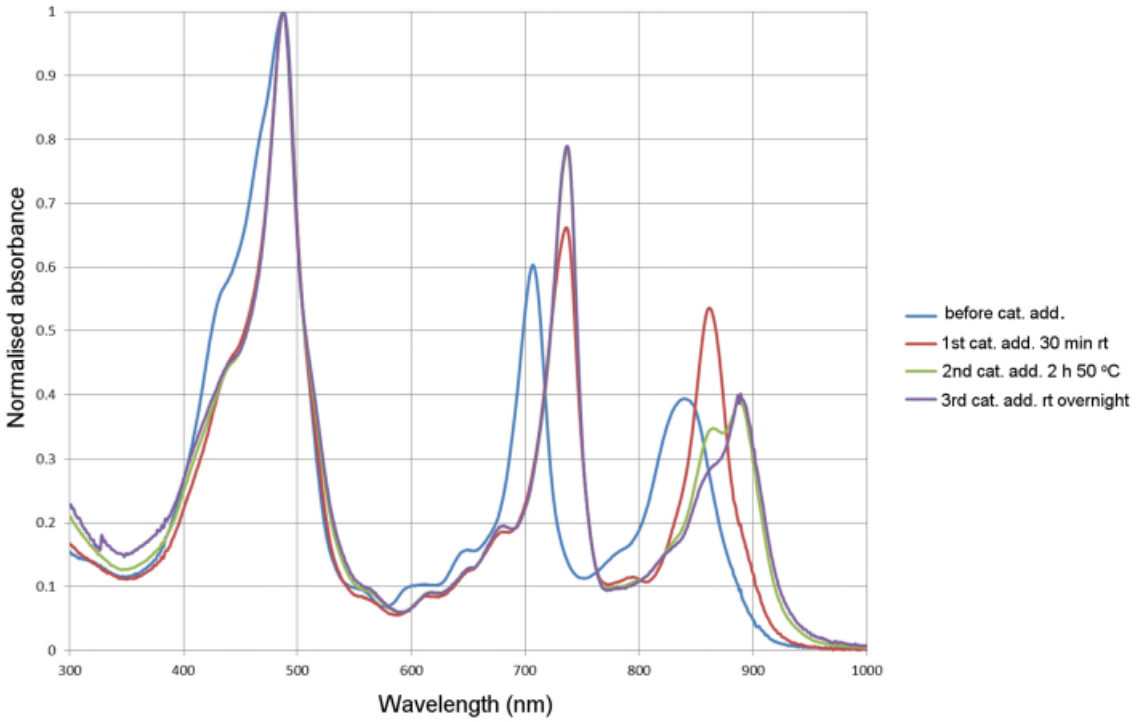

Figure 2.19 UV-vis-NIR ($CHCl_3$, 298 K) monitoring of the formation of the ring-ring complex from ***c*-P12$_{C8}$** and Pd tetramer **FD-PdP4py4**.

After purification over aluminium oxide and a small SEC column, analytical GPC indicated the presence of the desired ring-ring complex as the main component at 27.01 min (**Figure 2.20**). The side products with different retention times show very similar UV profiles. The desired complex was further purified on recycling GPC eluting with toluene and isolated in 39% yield. The desired complex ***c*-P12$_{THS}$·*c*-PdP12py12** was further identified by ^{1}H NMR, MALDI-ToF mass spectrometry and small angle X-ray scattering (SAXS) technique.

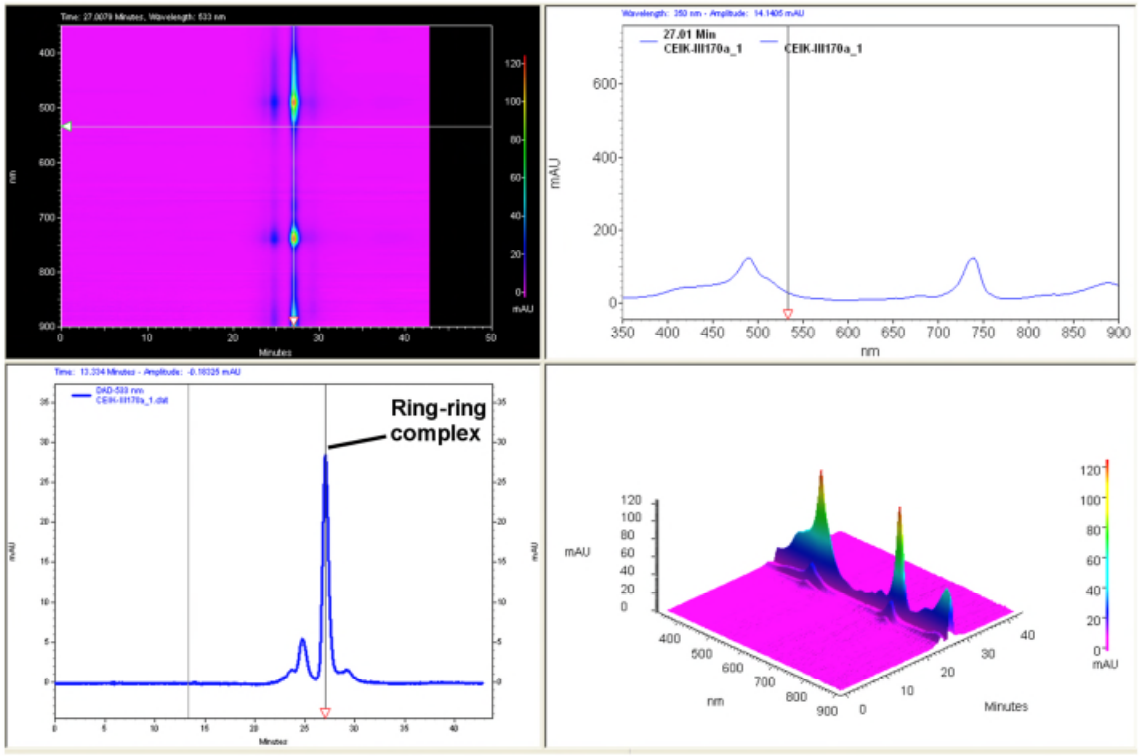

Figure 2.20 GPC traces (detection at 533 nm, toluene) of crude product after removal of insoluble materials and catalysts.

2.5.2 Structural details of *c*-P12$_{C8}$·*c*-PdP12py12 complex

MALDI-ToF mass spectrum (**Figure 2.21**) indicates a signal corresponding to the desired ring-ring complex ***c*-P12$_{C8}$·*c*-PdP12py12** at *m*/*z* 31,660 and a signal corresponding to a ring-ring complex with one additional ***c*-P12$_{C8}$** at *m*/*z* 44,603. The template ***c*-P12$_{C8}$** (at *m*/*z* 13,037) and its aggregation dimer (at *m*/*z* 26,013) are also detected. The aggregation is also seen by broad ^{1}H NMR of this material (**Figure 2.22**).

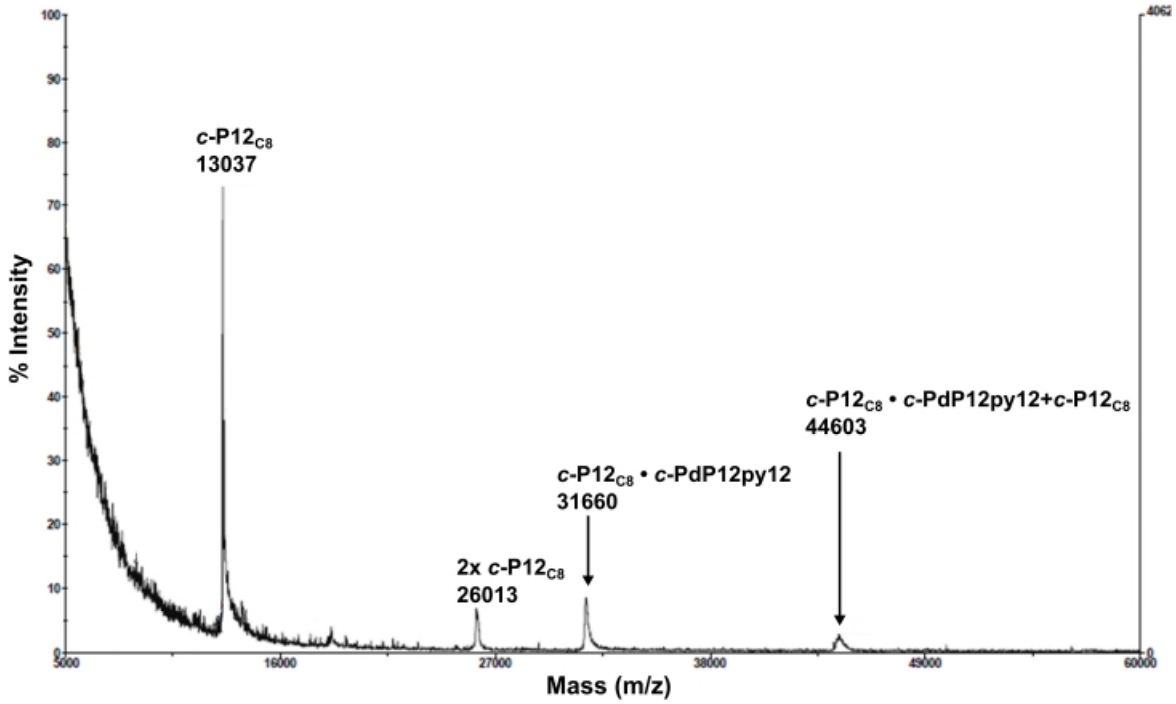

Figure 2.21 MALDI-MS of ring-ring complex (Swansea National MassSpec Service).

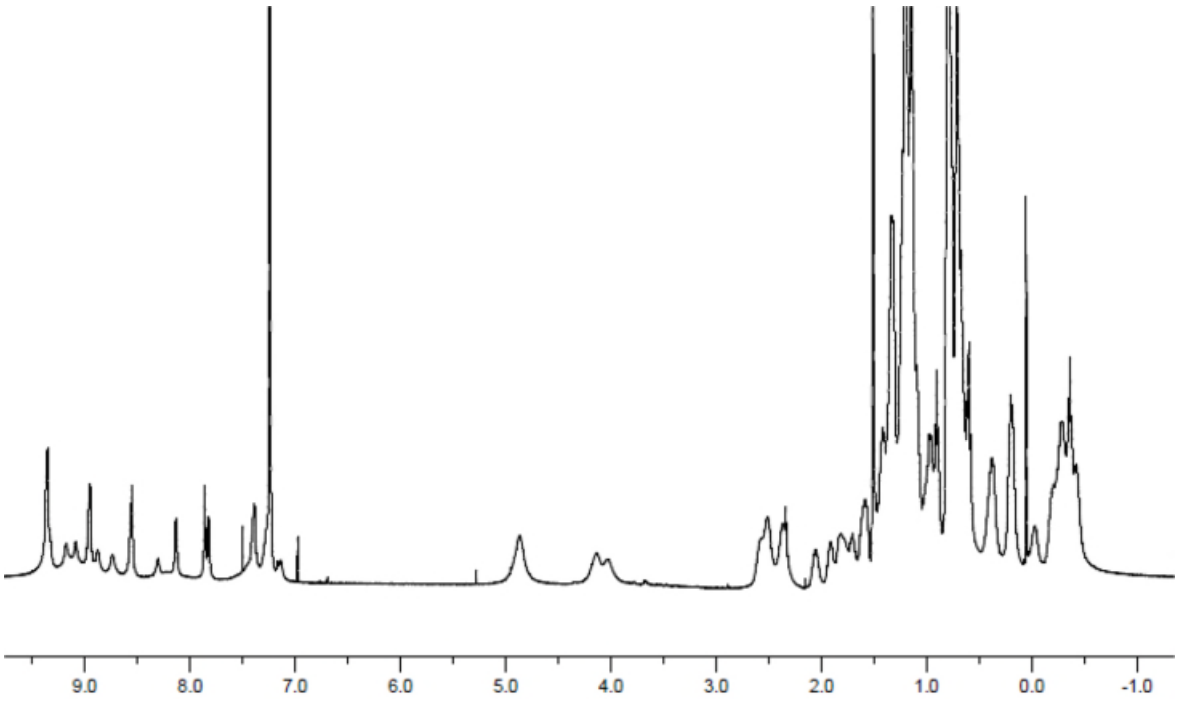

Figure 2.22 ^{1}H NMR in $CDCl_3$ of the purified ring-ring complex ***c*-P12$_{C8}$·*c*-PdP12py12**.

Solution-phase small angle X-ray scattering (SAXS) is the alternative tool for characterising synthetic supramolecular structures[20,22,25] without growing single crystals. The method gives the information on the overall size and shape of molecules. The SAXS curve is the electronic pair-distribution function (PDF), which is the normalised probability of a pair of electron density at particular distances. Peaks in the PDF can often be assigned to distances between parts of the molecule with high electron density (e.g. metal atoms).

SAXS analysis on the complex ***c*-P12$_{C8}$·*c*-PdP12py12** was performed to further confirm its identity (**Figure 2.23**). The scattering data were acquired at Diamond Light Source, UK with the assistance of Dr. Marc Malfois. The experimental PDF data are in good agreement with those obtained from the theoretical model (**Figure 2.23**). The PDF from raw scattering data (**Figure 2.23-right**) features 12 Å and 48 Å peaks, values corresponding to the shortest Pd-Zn distance (10 Å) in the complex and the diameter of the complex (48 Å).

The preliminary identification data presented above suggest that this ring-ring templating is a promising strategy to prepare a new ring of identical size by using the ring template ***c*-P12$_{C8}$**.

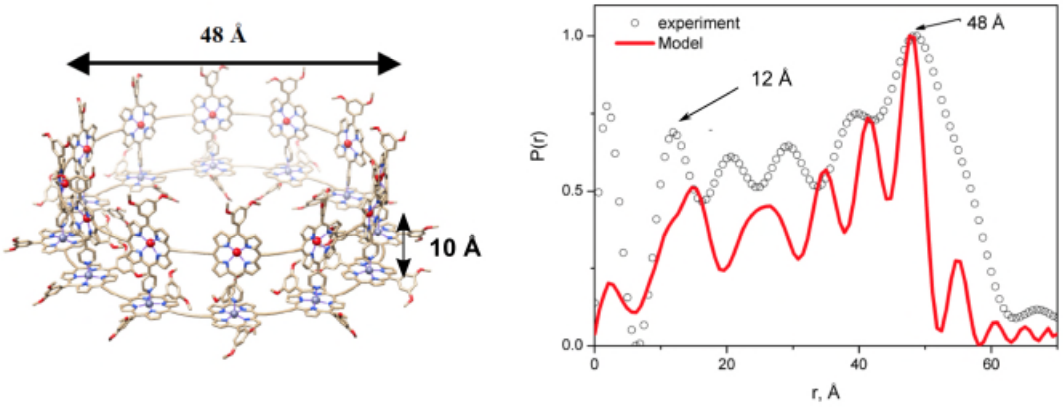

Figure 2.23 left) Molecular models used for fitting of and comparison with experimental data. The geometry was optimised by molecular mechanics using HyperChem's MM+ force field. right) Experimental (black circles) and model based (red line) pair distribution function (PDF), obtained using the software *Gnom*.

2.5.3 The synthesis of *c*-H$_2$P12py12 from free-base porphyrin dimer and 12-porphyrin ring

In the long term, it would be interesting to study energy transfer in the ring-ring complex. Pd porphyrins, as known in oxygen sensing might not be good candidates for this study because their phosphorescence can be quenched by oxygen at room temperature[26,27] and they also have rapid

intersystem-crossing from S_1 to T_1.[28] Thus, we introduced the free-base porphyrins which are not only interesting in energy transfer as described in the previous sections, but also because the synthesis of the corresponding nanorings is challenging.

Similarly to the previous section the ring-ring template effect is applied to the synthesis of ***c*-H$_2$P12py12** employing the fully deprotected free-base dimer **FD-H2P2py2** as a substrate instead of the palladium tetramer, and ***c*-P12$_{C8}$** as a template. The challenge lies in the fact that the standard Pd-catalysed coupling catalysts: $Pd(PPh_3)_2Cl_2$ and CuI previously used for ***c*-P12$_{C8}$·*c*-PdP12py12** can easily lead to Cu insertion in the free-base porphyrins of the dimer substrate. The Cu-free Glaser coupling conditions were thus considered in the ring-ring templated synthesis of free-base 12-nanoring ***c*-H2P12py12**.

Initially, we tested the published Cu-free condition[29] on a model system, by treatment of a monodeprotected Zn porphyrin monomer with stoichiometric amount of $Pd(PPh_3)_2Cl_2$ in toluene/triethylamine (5:l) in air at 50 °C, affording the butadiyne-linked porphyrin dimer (**Figure 2.24**) in 70% isolated yield.

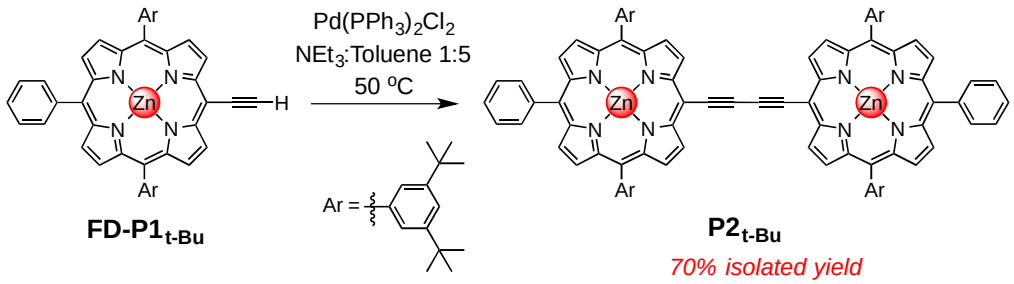

Figure 2.24 Synthesis of a Zn porphyrin dimer with stoichiometric amount of $Pd(PPh_3)_2Cl_2$ in toluene/triethylamine (5:l) in air at 50 °C

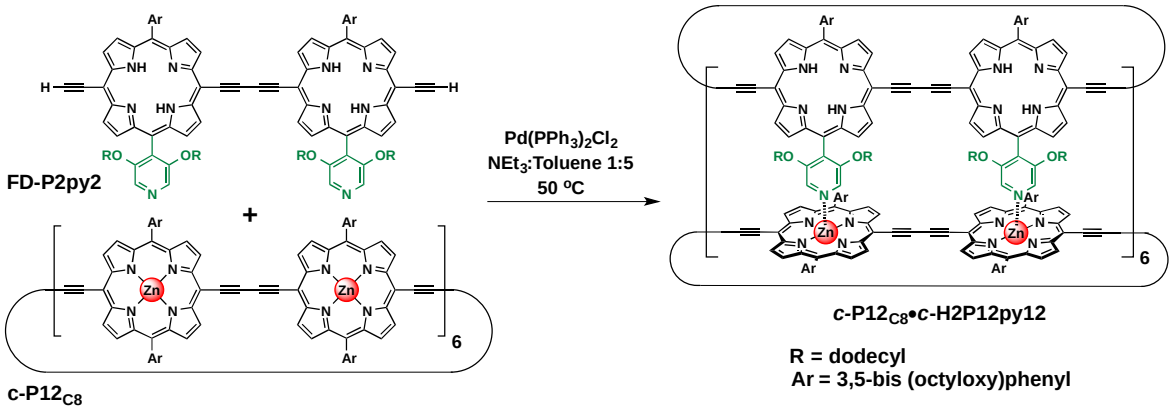

Figure 2.25 The ring-ring templating reaction of the free-base nanoring ***c*-H2P12py12** with stoichiometric amount of $Pd(PPh_3)_2Cl_2$ in toluene/triethylamine (5:l) in air at 50 °C

Following the promising initial result, similar conditions were used to test the ring-ring synthesis of ***c*-H2P12py12** (**Figure 2.25**). The reaction was monitored by UV-vis spectroscopy (**Figure 2.26**). Additional coupling reagent was added until no absorption change was observed. In the final absorption spectrum, the Q-bands of the free-base dimer **P2py2** at 638 and 720 nm are slightly red-shifted, indicating the formation of longer free-base oligomers and the Q-band of the 12-ring at 825 nm does not shift, reflecting no planarisation. Then, the reaction mixture was passed through an alumina plug to remove all the coupling reagents. Purification of the crude mixture by GPC eluting with toluene/1% pyridine was not successful since the solubility of the free-base porphyrin oligomers bearing pyridyl groups is poor in this solvent system. Thus, the crude product was investigated without further purification.

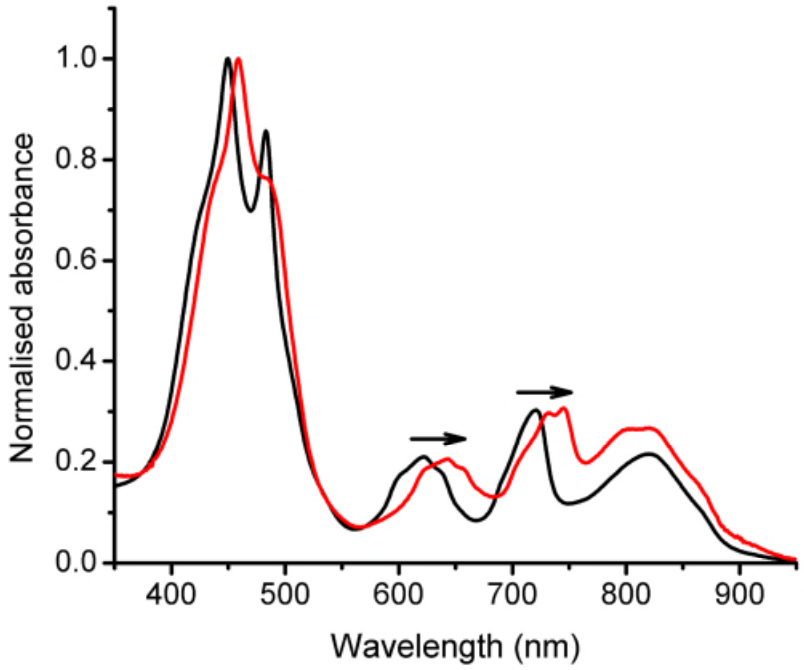

Figure 2.26 UV-vis absorption spectra of the ring-ring templating reaction of the free-base nanoring ***c*-H2P12py12**: before addition of the coupling reagents (black) and after several times of addition of the coupling reagents and heating at 50 °C until the absorption spectra remain unchanged (red).

Investigation of the crude mixture was performed by MALDI-ToF and ^{1}H NMR. For MALDI-ToF, no mass signal at *m*/*z* 17,184 corresponding to the free-base nanoring ***c*-H2P12py12** was observed in the spectrum. Only two signals corresponding to free-base dimer at *m*/*z* 3,183 (expected 2,868) and ***c*-P12$_{C8}$** at *m*/*z* 13,050 (expected 13,018) were detected. ^{1}H NMR spectrum of the ring-ring templating product is also inconclusive due to the broadening in the spectrum (**Figure 2.28**).

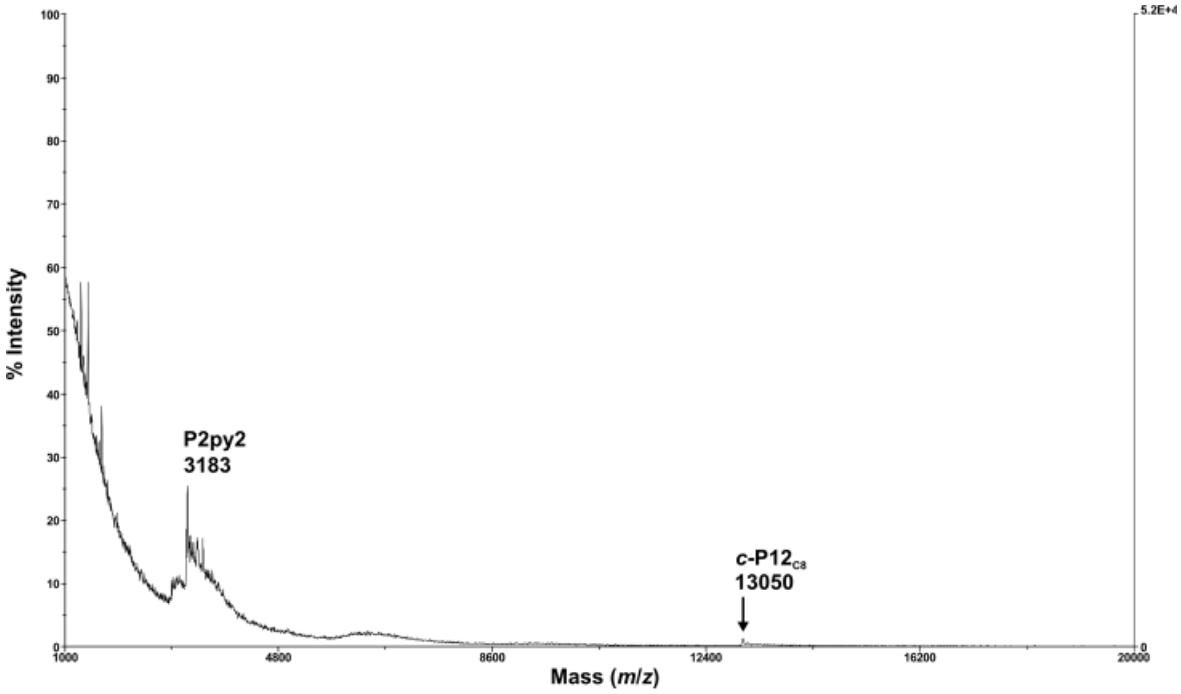

Figure 2.27 MALDI-ToF analysis of the crude product from the ring-ring templating synthesis of the free-base nanoring ***c*-H2P12py12**; full range (spectrum acquired by the EPSRC National Mass Spectrometry Center at Swansea University).

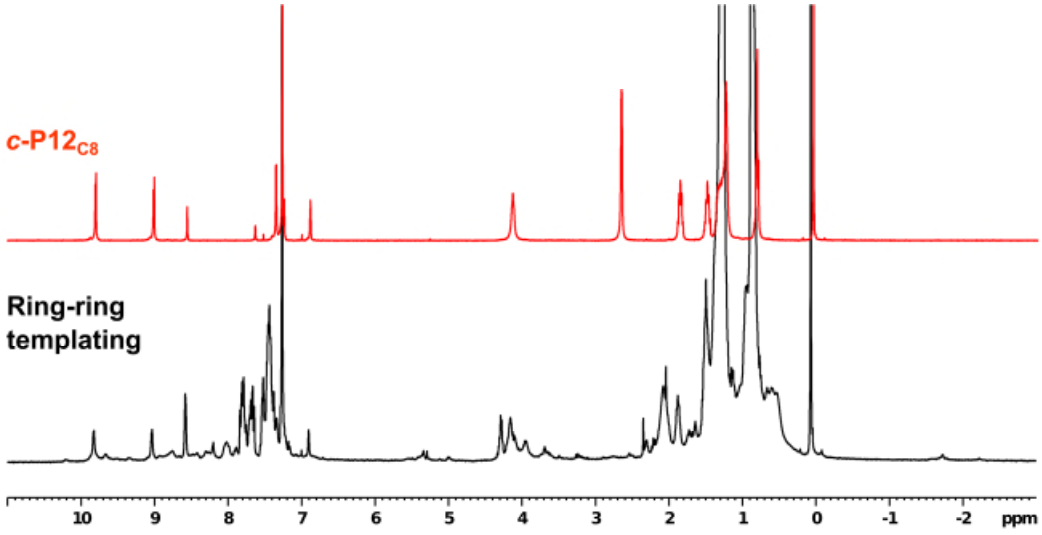

Figure 2.28 ^{1}H NMR spectra of the crude product from the ring-ring templating synthesis of the free-base nanoring ***c*-H2P12py12** (bottom) compared to unbound ***c*-P12$_{C8}$** (top) ($CDCl_3$, 298 K, 400 MHz)

In contrast to the synthesis of Pd 12-ring with the template ***c*-P12$_{C8}$** in which the ring-ring template effect is clearly present, for the synthesis of free-base 12-nanoring, preliminary results from MALDI-ToF and ^{1}H NMR are still inconclusive, and careful consideration must be given to the system under investigation. Heating at 50 °C in the Cu-free coupling conditions might decrease

the binding strength of the dimer-ring complex before coupling, which may induce the polymerisation of the free-base dimer substrate. Unfortunately, due to a lack of time and shortage of material, no further experimental work was completed on this project and my focus switched to linear templating where the same concept can be utilised with more promising results as described in **Chapter 4**.

2.6 Summary

In summary, we studied two synthetic supramolecular complexes with analogies to natural LH2 antenna systems. Extremely rapid energy transfer from porphyrin dimer antenna molecules to the 12-porphyrin nanoring acceptor was observed in time-resolved PL measurements, which doubles in rate upon the addition of a second acceptor nanoring. These systems have energy transfer rates that are comparable to those observed in natural light harvesting systems, making them interesting models for understanding energy transfer in natural light harvesting systems.

The extension of this project in the ring-ring template-directed synthesis by using one ring to produce another complementary ring is effective for the formation of the metalloporphyrin nanoring. The free-base porphyrin nanoring which may be a promising candidate for fluorescence applications, however, still needs further investigation.

2.7 Experimental section

2.7.1 General methods

All chemicals were purchased from commercial suppliers and used without further purification unless otherwise noted. Dry THF, CH_2Cl_2, chloroform and toluene were obtained by passing through alumina under N_2 pressure. Diisopropylamine (DIPA) was dried over calcium hydride, distilled and stored under nitrogen over molecular sieve. All manipulations of air- or water-sensitive compounds were performed using standard high-vacuum techniques. Flash column chromatography was performed on Merck silica gel 60 (40–63 μm). For TLC Merck silica gel 60 F_{254} aluminum sheets were used. Aluminum oxide, activated, basic, Brockmann I, standard grade,

~150 mesh, 58 Å from Sigma Aldrich was used. For size exclusion chromatography Biobeads SX1 (crosslinked polystyrene) were used under gravity elution. "Petrol ether" (PE) always refers to petrol ether 40/60. ^{1}H and ^{13}C NMR spectra were recorded on a BrukerAvance 400 (400.13 and 100.64 MHz), a Bruker DQX 400 (400.13 and 100.64 MHz), a Bruker DRX 500 and BrukerAvance II 500 (500.13 and 125.77 MHz) at 298 K unless otherwise stated. TopSpin (Version 2.1) and Spinworks was used. Chemical shifts (δ in ppm) are referenced to solvent residual peaks ($CDCl_3$ at δ_H 7.24, δ_C 77.0). Abbreviations for ^{1}H-NMR data: *s* = singlet, *d* = doublet, *t* = triplet, *m* = multiplet, "t" = pseudo triplet, br = broad. Abbreviations for ^{13}C-DEPTQ-NMR data: *u* = up (CH_3 or CH), *d* = down (CH_2 or C_q). Peaks were assigned based on H,H-COSY, H,C-HMQC and H,C-HMBC correlation spectra. MALDI-TOF-MS were measured with a Waters MALDI Micro MX or by Swansea National Mass Spectrometry Service. Absorption spectra were recorded at 25 °C with a Perkin–Elmer Lambda 20 photospectrometer using quartz 1 cm cuvettes (3 mL).

For GPC the following systems were used:

a) Analytical System: VWR Hitachi Lachrom Elite (pump L-2130, Autosampler L-2200, Diode Array Detector L-2450, Column oven L-2350)

b) Recycling System: Shimadzu (prominence communication bus module CBM-20A, prominence UV-vis detector SPD-20A, prominence liquid chromatograph LC-20AD, prominence degassing unit DGU-$20A_{3R}$, Shimadzu valve unit FCV-$20AH_2$), detection wavelengths: 371 nm and 500 nm

The following GPC column systems were used:

a) Analytical: PL columns in sequence: precolumn PLgel, PLgel 3 μm MIXED-E (2 x 30 cm), PLgel 5 μm MIXED-D (2 x 30 cm), PLgel 5 μm 1000 Å (30 cm)

b) Preparative (recycling): Japan Analytical Industry columns in sequence: precolumn JAIGEL-H-P, JAIGEL-3H, JAIGEL-4H

c) Analytical: Japan Analytical Industry columns in sequence: precolumn JAIGEL-H-P, JAIGEL-3H-A, JAIGEL-4H-A

2.7.2 Synthetic procedures

2.7.2.1 Synthesis of free-base pyridyl-substituted porphyrin dimer **P2Py2**

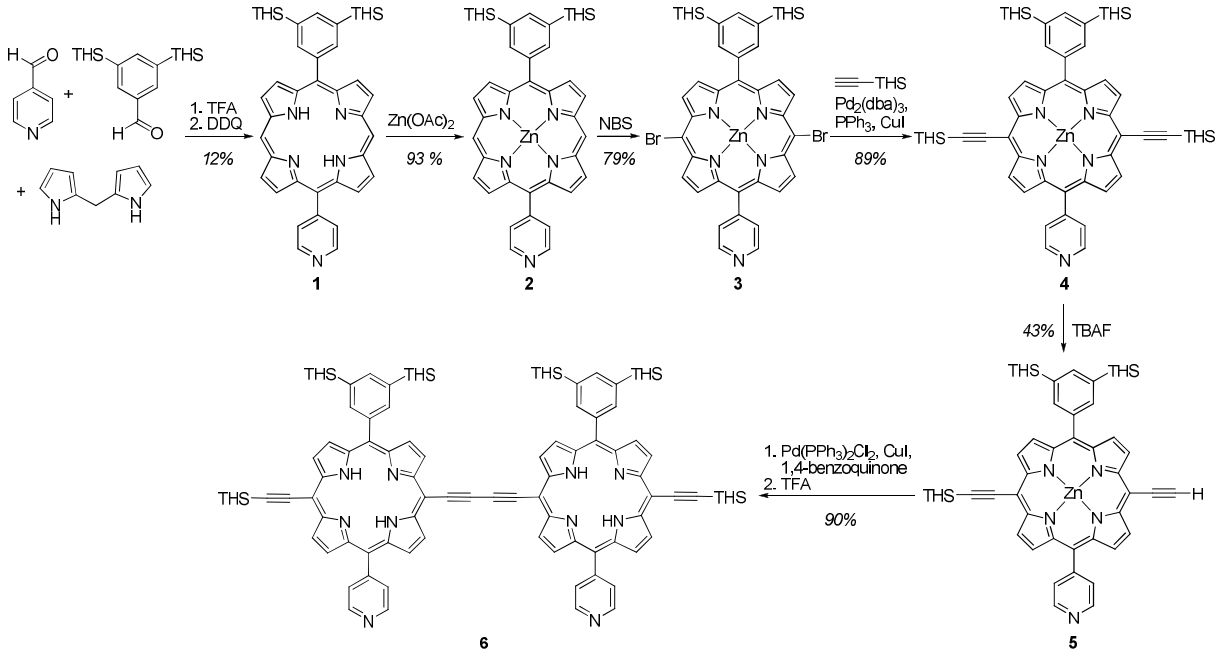

Scheme 2.1 Overview of the synthesis of free-base pyridyl-substituted porphyrin dimer **P2Py2** (THS = $Si(C_6H_{13})_3$). The starting aldehyde, 3,5-bis(trihexylsilyl)benzaldehyde, was synthesised as published literature.[30]

5-(4-pyridyl)-15-(3,5-bis(trihexylsilyl)phenyl)-porphyrin **1**

In a 3-L round-bottom-flask, equipped with a stir bar DCM (1900 mL) was placed. The flask was sealed with a suba-seal and evacuated down to 1 mbar followed by backfilling with nitrogen three times. Light was excluded by wrapping the flask with aluminium foil. 3,5-Bis-(trihexylsilyl)-benzaldehyde (3.04 g, 4.51 mmol, 1.0 equiv.) was dissolved in some of the DCM and added. Dipyrromethane (2.02 g, 13.8 mmol, 3.06 equiv.) was added. The flask was sealed again and flushed with nitrogen. 4-Pyrridylcarbaldehyde (0.85 mL, 9.02 mmol, 2.0 equiv.) was added. The mixture was deoxygenated again by evacuating and backfilling with nitrogen. Trifluoroacetic acid (2.14 mL, 28.0 mmol, 6.20 equiv.) was added over a period of 10 min under vigorous stirring. Stirring was continued for 3 h. DDQ (3.89 g, 17.1 mmol, 3.8 equiv.) was added. After 30 min stirring, triethylamine (11.4 mL, 81 mmol, 18 equiv.) was added. After stirring for 30 min, the volume was reduced and the remaining dark solution filtered over a plug of silica eluting with DCM/MeOH (98:2). The solvent was removed from the filtrate. The dark residue was purified by

column chromatography on silica initially eluting with petrol ether/DCM 19:1 collecting a red fraction, that consists of 5,15-bis-(3,5-bis(trihexylsilyl)phenyl)-porphyrin (662 mg, 0.416 mmol, 18%). Eluent was changed to DCM/Et_3N (99:1) and then DCM/MeOH/Et_3N (97:2:1). A dark fraction was collected that contained the desired product. After removing the solvent this fraction was subjected again to flash chromatography (silica, eluent: DCM/Et_3N 99:1). A red fraction was collected containing pure **1** (444 mg, 0.432 mmol, 10%). Another fraction that contained **1** was again purified by column chromatography, allowing the separation of additional product (129 mg, 0.126 mmol, 3%; contains minor impurities). Total yield: 573 mg (12%). TLC: R_f (DCM/MeOH 98:2) = 0.42; ^{1}H-NMR (500 MHz, $CDCl_3$): δ = 10.35 (s, 2H, *meso*-H), 9.43 (d, *J* = 4.6 Hz, 2H, β-H), 9.40 (d, *J* = 4.6 Hz, 2H, β-H), 9.10 (d, *J* = 4.6 Hz, 2H, β-H), 9.08 (m, 2H, py-H), 9.03 (d, *J* = 4.6 Hz, 2H, β-H), 8.34 (s, 2H, *o*-H), 8.22 (m, 2H, py-H), 8.02 (s, 1H, *p*-H), 1.57–1.47 (m, 12H, alkyl-H), 1.45–1.25 (m, 36H, alkyl-H), 1.01–0.93 (m, 12H, alkyl-H), 0.93–0.86 (m, 18H, alkyl-H), –3.10 (s, 1H, N*H*), –3.12 (s, 1H, N*H*); ^{13}C-DEPTQ-NMR (125 MHz, $CDCl_3$): δ = 149.8 (d, 1C, py-C), 148.5 (u, 2C, py-C), 147.5 (d, 2C, α-C), 146.1 (d, 2C, α-C), 145.4 (d, 2C, α-C), 145.2 (d, 2C, α-C), 141.0 (u, 2C, *o*-C), 139.4 (u, 1C, *p*-C), 139.3 (d, 1C, *ipso*-C), 135.5 (d, 2C, *m*-C), 132.2 (u, 2C, β-C), 131.6 (u, 2C, β-C), 131.5 (u, 2C, β-C), 130.1 (u, 2C, β-C), 129.8 (u, 2C, py-C), 121.4 (d, 1C, *meso*-C), 115.0 (d, 1C, *meso*-C), 105.6 (u, 2C, *meso*-C), 33.5 (d, 6C, alkyl-C), 31.6 (d, 6C, alkyl-C), 24.1 (d, 6C, alkyl-C), 22.7 (d, 6C, alkyl-C), 14.2 (u, 6C, alkyl-C), 12.7 (d, 6C, alkyl-C); *m/z* (MALDI-TOF): 1028.4 ($C_{67}H_{97}N_5Si_2$ requires 1028.74).

[5-(4-pyridyl)-15-(3,5-bis(trihexylsilyl)phenyl)-porphyrinato]zinc(II) **2**

Porphyrin **1** (251 mg, 0.244 mmol, 1.0 equiv.) was dissolved in chloroform (21 mL). A solution of zinc acetate-dihydrate (270 mg, 1.23 mmol, 5.0 equiv.) in methanol (3 mL) was added. The mixture was stirred at 40 °C for 2 h. The mixture was filtered over a plug of silica eluting with DCM/pyridine (99:1). The solvent was removed from the pink filtrate. The pink residue was dried in high vacuum yielding the desired product **2**. Yield: 0.264 g (93 %). ^{1}H NMR (500 MHz, $CDCl_3$+1% pyridine-d_5): δ = 10.22 (s, 2H, *meso*-H), 9.36 (d, *J* = 4.3 Hz, 2H, β-H), 9.35 (d, *J* = 4.2 Hz, 2H, β-H), 9.07 (d, *J* = 4.4 Hz, 2H, β-H), 8.89 (d, *J* = 4.4 Hz, 2H, β-H), 8.42 (br, 2H, py-

H), 8.29 (d, *J* = 0.8 Hz, 2H, *o*-H), 8.03 (m, 2H, py-H), 7.98 (t, *J* = 1.0 Hz 1H, *p*-H), 1.52–1.43 (m, 12H, C*H*$_2$), 1.39–1.31 (m, 12H, C*H*$_2$), 1.31–1.22 (m, 24H, C*H*$_2$), 0.95–0.89 (m, 12H, C*H*$_2$), 0.87-0.81 (m, 18H, C*H*$_3$); ^{13}C-DeptQ-NMR (125 MHz, $CDCl_3$+1% pyridine-d_5): δ = 151.8 (d, 1C, py-C), 150.4 (d, 2C, α-C), 149.6 (d, 2C, α-C), 149.3 (d, 2C, α-C), 148.6 (d, 2C, α-C), 147.1 (u, 2C, py-C), 141.1 (d, 1C, *ipso*-C), 140.9 (u, 2C, *o*-C), 138.8 (u, 1C, *p*-C), 134.5 (d, 2C, *m*-C), 132.7 (u, 2C, β-C), 131.9 (u, 2C, β-C), 131.4 (u, 2C, β-C), 131.0 (u, 2C, β-C), 129.8 (u, 2C, py-C), 121.7 (d, 1C, *meso*-C), 115.1 (d, 1C, *meso*-C), 106.0 (u, 2C, *meso*-C), 33.5 (d, 6C, *C*H$_2$), 31.6 (d, 6C, *C*H$_2$), 24.0 (d, 6C, *C*H$_2$), 22.6 (d, 6C, *C*H$_2$), 14.1 (u, 6C, *C*H$_3$), 12.6 (d, 6C, *C*H$_2$); *m/z* (MALDI-TOF): 1090.7 ($C_{67}H_{95}N_5Si_2Zn$ requires 1090.65).

[5,15-dibromo-10-(4-pyridyl)-20-(3,5-bis(trihexylsilyl)phenyl)-porphyrinato]zinc(II) **3**

Porphyrin **2** (0.230 g, 0.196 mmol, 1.0 equiv.) was dissolved in chloroform (6.6 mL). Pyridine (0.13 mL) was added. *N*-Bromosuccinimide (69.0 mg, 0.388 mmol, 1.98 equiv.) was dissolved in chloroform (9.5 mL) and added to the stirred red solution of the porphyrin **2** via a dropping funnel over a period of 15 min. The reaction mixture turned green during the addition. The mixture was stirred for further 10 min. Acetone (0.2 mL) was added. The mixture was filtered over a plug of silica eluting with DCM/pyridine (99:1). The solvent was removed from the filtrate. The product **3** was precipitated by dissolving in DCM and layering with MeOH. The green precipitate was washed with methanol and dried in high vacuum. Yield: 194 mg (79%). ^{1}H-NMR (500 MHz, $CDCl_3$+1% pyridine-d_5): δ = 9.57 (d, *J* = 4.7 Hz, 2H, β-H), 9.56 (d, *J* = 4.6 Hz, 2H, β-H), 8.84 (m, 2H, py-H), 8.77 (d, *J* = 4.6 Hz, 2H, β-H), 8.67 (d, *J* = 4.7 Hz, 2H, β-H), 8.10 (s, 2H, *o*-H), 7.94 (m, 2H, py-H), 7.90 (s, 1H, *p*-H), 1.42–1.33 (m, 12H, C*H*$_2$), 1.29–1.22 (m, 12H, C*H*$_2$), 1.21–1.13 (m, 24H, C*H*$_2$), 0.85–0.79 (m, 12H, C*H*$_2$), 0.77–0.71 (m, 18H, C*H*$_3$); ^{13}C-DeptQ-NMR (125 MHz, $CDCl_3$+1% pyridine-d_5): δ = 150.8 (d, 2C, α-C), 150.7 (d, 1C, py-C), 150.1 (d, 2C, α-C), 149.8 (d, 2C, α-C), 149.2 (d, 2C, α-C), 147.7 (u, 2C, py-C), 140.4 (u, 2C, *o*-C), 140.3 (d, 1C, *ipso*-C), 138.8 (u, 1C, *p*-C), 134.5 (d, 2C, *m*-C), 133.4 (u, 2C, β-C), 133.2 (u, 2C, β-C), 132.6 (u, 2C, β-C), 132.1 (u, 2C, β-C), 129.3 (u, 2C, py-C), 123.8 (d, 1C, *meso*-C), 117.5 (d, 1C, *meso*-C), 104.8 (d, 2C,

meso-C), 33.2 (d, 6C, *C*H_2), 31.3 (d, 6C, *C*H_2), 23.7 (d, 6C, *C*H_2), 22.3 (d, 6C, *C*H_2), 13.9 (d, 6C, *C*H_3), 12.4 (d, 6C, *C*H_2); *m/z* (MALDI-TOF): 1249.3 ($C_{67}H_{93}Br_2N_5Si_2Zn$ requires 1250.47).

[5-(4-pyridyl)-10,20-bis(trihexylsilylethynyl)-15-(3,5-bis(trihexylsilyl)-phenyl)-porphyrinato]zinc(II) **4**

Porphyrin **3** (0.182 g, 0.146 mmol, 1.0 equiv.), $Pd_2(dba)_3$ (13.8 mg, 0.015 mmol, 10 mol%), PPh_3 (11.5 mg, 0.044 mmol, 30 mol%) and CuI (8.3 mg, 0.044 mmol, 30 mol%) were placed in a heat-dried 2-neck 50 mL round-bottom-flask equipped with a tap and a stir bar. The second opening was sealed with a suba seal and the flask was evacuated and backfilled with nitrogen three times. In a heat-dried 2-neck round-bottom-flask with nitrogen inlet and septum dry toluene (10 mL), dry diisopropylamine (12 mL) and THS-acetylene (170 µL, 0.438 mmol, 3.0 equiv.) were freeze-pump-thaw degassed. The solution was cannulated to the solids. The reaction mixture was heated under nitrogen to 50 °C and kept at this temperature for 2.3 h. The reaction mixture was filtered over a plug of silica eluting with DCM/pyridine (99:1). The solvents were removed from the green filtrate under reduced pressure. The residue was subjected to column-chromatography on silica eluting with petrol ether/EtOAc/pyridine (10:1:1). The desired product **4** (232 mg, 89 %) was isolated in form of a dark purple semi-solid. TLC: R_f (petrol ether/EtOAc/pyridine 10:1:1) = 0.50; ^{1}H-NMR (500 MHz, $CDCl_3$+1% pyridine-d_5): δ = 9.65 (d, *J* = 4.5 Hz, 2H, β-H), 9.62 (d, *J* = 4.5 Hz, 2H, β-H), 8.80 (d, *J* = 4.5 Hz, 2H, β-H), 8.69 (d, *J* = 4.5 Hz, 2H, β-H), 8.61 (br s, 2H, py-H), 8.18 (d, *J* = 0.7 Hz, 2H, *o*-H), 8.00 (d, *J* = 5.4 Hz, 2H, py-H), 7.96 (br s, 1H, *p*-H), 1.78–1.69 (m, 12H, alkyl-CH_2), 1.55–1.41 (m, 24H, alkyl- CH_2), 1.41–1.21 (m, 60H, alkyl-CH_2) 1.03–0.95 (m, 12H, alkyl-CH_2), 0.94–0.79 (m, 48H, alkyl-CH_2 and alkyl-CH_3); ^{13}C-deptQ-NMR (125 MHz, $CDCl_3$+1% pyridine-d_5): δ = 152.4 (d, 2C, α-C), 152.3 (d, 2C, α-C), 151.2 (d, 1C, py-C), 150.5 (d, 2C, α-C), 148.7 (d, 2C, α-C), 147.5 (u, 2C, py-C), 140.7 (d, 1C, *ipso*-C), 140.3 (u, 2C, *o*-C), 139.0 (u, 1C, *p*-C), 134.6 (d, 2C, *m*-C), 132.8 (u, 2C, β-C), 131.5 (u, 2C, β-C), 131.3 (u, 2C, β-C),131.0 (u, 2C, β-C), 129.5 (u, 2C, py-C), 124.3 (d, 1C, *meso*-C), 118.1 (d, 1C, *meso*-C), 109.2 (d, 2C, *meso*-C), 101.2 (d, 1C, ethynyl-C), 99.7 (d, 1C, ethynyl-C), 33.5 (d, 6C, *C*H_2), 33.3 (d, 6C, *C*H_2), 31.6 (d, 6C, *C*H_2), 31.5 (d, 6C, *C*H_2), 24.3 (d, 6C, *C*H_2), 24.0 (d, 6C, *C*H_2), 22.6 (d, 6C,

CH_2), 22.6 (d, 6C, *C*H_2), 14.1 (u, 6C, *C*H_3), 14.1 (u, 6C, *C*H_3), 13.8 (d, 6C, *C*H_2), 12.6 (d, 6C, *C*H_2); *m/z* (MALDI-TOF): 1705.1 ($C_{107}H_{171}N_5Si_4Zn$ requires 1705.20); UV-vis: λ_{max} [nm] ($CHCl_3$+1% pyridine) = 440, 577, 629.

[5-ethynyl-10-(4-pyridyl)-15-trihexylsilylethynyl-20-(3,5-bis(trihexylsilyl)phenyl)-porphyrinato]zinc(II) **5**

Porphyrin **4** (467 mg, 0.262 mmol, 1.0 equiv.) was dissolved in dry DCM (8 mL) and $CHCl_3$ (8 mL). Pyridine (0.21 mL) was added. Under stirring TBAF solution (1.0 M in THF; 0.18 mL, 0.18 mmol, 0.7 equiv.) was added drop-wise. The reaction was monitored by TLC. After 20 min a good product ratio was reached. Calcium chloride (50 mg) was added and the mixture was filtered over a plug of silica eluting with DCM/pyridine (50:1). The solvent was removed from the green filtrate and the residue was subjected to column-chromatography on silica eluting with petrol ether/EtOAc/pyridine 20:2:1 → 20:8:1. Recovered starting material **4** (108 mg, 23%), desired product **5** (170 mg, 43%), and fully deprotected material (87.3 mg, 27%) were isolated in form of their pyridyl-complexes as dark purple semi-solids. TLC: R_f (petrol ether/EtOAc/pyridine 10:1:1) = 0.34; ^{1}H-NMR (400 MHz, $CDCl_3$+1% pyridine-d_5): δ = 9.66 (d, *J* = 4.6 Hz, 1H, β-H), 9.65 (d, *J* = 4.6 Hz, 1H, β-H), 9.62 (d, *J* = 4.6 Hz, 1H, β-H), 9.61 (d, *J* = 4.6 Hz, 1H, β-H), 8.97 (m, 2H, py-H), 8.81 (d, *J* = 4.5 Hz, 1H, β-H), 8.80 (d, *J* = 4.5 Hz, 1H, β-H), 8.76 (d, *J* = 4.6 Hz, 1H, β-H), 8.75 (d, *J* = 4.6 Hz, 1H, β-H), 8.16 (d, *J* = 0.8 Hz, 2H, *o*-H), 8.08 (m, 2H, py-H), 7.94 (br, 1H, *p*-H), 4.12 (s, 1H, ethynyl-H), 1.77–1.67 (m, 6H, alkyl-H), 1.54–1.19 (m, 66H, alkyl-H), 1.01–0.94 (m, 6H, alkyl-H), 0.92–0.79 (m, 39H); *m/z* (MALDI-TOF): 1422.3 ($C_{89}H_{133}N_5Si_3Zn$ requires 1422.9).

Dimerisation of 5-ethynyl-10-(4-pyridyl)-15-trihexylsilylethynyl-20-(3,5-bis(trihexylsilyl)-phenyl)-porphyrin (Synthesis of porphyrin dimer **6**, **P2py2**)

$Pd(PPh_3)_2Cl_2$ (2.0 mg, 2.9 μmol, 8.1 mol%), copper(I) iodide (3.3 mg, 17 μmol, 0.49 equiv.) and 1,4-benzoquinone (7.8 mg, 72 μmol, 2.1 equiv.) were dissolved in dry toluene (3 mL) and dry DIPA at 20 °C. The yellow solution was added to porphyrin **5** (52.6 mg, 35.0 μmol, 1.0 equiv.). The reaction mixture was stirred at 20 °C for 3 h. The reaction mixture was filtered over a plug of silica eluting with DCM/pyridine (50:1). Solvents were removed from the filtrate under reduced

pressure. The resulting dark purple/green solid was dissolved in chloroform (5 mL). TFA (0.15 mL, 1.9 mmol, 100 equiv.) was added dropwise under stirring. After 10 min pyridine (0.4 mL) was added and the green mixture was directly filtered over a plug of silica eluting with DCM/pyridine (99:1). Solvents were removed from the filtrate under reduced pressure. The dark purple residue was dissolved in chloroform and filtered. The volume was reduced and the product was precipitated by layering methanol. The dark purple precipitate was washed with methanol and dried in high vacuum affording dimer **6**, **P2Py2** (42.8 mg, 90 %). ^{1}H NMR (500 MHz, $CDCl_3$): δ = 9.87 (d, *J* = 4.7 Hz, 2H, β-H), 9.82 (d, *J* = 4.7 Hz, 2H, β-H), 9.65 (d, *J* = 4.7 Hz, 2H, β-H), 9.61 (d, *J* = 4.6 Hz, 2H, β-H), 9.08 (d, *J* = 4.8 Hz, 4H, py-H), 8.90 (d, *J* = 4.7 Hz, 2H, β-H), 8.86 (d, *J* = 4.6 Hz, 2H, β-H), 8.81 (d, *J* = 4.4 Hz, 2H, β-H), 8.75 (d, *J* = 4.5 Hz, 2H, β-H), 8.26 (s, 4H, *o*-H), 8.18 (m, 4H, py-H), 8.01 (s, 2H, *p*-H), 1.80–1.69 (m, 12H, alkyl-H), 1.52–1.19 (m, 132H, alkyl-H), 1.05–0.98 (m, 12H, alkyl-H), 0.97–0.76 (m, 78H, alkyl-H), –1.91 (s, 4H, N-*H*); ^{13}C-deptQ-NMR (125 MHz, $CDCl_3$): δ = 149.5 (d, 2C, py-C), 148.5 (u, 4C, py-C), 140.5 (u, 4C, *o*-C), 139.6 (u, 2C, *p*-C), 139.2 (d, 2C, *ipso*-C), 135.5 (d, 4C, *m*-C), 129.3 (u, 4C, py-C), 124.4 (d, 2C, *meso*-C), 118.3 (d, 2C, *meso*-C), 107.5 (d, 2C, *meso*-C), 102.5 (d, 2C, *meso*-C or ethynyl-C), 102.4 (d, 2C, *meso*-C or ethynyl-C), 99.5 (d, 2C, ethynyl-C), 87.3 (d, 2C, ethynyl-C), 82.9 (d, 2C, ethynyl-C), 33.5 (d, 12C, *C*H_2), 33.3 (d, 6C, *C*H_2), 31.6 (d, 18C, *C*H_2), 24.3 (d, 6C, *C*H_2), 24.0 (d, 12C, *C*H_2), 22.7 (d, 18C, *C*H_2), 14.2 (u, 18C, *C*H_3), 13.7 (d, 6C, *C*H_2), 12.6 (d, 12C, *C*H_2) [Signals for α- and β-carbons are not visible due to the chemical exchange of the N-H protons]. *m/z* (MALDI-TOF): 2715.1 ($C_{178}H_{268}N_{10}Si_6$ requires 2717.0); UV-vis: λ_{max} [nm] (ε/mol^{-1} L cm^{-1}) (DCM) = 419 (144,000), 449 (285,000), 483 (141,000), 538 (16,300), 606 (45,200), 626 (59,000), 641 (47,700), 729 (81,200); λ_{max} [nm] (ε/mol^{-1} L cm^{-1}) (toluene) = 451 (336,000), 486 (137,000), 608 (54,700), 628 (59,700), 732 (84,000); Fluorescence: λ_{max} [nm] ($CHCl_3$) = 732 (excitation λ_{ex} = 475 nm).

2.7.2.2 Synthesis of **c-P12$_{THS}$**

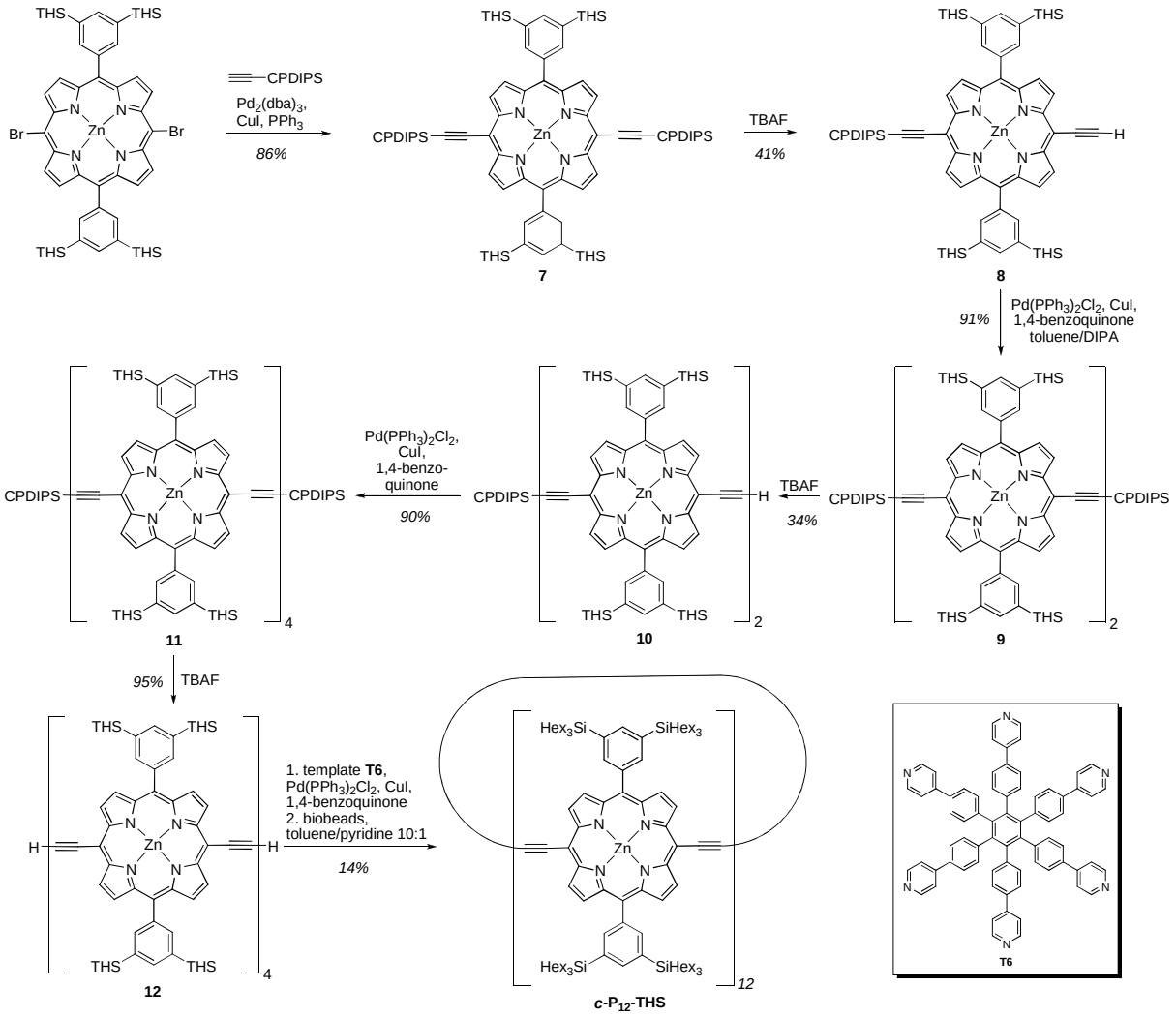

Scheme 2.2 Overview of the synthesis of ***c*-P12$_{THS}$** (THS = $Si(C_6H_{13})_3$, CPDIPS = $Si(C_3H_6CN)(CH(CH_3)_2)_2$).

[5,15-bis-((3-cyanopropyl)diisopropylsilyl)ethynyl-10,20-bis-(3,5-bis-(trihexylsilyl)-phenyl)porphyrinato]zinc(II) **7**

Dibromoporphyrin[30] (646 mg, 0.356 mmol, 1.0 equiv.), $Pd_2(dba)_3$ (34.8 mg, 0.038 mmol, 0.11 equiv.), triphenylphosphine (28.0 mg, 0.107 mmol, 0.30 equiv.) and copper(I) iodide (21.4 mg, 0.112 mmol, 0.32 equiv.) were placed in a heat-dried Schlenk flask equipped with a magnetic stirrer bar. The flask was sealed and evacuated and backfilled with nitrogen three times. Dry, freeze-pump-thaw degassed toluene (27 mL) was added. CPDIPS-acetylene[31] (259 mg, 1.24 mmol, 3.5 equiv.) was dissolved in dry DIPA (22.5 mL). The mixture was degassed by bubbling through nitrogen. The degassed solution was added to the reaction mixture. The resulting

mixture was stirred at 50 °C for 2 h. The reaction mixture was filtered over a plug of silica eluting with DCM. The solvent was removed from the filtrate. The residue was purified be column chromatography on silica eluting with PE/DCM 2:1 →3:2. The product **7** was obtained in form of a green-purple oil (631 mg, 86%). TLC: R_f (PE/DCM 2:1) = 0.23; ^{1}H-NMR (500 MHz, $CDCl_3$): δ = 9.67 (d, *J* = 4.5 Hz, 4H, β-H), 8.89 (d, *J* = 4.6 Hz, 4H, β-H), 8.20 (s, 4H, *o*-H), 7.97 (s, 2H, *p*-H), 2.52 (t, *J* = 6.9 Hz, 4H, propyl-CH_2), 2.21–2.13 (m, 4H, propyl-CH_2), 1.51–1.22 (m, 124H, CH_2, isopropyl-C*H* and isopropyl-CH_3), 1.17–1.12 (m, 4H, propyl-CH_2), 0.94–0.87 (m, 24H, CH_2), 0.87–0.81 (m, 36H, CH_3); ^{13}C-deptQ-NMR (125 MHz, $CDCl_3$): δ = 152.2 (d, 4C, α-C), 150.6 (d, 4C, α-C), 140.2 (d, 2C, ipso-C), 140.1 (u, 4C, *o*-C), 139.3 (u, 2C, *p*-C), 134.9 (d, 4C, *m*-C), 133.1 (u, 4C, β-C), 130.9 (u, 4C, β-C), 124.1 (d, 2C, meso-C), 119.6 (d, 2C, *C*N), 110.0 (d, 2C, alkyl-C), 101.1 (d, 2C, meso-C), 97.0 (d, 2C, alkyl-C), 33.5 (d, 12C, *C*H_2), 31.6 (d, 12C, *C*H_2), 24.0 (d, 12C, *C*H_2), 22.6 (d, 12C, *C*H_2), 21.6 (d, 2C, propyl-*C*H_2), 21.0 (d, 2C, propyl-*C*H_2), 18.6 (u, 4C, isopropyl-*C*H_3), 18.3 (u, 4C, isopropyl-*C*H_3), 14.1 (u, 12C, *C*H_3), 12.6 (d, 12C, *C*H_2), 12.3 (u, 4C, isopropyl-*C*H), 10.1 (d, 2C, propyl-*C*H_2); *m/z* (MALDI-TOF): 2066.2 ($C_{128}H_{210}N_6Si_6Zn$ requires 2066.46).

[5-((3-cyanopropyl)diisopropylsilyl)ethynyl-15-ethynyl-10,20-bis-(3,5-bis-(trihexylsilyl)-phenyl)porphyrinato]zinc(II) **8**

Porphyrin **7** (140 mg, 0.067 mmol, 1.0 equiv.) was dissolved in DCM (8 mL), chloroform (8 mL) and pyridine (1.3 mL). The solution was cooled in an ice-water bath. TBAF solution, 1.0 M in THF, (0.054 mL, 0.054 mmol, 0.8 equiv.) was added and the reaction monitored by TLC (silica, eluent: PE/DCM 2:1). When a good product ratio had been reached the mixture was filtered over a plug of silica eluting with DCM+1% pyridine. The solvent was removed from the filtrate. The residue was purified by column chromatography on silica eluting with PE/chloroform + 0.5% pyridine 20:1 →1:1, providing di-deprotected product (18 mg, 15%), desired product **8** (54.9 mg, 41%) and, after additional precipitation from chloroform/methanol, starting material (54.8 mg, 0.022 mmol, 33%). (The fraction obtained from column chromatography that contained the starting material also contained CPDIPSF, which was easily removed by precipitation from chloroform

with methanol.) TLC: R_f (PE/DCM 2:1) = 0.52; ^{1}H-NMR (200 MHz, $CDCl_3$): δ = 9.63 (d, *J* = 4.6 Hz, 2H, β-H), 9.61 (d, *J* = 4.5 Hz, 2H, β-H), 8.84 (d, *J* = 4.7 Hz, 2H, β-H), 8.82 (d, *J* = 4.7 Hz, 2H, β-H), 8.18 (s, 4H, *o*-H), 7.95 (s, 2H, *p*-H), 4.12 (s, 1H, ethynyl-H), 2.51 (t, *J* = 6.9 Hz, 2H, propyl-CH_2), 2.24–2.09 (m, 2H, propyl-CH_2), 1.51–1.21 (m, 110H, CH_2, isopropyl-C*H* and isopropyl-CH_3), 1.18–1.08 (m, 2H, propyl-CH_2), 0.95–0.78 (m, 60H, CH_2 and CH_3); *m/z* (MALDI-TOF): 1884.6 ($C_{118}H_{191}N_5Si_5Zn$ requires 1884.33).

Dimerisation of [5-((3-cyanopropyl)diisopropylsilyl)ethynyl-15-ethinyl-10,20-bis-(3,5-bis-(trihexylsilyl)-phenyl)porphyrinato]zinc(II) (Synthesis of porphyrin dimer **9**)

$Pd(PPh_3)_2Cl_2$ (1.5 mg, 2.1 µmol, 0.16 equiv.), copper(I) iodide (3.3 mg, 17 µmol, 1.3 equiv.) and 1,4-benzoquinone (5.5 mg, 51 µmol, 3.8 equiv.) were dissolved in dry toluene (2.4 mL) and dry DIPA (0.75 mL). The solution was added to porphyrin **8** (54 mg, 27 µmol, 2.0 equiv.). The mixture was stirred at RT for 40 min (TLC-control (silica, eluent PE/DCM 2:1) indicated full conversion after 20 min). The reaction mixture was filtered over a plug of silica eluting with chloroform+1% pyridine. The solvent was removed from the filtrate. The residue was purified by passing over a SEC eluting with toluene producing a dark green product (48.2 mg, 91%). TLC: R_f (PE/DCM 2:1) = 0.41; ^{1}H-NMR (500 MHz, $CDCl_3$): δ = 9.91 (d, *J* = 4.6 Hz, 4H, β-H), 9.66 (d, *J* = 4.6 Hz, 4H, β-H), 8.96 (d, *J* = 4.6 Hz, 4H, β-H), 8.90 (d, ^{3} *J* = 4.6 Hz, 4H, β-H), 8.26 (s, 8H, *o*-H), 7.99 (s, 4H, *p*-H), 2.54 (t, *J* = 6.9 Hz, 4H, propyl-CH_2), 2.23–2.14 (m, 4H, propyl-CH_2), 1.53–1.22 (m, 220H, CH_2, isopropyl-C*H* and isopropyl-CH_3), 1.19–1.13 (m, 4H, propyl-CH_2), 0.96–0.89 (m, 48H, CH_2), 0.88–0.83 (m, 72H, CH_3); ^{13}C-deptq-NMR (125 MHz, $CDCl_3$): δ = 153.0 (d, 4C, α-C), 152.2 (d, 4C, α-C), 150.7 (d, 4C, α-C), 150.4 (d, 4C, α-C), 140.4 (u, 8C, *o*-C), 140.2 (d, 4C, *ipso*-C), 139.2 (u, 4C, *p*-C), 135.0 (d, 8C, *m*-C), 133.3 (u, 4C, β-C), 133.1 (u, 4C, β-C), 130.9 (u, 8C, β-C), 124.5 (d, 4C, meso-C), 119.7 (d, 2C, *C*N), 110.3 (d, 2C, alkynyl-C), 101.4 (d, 2C, meso-C), 100.2 (d, 2C, meso-C), 97.0 (d, 2C, alkynyl-C), 87.5 (d, 2C, alkynyl-C), 82.5 (d, 2C, alkynyl-C), 33.5 (d, 24C, *C*H_2-hexyl), 31.6 (d, 24C, *C*H_2-hexyl), 24.0 (d, 24C, *C*H_2-hexyl), 22.7 (d, 24C, *C*H_2-hexyl), 21.6 (d, 2C, *C*H_2-cyanopropyl), 21.0 (d, 2C, *C*H_2-cyanopropyl), 18.6 (u, 4C, *C*H_3-isopropyl), 18.3 (u, 4C, *C*H_3-isopropyl), 14.2 (u, 24C, *C*H_3-hexyl), 12.6 (d, 24C, *C*H_2-

hexyl), 12.3 (u, 4C, *C*H-isopropyl), 10.1 (d, 2C, *C*H_2-cyanopropyl); *m/z* (MALDI-TOF): 3765.2 ($C_{236}H_{380}N_{10}Si_{10}Zn_2$ requires 3768.6).

Monodeprotected porphyrin dimer **10**

Dimer **9** (48.2 mg, 12.3 µmol, 1.0 equiv.) was dissolved in chloroform (1.6 mL), DCM (1.6 mL) and pyridine (0.25 mL). The mixture was cooled in an ice-water bath. TBAF solution, 1.0 M in THF, (0.01 mL, 10 µmol, 0.8 equiv.) was added. The reaction was monitored by TLC (silica, eluent: PE/DCM 3:1). Once a good product ratio had been reached the mixture was filtered over a plug of silica eluting with chloroform+1% pyridine. The solvent was removed from the filtrate. The residue was purified by column chromatography on silica eluting with PE/chloroform + 0.5% pyridine 20:1→1:1. This afforded di-deprotected dimer (5.3 mg, 12%), desired mono-deprotected dimer **10** (16 mg, 34%) and starting material **9** (18 mg, 37%). TLC: R_f (PE/DCM 3:1) = 0.38; ^{1}H-NMR (400 MHz, $CDCl_3$): δ = 9.86 (d, *J* = 4.6 Hz, 2H, β-H), 9.85 (d, *J* = 4.6 Hz, 2H, β-H), 9.65 (d, *J* = 4.6 Hz, 2H, β-H), 9.61 (d, *J* = 4.6 Hz, 2H, β-H), 8.93 (d, *J* = 4.6 Hz, 2H, β-H), 8.90 (d, *J* = 4.6 Hz, 2H, β-H), 8.85 (d, *J* = 4.8 Hz, 2H, β-H), 8.84 (d, *J* = 4.6 Hz, 2H, β-H), 8.24 (s, 4H, *o*-H), 8.23 (s, 4H, *o*-H), 7.97 (s, 4H, *p*-H), 4.15 (s, 1H, alkynyl-H), 2.53 (t, *J* = 6.9 Hz, 2H, propyl-CH_2), 2.23–2.13 (m, 2H, propyl-CH_2), 1.51–1.21 (m, 206H, CH_2, isopropyl-C*H* and isopropyl-CH_3), 1.17–1.11 (m, 2H, propyl-CH_2), 0.96–0.78 (m, 120H, CH_2 and CH_3); *m/z* (MALDI-TOF): 3584.7 ($C_{226}H_{361}N_9Si_9Zn_2$ requires 3587.5).

Protected porphyrin tetramer **11**

$Pd(PPh_3)_2Cl_2$ (1.0 mg, 1.4 µmol, 0.3 equiv.), copper(I) iodide (1.4 mg, 7.4 µmol, 1.8 equiv.) and 1,4-benzoquinone (1.8 mg, 17 µmol, 4.0 equiv.) were dissolved in dry toluene (0.5 mL) and dry DIPA (0.15 mL). The solution was added to porphyrin dimer **10** (16 mg, 4.2 µmol, 1.0 equiv.). The mixture was stirred at 20 °C for 3.5 h. The reaction mixture was filtered over a plug of silica eluting with chloroform+1% pyridine. The solvent was removed from the filtrate. The residue was dissolved in chloroform and filtered over a microfilter. The volume of the filtrate was reduced and the product precipitated by layering methanol. The precipitate was washed with methanol and dried in vacuum affording the desired product **11** (14 mg, 90%). ^{1}H-NMR (500 MHz, $CDCl_3$): δ = 9.97–

9.95 (m, 12H, β-H), 9.71 (d, *J* = 4.5 Hz, 4H, β-H), 9.04–9.03 (m, 8H, β-H), 9.00 (d, *J* = 4.5 Hz, 4H, β-H), 8.94 (d, *J* = 4.7 Hz, 4H, β-H), 8.35 (s, 8H, *o*-H), 8.29 (s, 8H, *o*-H), 8.04 (s, 4H, *p*-H), 8.02 (s, 4H, *p*-H), 2.55 (t, *J* = 6.7 Hz, 4H, propyl-CH_2), 2.24–2.17 (m, 4H, propyl-CH_2), 1.55–1.15 (m, 416H, CH_2, isopropyl-C*H*, isopropyl-CH_3 and propyl-CH_2), 1.01–0.79 (m, 240H, CH_2 and CH_3); ^{13}C-deptq-NMR (125 MHz, $CDCl_3$): δ = 153.1 (d, 12C, α-C), 152.3 (d, 4C, α-C), 150.8 (d, 4C, α-C), 150.7 (d, 8C, α-C), 150.5 (d, 4C, α-C), 140.7 (u, 8C, *o*-C), 140.4 (u, 8C, *o*-C), 140.1 (d, 4C, *ipso*-C), 140.0 (d, 4C, *ipso*-C), 139.4 (u, 4C, *p*-C), 139.3 (u, 4C, *p*-C), 135.2 (d, 8C, *m*-C), 135.1 (d, 8C, *m*-C), 133.5 (u, 16C, β-C), 133.2 (u, 4C, β-C), 131.1 (u, 4C, β-C), 131.0 (u, 8C, β-C), 125.0 (d, 4C, meso-C), 124.6 (d, 4C, meso-C), 119.7 (d, 2C, *C*N), 110.0 (d, 2C, alkynyl-C), 101.6 (d, 2C, meso-C), 100.9 (d, 2C, meso-C), 100.8 (d, 2C, meso-C), 100.3 (d, 2C, meso-C), 97.3 (d, 2C, alkynyl-C), 87.5 (d, 4C, alkynyl-C), 87.4 (d, 2C, alkynyl-C), 82.8 (d, 4C, alkynyl-C), 82.5 (d, 2C, alkynyl-C), 33.6 (d, 24C, *C*H_2-hexyl), 33.5 (d, 24C, *C*H_2-hexyl), 31.7 (d, 24C, *C*H_2-hexyl), 31.6 (d, 24C, *C*H_2-hexyl), 24.1 (d, 24C, *C*H_2-hexyl), 24.0 (d, 24C, *C*H_2-hexyl), 22.8 (d, 24C, *C*H_2-hexyl), 22.7 (d, 24C, *C*H_2-hexyl), 21.6 (d, 2C, *C*H_2-cyanopropyl), 21.1 (d, 2C, *C*H_2-cyanopropyl), 18.6 (u, 4C, *C*H_3-isopropyl), 18.4 (u, 4C, *C*H_3-isopropyl), 14.2 (u, 48C, *C*H_3-hexyl), 12.7 (d, 48C, *C*H_2-hexyl), 12.3 (u, 4C, *C*H-isopropyl), 10.1 (d, *C*H_2-cyanopropyl); *m/z* (MALDI-TOF): 7164.1 ($C_{452}H_{720}N_{18}Si_{18}Zn_4$ requires 7174.0); UV-vis: λ_{max} [nm] (rel. intensity) (toluene) = 441 (0.68, shoulder), 466 (1.0), 491 (0.69, shoulder), 592 (0.07), 773 (0.44), 805 (0.40, shoulder).

Deprotected porphyrin tetramer **12**

Protected porphyrin tetramer **11** (43.3 mg, 5.78 μmol, 1.0 equiv.) was dissolved in DCM (3 mL) and pyridine (0.07 mL). Under stirring TBAF-solution (1.0 M in THF, 0.015 mL, 15 μmol, 2.5 equiv.) was added. The reaction was monitored by TLC (eluent: PE/DCM 3:1). After 15 min the mixture was filtered over silica eluting with DCM+1% pyridine. The solvent was removed from the filtrate. The residue was dissolved and filtered over a plug of silica eluting with PE/DCM 10:1 +0.5% pyridine (to remove CPDIPS-fluoride). Yield: 39 mg (95%). TLC: R_f (PE/DCM 3:1) = 0.97; ^{1}H-NMR (400 MHz, $CDCl_3$): 9.90–9.87 (m, 12H, β-H), 9.67 (d, *J* = 4.7 Hz, 4H, β-H), 8.97–8.94 (m, 12H, β-H), 8.88 (d, *J* = 4.5 Hz, 4H, β-H), 8.30 (s, 8H, *o*-H), 8.26 (s, 8H, *o*-H), 8.00 (s, 4H,

p-H), 7.98 (s, 4H, *p*-H), 4.16 (s, 2H, alkynyl-H), 1.55–1.20 (m, 384H, CH_2), 0.99–0.82 (m, 240H, CH_2 and CH_3); UV-vis: λ_{max} [nm] ($CHCl_3$) = 457, 584, 755.

Porphyrin nanoring **c-P12$_{THS}$**

The template **T6**[12] (3.7 mg, 3.7 µmol, 1.0 equiv.) was dissolved in chloroform (3.6 mL) and methanol (20 µL) under sonication. The clear solution was added to the porphyrin tetramer **12** (39.3 mg, 5.51 µmol, 1.5 equiv.), which had been dissolved in chloroform (8.5 mL). The mixture was sonicated for 20 min. The solvent was removed and the residue dried under vacuum. Afterwards the complex was dissolved in dry chloroform (33.5 mL). $Pd(PPh_3)_2Cl_2$ (5.5 mg, 7.8 µmol, 2.1 equiv.), copper(I) iodide (7.2 mg, 38 µmol, 10 equiv.) and 1,4-benzoquinone (15.7 mg, 145 µmol, 40 equiv.) were dissolved in dry chloroform (3.6 mL) and dry DIPA (0.1 mL) under sonication. The solution was added to the porphyrin/template mixture. The reaction mixture was stirred at 20 °C and monitored by UV-vis. After 2 h more catalyst ($Pd(PPh_3)_2Cl_2$ (5.6 mg, 8.0 µmol, 2.2 equiv.), copper(I) iodide (7.2 mg, 38 µmol, 10 equiv.) and 1,4-benzoquinone (15.3 mg, 142 µmol, 39 equiv.) dissolved in dry chloroform (3.6 mL) and dry DIPA (0.1 mL)) was added. After 50 min no change was observed so the mixture was heated to 50 °C for 70 min. Then more catalyst ($Pd(PPh_3)_2Cl_2$ (5.7 mg, 8.1 µmol, 2.2 equiv.), copper(I) iodide (7.0 mg, 37 µmol, 10 equiv.) and 1,4-benzoquinone (16.8 mg, 155 µmol, 42 equiv.) dissolved in dry chloroform (3.6 mL) and dry DIPA (0.1 mL)) was added and the reaction mixture stirred at 50 °C for 2 h. Subsequently the reaction mixture was stirred at 20 °C over night. Since further change was observed by UV-vis catalyst ($Pd(PPh_3)_2Cl_2$ (5.7 mg, 8.0 µmol, 2.2 equiv.), copper(I)iodide (7.3 mg, 38 µmol, 10 equiv.) and 1,4-benzoquinone (16.4 mg, 152 µmol, 41 equiv.) dissolved in dry chloroform (3.6 mL) and dry DIPA (0.1 mL)) was added again and the reaction mixture heated to 50 °C for 2.75 h. The reaction mixture was filtered over a plug of silica eluting with PE/chloroform 9:1. The solvent was removed from the filtrate. The residue was dissolved in PE/chloroform 10:1 and passed over a plug of silica eluting with PE/chloroform 10:1. The solvent was removed from the filtrate. The resulting brown solid was dissolved in toluene/pyridine 9:1 and passed over a SEC column eluting with toluene/pyridine 9:1. The brown band was collected and the solvent removed.

The brown residue was dissolved in toluene+1%pyridine, filtered over a microfilter and purified by recycling GPC. The product was precipitated from chloroform by layering methanol repeatedly to remove residual pyridine to yield ***c*-P12$_{THS}$** (5.3 mg, 14%). TLC: R_f (PE/$CHCl_3$/py 8:1:1) = 0.83; ^{1}H NMR (500 MHz, $CDCl_3$): δ = 9.85 (d, *J* = 4.6 Hz, 48H, β-H), 8.93 (d, *J* = 4.4 Hz, 48H, β-H), 8.27 (s, 48H, *o*-H), 7.99 (s, 24H, *p*-H), 1.51–1.44 (m, 288H, CH_2), 1.38–1.24 (m, 864H, CH_2), 0.94–0.90 (m, 288H, CH_2), 0.85–0.82 (m, 432H, CH_3); ^{13}C{^{1}H}-NMR (125 MHz, $CDCl_3$): δ = 152.8 (48C, α-C), 150.5 (48C, α-C), 140.6 (48C, *o*-C), 140.1 (24C, *ipso*-C), 139.3 (24C, *p*-C), 135.0 (48C, *m*-C), 133.3 (48C, β-C), 130.9 (48C, β-C), 124.9 (24C, *meso*-C), 100.7 (24C, *meso*-C), 89.3 (24C, alkynyl-C), 84.0 (24C, alkynyl-C); *m/z* (MALDI-TOF): 20597 ($C_{1296}H_{2040}N_{48}Si_{48}Zn_{12}$ requires 20425); UV-vis: λ_{max} [nm] (toluene) = 471, 489, 588, 779; λ_{max} [nm] (toluene+1% pyridine) = 473, 489, 597, 822.

2.7.2.3 Synthesis of free-base tetrapyridyl-substituted porphyrin dimer

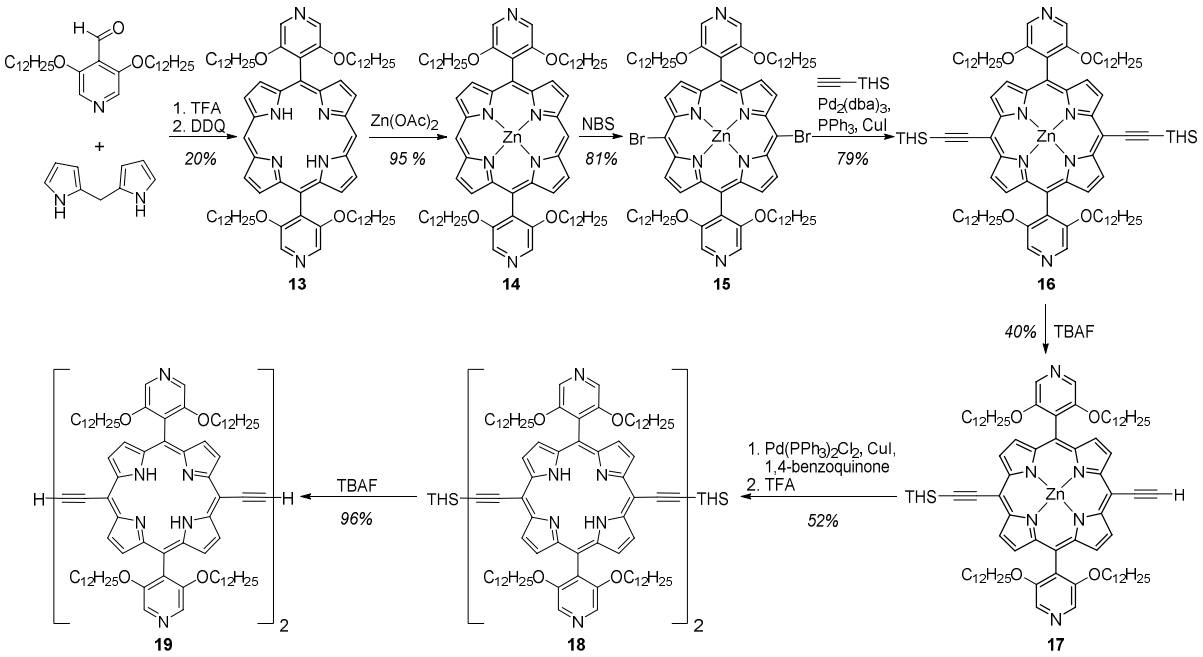

Scheme 2.3 Overview of the synthesis of free-base tetrapyridyl-substituted porphyrin dimer (THS = $Si(C_6H_{13})_3$). The starting aldehyde, 3,5-bis-(dodecyloxy)isonicotinaldehyde, was synthesised according to publications.[32,33]

3,5-Bis(dodecyloxy)isonicotinaldehyde

A solution of 3,5-bis(dodecyloxy)pyridine (0.500 g, 1.12 mmol) in dry THF (6 mL) was degassed by pumping and feeding N_2 back three times and then *n*-BuLi (2.5 M in hexane, 0.600 mL, 1.45 mmol) was added slowly at 0 °C under N_2. (Do not let the solution freeze while adding the BuLi). The reaction mixture was stirred for 30 min at room temperature. Dry DMF was added (0.13 mL, 1.68 mmol). After stirring for 24 h, water (0.2 mL) was added to stop the reaction. The aqueous layer was extracted with diethyl ether (3 × 5 mL). The combined organic layers were washed with water (2 × 5 mL) and dried over $MgSO_4$ and then the solvent was removed under reduced pressure. Chromatography through a short silica column and recrystallisation from hot methanol afforded the desired product as a white solid (269 mg, 50% yield). ^{1}H-NMR (500 MHz, $CDCl_3$): δ = 10.52 (s, 1H, C*H*O), 8.10 (s, 2H, py-H), 4.15 (t, *J* = 6.4 Hz, 4H, OC*H*$_2$), 1.87-1.80 (m, 4H, alkyl-H), 1.50 –1.43 (m, 4H, alkyl-H), 1.31–1.20 (m, 32H, alkyl-H), 0.87 (t, $^3J_{HH}$ = 6.4 Hz, 6H, alkyl-H); ^{13}C{^{1}H}-NMR (125 MHz, $CDCl_3$): δ = 181.8 (1C, *C*HO), 154.6 (2C, py-C), 128.6 (2C, py-C), 69.9 (2C, O*C*H$_2$), 31.9-22.6 (40C, *C*H$_2$), 14.1 (4C, *C*H$_3$).

5,15-bis-(3,5-bis(dodecyloxy)pyridyl)-porphyrin **13**

Dipyrromethane (307 mg, 2.10 mmol, 1.0 equiv.) and 3,5-bis-(dodecyloxy)-isonicotinaldehyde (1.0 g, 2.1 mmol, 1.0 equiv.) were dissolved in CH_2Cl_2 (375 mL). The reaction mixture was deoxygenated by evacuating and feeding back N_2. Trifluoroacetic acid (0.50 mL, 6.30 mmol, 3.0 equiv.) was added. After stirring in the dark for 3 h DDQ (906 mg, 3.99 mmol, 1.90 equiv.) was added and the mixture stirred for 20 min before Et_3N (1.14 mL, 8.19 mmol, 3.90 equiv.) was added to quench the acid. The mixture was passed through a short silica gel column eluting with CH_2Cl_2/pyridine (90: 10) to separate the tarry side products. The solvent was removed from the filtrate under reduced pressure. The residue was subjected to column-chromatography on silica eluting with petrol ether/CH_2Cl_2/pyridine (60:40:2→50:50:2). The product was recrystallised by layer addition (CH_2Cl_2/MeOH) to give a bright purple powder (256 mg, 20%). ^{1}H NMR (400 MHz, $CDCl_3$): δ = 10.21 (s, 2H, *meso*-H), 9.31 (d, *J* = 4.4 Hz, 4H, β-H), 8.94 (d, *J* = 4.4 Hz, 4H, β-H), 8.52 (s, 4H, py-H), 3.97 (t, *J* = 6.4 Hz, 8H, OC*H*$_2$), 1.37– 0.47 (m, 92H, alkyl-H), –3.11 (s, 2H,

N*H*); $^{13}C\{^1H\}$-NMR (125 MHz, $CDCl_3$): δ = 155.6 (4C, py-C), 146.5 (4C, α-C), 145.2 (4C, α-C), 131.5 (4C, β-H), 130.1 (4C, β-H), 128.9 (4C, py-C), 127.0 (2C, py-C), 108.4 (2C, *meso*-C), 104.6 (2C, *meso*-C), 69.5 (4C, O*C*H_2), 31.9–22.6 (40C, *C*H_2), 14.1 (4C, *C*H_3); *m/z* (MALDI-TOF): 1202.44 ($C_{78}H_{114}N_6O_4$ requires 1201.91).

[5,15-bis-(3,5-bis(dodecyloxy)pyridyl)-porphyrinato]zinc(II) **14**

A solution of $Zn(OAc)_2{\cdot}2H_2O$ (214 mg, 1.17 mmol, 5.00 equiv.) in methanol (1 mL) was added to a solution of 5,15-bis-(3,5-bis-(dodecyloxy)pyridyl)-porphyrin (**13**) (280 mg, 0.233 mmol, 1.0 equiv.) in $CHCl_3$ (25 mL). The mixture was stirred at 50 °C for 5 h. The solvent was removed and the residue purified by passing over a short silica plug, eluting with CH_2Cl_2/pyridine 99:1. Precipitation from CH_2Cl_2 by layering MeOH afforded the desired product as a bright purple powder (281 mg, 95% yield). The product was used in the next step without further purification. ^{1}H-NMR (500 MHz, $CDCl_3$+1% pyridine-d_5): δ = 10.03 (s, 2H, *meso*-H), 9.25 (d, *J* = 4.4 Hz, 4H, β-H), 8.92 (d, *J* = 4.4 Hz, 4H, β-H), 8.36 (s, 4H, py-H), 3.89 (t, *J* = 6.4 Hz, 8H, OC*H*$_2$), 1.27–0.40 (m, 92H, alkyl-H); *m/z* (MALDI-TOF): 1264.96 ($C_{78}H_{116}N_6O_4Zn$ requires 1263.83).

[5,15-dibromo-10,20-(3,5-bis(dodecyloxy)pyridyl)-porphyrinato]zinc(II) **15**

A solution of *N*-bromosuccinimide (78.8 mg, 0.44 mmol, 2.0 equiv.) in $CHCl_3$ (12 mL) was added dropwise to a solution of porphyrin **14** (281 mg, 0.221 mmol, 1.0 equiv.) in $CHCl_3$ (10 mL) and pyridine (0.17 mL) under exclusion of light. After the addition, the reaction mixture was stirred for further 10 min before acetone (0.2 mL) was added to quench the reaction. The mixture was filtered over a plug of silica eluting with PE:EtOAc:pyridine 10:1:1. The solvent was removed under reduced pressure. The product was precipitated from chloroform by layer addition of methanol to give a purple powder (256 mg, 81% yield). ^{1}H-NMR (400 MHz, $CDCl_3$+1% pyridine-d_5): δ = 9.54 (d, *J* = 4.7 Hz, 4H, β-H), 8.73 (d, *J* = 4.7 Hz, 4H, β-H), 8.47 (s, 4H, py-H), 3.94 (t, *J* = 6.4 Hz, 8H, OC*H*$_2$), 1.22–1.06 (m, 24H, C*H*$_2$), 0.99–0.78 (m, 40H, C*H*$_2$), 0.75–0.66 (m, 10H, C*H*$_2$), 0.54–0.39 (m, 18H, C*H*$_2$, C*H*$_3$). $^{13}C\{^1H\}$-NMR (125 MHz, $CDCl_3$): δ = 155.5 (4C, py-C), 150.0 (4C, α-C), 149.8 (4C, α-C), 133.1 (4C, β-H), 131.8 (4C, β-H), 128.7 (4C, py-C), 128.4 (2C, py-C),

110.8 (2C, *meso*-C), 104.1 (2C, *meso*-C), 69.3 (4C, O*C*H_2), 31.8-22.6 (40C, *C*H_2), 14.0 (4C, *C*H_3); *m/z* (MALDI-TOF): 1422.67 ($C_{78}H_{112}Br_2N_6O_4Zn$ requires 1423.65).

[5,15-bis-(3,5-bis(dodecyloxy)-pyridyl)-10,20-trihexylsilylethynyl-porphyrinato]zinc(II) **16**

Porphyrin **15** (255 mg, 0.179 mmol, 1.0 equiv.), $Pd_2(dba)_3$ (16.5 mg, 0.018 mmol, 10 mol%), PPh_3 (14.2 mg, 0.054 mmol, 30 mol%) and CuI (10.3 mg, 0.054 mmol, 30 mol%) were combined in a heat dried 2-neck round bottom flask and then evacuated and back filled with N_2 three times. Dry toluene (15 mL) and pyridine (0.7 mL) were added and freeze-pump-thaw degassed 3 times. Dry DIPA (18 mL) and THS-acetylene (0.17 mL, 0.448 mmol, 2.50 equiv.) were added at 20 °C. The reaction mixture was stirred at 50 °C for 2.5 h, then filtered over a plug of silica eluting with CH_2Cl_2/pyridine 99:1. The solvent was removed under reduced pressure. The residue was subjected to column-chromatography on silica eluting with petroleum ether: EtOAc: pyridine 15:1:0.5 to afford the desired product as a green solid (265 mg, 79% yield). ^{1}H-NMR (400 MHz, $CDCl_3$+1% pyridine-d_5): δ = 9.52 (d, *J* = 4.4 Hz, 4H, β-H), 8.68 (d, *J* = 4.4 Hz, 4H, β-H), 8.46 (s, 4H, py-H), 3.90 (t, *J* = 6.4 Hz, 8H, OC*H*$_2$), 1.50–1.43 (m, 8H, C*H*$_2$), 1.36–1.29 (m, 66H, C*H*$_2$), 1.17–0.75 (m, 66H, C*H*$_2$), 0.68–0.43 (m, 44H, C*H*$_2$, C*H*$_3$). ^{13}C{^{1}H}-NMR (125 MHz, $CDCl_3$): δ = 155.6 (4C, py-C), 152.1 (4C, α-C), 149.3 (4C, α-C), 131.2 (4C, β-H), 130.9 (4C, β-H), 128.9 (4C, py-C), 128.7 (2C, py-C), 111.2 (2C, *meso*-C), 109.5 (2C, *meso*-C), 100.3 (2C, ethynyl-C), 98.3(2C, ethynyl-C), 69.6 (4C, O*C*H_2), 33.4–22.6 (64C, *C*H_2), 14.1 (4C, *C*H_3), 13.8 (6C, *C*H_3), 13.0 (6C, Si*C*H_2); *m/z* (MALDI-TOF): 1877.25 ($C_{118}H_{190}N_6O_4Si_2Zn$ requires 1878.4).

[5,15-bis-(3,5-bis(dodecyloxy)pyridyl)-10-ethynyl-20-trihexylsilylethynyl–porphyrinato]zinc(II) **17**

TBAF (1.0 M in THF, 0.097 mL, 0.097 mmol, 0.70 equiv.) was added to a solution of protected pyridyl porphyrin monomer **16** (260 mg, 0.138 mmol, 1.0 equiv.) in 1:1 CH_2Cl_2:$CHCl_3$ (10 mL). The reaction mixture was stirred at 20 °C and monitored by TLC. Upon completion (1 h), the reaction mixture was passed immediately over a short plug of silica (DCM/pyridine 99:1). Purification by column chromatography (petrol ether:EtOAc:pyridine 10:1:0.5) provided the desired product as a green solid (220 mg, 43% yield). ^{1}H-NMR (400 MHz, $CDCl_3$+1%

pyridine-d_5): δ = 9.56 (“t”, *J* = 4.4 Hz, 4H, β-H), 8.72 (dd, *J* = 4.4 Hz, 4H, β-H), 8.48 (s, 4H, py-H), 4.03 (s, 1H, ethynyl-H), 3.90 (m, 8H, OCH_2), 1.73–1.71 (m, 6H, CH_2), 1.55–1.47 (m, 6H, CH_2), 1.40–1.04 (m, 38H, CH_2), 0.99–0.80 (m, 47H, CH_2, CH_3), 0.74–0.60 (m, 6H, CH_2), 0.57–0.46 (m, 28H, CH_2, CH_3); *m/z* (MALDI-TOF): 1596.10 ($C_{100}H_{152}N_6O_4SiZn$ requires 1595.18).

Dimerisation of 5,15-bis-(3,5-bis(dodecyloxy)pyridyl)-10-ethynyl-20-trihexylsilylethynyl–porphyrin (Synthesis of porphyrin dimer **18**)

$Pd(PPh_3)_2Cl_2$ (3.3 mg, 4.7 µmol, 8.1 mol%), CuI (4.1 mg, 0.03 mmol, 0.49 equiv.) and benzoquinone (13.4 mg, 0.124 mmol, 2.10 equiv.) were combined. The reagents were dissolved in dry toluene (5.5 mL) and dry DIPA (1.25 mL) and then added into a stirred solution of monodeprotected porphyrin monomer **17** (94.0 mg, 0.06 mmol, 1.0 equiv.) in dry toluene (5.5 mL) and dry DIPA (1.25 mL). The reaction mixture was stirred at 20 °C and monitored by TLC (10:1:0.5 PE:EtOAc:pyridine). Upon completion (2 h), the mixture was passed over a plug of silica (CH_2Cl_2/pyridine 99:1). Solvents were removed from the filtrate under reduced pressure. The residue was further purified by chromatography on SEC-column eluting with toluene producing a green solid. The green solid was dissolved in chloroform (8.0 mL). TFA (0.34 mL, 4.46 mmol, 100 equiv.) was added under stirring. The mixture was stirred for 10 min, and then quenched with pyridine (0.5 mL). The mixture was filtered directly over a plug of silica eluting with chloroform. The solvent was removed from the filtrate and the residue dried in vacuum to obtain the desired product as green solid (47 mg, 52% yield). ^{1}H-NMR (400 MHz, $CDCl_3$): δ = 9.79 (d, *J* = 4.8 Hz, 4H, β-H), 9.57 (d, *J* = 4.8 Hz, 4H, β-H), 8.81 (d, *J* = 4.8 Hz, 4H, β-H), 8.71 (d, *J* = 4.8 Hz, 4H, β-H), 8.53 (s, 8H, py-H), 4.01 (t, *J* = 5.6 Hz, 16H, OCH_2), 1.81–1.78 (m, 12H, CH_2), 1.60–1.36 (m, 40H, CH_2), 1.01–0.81 (m, 128H, CH_2), 0.76–0.73 (m, 34H, CH_2, CH_3), 0.68–0.57 (m, 48H, CH_2, CH_3). ^{13}C-deptQ-NMR (125 MHz, $CDCl_3$): δ = 155.5 (d, 8C, py-C), 128.9 (u, 8C, py-C), 126.9 (d, 4C, py-C), 111.8 (d, 4C, *meso*-C), 107.7 (d, 2C, *meso*-C), 101.5 (d, 2C, *meso*-C or ethynyl-C), 101.1 (d, 2C, *meso*-C or ethynyl-C), 98.8 (d, 2C, ethynyl-C), 87.0 (d, 2C, ethynyl-C), 82.4 (d, 2C, ethynyl-C), 69.7 (d, 8C, O*C*H_2), 33.4–22.6 (d, 128C, *C*H_2), 14.2 (u, 8C, *C*H_3), 14.0 (u, 6C, *C*H_3), 12.6 (d, 6C, Si*C*H_2) [Signals for α- and β-carbons are not visible due to the chemical exchange of

the N-H protons]. *m/z* (MALDI-TOF): 3062.00 ($C_{100}H_{152}N_6O_4SiZn$ requires 3063.36); λ_{max} [nm] (ε/mol^{-1} L cm^{-1}) (toluene) = 453 (3.33×10^5), 486 (1.94×10^5), 533 (2.38×10^4), 606 (6.75×10^4), 625 (7.60×10^4), 641 (6.42×10^4), 726 (1.05×10^5).

Deprotected porphyrin dimer **19**

The protected porphyrin dimer **18** (10.0 mg, 3.26 μM, 1.0 equiv.) was dissolved in CH_2Cl_2 (2 mL). TBAF (1.0 M in THF, 0.013 mL, 0.013 mmol, 4.0 equiv.) was added to the solution. The mixture was stirred for 30 min. Methanol (4 mL) was added, which resulted in the precipitation of the product that was filtered off and washed with methanol. The desired product was afforded as a green solid (7.8 mg, 96% yield). ^{1}H-NMR (400 MHz, $CDCl_3$): δ = 9.80 (d, *J* = 4.6 Hz, 4H, β-H), 9.59 (d, *J* = 4.6 Hz, 4H, β-H), 8.83 (d, *J* = 4.6 Hz, 4H, β-H), 8.75 (d, *J* = 4.6 Hz, 4H, β-H), 8.53 (s, 8H, py-H), 4.17 (s, 2H, ethynyl-H), 4.02 (t, *J* = 6.4 Hz, 16H, OC*H*$_2$), 1.16–0.56 (m, 184H, C*H*$_2$, C*H*$_3$); ^{13}C{^{1}H}-NMR (125 MHz, $CDCl_3$): δ = 155.5 (8C, py-C), 128.0 (12C, py-C), 111.6 (4C, *meso*-C), 99.7 (2C, *meso*-C or ethynyl-C), 99.1 (2C, *meso*-C or ethynyl-C), 87.0 (2C, ethynyl-C), 85.2 (2C, *meso*-C or ethynyl-C), 84.4 (2C, *meso*-C or ethynyl-C), 82.5 (2C, ethynyl-C), 69.8 (8C, O*C*H$_2$), 31.8–22.6 (80C, *C*H$_2$), 14.1 (8C, *C*H$_3$) [Signals for α- and β-carbons are not visible due to the chemical exchange of the N-H protons]. λ_{max} [nm] (ε/mol^{-1} L cm^{-1}) (toluene) = 450 (2.62×10^5), 483 (1.79×10^5), 530 (2.28×10^4), 719 (7.64×10^4). *m/z* (MALDI-TOF): 2498.30 ($C_{164}H_{230}N_{12}O_8$ requires 2497.81).

2.7.3 The ring-ring templating synthesis of the complex *c*-P12$_{C8}$·*c*-PdP12py12 from Pd tetramer FD-PdP4py4

***c*-P12$_{C8}$** (7.9 mg, 0.61 μmol, 1.0 equiv.) and fully deprotected Pd tetramer **FD-PdP4py4** (11.7 mg, 1.89 μmol, 3.10 equiv.) were dissolved in dry chloroform (7 mL). $Pd(PPh_3)_2Cl_2$ (1.6 mg, 2.3 μmol, 3.8 equiv.), CuI (2.1 mg, 11 μmol, 18 equiv.) and 1,4-benzoquinone (4.9 mg, 45 μmol, 74 equiv.) were dissolved in dry chloroform (0.6 mL) and dry DIPA (0.07 mL). The solution was added to the reaction mixture. The reaction was monitored by UV-vis. The mixture was stirred for 1 h at rt. Then, $Pd(PPh_3)_2Cl_2$ (1.7 mg, 2.4 μmol, 3.9 equiv.), CuI (2.1 mg, 11 μmol, 18 equiv.) and

1,4-benzoquinone (4.5 mg, 41 µmol, 67 equiv.) were dissolved in dry chloroform (0.6 mL) and dry DIPA (0.07 mL). The solution was added to the reaction mixture, which was then heated to 50 °C for 2 h. Subsequently, $Pd(PPh_3)_2Cl_2$ (1.9 mg, 2.7 µmol, 4.4 equiv.), CuI (2.4 mg, 13 µmol, 21 equiv.) and 1,4-benzoquinone (4.9 mg, 45 µmol, 74 equiv.) were dissolved in dry chloroform (0.6 mL) and dry DIPA (0.07 mL). The catalyst solution was added to the reaction mixture, which was then stirred over night at rt in the dark. The reaction mixture was filtered over a plug of aluminiumoxide eluting with chloroform. The solvent was removed from the filtrate and the residue dissolved in toluene. The solution was filtered over a paper filter. The solvent was removed from the filtrate. The residue was purified over a small SEC column eluting with toluene to remove benzoquinone. The brown product band was collected and the solvent removed (14.8 mg). The residue was purified by recycling GPC eluting with toluene. 7.7 mg (0.24 µmol, 39%) of the ring-ring complex were isolated. The characterisation of the ring-ring complex is described in the main text.

2.7.4 Synthesis of dimer $P2_{t\text{-}Bu}$

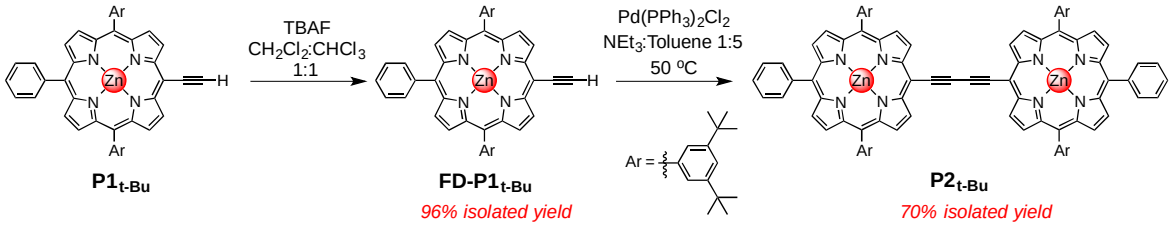

Scheme 2.4 Synthesis of dimer $\mathbf{P2_{t\text{-}Bu}}$

Fully deprotected monomer $\mathbf{FD\text{-}P1_{t\text{-}Bu}}$

The protected monomer $\mathbf{P1_{t\text{-}Bu}}$ was synthesised as published.[34] $\mathbf{P1_{t\text{-}Bu}}$ (20.0 mg, 0.022 mmol) was dissolved in DCM (0.8 mL) and then added pyridine (35.0 µL). TBAF (1 M in THF) (0.088 mL, 0.088 mmol) was added to the solution mixture. The reaction mixture was stirred for 30 min. Upon reaction was complete, methanol was added and the product precipitated. Then filtered the product and washed with methanol. It afforded the product as green solid (18.0 mg, 96% yield). ^{1}H-NMR (400 MHz, $CDCl_3$+1% d_5-pyridine, 298 K): δ_H 9.68 (d, 2H, J = 8.0 Hz, β-H), 8.94 (d, 2H,

J = 4.0 Hz, *β*-H), 8.78 (dd, 4H, *J* = 8.0, 4.0 Hz, *β*-H), 8.12 (m, 2H, *p*-H), 7.99 (s, 4H, *o*-H), 7.74 (m, 2H, Ph-H), 7.65 (m, 4H, Ph-H), 4.11 (s, 1H, ethinyl-H), 1.49 (s, 36H,CH_3).

Porphyrin Dimer **P2$_{t\text{-}Bu}$**

Fully deprotected monomer **FD-P1$_{t\text{-}Bu}$** (2.0 mg, 5.0 mM, 1.0 equiv.) was coupled in a 0.5 mL solution of toluene/triethylamine (5:1) in 5 mL reaction flask at 50 °C equipped with a reflux condenser open to the air. A stoichiometric amount (0.83 mg, 2.5 mM, 2.0 equiv.) of $Pd(PPh_3)_2Cl_2$ was added into the reaction flask. The reaction was monitored by TLC. Upon completion, the solution mixture was passed through a short silica gel plug (DCM+1%pyridine). After that, chromatography on SEC-column (toluene) gave the desired product as green solid (1.4 mg, 70% yield). ^{1}H-NMR (400 MHz, $CDCl_3$+1% d_5-pyridine, 298 K): δ_H 9.95 (d, 4H, *J* = 4.6 Hz, *β*-H), 9.04 (d, 4H, *J* = 4.6 Hz, *β*-H), 8.82 (d, 4H, *J* = 4.0 Hz, *β*-H), 8.78 (d, 4H, *J* = 4.0 Hz, *β*-H), 8.17 (m, 4H, *p*-H), 8.06 (d, 8H, *J* = 1.6 Hz, *o*-H), 7.79 (m, 4H, Ph-H), 7.70 (m, 6H, Ph-H), 1.54 (s, 72H,CH_3).

2.7.5 The ring-ring templating synthesis of the complex *c*-P12$_{C8}$·*c*-PdP12py12 from free-base dimer FD-P2py2

The protected porphyrin dimer **P2py2** (34.6 mg, 10.0 μmol, 1.0 equiv.) was dissolved in CH_2Cl_2 (2.5 mL). TBAF (1.0 M in THF, 25.0 μL, 25.0 μmol, 2.5 equiv.) was added to the solution. The mixture was stirred for 30 min. Methanol (5 mL) was added, which resulted in the precipitation of the product that was filtered off and washed with methanol. The desired product **FD-P2py2** was afforded as a green solid (30.1 mg, 87% yield).

^{1}H-NMR (400 MHz, $CDCl_3$): δ = 9.83 (t, *J* = 4.4 Hz, 4H, β-H), 9.62 (t, *J* = 4.4 Hz, 4H, β-H), 8.93 (d, *J* = 4.5 Hz, 2H, β-H), 8.83 (t, *J* = 5.4 Hz, 4H, β-H), 8.75 (d, *J* = 3.6 Hz, 2H, β-H), 8.53 (s, 4H, py-H), 8.29 (s, 4H, *o*-H), 8.03 (s, 2H, *p*-H), 4.19 (s,2H, ethinyl-H), 4.02 (t, *J* = 6.0 Hz, 8H, OCH_2), 1.52–1.24 (m, 200H, alkyl-H), 1.09–0.47 (m, 300H, alkyl-H), -1.90 (s, 4H, N*H*).

m/z (MALDI-TOF): 2889.56 ($C_{190}H_{288}N_{10}O_4Si_4$ requires 2889.19)

***c*-P12$_{C8}$** (4.9 mg, 0.38 μmol, 1.0 equiv.) and fully deprotected Pd tetramer **FD-P2py2** (6.6 mg, 2.3 μmol, 6.0 equiv.) were dissolved in dry toluene (5.0 mL). $Pd(PPh_3)_2Cl_2$ (1.9 mg, 2.6 μmol, 3.8

equiv.) and NEt_3 (1.0 mL) were added into the reaction mixture. Then the reaction was heated at 50 °C and was monitored by UV-vis spectroscopy. The catalyst was added to the reaction mixture again at the same amount after 3, 6 and 24 h. When there is no change in UV-vis spectra, the reaction mixture was filtered over a plug of aluminiumoxide eluting with chloroform. The solvent was removed from the filtrate and the residue dissolved in toluene. The solution was filtered over a paper filter. The solvent was removed from the filtrate. The residue was purified over a small SEC column eluting with toluene to remove undesired polymers. The crude product band was collected and the solvent removed. The residue was purified by recycling GPC eluting with toluene/1% pyridine. The characterisation of the ring-ring complex is described in the main text.

2.8 References

(1) van Grondelle, R.; Dekker, J. P.; Gillbro, T.; Sundstrom, V. *Biochim. Biophys. Acta* **1994**, *1187*, 1–65.

(2) McDermott, G.; Prince, S. M.; Freer, A. A.; Hawthornthwaite-Lawless, A. M.; Papiz, M. Z.; Cogdell, R. J.; Isaacs, N. W. *Nature* **1995**, *374*, 517–521.

(3) Cogdell, R. J.; Fyfe, P. K.; Barrett, S. J.; Prince, S. M.; Freer, A. A.; Isaacs, N. W.; McGlynn, P.; Hunter, C. N. *Photosynth. Res.* **1996**, *48*, 55–63.

(4) Jimenez, R.; Dikshit, S. N.; Bradforth, S. E.; Fleming, G. R. *J. Phys. Chem.* **1996**, *100*, 6825–6834.

(5) Scholes, G. D.; Fleming, G. R. *J. Phys. Chem. B* **2000**, *104*, 1854–1868.

(6) Gust, D.; Moore, T. A.; Moore, A. L. *Acc. Chem. Res.* **2001**, *34*, 40–48.

(7) Terazono, Y.; Kodis, G.; Bhushan, K.; Zaks, J.; Madden, C.; Moore, A. L.; Moore, T. A.; Fleming, G. R.; Gust, D. *J. Am. Chem. Soc.* **2011**, *133*, 2916–2922.

(8) Aratani, N.; Kim, D.; Osuka, A. *Acc. Chem. Res.* **2009**, *42*, 1922–1934.

(9) Wasielewski, M. R. *Acc. Chem. Res.* **2009**, *42*, 1910–1921.

(10) Jiang, H. W.; Ham, S.; Aratani, N.; Kim, D.; Osuka, A. *Chem. Eur. J.* **2013**, *19*, 13328–13336.

(11) Song, H. E.; Taniguchi, M.; Speckbacher, M.; Yu, L.; Bocian, D. F.; Lindsey, J. S.; Holten, D. *J. Phys. Chem. B* **2009**, *113*, 8011–8019.

(12) Hoffmann, M.; Karnbratt, J.; Chang, M.-H.; Herz, L. M.; Albinsson, B.; Anderson, H. L. *Angew. Chem.- Int. Ed.* **2008**, *47*, 4993–4996.

(13) Sprafke, J. K.; Kondratuk, D. V; Wykes, M.; Thompson, A. L.; Ho, M.; Drevinskas, R.; Chen, W.; Yong, C. K.; Joakim, K.; Bullock, J. E.; Malfois, M.; Wasielewski, M. R.; Albinsson, B.; Herz, L. M.; Zigmantas, D.; Beljonne, D.; Anderson, H. L. *J. Am. Chem. Soc.* **2011**, *133*, 17262–17273.

(14) Matsushita, M.; Ketelaars, M.; van Oijen, A. M.; Köhler, J.; Aartsma, T. J.; Schmidt, J. *Biophys. J.* **2001**, *80*, 1604–1614.

(15) Ketelaars, M.; van Oijen, A. M.; Matsushita, M.; Kohler, J.; Schmidt, J.; Aartsma, T. J. *Biophys. J.* **2001**, *80*, 1591–1603.

(16) Wilson, S. G.; Anderson, H. L. *Chem. Commun.* **1999**, 1539–1540.

(17) Tsuda, A.; Hu, H.; Tanaka, R.; Aida, T. *Angew. Chem.- Int. Ed.* **2005**, *44*, 4884–4888.

(18) Aimi, J.; Oya, K.; Tsuda, A.; Aida, T. *Angew. Chem.- Int. Ed.* **2007**, *46*, 2031–2035.

(19) Aimi, J.; Nagamine, Y.; Tsuda, A.; Muranaka, A.; Uchiyama, M.; Aida, T. *Angew. Chem.- Int. Ed.* **2008**, *47*, 5153–5156.

(20) O'Sullivan, M. C.; Sprafke, J. K.; Kondratuk, D. V; Rinfray, C.; Claridge, T. D. W.; Saywell, A.; Blunt, M. O.; O'Shea, J. N.; Beton, P. H.; Malfois, M.; Anderson, H. L.

Nature **2011**, *469*, 72–75.

(21) Kondratuk, D. V; Perdigao, L. M. A.; Sullivan, M. C. O.; Svatek, S.; Smith, G.; Shea, J. N. O.; Beton, P. H.; Anderson, H. L. *Angew. Chem. - Int. Ed.* **2012**, *51*, 6696–6699.

(22) Kondratuk, D. V; Sprafke, J. K.; O'Sullivan, M. C.; Perdigao, L. M. A.; Saywell, A.; Malfois, M.; O'Shea, J. N.; Beton, P. H.; Thompson, A. L.; Anderson, H. L. *Chem. Eur. J.* **2014**, *20*, 12826–12834.

(23) Parkinson, P.; Aharon, E.; Chang, M. H.; Dosche, C.; Frey, G. L.; Koehler, A.; Herz, L. M. *Phys. Rev. B* **2007**, *75*, 165206/1–165206/6.

(24) Cogdell, R. J.; Gall, A.; Köhler, J. *Q. Rev. Biophys.* **2006**, *39*, 227–324.

(25) Putnam, C. D.; Hammel, M.; Hura, G. L.; Tainer, J. a. *Q. Rev. Biophys.* **2007**, *40*, 191–285.

(26) Mills, A.; Lepre, A. *Anal. Chem.* **1997**, *69*, 4653–4659.

(27) Borisov, S. M.; Zenkl, G.; Klimant, I. *ACS Appl. Mater. Interfaces* **2010**, *2*, 366–374.

(28) Kee, H. L.; Bhaumik, J.; Diers, J. R.; Mroz, P.; Hamblin, M. R.; Bocian, D. F.; Lindsey, J. S.; Holten, D. *J. Photochem. Photobiol. A Chem.* **2008**, *200*, 346–355.

(29) Wagner, R. W.; Johnson, T. E.; Li, F.; Lindsey, J. S. *J. Org. Chem.* **1996**, *60*, 5266–5273.

(30) Grozema, F. C.; Houarner-Rassin, C.; Prins, P.; Siebbeles, L. D. A.; Anderson, H. L. *J. Am. Chem. Soc.* **2007**, *129*, 13370–13371.

(31) Gaefke, G.; Höger, S. *Synthesis.* **2008**, *14*, 2155–2157.

(32) Féau, C.; Klein, E.; Kerth, P.; Lebeau, L. *Synth. Commun.* **2010**, *40*, 3033–3045.

(33) Kiriya, D.; Chang, H.-C.; Kitagawa, S. *J. Am. Chem. Soc.* **2008**, *130*, 5515–5522.

(34) Wong, J. *Porphyrin-Squaraine Dyes for Photocells*, Part II thesis, University of Oxford, Oxford, **2013**.

Chapter 3

Size-Independent Energy Transfer in Biomimetic Nanoring Complexes

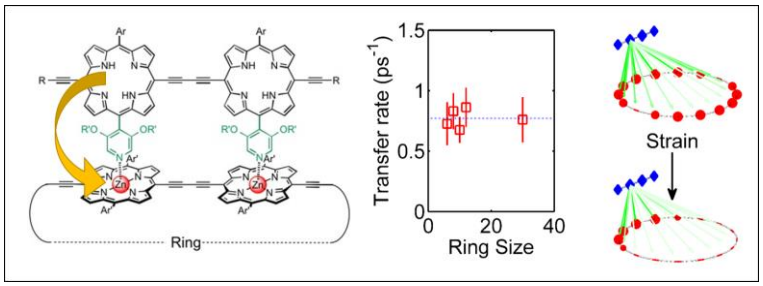

Supramolecular antenna-ring complexes are of great interest due to their presence in natural light-harvesting complexes. While such systems are known to provide benefits through robust and efficient energy funnelling, the relationship between molecular structure, strain and energy dynamics is highly complex. This chapter presents a synthetic antenna-nanoring system based on a series of conjugated porphyrin chromophores so as to explore such effects. By varying the size of the acceptor nanoring, we reveal the interplay between antenna-nanoring binding, local strain and energy dynamics on the picosecond timescale. Binding of the antenna unit creates a local strain in the nanoring, and this strain was measured as a function of the size of the nanoring, by UV-vis-NIR titration, providing information on the conformational flexibility of the system. Surprisingly, the energy transfer rate is independent of nanoring size, indicating the existence of strain-localised acceptor states, spread over about six porphyrin units, arising from the non-covalent antenna-nanoring association.

Parts of the results in this chapter will be published in the following article:

Size-Independent Energy Transfer in Biomimetic Nanoring Complexes
Parkinson, P.; Kamonsutthipaijit, N.; Anderson, H. L.; Herz, L. M. *ACS Nano.* **2016**, [Online early access]. DOI: 10.1021/acsnano.6b01265. Published online: May 13, 2016.

3.1 Background information

Supramolecular complexes of chromophores arranged in a cyclic structure are of interest for energy harvesting applications, due to their occurrence in natural light harvesting systems such as the LH2 complex of *Rhodopseudomo-nas acidophilia*.[1] While it might be presumed that the size of the natural systems are optimised for solar light harvesting in their specific environments, studies of the relationship between the rate of energy transfer and the size of the acceptor nanoring are extremely challenging. Previous investigations on dendritic synthetic light harvesting molecules have revealed a decrease in transfer efficiency as molecule size increases,[2,3] however until now, systematic study has typically been prohibited by synthetic challenges.

In this chapter we investigate the energy transfer from a porphyrin dimer antenna (**P2py2**) to nanorings of different sizes (***c*-P6**, ***c*-P8**, ***c*-P10**, ***c*-P12** and ***c*-P30**, **Figure 3.1**).[2,4–7] These systems provide a highly controlled synthetic framework with a well-defined supramolecular topology. The binding constants for these complexes, determined by UV-vis-NIR titration, provide a direct experimental measure of the mechanical rigidity of the nanorings, and of the strain imposed by binding the antenna unit to each nanoring. By combining stoichiometry, photophysics, binding constant and strain calculations with modelling of energy transfer rates, we demonstrate the existence of strain-localised acceptor states that remarkably cause the energy transfer rate to be independent of nanoring size.

Time-resolved photoluminescence and modelling energy transfer from dimer-nanoring complexes were performed and analysed in collaboration with Dr. Patrick Parkinson and Dr. Laura Herz (Department of Physics, University of Oxford).

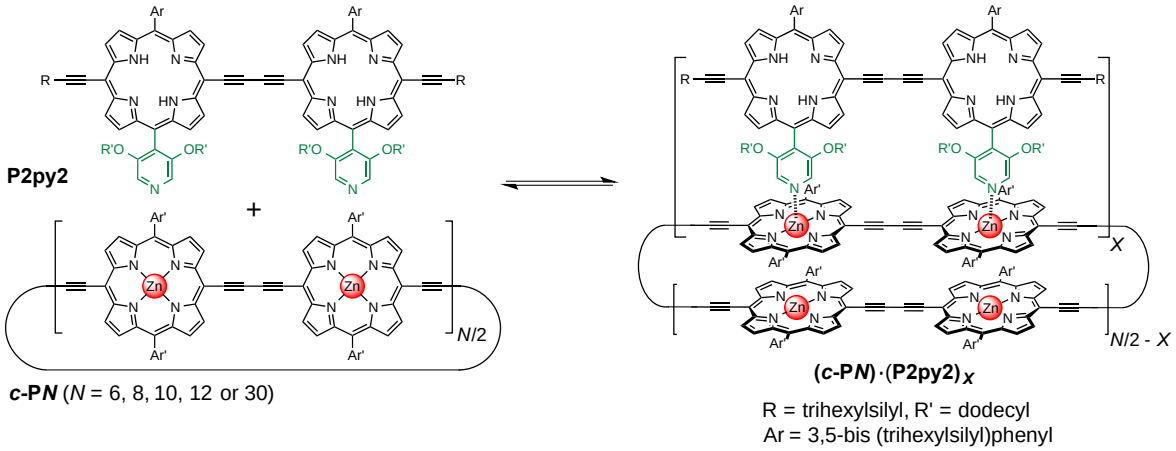

Figure 3.1 Formation of supramolecular double strand porphyrin nanoring complexes from ***c*-P*N*** and **P2py2**. Ar = 3,5-bis(trihexylsilyl)phenyl, Ar' = 3,5-bis(octyloxy)phenyl, R = trihexylsilyl, R' = dodecyl.

3.2 Synthesis of self-assembled components

The porphyrin nanorings were synthesised according to the established procedures using Pd/Cu catalysed-oxidative coupling of linear porphyrin oligomers with templates.[8–11] The free-base dimer was prepared following the methods developed in Anderson's group as shown in **Scheme 3.1** (see more detail in the experimental section).

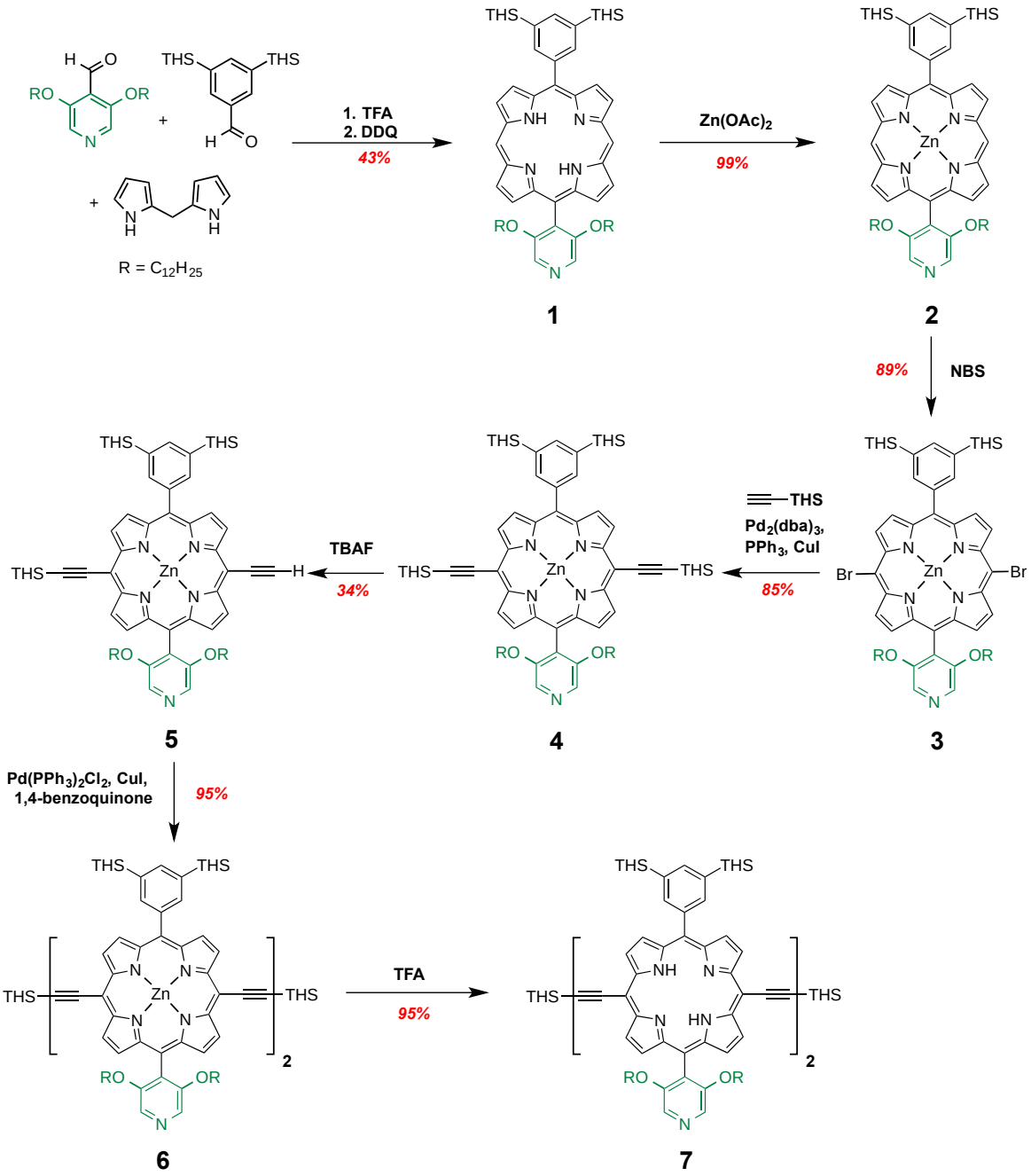

Scheme 3.1 Overview of the synthesis of free-base dipyridyl-substituted porphyrin dimer **P2py2**. THS = $Si(C_6H_{13})_3$ and R = *n*-$C_{12}H_{25}$.

3.3 Determination of stoichiometry

3.3.1 Job plot method

Each free-base **P2py2** antenna unit can bind to the zinc-porphyrin nanorings via two Zn-N coordination sites, so that a ***c*-P*N*** nanoring with *N* zinc centres might be expected to bind up to *N*/2 antenna units to form a complex of the type ***c*-P*N*·(P2py2)$_{N/2}$** (**Figure 3.1** when *X* = *N*/2). We

started this study by testing whether complexes of this stoichiometry are formed, using the Job plot method of continuous variation,[12,13] by means of UV-vis-NIR spectroscopy. In these titrations, the total concentration of all the components was kept constant while varying the molar ratio of host (***c*-P*N***) to guest (**P2py2**). The stoichiometry of each complex was obtained from the abscissa of the maximum of the Job plot, where the *x*- and *y*-axes are given by

$$x = [H]/([H] + [G]) \qquad \textbf{(eq. 3.1)}$$

$$y = A_{obs} - \varepsilon_H \cdot [H] - \varepsilon_G \cdot [G] \qquad \textbf{(eq. 3.2)}$$

where [H] and [G] are the total concentrations of host (***c*-P*N***) and guest (**P2py2**) at the initial state, respectively; A_{obs} is the observed absorbance at a specific wavelength; ε_H and ε_G are the molar absorption coefficients of the host and guest at that wavelength, respectively. The *x* error bars reflect uncertainty in [H] and [G] (originating from uncertainty in ε_H and ε_G).

The resulting Job plots and UV-vis-NIR spectra are shown in **Figure 3.2a–e**. The changes in the absorption spectra on binding show that the dimers absorb at shorter wavelengths than the nanorings, and that complexation results in a slight red-shift of the Q-bands, due to the effects of local planarisation on exciton delocalisation.

The Job plot for ***c*-P6** shows that a 1:2 complex is formed instead of the expected 1:3 complex. This conclusion was confirmed by ^{1}H NMR titration (see the details in the next **Section 3.3.2**). The formation of a 1:2 complex, but not a 1:3 complex, can be explained by the increased strain in the ring upon binding **P2py2** to ***c*-P6**.

The three medium-sized nanorings ***c*-P8**, ***c*-P10** and ***c*-P12** give the expected Job peaks at 0.20, 0.17 and 0.14 respectively, indicating that the stoichiometries of their complexes are 1:4 (***c*-P8**), 1:5 (***c*-P10**) and 1:6 (***c*-P12**). The largest nanoring tested in this study, ***c*-P30**, gave a Job peak at 0.20 indicating formation of a 1:4 complex, instead of the expected 1:15 complex. This surprising behaviour may be attributed to aggregation of the very large nanoring, either intermolecularly or intramolecularly, to form a hairpin folded conformation.[14]

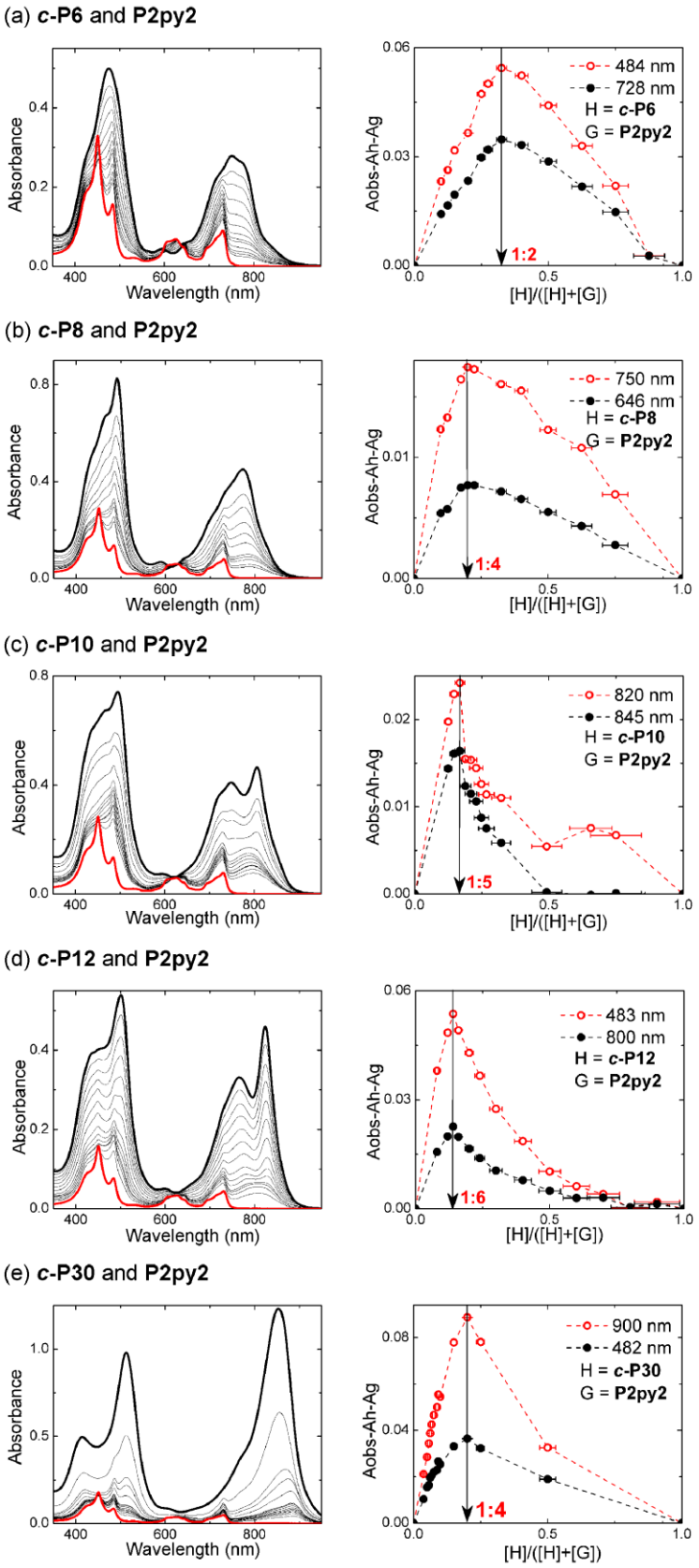

Figure 3.2 Job plots for nanorings-dimer complexes (all in toluene at 298 K). (Left) The UV-vis-NIR spectra upon varying mole fraction of nanoring from 0 to 1 in thick red to black lines. (Right) Job plots of the complex formations with red and black dots corresponding to the absorbance difference as shown in the legend. Red and black dashed lines are given as a guide to the eye.

3.3.2 ^{1}H NMR of *c*-P6•P2py2 complex to confirm the stoichiometry

A ^{1}H NMR titration was performed to test the conclusion of the Job plot on the formation of a 1:2 complex between ***c*-P6** and **P2py2**. Upon adding dimer **P2Py2** to ***c*-P6**, the appearance of a new complex and the shifting of all peaks corresponding to ***c*-P6** were observed (**Figure 3.4**). The rate of exchange is intermediate between fast and slow, resulting in broadening of the resonances, so that it was not possible to gain much information directly from the resonances of ***c*-P6** or **P2py2**. At the start of the titration, 6.0 equivalents of pyridine were present and bound to the 6-ring. (The amount of pyridine was determined from the ^{1}H NMR spectrum at 0.0 equivalent of **P2py2** using the integration of the pyridine in comparison to the value of the porphyrin ***c*-P6**.) The pyridine that was initially bound to ***c*-P6** was replaced by dimer during the titration, because when **P2Py2** chelates to ***c*-P6** it binds much more strongly than monodentate pyridine (**Figure 3.3**). Therefore, the shift of the peaks corresponding to the pyridine could be used to monitor the fraction of bound pyridine, and thus to determine how many equivalents of dimer bind to each 6-ring.

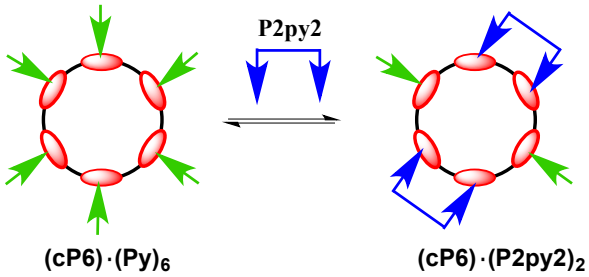

Figure 3.3 Possible displacement of pyridine (green arrows) with **P2py2** during ^{1}H NMR titration of ***c*-P6** with **P2Py2** when pyridine is present.

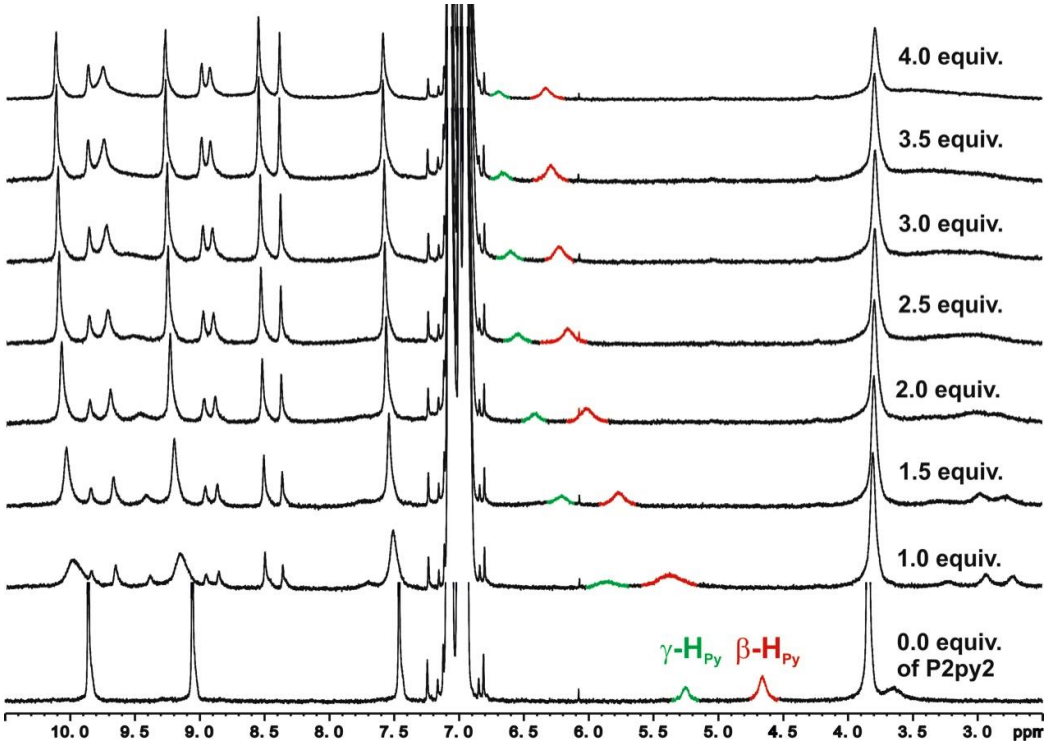

Figure 3.4 ^{1}H NMR titration of ***c*-P6·(Py)$_6$** with **P2Py2** (toluene-d_8, 298 K, 500 MHz, [***c*-P6**] = 0.22 mM) and assignment of ratio of **P2Py2**/***c*-P6**. Red and green peaks correspond to β- and γ-protons on pyridine, respectively.

We calculated the chemical shift of the peaks corresponding to the β- and γ-pyridine protons during the titration using the equation:

$$\delta_{obs} = \frac{[\mathbf{Py}]_{\mathbf{free}}}{[\mathbf{Py}]_{\mathbf{tot}}}\delta_{free} + \frac{[\mathbf{Py}]_{\mathbf{bound}}}{[\mathbf{Py}]_{\mathbf{tot}}}\delta_{bound} \qquad \textbf{(eq. 3.3)}$$

where $[\mathbf{Py}]_{\mathbf{free}}$, $[\mathbf{Py}]_{\mathbf{bound}}$ and $[\mathbf{Py}]_{\mathbf{tot}}$ are concentrations of free, bound and total pyridine in the titration, respectively; δ_{obs}, δ_{free} and δ_{bound} (ppm) are chemical shifts corresponding to β- or γ-protons of observed, free and fully bound pyridine, respectively. The chemical shifts corresponding to free β- and γ-pyridine are δ = 6.67 and 6.99 ppm, respectively (measured by recording the ^{1}H NMR spectrum of pyridine in toluene-d_8).

As there is no consumption of components, it is true that

$$[\mathbf{Py}]_{\mathbf{tot}} = [\mathbf{Py}]_{\mathbf{bound}} + [\mathbf{Py}]_{\mathbf{free}} \qquad \textbf{(eq. 3.4)}.$$

$[\mathbf{Py}]_{\mathbf{bound}}$ can be obtained from the binding constant K_{py}, making the following assumptions. Prior to additional of dimer, all 6 sites of Zn on the 6-ring are available for binding pyridine. After additional of up to two equivalents of dimer, some of the Zn sites bind dimer to form a 1:2

complex, making them unavailable for binding weak ligands such as pyridine. When more than two equivalents of dimer are added, only two Zn sites are available for binding pyridine; they can bind to either pyridine and/or excess dimer which acts as the competitive ligand. We assume that the dimer can bind to these remaining sites as a non-chelating ligand, so the concentration of these pyridine sites is twice the concentration of excess dimer. Thus, after more than two equivalents of dimer, the effective pyridine concentration is not only obtained from the concentration of simply pyridine but also two times of concentration of excess dimer.

Then, [eff. **Py**]$_{\mathbf{bound}}$ is given from

$$[\text{eff. }\mathbf{Py}]_{\mathbf{bound}} = \frac{\left(K_{\text{py}}([\mathbf{eff.Zn}]_{\mathbf{tot}} + [\mathbf{eff.Py}]_{\mathbf{tot}}) + 1\right) - \sqrt{\left(K_{\text{py}}([\mathbf{eff.Zn}]_{\text{tot}} + [\mathbf{eff.Py}]_{\mathbf{tot}}) + 1\right)^2 - 4K_{\text{py}}^2[\mathbf{eff.Zn}]_{\mathbf{tot}}[\mathbf{eff.Py}]_{\mathbf{tot}}}}{2K_{\text{py}}}$$

(eq. 3.5)

where K_{py} is the association constant between pyridine and porphyrin monomer (K_{py} = (2.58 ± 0.26) × 10^4 M^{-1}, see detail in the determination of reference constants **Section 3.4.3a**); [**eff. Zn**]$_{\text{tot}}$ is the total concentration of the available Zn sites to weak binding of ligands such as pyridine; [**eff. Py**]$_{\text{tot}}$ is the total concentration of the effective pyridine sites. [**eff. Zn**]$_{\text{tot}}$ and [**eff. Py**]$_{\text{tot}}$ are derived from the 1:2 assumption below:

For [**eff. Zn**]$_{\text{tot}}$

Condition a) if the amount of dimer is less than or equal to 2 equivalents, then all dimers are bound to the 6-ring, giving:

$$[\mathbf{eff.Zn}]_{\mathbf{tot}} = \mathbf{6}[\mathbf{cP6}]_{\mathbf{tot}} - \mathbf{2}[\mathbf{P2py2}]_{\mathbf{tot}} \quad \textbf{(eq. 3.6)}$$

Condition b) if the amount of dimer is more than 2 equivalents, then there are only 2 sites of zinc available on each 6-ring, giving:

$$[\mathbf{eff.Zn}]_{\mathbf{tot}} = \mathbf{2}[\mathbf{cP6}]_{\mathbf{tot}} \quad \textbf{(eq. 3.7)}$$

For [**eff. Py**]$_{\text{tot}}$

Condition a) if the amount of dimer is less than or equal to 2 equivalents, then all dimers are bound to the 6-ring and the total concentration of effective pyridine is just the total concentration of ordinary pyridine, [**Py**]$_{\text{tot}}$, giving

$$[\mathbf{eff.Py}]_{\mathbf{tot}} = [\mathbf{Py}]_{\mathbf{tot}} \quad \textbf{(eq. 3.8)}$$

and $$[\mathbf{Py}]_{\mathbf{bound}} = [\mathbf{eff.Py}]_{\mathbf{bound}} \quad \textbf{(eq. 3.9)}.$$

Condition b) if the amount of dimer is more than 2 equivalents, then the excess dimer can also compete with the pyridine to bind to the zinc site. If we consider the dimer as two sites of pyridine, we obtain

$$[\mathbf{eff.Py}]_{\mathbf{tot}} = [\mathbf{Py}]_{\mathbf{tot}} + \mathbf{2}[\mathbf{non-chelating\ dimer}]_{\mathbf{tot}} \quad \textbf{(eq. 3.10)}.$$

Since we assume that two dimers can be bound on the 6-ring, it is true that

$$[\mathbf{non-chelating\ dimer}]_{\mathbf{tot}} = [\mathbf{P2py2}]_{\mathbf{tot}} - \mathbf{2}[\mathbf{cP6}]_{\mathbf{tot}} \quad \textbf{(eq. 3.11)}.$$

Then,

$$[\mathbf{eff.Py}]_{\mathbf{tot}} = [\mathbf{Py}]_{\mathbf{tot}} + \mathbf{2}[\mathbf{P2py2}]_{\mathbf{tot}} - \mathbf{4}[\mathbf{cP6}]_{\mathbf{tot}} \quad \textbf{(eq. 3.12)}$$

and $$[\mathbf{Py}]_{\mathbf{bound}} = [\mathbf{eff.Py}]_{\mathbf{bound}} \times \left(\frac{[\mathbf{Py}]_{\mathbf{tot}}}{[\mathbf{Py}]_{\mathbf{tot}} + \mathbf{2}[\mathbf{P2py2}]_{\mathbf{tot}} - \mathbf{4}[\mathbf{cP6}]_{\mathbf{tot}}}\right) \quad \textbf{(eq. 3.13)}.$$

This equation was combined with **Equations 3.5** and **3.3** to calculate the chemical shifts of the pyridine signals over the course of the titration as shown in **Figure 3.5**. The predicted chemical shifts of pyridine are in very good agreement with the empirical data from the titration, indicating that the 1:2 assumption is valid and only two dimers are bound to 6-ring. This 1:2 ratio can be explained by the increased strain in the ring upon binding **P2py2** to ***c*-P6**, which may straighten out the binding sites on ***c*-P6**. This may disfavour the formation of the 1:3 (***c*-P6**:**P2py2**) complex.

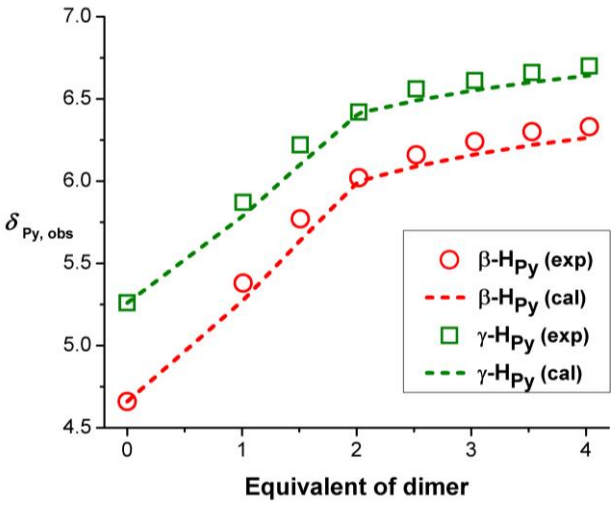

Figure 3.5 Changes in the chemical shift of the pyridine protons on titration of ***c*-P6•(py)$_6$** with **P2py2**, showing the γ-proton (green square) and β-proton (red circle) with various equivalent of dimer **P2py2**. The simulated data were calculated by equation 3.3 (green dash line, γ-proton and red dash line, β-proton).

3.4 Investigation of binding strain

We investigated the thermodynamic stabilities of the ***c*-P*N*·(P2py2)$_X$** complexes, as a function of ring-size, to probe the flexibility of the nanorings and to study the role of the non-covalent dimer-nanoring association on the acceptor state. The binding constants of complexes can be determined by UV-vis-NIR titrations and these values can be used to calculate the strain energy of complex formation as will described in **Section 3.4.4**.

3.4.1 UV-vis-NIR formation titration

At the first attempt to determine the binding constant (K_f) in toluene at 25 °C, UV-vis-NIR formation titrations of **(*c*-P*N*)·(P2py2)**$_{N/2}$ complexes were performed. The dimer was added to the nanoring and the total concentration of the nanorings was kept constant during the titration to inspect the isosbesticity and to simplify the analysis of the data. Binding constants were determined from the titration curves using a 1:1 binding model (i.e. the dimer ligands behave independently in their binding to *N*-ring, and *N*-ring is treated as *N*/2 dimer sites). Isosbestic behaviour would be observed if this assumption were fulfilled in the actual system. The binding isotherm was analysed by fitting in Origin® software, assuming a 1:1 binding situation. K_f was evaluated by

$$\frac{A-A_0}{A_f-A_0} = \frac{(K_f([L]_0+[P]_0)+1)-\sqrt{(K_f([L]_0+[P]_0)+1)^2-4K_f^2[P]_0[L]_0}}{2K_f[P]_0}, \qquad \textbf{(eq. 3.14)}$$

where A is the observed absorption at a specific wavelength or difference of absorption at two wavelengths; A_0 is the starting absorption at this wavelength or difference of absorption in these two wavelengths; A_f is the asymptotic final absorption at this wavelength or difference of absorption in these two wavelengths; K_f is the association constant between ligand and porphyrin host; [L] is the concentration of ligand; $[P]_0$ is the concentration of porphyrin host. The detailed derivation of the equation is shown in **Appendix**.

For the formation titration of ***c*-P10** and ***c*-P12**-dimer complexes, we encountered aggregation problems between the nanorings at the initial points of the titration, so these initial points were excluded from the analysis.

The UV-vis-NIR formation titration spectra are shown in **Figures 3.6–3.9**. The binding constants of the complexes are mostly too strong ($K_f > 10^7$ M^{-1} as listed in **Table 3.1**) to be determined from formation titrations. Thus, denaturation titrations were used to determine K_f indirectly by quantifying the ability of pyridine to break up the complexes, via the denaturation constant K_{dn} as described in the next section.

Table 3.1 Binding constants of **c-P*N*** with **P2py2** (1:1 association constant, M^{-1}) determined by direct titration

c*-P*N	K_f, M^{-1}		
	Run 1	Run 2	Average
***c*-P6**	$(1.26 \pm 0.33) \times 10^7$	$(1.05 \pm 0.15) \times 10^7$	$(1.16 \pm 0.18) \times 10^7$
***c*-P8**	$(2.88 \pm 0.41) \times 10^7$	$(3.07 \pm 0.47) \times 10^7$	$(2.98 \pm 0.31) \times 10^7$
***c*-P10**	$(1.70 \pm 0.19) \times 10^7$	$(1.43 \pm 0.18) \times 10^7$	$(1.57 \pm 0.13) \times 10^7$
***c*-P12**	$(2.79 \pm 0.59) \times 10^7$	$(2.71 \pm 0.47) \times 10^7$	$(2.75 \pm 0.37) \times 10^7$

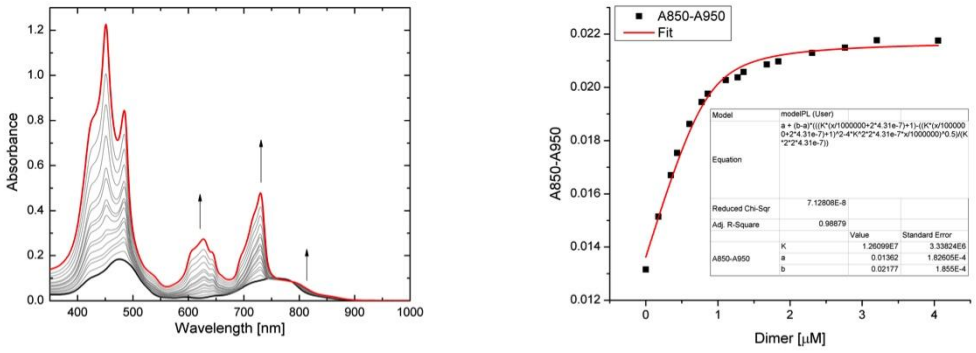

Figure 3.6 UV-vis-NIR formation titration of **c-P6** ([**c-P6**] = 4.31×10^{-7} M) with **P2py2** in toluene at 298 K (Run 1: R^2 = 0.989; Run 2: R^2 = 0.995). (left) Changes in absorption upon addition of **P2py2**. Arrows indicate areas of increasing and decreasing absorption during the titration; (right) Binding isotherm (black dots) derived from absorption data at λ = 850 – 950 nm and fit obtained from Origin® (red line).

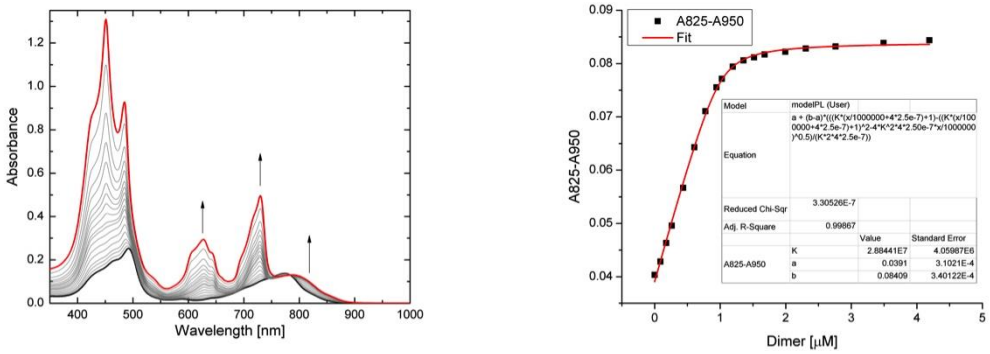

Figure 3.7 UV-vis-NIR formation titration of ***c*-P8** (**[*c*-P8]** = 2.50×10^{-7} M) with **P2py2** in toluene at 298 K (Run 1: R^2 = 0.999; Run 2: R^2 = 0.998). (left) Changes in absorption upon addition of **P2py2**. Arrows indicate areas of increasing and decreasing absorption during the titration; (right) Binding isotherm (black dots) derived from absorption data at λ = 825 – 950 nm and fit obtained from Origin® (red line).

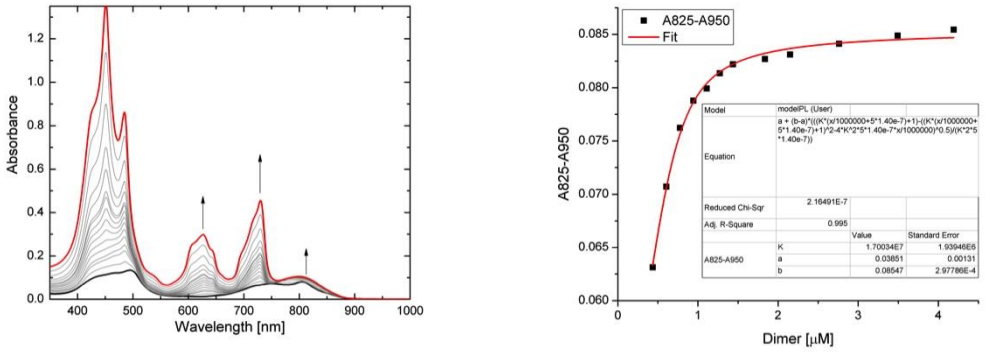

Figure 3.8 UV-vis-NIR formation titration of ***c*-P10** ([**c-P10**] = 1.40×10^{-7} M) with **P2py2** in toluene at 298 K (Run 1: R^2 = 0.995; Run 2: R^2 = 0.992). (left) Changes in absorption upon addition of **P2py2**. Arrows indicate areas of increasing and decreasing absorption during the titration; (right) Binding isotherm (black dots) derived from absorption data at λ = 825 – 950 nm and fit obtained from Origin® (red line).

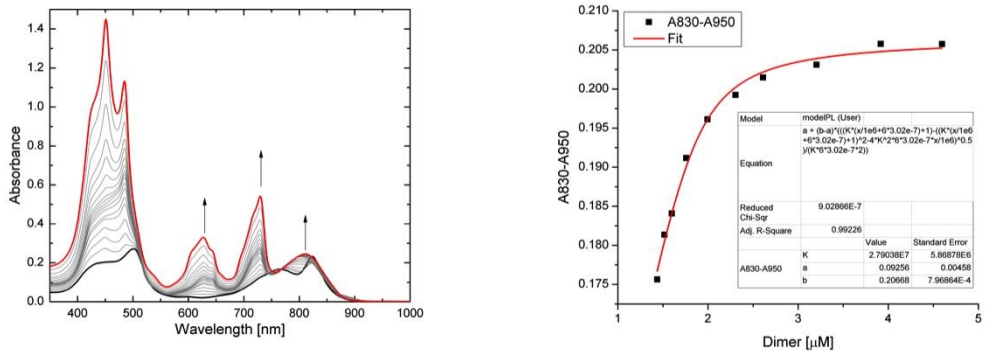

Figure 3.9 UV-vis-NIR formation titration of with ***c*-P12** ([**c-P12**] = 3.02×10^{-7} M) with **P2py2** in toluene at 298 K (Run 1: R^2 = 0.992; Run2: R^2 = 0.996). (left) Changes in absorption upon addition of **P2py2**. Arrows indicate areas of increasing and decreasing absorption during the titration; (right) binding isotherm (black dots) derived from absorption data at λ = 830 – 950 nm and fit obtained from Origin® (red line).

3.4.2 UV-vis-NIR denaturation titration

The self-assembled complexes were generated by titrating solutions of ***c*-P*N*** (*N* = 6, 8, 10 and 12) in toluene with pyridyl substituted-porphyrin dimer **P2py2.** UV-vis-NIR denaturation titrations were used to determine K_f indirectly via the denaturation constant K_{dn}. At approximately 10^{-6} M in toluene at 25 °C, a large excess of pyridine was titrated to the complexes of (***c*-P*N*)•(P2py2)**$_{N/2}$ (except for ***c*-P6**, which is a (***c*-P6**)•(**P2py2**)$_2$ complex) to displace bidentate ligand **P2py2**. The denaturation data were analysed by fitting in Origin® software, assuming a 1:1 binding situation. K_{dn} was evaluated by

$$K_{\mathrm{dn}} = \frac{[\mathrm{c{-}P}\boldsymbol{N}\cdot \mathrm{Py}_2][\mathrm{P2py2}]}{[\mathrm{c{-}P}\boldsymbol{N}\cdot \mathrm{P2py2}][\mathrm{Py}]^2} \quad , \qquad \textbf{(eq. 3.15)}$$

where [Py] is the concentration of pyridine. The corresponding binding isotherm was given by

$$\frac{A-A_0}{A_f-A_0} = \frac{-K_{\mathrm{dn}}[\mathrm{Py}]^2+\sqrt{K_{\mathrm{dn}}^2[\mathrm{Py}]^4+4K_{\mathrm{dn}}[\mathrm{Py}]^2[\mathrm{P}]_0}}{2[\mathrm{P}]_0} \quad , \qquad \textbf{(eq. 3.16)}$$

where A is the observed absorption at a specific wavelength or difference of absorption at two wavelengths; A_0 is the starting absorption at this wavelength or difference of absorption in these two wavelengths; A_f is the asymptotic final absorption at this wavelength or difference of absorption in these two wavelengths; K_{dn} is the denaturation constant between **P2py2** and the porphyrin nanoring complex; [Py] is the concentration of pyridine and $[P]_0$ is the concentration of porphyrin nanoring complex. Since we are using a 1:1 binding model, the $[P]_0$ is a 2, 4, 5 or 6-fold multiple of the concentration of ***c*-P6**, ***c*-P8**, ***c*-P10** and ***c*-P12**, respectively as they have multiple porphyrin units inside each molecule. The detailed derivation of this equation is shown in the **Appendix**.

The UV-vis-NIR denaturation titrations are shown in **Figures 3.10-3.13**. Binding isotherms derived from the changes in absorption at two specific wavelengths. Wavelengths were chosen which gave the greatest increase and decrease in absorption during each titration, within the same region of the spectrum. We use a difference in absorption, resulting from complexation, to avoid any effects that might cause variation in the baseline, since such artefacts would cause a rise or fall

in the absorption at both wavelengths. Binding isotherms were analysed by simulation with **Equation 3.14** to give the smooth curves plotted in **Figures 3.10-3.13 (right)**, with just three free parameters (A_0, A_f, and K_{dn}). The resulting values of K_{dn} are listed in **Table 3.2** in **Section 3.4.3b**.

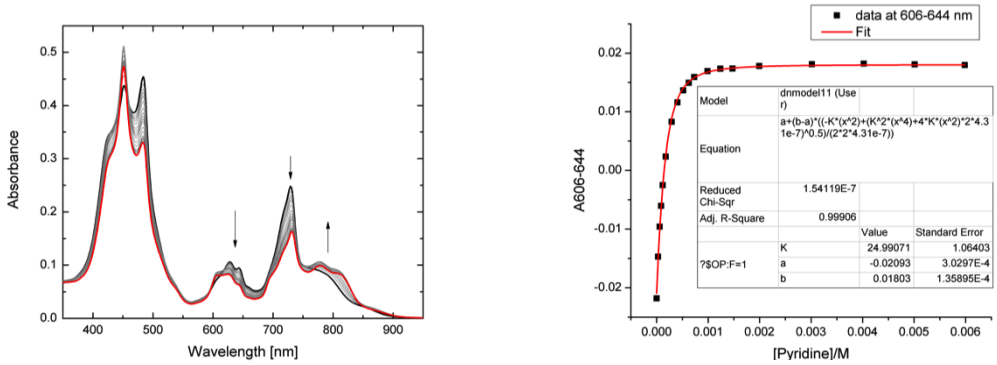

Figure 3.10 UV-vis-NIR denaturation titration of **(*c*-P6)•(P2py2)$_2$** ([complex] = 4.31 × 10^{-6} M) with pyridine in toluene at 298 K (Run1: R^2 = 0.999; Run2: R^2 =0.999). (left) Changes in absorption upon addition of pyridine. Arrows indicate areas of increasing and decreasing absorption during the titration; (right) Binding isotherm (black dots) derived from absorption data at λ = 606 – 644 nm and fit obtained from Origin® (red line).

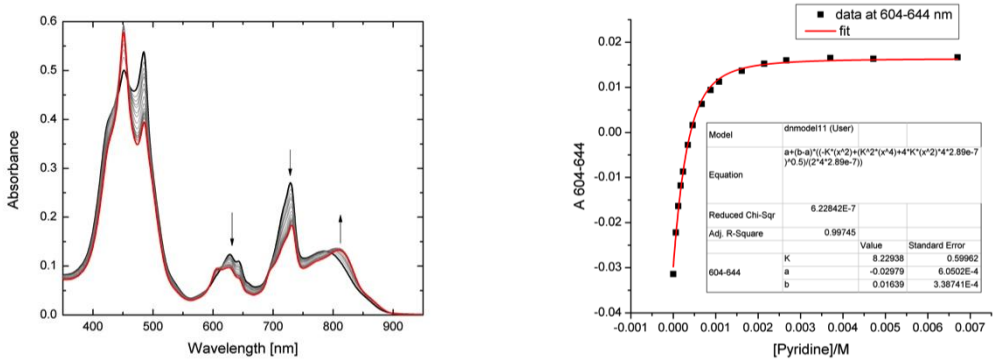

Figure 3.11 UV-vis-NIR denaturation titration of **(*c*-P8)•(P2py2)$_4$** ([complex] = 2.89 × 10^{-7} M) with pyridine in toluene at 298 K (Run 1: R^2 = 0.997; Run 2: R^2 = 0.997). (left) Changes in absorption upon addition of pyridine. Arrows indicate areas of increasing and decreasing absorption during the titration; (right) Binding isotherm (black dots) derived from absorption data at λ = 604 – 644 nm and fit obtained from Origin® (red line).

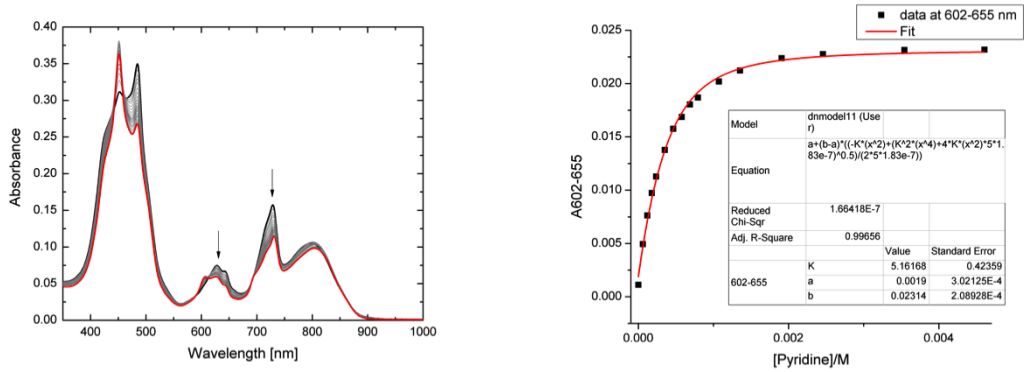

Figure 3.12 UV-vis-NIR denaturation titration of **(*c*-P10)•(P2py2)$_5$** ([complex] = 1.83 × 10^{-7} M) with pyridine in toluene at 298 K (Run 1: R^2 = 0.997; Run 2: R^2 = 0.996). (left) Changes in absorption upon

addition of pyridine. Arrows indicate areas of increasing and decreasing absorption during the titration; (right) Binding isotherm (black dots) derived from absorption data at λ = 602 – 655 nm and fit obtained from Origin® (red line).

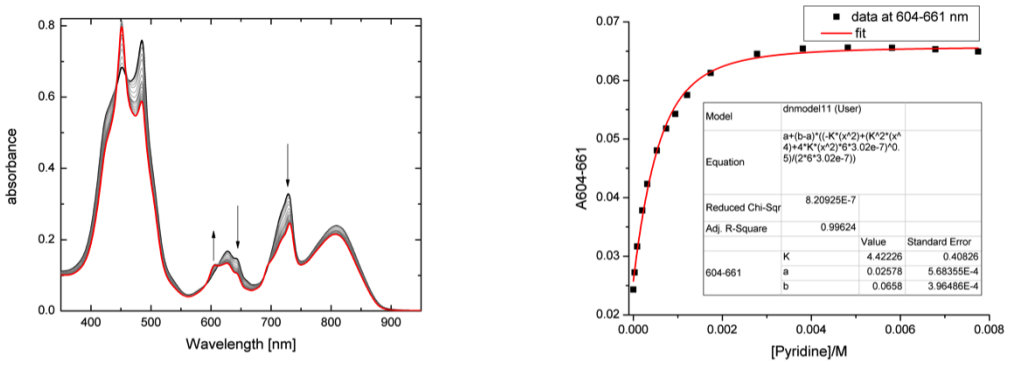

Figure 3.13 UV-vis-NIR denaturation titration of **(c-P12)•(P2py2)$_6$** ([complex] = 3.02 × 10^{-7} M) with pyridine in toluene at 298 K (Run 1: R^2 = 0.996; Run 2: R^2 = 0.998). (left) Changes in absorption upon addition of pyridine. Arrows indicate areas of increasing and decreasing absorption during the titration; (right) Binding isotherm (black dots) derived from absorption data at λ = 604 – 661 nm and fit obtained from Origin® (red line).

3.4.3 Calculation of the formation constant K_f

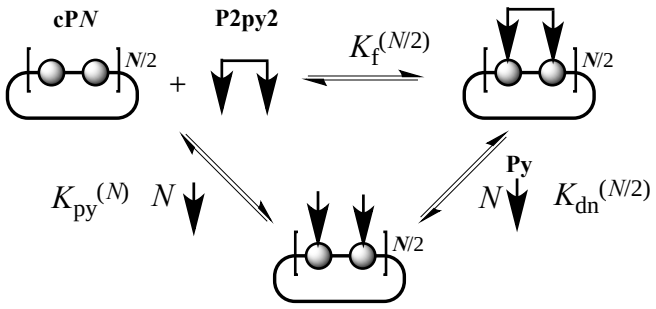

Figure 3.14 Generic thermodynamic cycle for the formation of a double strand complex.

The formation constants K_f for nanoring-dimer complexes were calculated indirectly using the denaturation constants from

$$K_f = \frac{K_{py}^2}{K_{dn}} \quad \textbf{(eq. 3.17),}$$

where K_{py} is the formation constant for the binding of pyridine to porphyrin monomer (detail of determination of K_{py} as described below) and K_{dn} is the denaturation constant of the nanoring-dimer complexes with pyridine.

As a result, to derive K_f of nanoring-dimer complexes by **Equation 3.15**, K_{py} is needed and the binding constant of **P2py2** to porphyrin dimer is also required as a reference in comparison to the binding constants of the family of nanoring-dimer complexes as follows.

a) Determination of reference constants

The binding constant of pyridine to porphyrin monomer complex (K_{py}) was derived by UV-vis-NIR formation titration of pyridine with porphyrin monomer (**Figure 3.15**).

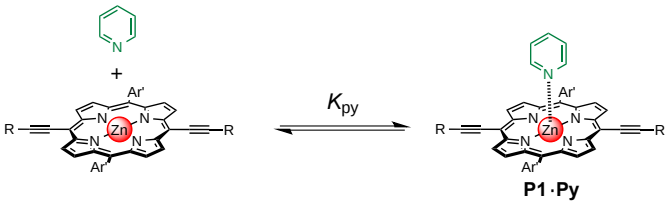

Figure 3.15 Formation of pyridine and porphyrin monomer complex (**P1•Py**). Ar' = 3,5-bis(octyloxy)phenyl, R = trihexylsilyl.

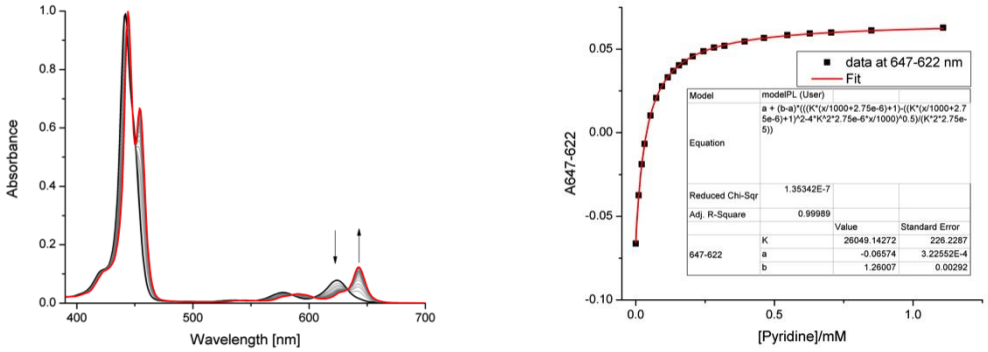

Figure 3.16 UV-vis-NIR formation titration of **P1** ([**P1**] = 2.75×10^{-6} M) with pyridine in toluene at 298 K; (Run 1, R^2 = 0.9999; Run2, R^2 =0.9998); K_{py} = (2.58 ± 0.26) × 10^4 M^{-1}. (left) Changes in absorption upon addition of pyridine. Arrows indicate areas of increasing and decreasing absorption during the titration; (right) Binding isotherm (black dots) derived from absorption data at λ = 647 – 622 nm and fit obtained from Origin® (red line).

The empirical data were in excellent agreement with the theoretically derived 1:1 binding **Equation 3.14**, resulting in to K_{py} = (2.58 ± 0.26) × 10^4 M^{-1} (**Figure 3.16**). Monomer was used instead of the cyclic porphyrin oligomers to model this interaction in order to avoid the initial aggregation of the nanorings during this titration.

Likewise, the binding constant of **P2py2** to porphyrin dimer was also elucidated as a reference in comparison to the binding constants of the family of nanoring-dimer complexes (**Figure 3.17**).

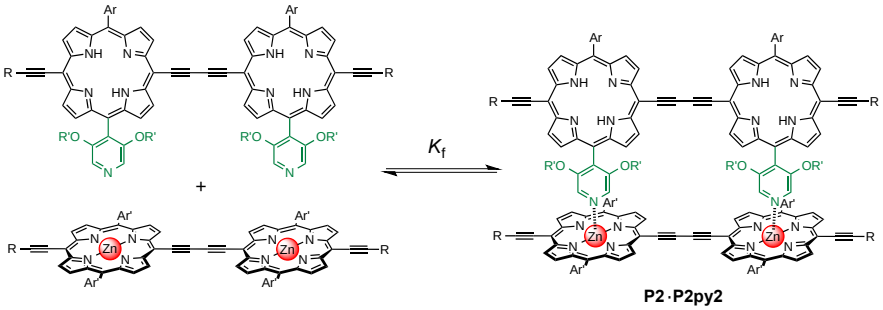

Figure 3.17 Formation of **P2py2** and porphyrin dimer complex (**P2•P2py2**). Ar = 3,5-bis(trihexylsilyl)phenyl, Ar' = 3,5-bis(octyloxy)phenyl, R = trihexylsilyl, R' = dodecyl.

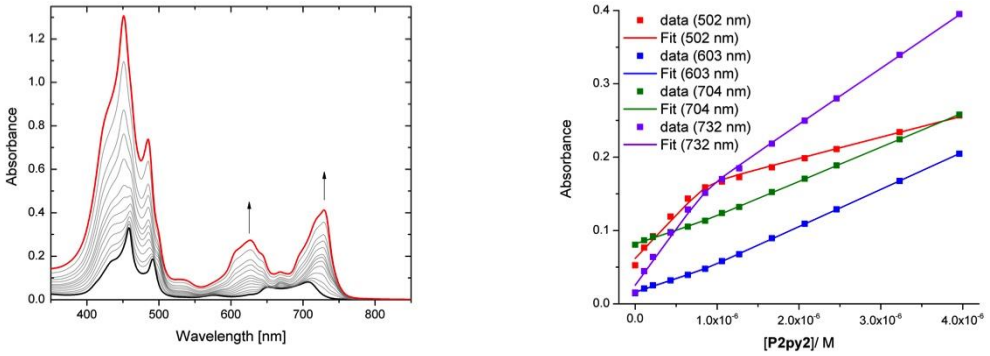

Figure 3.18 UV-vis-NIR formation titration of **P2** ([**P2**] = 8.71 × 10^{-7} M) with **P2py2** in toluene at 298 K (K_f = (1.74 ± 0.20) × 10^8 M^{-1}). (left) Changes in absorption upon addition of **P2py2**. Arrows indicate areas of increasing absorption during the titration; (right) Binding isotherm (dots) derived from absorption data at various wavelengths and fit obtained from SPECFIT (line). The increment after addition of 1 equivalent of **P2py2** is attributed to the absorption overlapping between excess **P2py2** and the complex.

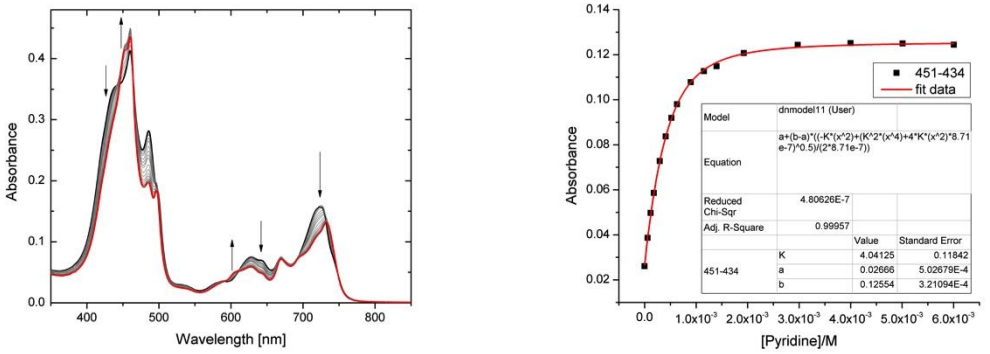

Figure 3.19 UV-vis-NIR denaturation titration of **P2•P2py2** ([complex] = 8.71 × 10^{-7} M) with pyridine in toluene at 298 K (Run1: R^2 = 0.9996; Run2: R^2 =0.999). (left) Changes in absorption upon addition of pyridine. Arrows indicate areas of increasing and decreasing absorption during the titration; (right) Binding isotherm (black dots) derived from absorption data at λ = 451 – 434 nm and fit obtained from Origin® (red line).

The binding isotherm of dimer-dimer formation was too sharp and the increment after addition of 1.0 equivalent of dimer due to the overlapping absorption between the complex and excess

dimer. This makes the difficulty to obtain a curve fitting a 1:1 model for formation from **Equation 3.14** (**Figure 3.18**). The first attempt to fit the data using a 1:1 model calculated by SPECFIT provided good agreement between the empirical data and simulated data, giving $K_f = (1.74 \pm 0.20) \times 10^8$ M^{-1}. Nevertheless, the binding constant of this complex is too strong ($K_f > 10^7$ M^{-1}). The breakup titration was therefore performed to confirm K_f from SPECFIT again and fitted successfully using **Equation 3.16** (**Figure 3.19**), giving $K_{dn} = 3.98 \pm 0.10$ M^{-1}. $K_f = (1.67 \pm 0.34) \times 10^8$ M^{-1} was calculated using the thermodynamic cycle (**Equation 3.17**) and is listed in **Table 3.2**. The two values of K_f from SPECFIT and from the breakup titration are in good agreement.

b) Summary of denaturation and formation constants of nanoring-dimer complexes

K_{dn} evaluated by **Equation 3.16** and K_f calculated by **Equation 3.17** are listed in **Table 3.2**. The binding constants for the various sizes of porphyrin nanoring with dimer are compared graphically in **Figure 3.20**.

Table 3.2 Denaturation constants of nanoring-dimer complexes with pyridine and formation constants of nanoring-dimer complexes determined via denaturation titrations

P*N*	K_{dn}, M^{-1}			K_f, M^{-1}
	Run 1	Run 2	Average	
P2	4.04 ± 0.20	3.92 ± 0.20	3.98 ± 0.14	$(1.67 \pm 0.34) \times 10^8$
***c*-P6**	25.0 ± 1.25	26.0 ± 1.30	25.5 ± 0.90	$(2.60 \pm 0.53) \times 10^7$
***c*-P8**	8.73 ± 0.66	8.23 ± 0.60	8.48 ± 0.45	$(7.82 \pm 1.60) \times 10^7$
***c*-P10**	5.16 ± 0.52	5.29 ± 0.53	5.23 ± 0.37	$(1.27 \pm 0.27) \times 10^8$
***c*-P12**	4.42 ± 0.44	4.55 ± 0.46	4.49 ± 0.32	$(1.48 \pm 0.31) \times 10^8$

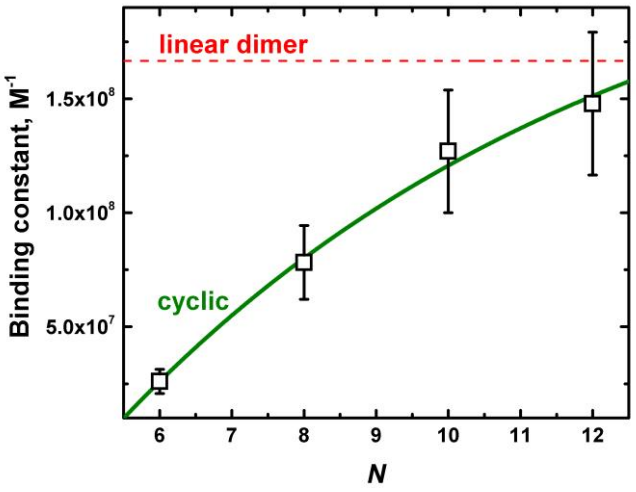

Figure 3.20 Comparison of the formation constants as a function of ring size. The red dash line is the level of binding constant of linear dimer-dimer complex. The green line is a guide for the eye.

Comparison of the binding constants of the various nanorings with **P2py2** reveals that K_f increases as the nanoring becomes larger. The binding constant of ***c*-P12** with **P2py2** is close to the affinity of the linear zinc porphyrin dimer **P2** for **P2py2** [$(1.7 \pm 0.3) \times 10^8$ M^{-1}], implying that each segment of ***c*-P12** behaves almost like a linear oligomer.

3.4.4 Calculation of strain energy

The strain energy, ΔG_{strain} of complex formation was estimated by comparing the stability of ***c*-P*N*·P2py2** with that of the unstrained dimer complex **P2·P2py2**, using **Equation 3.18**,

$$\Delta G_{strain} = \Delta G_{binding,\ \mathbf{P2}} - \Delta G_{binding,\ \textit{c}\text{-P}\textit{N}} \qquad \textbf{(eq. 3.18)}$$

where $\Delta G_{binding} = -RT \ln(K_f)$. The results, listed in **Table 3.3** and plotted against ring-size in **Figure 3.21**, show that ΔG_{strain} decreases with the size of the rings.

Table 3.3 Formation constants and binding strain of nanoring-dimer complexes[a]

porphyrin host	K_f, M^{-1}	ΔG_{strain}, kJ mol^{-1}
***l*-P2**	$(1.7 \pm 0.3) \times 10^8$	0
***c*-P6**	$(2.6 \pm 0.5) \times 10^7$	4.60 ± 0.71
***c*-P8**	$(7.8 \pm 1.6) \times 10^7$	1.87 ± 0.72
***c*-P10**	$(1.3 \pm 0.3) \times 10^8$	0.67 ± 0.73
***c*-P12**	$(1.5 \pm 0.3) \times 10^8$	0.30 ± 0.73

[a] Errors estimated from at least two replicates.

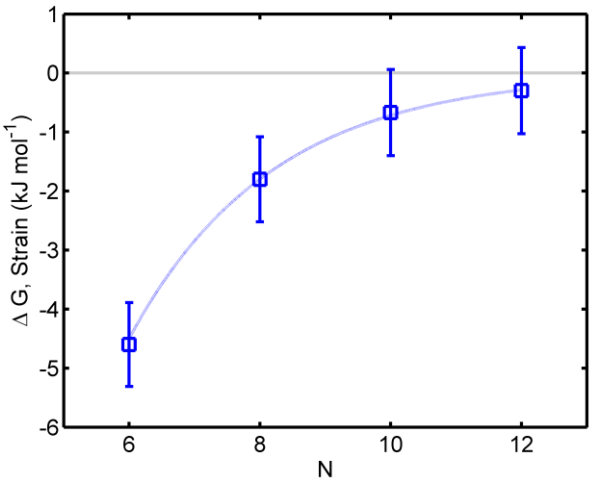

Figure 3.21 Calculated strain energy of ring-dimer complexes from binding constants as a function of the number of the porphyrin units *N*. The blue line is a guide to the eye.

The strain in the nanorings, and the increase in strain caused by binding **P2py2**, was analysed using molecular mechanics calculations. The geometries of all nanoring structures were calculated using the MM+ force field in HyperChem (**Figure 3.22**). The decrease in curvature as the rings become larger results in a change in distance between neighbouring zinc centers; the Zn-Zn distances are 12.1, 12.2, 12.4 and 12.5 Å for ***c*-P6**, ***c*-P8**, ***c*-P10** and ***c*-P12**, respectively. The structure of ***c*-P12** is the most flexible and its calculated Zn-Zn distance is close to that of the linear dimer **P2** (12.8 Å). The finding that only two **P2py2** dimer antenna units bind to the zinc porphyrin sites on ***c*-P6** raises the question of whether the dimers sit close (1,3) or opposite (1,4) to each other

on the 6-ring. Models of these complexes from molecular mechanics calculations (**Figure 3.23**) indicate that the geometry with the dimers further apart (1,4) is lower in energy.

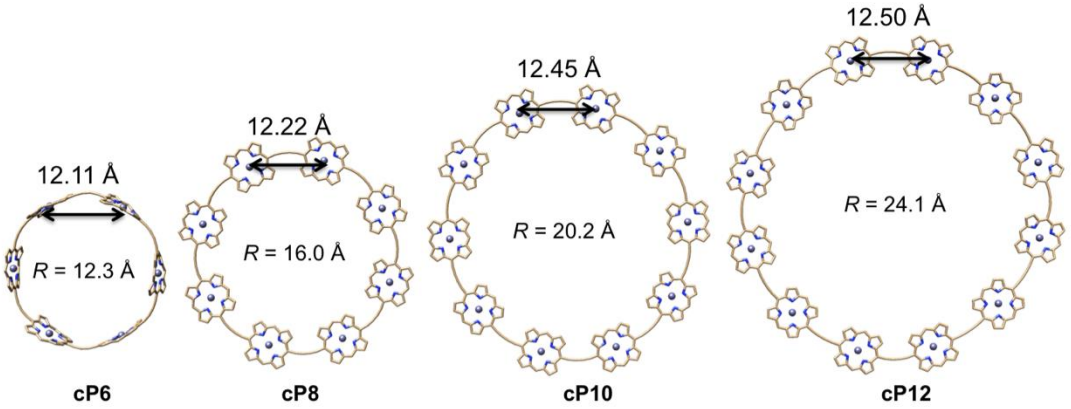

Figure 3.22 The models of ***c*-P*N*** from 6- to 12-rings are energy minimised geometries calculated using MM+ force field in HyperChem. R is the radius measured to Zn centres.

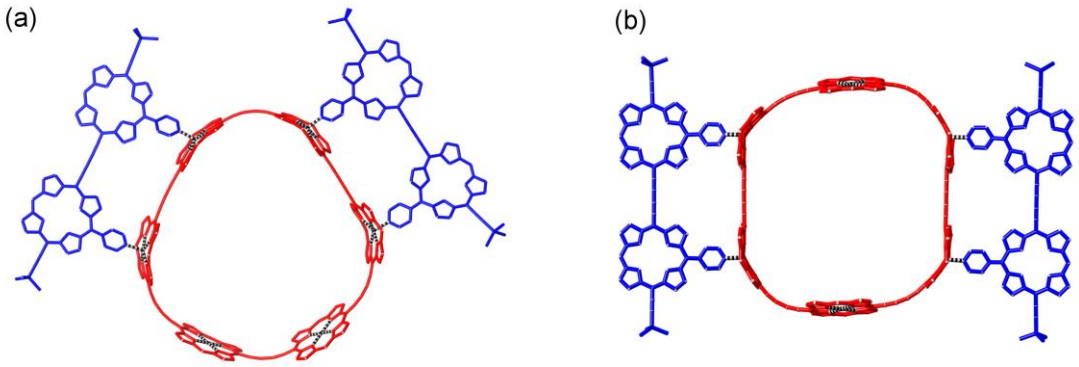

Figure 3.23 Geometries of two possible isomers of the 6-ring-dimer complex from molecular mechanics calculations (MM+ force field; HyperChem). (a) Close dimers-ring complex (1,4); (b) Opposite dimers-ring complex (1,3); the aryl groups and side chains were omitted to simplify the calculations.

3.5 Energy transfer study

This section was most carried out by Dr. Patrick Parkinson and Dr. Laura Herz (Department of Physics, University of Oxford).

Porphyrin nanorings generally show fully delocalization lengths for nanoring acceptors of between 6 and 12 units, resulting in a redshift in absorption with increasing nanoring size,[15] along with a reduction in radiative rate linked to a symmetry-forbidden ground state.[16] In the antenna-nanoring complex, one would expect this to cause a decrease in energy transfer rate within the Förster framework, because of the increased 'centre-of-mass' distance between the donor and acceptor states. However, we demonstrate here that, surprisingly, the non-covalent binding of an

antenna molecule instead leads to strain-induced localisation of the exciton state on the nanoring, resulting in energy transfer from the dimer antenna to the nanoring being independent of nanoring size.

3.5.1 Time-resolved photoluminescence

Upon photoexcitation of antennae in complexes of both natural[17] and synthetic systems,[18] energy transfer occurs to the nanoring with almost 100% efficiency, suggesting ultrafast quenching of the antenna emission resulting from energy transfer to the nanoring acceptor.

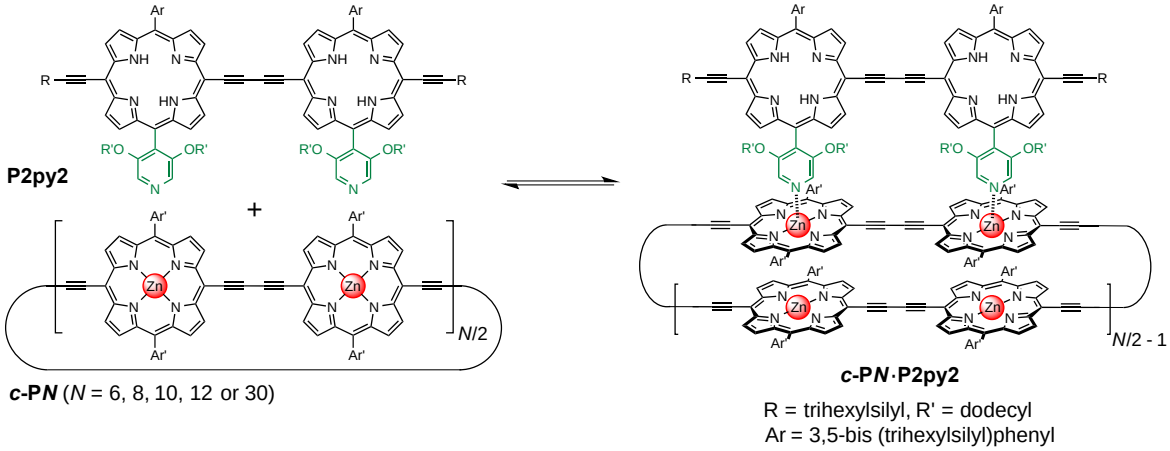

Figure 3.24 Formation of dimer-nanoring complexes from one **P2py2** bound per ***c*-P*N*** for energy transfer study.

We experimentally evaluate the energy transfer dynamics in complexes consisting of one porphyrin dimer (**P2py2**) bound per porphyrin nanoring (**Figure 3.24**), by monitoring the relative photoluminescence decay of the dimers, as described in the experimental section. The complexes were prepared at millimolar concentrations in toluene. The dimer was also displaced from the complex by the addition of an excess of pyridine (>1% *v*/*v*) to give a reference sample. **Figure 3.25** shows the photoluminescence ratio of the dimer between the assembled and disassembled states along with mono-exponential fits. The energy transfer rate for each complex is given in **Figure 3.25**; strikingly, there is no significant deviation from a $(1.3\ \text{ps})^{-1}$ transfer rate as the nanoring size is varied between 6 and 30 porphyrin units. A constant energy transfer rate as a function of acceptor size is unexpected in porphyrin nanoring systems, as the absorbing (initially generated) lowest lying excited state is thought to be highly delocalised for most of the studied molecules.[15]

Such delocalisation introduces an increasing spatial separation between the donor molecule and the 'centre-of-mass' of the exciton generated on the acceptor nanoring, reducing the coupling in the Förster resonance energy transfer framework.

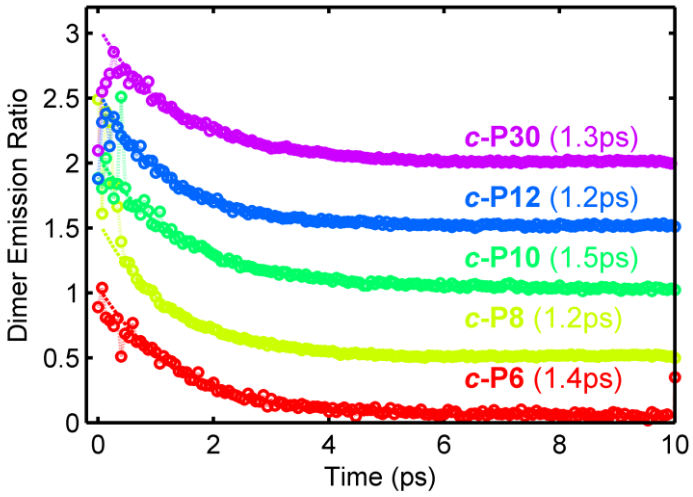

Figure 3.25 The ratio between the time-resolved dimer photoluminescence in the assembled and disassembled state isolating the dimer to nanoring energy transfer pathway is shown for the five nanoring sizes (circles; vertically offset for clarity). A mono-exponential fit (dashed line) is also shown, with the time constant for each complex given. An excitation wavelength of 627 nm was used.

The experimental result suggests that there is a preferred acceptor state that is essentially unchanging with nanoring size. Such constant energy transfer could arise from coupling to a localised absorbing state on the nanoring which would, however, have to be statically correlated with the antenna position. Uncorrelated localisation would lead to a reduction in transfer rate with nanoring size, as a randomly placed acceptor site would be further from the antenna (on average) for larger rings. It is therefore proposed that the attachment of an antenna dimer induces a localised acceptor state immediately below the attachment point. The formation of this state is therefore most likely directly related to the binding process itself.

3.5.2 Modelling energy transfer

While the importance of structural disorder on the energy transfer dynamics in conjugated molecules is well known, the specific influence of a small change – such as introducing an antenna molecule – is typically hard to assess. Here we present a sensitive probe of how the exciton state on the nanoring is influenced by associated structural changes that in turn impact on the energy

landscape. By combining ultrafast spectroscopy with associated modelling, we are able to link the observed energy dynamics with explicit models representing fundamentally different acceptor states.

We have demonstrated that there is no significant change in energy transfer rate with nanoring size, and that coupling to a donor dimer leads to non-negligible strain on the nanoring, with a local planarisation and suppression of torsional motion. To quantitatively assess the influence of localisation, strain and choice of absorbing states we have calculated the energy transfer rates in this system as a function of ring size for three different models as shown in **Figure 3.26**, as follows:

(1) Model 1 takes the standard Förster point-dipole approach, for which we assume an acceptor dipole to be situated at the centre of the nanoring and calculate the energy transfer rate using the traditional point-dipole model,[19]

(2) Model 2 assumes a fully delocalised (k =1, see the explanation of this delocalised state in **Chapter 1**) absorbing state on the nanoring, with the energy transfer between dimer and nanoring evaluated using the line-dipole model,[20] and

(3) Model 3 assumes an absorbing state of extent N_a localised below the dimer, with the energy transfer rate calculated using the line-dipole approach.

For Model 3, the effect of partial localisation of the absorbing state over N_a units of the ring below the donor dimer is considered. We use absorption spectra for a range of complementary porphyrin oligomers on a suitable template to compute energy transfer rates that are then contrasted with the experimental data (see **Figures 3.26**). By use of the oligomer as a model, we find that a description of the localised distorted state extending over N_a = 6 units offers best match between experimental data and calculations for Model 3, suggesting that strain resulting from dimer attachment weakens the effective conjugation of the absorption state only to a certain extent.

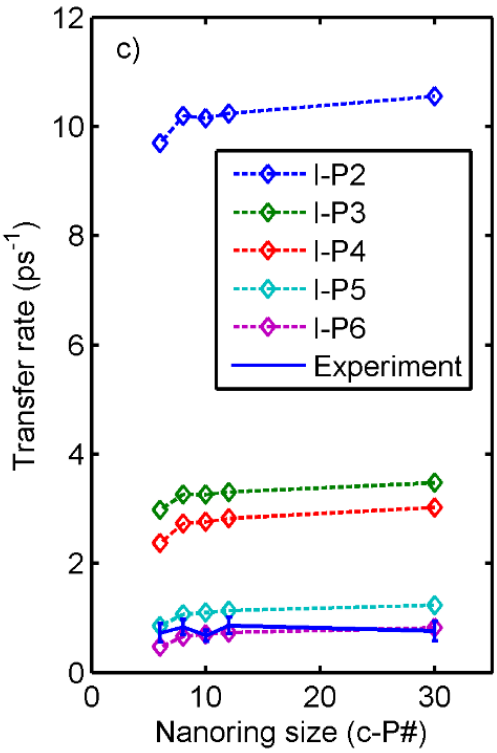

Figure 3.26 Calculation of overall transfer rate for different choices of acceptor state. The experimental results match most closely to energy transfer to a linear 6-porphyrin acceptor state, used for the modelling.

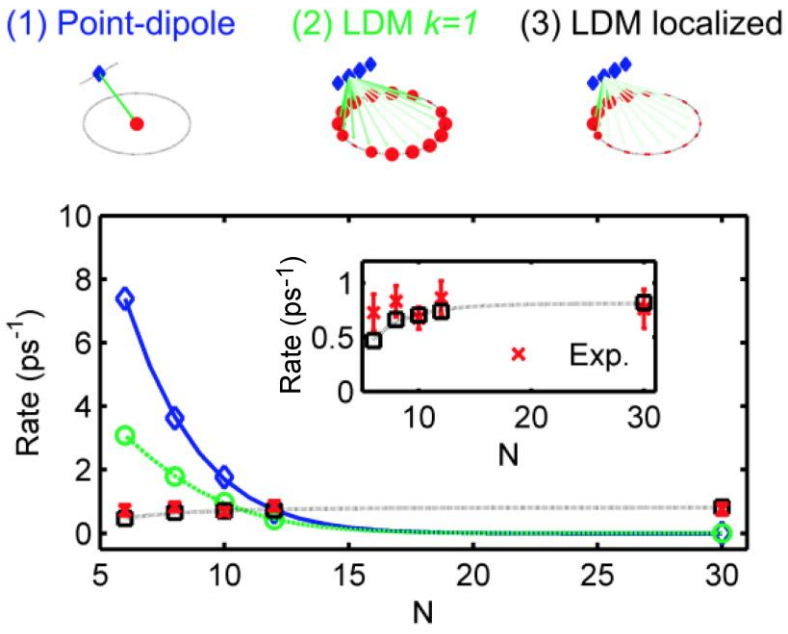

Figure 3.27 (Top) Schematic of three energy transfer models for the dimer ***c*-P8** system; (left) point-dipole model, (centre) line-dipole model with fully delocalised nanoring state and (right) line-dipole model with partially localised (N_a = 6) acceptor state. Arrows indicate sub-dipole coupling elements. (Bottom) Modelled data for energy transfer rate. The (1) point-dipole model is shown in blue, (2) line-dipole model in green and (3) localised dimer model in black. Experimental data is shown in red (bottom panel only). The inset shows the dimer model and experimental data only. All lines are guides to the eye.

Figure 3.26 shows the predicted energy transfer rate as a function of nanoring size from three models: Model 1 and 2 for full-nanoring absorbing state and Model 3 for localised absorbing state. It can be seen that Model 3 provides both a qualitative and quantitatively excellent agreement with the experimental data, strongly supporting the emergence of a localised state upon non-covalent binding of an antenna molecule. In particular, Model 3 is the only approach that mirrors the observed independence of energy transfer rates on ring size.

The origin of the emergence of a localised state can be related to two effects; firstly, the strain applied during binding, and secondly, the local suppression of torsional motion. Deviation from perfect circular shape is known to create localised states[16] due to backbone distortion. Torsional motion has also been related as a key driver towards disorder and (de-)localisation in a number of conjugated systems.[21,22] These features are highly relevant, as in the assembled dimer-nanoring complexes the torsional angle between the two bound porphyrins is locked, which often generates a higher conjugation, localised state,[23] as experimentally shown for cyclic oligothiophene molecules with planarising linkers[24] and porphyrin dimers.[25] It is logical therefore, that the non-covalent addition of an antenna molecule onto a nanoring structure induces significant strain, resulting in the distortion of the energetic environment and the emergence of localised states. The use of strain in the synthetic nanoring systems presented here provides a new tool to control local exciton states in multi-chromophoric complexes.

3.6 Summary

We present the energy transfer in a family of synthetic porphyrin light-harvesting complexes reminiscent of the natural LH2 antenna systems. Our ability to vary the ring size five-fold between 6 and 30 porphyrin units has enabled validity tests of energy transfer models. We were able to explore the effect of strain resulting from donor binding to the porphyrin nanorings via a study of binding affinities. Binding constants were shown to increase significantly with the size of the ring, consistent with host distortion and strain effect decreasing from the rigid 6-ring to the more flexible 12-ring. Our subsequent investigation shows that such strain also has significant impact on the energy transfer rates in the assembled systems. Upon varying the size of the nanoring from 6 to

30 porphyrin units, no change in energy transfer rate between the attached dimer and the nanoring was observed. These experimental results indicate that the absorbing state is independent of nanoring size, acting as a localised state centred below the antenna molecule. Simulation of energy transfer rates qualitatively and quantitatively agrees with the existence of a localised acceptor state limited to approximately 6 porphyrin units. Our work highlights an approach to exploit strain in large conjugated materials, to create efficient, size-independent synthetic energy funnelling for light-harvesting applications.

3.7 Experimental section

3.7.1 General methods

All chemicals were purchased from commercial suppliers and used without further purification unless otherwise stated. Dry toluene, THF, chloroform and CH_2Cl_2 were obtained by passing through a column of activated alumina under nitrogen pressure. Diisopropylamine (DIPA) was dried over calcium hydride, distilled and stored under nitrogen over molecular sieves (3 Å, 8–12 mesh). All manipulations of oxygen- or water-sensitive compounds were performed using standard high-vacuum techniques. Size exclusion chromatography was carried out on Biobeads SX1 (cross-linked polystyrene) under gravity elution. "Petrol ether" (PE) always refers to 40/60 petrol ether.

^{1}H and ^{13}C NMR spectra were recorded on a Bruker Avance 400 (400.13 and 100.64 MHz), a Bruker DQX 400 (400.13 and 100.64 MHz), a Bruker DRX 500 and Bruker Avance II 500 (500.13 and 125.77 MHz) at 298 K unless otherwise stated. TopSpin (Version 3.1) and Spinworks were used. Chemical shifts (δ in ppm) are referenced to solvent residual peaks ($CDCl_3$ at δ_H 7.26, δ_C 77.16 and toluene-d_8 at δ_H 2.08, 6.97, 7.01 and 7.09). Abbreviations for ^{1}H NMR data: s = singlet, d = doublet, t = triplet, *m* = multiplet, "t" = pseudo triplet, br = broad. Abbreviations for ^{13}C-DEPTQ-NMR data: u = up (CH_3 or CH), d = down (CH_2 or Cq).

MALDI-TOF-MS was measured with a Waters MALDI Micro MX spectrometer. *Trans*-2-[3-(4-tert-butylphenyl)-2-methyl-2-propenylidene]malononitrile (DTCB) was used as a matrix for all

MALDI-TOF measurements.

All UV-vis-NIR spectra were recorded at 25 °C on a Perkin-Elmer Lambda 25 photospectrometer using quartz 1 cm cuvettes. The concentration was calculated using the known extinction coefficient of the oligomer. For denaturation titrations, the volume of the ligand required was calculated and added to the cuvette. To this solution, aliquots of a stock solution of pyridine were added. The titrations were performed at a constant temperature of 25 °C, controlled by a thermostat. The curve fitting was carried out using Origin 8.5.1.

3.7.2 Synthetic procedures

3.7.2.1 Synthesis of known compounds

The porphyrin nanorings were synthesised according to the established procedures using Pd/Cu catalysed-oxidative coupling of linear porphyrin oligomers with templates.[8–11]

3.7.2.2 Synthesis of free-base dipyridyl-substituted porphyrin dimer (**P2py2**)

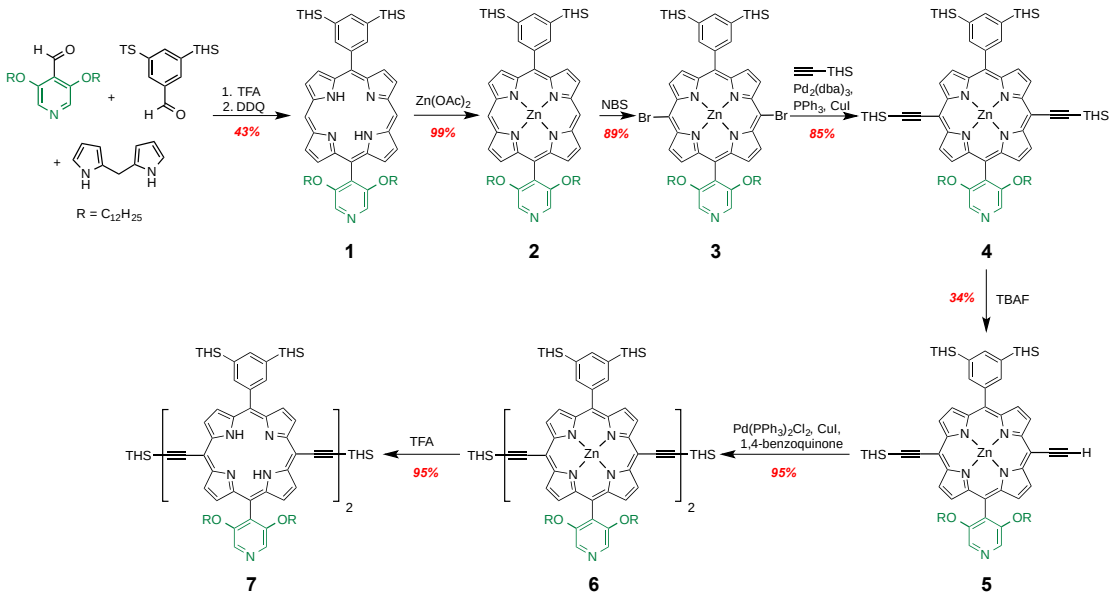

Scheme 3.2 Overview of the synthesis of free-base dipyridyl-substituted porphyrin dimer **P2py2**. THS = $Si(C_6H_{13})_3$ and R = *n*-$C_{12}H_{25}$. The starting aldehydes, 3,5-bis(trihexylsilyl)benzaldehyde and 3,5-bis-(dodecyloxy)isonicotinaldehyde, were synthesised according to references[26,27,28].

5-(3,5-Bis(dodecyloxy)-4-pyridyl)-15-(3,5-bis(trihexylsilyl)phenyl)-porphyrin **1**

In a 3 L round-bottom-flask, equipped with a stir bar DCM (1900 mL) (freshly opened bottle) was placed. The flask was sealed with a subaseal and evacuated down to 1 mbar followed by backfilling with nitrogen three times. Light was excluded by wrapping the flask with aluminium foil. 3,5-Bis-(dodecyloxy)isonicotinaldehyde (4.34 g, 9.12 mmol), 3,5-bis-(trihexylsilyl)benzaldehyde (3.10 g, 4.56 mmol) and dipyrrolemethane (2.0 g, 13.68 mmol) were added. The mixture was degassed again as described above. Trifluoroacetic acid (2.20 mL, 28.3 mmol) was added slowly over 5 min under vigorous stirring. The reaction mixture was stirred for 3 h. DDQ (4.66 g, 20.5 mmol) was added and stirring continued for 40 min. Triethylamine (11.4 mL, 82.1 mmol) was added and stirring continued for 30 min. The volume was reduced and the resulting dark solution filtered over a plug of silica eluting with DCM/MeOH (98:2). The solvent was removed from the dark filtrate. The dark residue was dissolved in DCM/MeOH (99:1) and purified by column chromatography (silica, eluent: DCM), resulting in two fractions. The second fraction was collected that contained the desired product. After removal of solvent, this fraction was dissolved in chloroform and precipitated with MeOH, producing compound **1** in the form of a purple oil (2.75 g, 43%).

TLC: R_f (DCM) = 0.31; ^{1}H-NMR (500 MHz, $CDCl_3$): δ = 10.24 (s, 2H, *meso*-H), 9.33 (d, $^3J_{HH}$ = 4.6 Hz, 2H, β-H), 9.31 (d, $^3J_{HH}$ = 4.5 Hz, 2H, β-H), 9.04 (d, $^3J_{HH}$ = 4.6 Hz, 2H, β-H), 8.91 (d, $^3J_{HH}$ = 4.5 Hz, 2H, β-H), 8.50 (s, 2H, py-H), 8.31 (s, 2H, *o*-H), 7.99 (s, 1H, *p*-H), 3.94 (t, $^3J_{HH}$ = 6.3 Hz, 4H, OCH_2), 1.53-1.44 (m, 12H, CH_2), 1.40-0.70 (m, 96H, CH_2 and CH_3), 0.62-0.54 (m, 4H, CH_2), 0.52-0.34 (m, 12H, CH_2), -3.04 (s, 1H, N*H*), -3.07 (s, 1H, N*H*); ^{13}C{^{1}H}-NMR (125 MHz, $CDCl_3$): δ = 155.6 (2C, py-C), 146.9 (4C, α-C), 145.2 (4C, α-C), 140.9 (2C, *o*-C), 139.5 (1C, *ipso*-C), 139.2 (1C, *p*-C), 135.2 (2C, *m*-C), 131.8 (2C, β-C), 131.1 (2C, β-C), 131.0 (2C, β-C), 130.0 (2C, β-C), 129.1 (2C, py-C), 127.1 (1C, py-C), 120.9 (1C, *meso*-C), 107.6 (1C, *meso*-C), 104.8 (2C, *meso*-C), 69.6 (2C, OCH_2), 33.5 (6C, CH_2), 31.8 (2C, CH_2), 31.6 (6C, CH_2), 29.3 (2C, CH_2), 29.2 (2C, CH_2), 29.1 (2C, CH_2), 29.0 (2C, CH_2), 28.9 (2C, CH_2), 28.5 (2C, CH_2), 28.5 (2C, CH_2), 25.1 (2C, CH_2), 24.0 (6C, CH_2), 22.6 (6C, CH_2), 22.6 (2C, CH_2), 14.1 (6C, CH_3), 14.1 (2C, CH_3), 12.7 (6C, CH_2).

[5-(3,5-Bis(dodecyloxy)-4-pyridyl)-15-(3,5-bis(trihexylsilyl)-phenyl)-porphyrinato]zinc(II) **2**

A solution of zinc acetate-dihydrate (1.77 g, 9.66 mmol) in MeOH (18.0 mL) was added into a solution of porphyrin **1** (2.75 g, 1.96 mmol) in $CHCl_3$ (140 mL). The mixture was stirred at 40 °C for 2 h then filtered over a plug of silica, eluting with DCM/pyridine (99:1). The solvent was removed from the pink filtrate and the residue was dried in high vacuum, yielding the desired product **2** (2.84 g, 99%) in the form of a pink, sticky solid.

^{1}H-NMR (500 MHz, $CDCl_3$+1% pyridine-d_5): δ = 10.08 (s, 2H, *meso*-H), 9.28 (d, $^3J_{HH}$ = 4.4 Hz, 2H, β-H), 9.25 (d, $^3J_{HH}$ = 4.5 Hz, 2H, β-H), 9.02 (d, $^3J_{HH}$ = 4.4 Hz, 2H, β-H), 8.89 (d, $^3J_{HH}$ = 4.4 Hz, 2H, β-H), 8.45 (s, 2H, py-H), 8.30 (s, 2H, *o*-H), 7.95 (s, 1H, *p*-H), 3.86 (t, $^3J_{HH}$ = 6.4 Hz, 4H, OCH_2), 1.51-1.42 (m, 12H, CH_2), 1.38-0.77 (m, 96H, CH_2 and CH_3), 0.71- 0.63 (m, 4H, CH_2), 0.48-0.43 (m, 8H, CH_2), 0.36-0.27 (m, 4H, CH_2); ^{13}C-deptQ-NMR (125 MHz, $CDCl_3$+1% pyridine-d_5): δ = (not all C detected) 155.8 (d, 2C, py-C), 149.8 (d, 2C, α-C), 149.2 (d, 2C, α-C), 140.9 (u, 2C, *o*-C), 138.6 (u, 1C, *p*-C), 134.4 (d, 2C, *m*-C), 132.1 (u, 2C, β-C), 131.8 (u, 2C, β-C), 130.9 (u, 2C, β-C), 130.9 (u, 2C, β-C), 129.1 (u, 2C, py-C), 120.9 (d, 1C, *meso*-C), 107.5 (d, 1C, *meso*-C), 105.3 (u, 2C, *meso*-C), 69.4 (d, 2C, OCH_2), 33.5 (d, 6C, CH_2), 31.8 (d, 2C, CH_2), 31.6 (d, 6C, CH_2), 29.4 (d, 2C, CH_2), 29.4 (d, 2C, CH_2), 29.2 (d, 2C, CH_2), 29.1 (d, 2C, CH_2), 29.0 (d, 2C, CH_2), 28.6 (d, 2C, CH_2), 28.5 (d, 2C, CH_2), 25.0 (d, 2C, CH_2), 24.0 (d, 6C, CH_2), 22.6 (d, 6C, CH_2), 14.1 (u, 6C, CH_3), 14.1 (u, 2C, CH_3), 12.7 (d, 6C, CH_2); *m/z* (MALDI-TOF): 1460.39 ($C_{91}H_{143}N_5O_2Si_2Zn$ requires 1461.02).

[5,15-Dibromo-10-(3,5-bis(dodecyloxy)-4-pyridyl)-20-(3,5-bis(trihexylsilyl)-phenyl)-porphyrinato]zinc(II) **3**

A solution of *N*-bromosuccinimide (NBS) (0.69 g, 3.89 mmol) in chloroform (180 mL) was added dropwise over 10 min to a stirred solution of zinc porphyrin **2** (2.84 g, 1.94 mmol) in pyridine (1.25 mL) and chloroform (70.0 mL). The reaction mixture was stirred at room temperature for 15 min before adding acetone (2 mL) to quench any excess NBS. The solution was concentrated and passed through a short silica plug, eluting with DCM/pyridine (99:1). The solvent was removed from the green filtrate. The green residue was dissolved in chloroform and

precipitated by layering methanol. The precipitate was washed with methanol and dried in high vacuum, affording the desired porphyrin **3** (2.80 g, 89%) in the form of purple highly viscous oil. ^{1}H-NMR (500 MHz, $CDCl_3$+1% pyridine-d_5): δ = 9.58 (d, $^{3}J_{HH}$ = 4.6 Hz, 2H, β-H), 9.55 (d, $^{3}J_{HH}$ = 4.6 Hz, 2H, β-H), 8.81 (d, $^{3}J_{HH}$ = 4.6 Hz, 2H, β-H), 8.70 (d, $^{3}J_{HH}$ = 4.7 Hz, 2H, β-H), 8.36 (s, 2H, py-H), 8.18 (s, 2H, *o*-H), 7.95 (s, *p*-H), 3.88 (t, $^{3}J_{HH}$ = 6.3 Hz, 4H, OCH_2), 1.49- 1.41 (m, 12H, CH_2), 1.37-0.76 (m, 96H, CH_2 and CH_3), 0.72-0.64 (m, 4H, CH_2), 0.53-0.44 (m, 8H, CH_2), 0.39-0.29 (m, 4H, CH_2); ^{13}C-deptQ-NMR (125 MHz, $CDCl_3$+1% pyridine-d_5): δ = 155.5 (d, 2C, py-C), 150.6 (d, 2C, α-C), 150.4 (d, 2C, α-C), 149.9 (d, 4C, α-C), 140.8 (d, 1C, *ipso*-C), 140.6 (u, 2C, *o*-C), 139.0 (u, 1C, *p*-C), 134.6 (d, 2C, *m*-C), 133.3 (u, 2C, β-C), 133.2 (u, 2C, β-C), 132.4 (u, 2C, β-C), 132.0 (u, 2C, β-C), 128.7 (u, 2C, py-C), 128.5 (d, 1C, py-C), 123.7 (d, 1C, *meso*-C), 110.1 (d, 1C, *meso*-C), 104.3 (d, 2C, *meso*-C), 69.3 (d, 2C, OCH_2), 33.5 (d, 6C, CH_2), 31.8 (d, 2C, CH_2), 31.6 (d, 6C, CH_2), 29.4 (d, 2C, CH_2), 29.3 (d, 2C, CH_2), 29.2 (d, 2C, CH_2), 29.2 (d, 2C, CH_2), 29.0 (d, 2C, CH_2), 28.7 (d, 2C, CH_2), 28.6 (d, 2C, CH_2), 25.1 (d, 2C, CH_2), 24.0 (d, 6C, CH_2), 22.6 (d, 6C, CH_2), 22.6 (d, 2C, CH_2), 14.1 (u, 6C, CH_3), 14.1 (u, 2C, CH_3), 12.6 (d, 6C, CH_2).

[5-(3,5-Bis(dodecyloxy)-4-pyridyl)-15-(3,5-bis(trihexylsilyl)-phenyl)-10,20-(trihexylsilylethynyl)-porphyrinato]zinc(II) **4**

Dibromoporphyrin **3** (2.80 g, 1.73 mmol, 1.0 equiv.), $Pd_2(dba)_3$ (155.7 mg, 0.17 mmol, 10 mol%), PPh_3 (136.4 mg, 0.52 mmol, 30 mol%) and CuI (99.0 mg, 0.52 mmol, 30 mol%) were placed in a heat-dried 2-neck 500 mL round-bottom-flask equipped with a tap and a stir bar. The second opening was sealed with a subaseal and the flask was evacuated and backfilled with nitrogen three times. In a heat-dried 2-neck round-bottom-flask with nitrogen inlet and septum, dry toluene (150 mL), dry diisopropylamine (180 mL) and THS-acetylene (1.35 mL, 5.19 mmol, 3.0 equiv.) were freeze-pump-thaw degassed. The solution was cannulated to the solids. The reaction mixture was heated under nitrogen to 50 °C and kept at this temperature for 2 h then filtered over a plug of silica eluting with DCM/pyridine (99:1). The solvents were removed from the green filtrate under reduced pressure. The residue was subjected to column-chromatography on silica eluting

with petrol ether/EtOAc/pyridine (10:0.5:1). Purification afforded the desired product **4** (3.06 g, 85 %).

^{1}H-NMR (400 MHz, $CDCl_3$+1% pyridine-d_5): δ = 9.59 (d, $^{3}J_{HH}$ = 4.0 Hz, 2H, β-H), 9.57 (d, $^{3}J_{HH}$ = 4.0 Hz, 2H, β-H), 8.79 (d, $^{3}J_{HH}$ = 4.0 Hz, 2H, β-H), 8.56 (d, $^{3}J_{HH}$ = 4.0 Hz, 2H, β-H), 8.47 (s, 2H, py-H), 8.21 (s, 2H, *o*-H), 7.96 (s, 1H, *p*-H), 3.90 (t, $^{3}J_{HH}$ = 6.4 Hz, 4H, OCH_2), 1.77–1.69 (m, 12H, alkyl-CH_2), 1.55–1.44 (m, 24H, alkyl- CH_2), 1.41–0.76 (m, 48H, alkyl-CH_2) 0.70–0.63 (m, 6H, alkyl-CH_3), 0.50–0.40 (m, 12H, alkyl-CH_3); ^{13}C-deptQ-NMR (125 MHz, $CDCl_3$+1% pyridine-d_5): δ = 155.7 (d, 2C, py-C), 152.3 (d, 2C, α-C), 152.1 (d, 2C, α-C), 150.0 (d, 2C, α-C), 149.7 (d, 2C, α-C), 141.0 (d, 1C, *ipso*-C), 140.4 (u, 2C, *o*-C), 139.0 (u, 1C, *p*-C), 134.5 (d, 2C, *m*-C), 132.4 (u, 2C, β-C), 131.5 (u, 2C, β-C), 131.1 (u, 2C, β-C), 130.6 (u, 2C, β-C), 129.0 (u, 2C, py-C), 128.9 (d, 1C, py-C), 124.0 (d, 1C, *meso*-C), 110.7 (d, 1C, *meso*-C), 109.5 (d, 2C, alkynyl-C), 100.6 (d, 2C, *meso*-C), 98.7 (d, 2C, alkynyl-C), 69.6 (d, 2C, OCH_2), 33.5 (d, 6C, CH_2), 33.4 (d, 6C, CH_2), 31.8 (d, 2C, CH_2), 31.7 (d, 6C, CH_2), 31.6 (d, 6C, CH_2), 29.4 (d, 2C, CH_2), 29.2 (d, 2C, CH_2), 29.2 (d, 2C, CH_2), 29.1 (d, 2C, CH_2), 28.9 (d, 2C, CH_2), 28.7 (d, 2C, CH_2), 28.6 (d, 2C, CH_2), 25.1 (d, 2C, CH_2), 24.4 (d, 6C, CH_2), 24.0(d, 6C, CH_2), 22.7 (d, 6C, CH_2), 22.6 (d, 2C, CH_2), 14.2 (u, 6C, CH_3), 14.2 (u, 6C, CH_3), 14.1 (u, 2C, CH_3), 13.9 (d, 6C, CH_2-Si), 12.7 (d, 6C, CH_2-Si); *m/z* (MALDI-TOF): 2071.90 ($C_{131}H_{219}N_5O_2Si_4Zn$ requires 2070.56).

[5-(3,5-Bis(dodecyloxy)-4-pyridyl)-10-ethinyl-15-(3,5-bis(trihexylsilyl)-phenyl)-20-(trihexylsilylethynyl)-porphyrinato]zinc(II) **5**

Porphyrin monomer **4** (3.0 g, 1.48 mmol, 1.0 equiv.) was dissolved in dry DCM (40 mL) and $CHCl_3$ (40 mL). Pyridine (4.0 mL) was added. Under stirring TBAF solution (1.0 M in THF; 1.03 mL, 1.03 mmol, 0.7 equiv.) was added dropwise. The reaction was monitored by TLC. After 20 min a good product ratio was reached. The mixture was filtered over a plug of silica eluting with DCM/pyridine (50:1). The solvent was removed from the green filtrate and the residue was subjected to column-chromatography on silica eluting with petrol ether/EtOAc/pyridine 20:2:1. Recovered starting material porphyrin monomer **4** (1.74 g, 57%), desired product **5** (893 mg, 34%),

and fully deprotected material (156.2 mg, 27%) were isolated in form of their pyridyl-complexes as dark purple semi-solids.

^{1}H-NMR (400 MHz, $CDCl_3$+1% pyridine-d_5): δ = 9.59 (m, 4H, β-H), 8.82 (t, $^{3}J_{HH}$ = 4.0 Hz, 2H, β-H), 8.71 (t, $^{3}J_{HH}$ = 4.4 Hz, 2H, β-H), 8.45 (s, 2H, py-H), 8.21 (s, 2H, *o*-H), 7.95 (s, 1H, *p*-H), 4.06 (s, 1H, ethynyl-H), 3.90 (t, $^{3}J_{HH}$ = 6.4 Hz, 4H, OCH_2), 1.77–1.69 (m, 6H, alkyl-CH_2), 1.53–0.37 (m, 83H, alkyl-CH_3); *m/z* (MALDI-TOF): 1790.29 ($C_{113}H_{181}N_5O_2Si_3Zn$ requires 1788.28).

Dimerisation of [5-(3,5-bis(dodecyloxy)-4-pyridyl)-10-ethinyl-15-(3,5-bis(trihexylsilyl)-phenyl)-20-(trihexylsilylethynyl)-porphyrinato]zinc(II) (synthesis of dimer **6**, **P2py2-Zn**)

$Pd(PPh_3)_2Cl_2$ (28.1 mg, 0.04 mmol, 8.0 mol%), copper(I) iodide (45.0 mg, 0.32 mmol, 0.65 equiv.) and 1,4-benzoquinone (102.7 mg, 0.95 mmol, 1.90 equiv.) were dissolved in dry toluene (50 mL) and dry DIPA (15 mL) at 20 °C. The yellow solution was added to monodeprotected-porphyrin **5** (893.0 mg, 0.5 mmol, 1.0 equiv.). The reaction mixture was stirred at 20 °C for 2 h then filtered over a plug of silica eluting with DCM/pyridine (99:1). Solvents were removed from the filtrate under reduced pressure and then the residue was purified by SEC-column chromatography, affording the desired dimer **6** in 95% yield (848.2 mg).

^{1}H-NMR (400 MHz, $CDCl_3$+1% pyridine-d_5): δ = 9.81 (d, *J* = 4.5 Hz, 2H, β-H), 9.78 (d, *J* = 4.5 Hz, 2H, β-H), 9.61 (d, *J* = 4.5 Hz, 2H, β-H), 9.58 (d, *J* = 4.5 Hz, 2H, β-H), 8.90 (d, *J* = 4.5 Hz, 2H, β-H), 8.81 (d, *J* = 4.5 Hz, 2H, β-H), 8.79 (d, *J* = 4.5 Hz, 2H, β-H), 8.71 (d, *J* = 4.5 Hz, 2H, β-H), 8.49 (s, 4H, py-H), 8.25 (s, 4H, *o*-H), 7.98 (s, 2H, *p*-H), 3.95 (t, *J* = 6.3 Hz, 8H, OCH_2), 1.77–1.69 (m, 12H, alkyl-H), 1.55–1.24 (m, 150H, alkyl-H), 1.00–0.45 (m, 230H, alkyl-H).; ^{13}C-deptQ-NMR (125 MHz, $CDCl_3$+1% pyridine-d_5): δ = 155.7 (d, 4C, py-C), 153.1 (d, 2C, α-C), 152.8 (d, 2C, α-C), 152.3 (d, 2C, α-C), 152.1 (d, 2C, α-C), 150.3 (d, 2C, α-C), 150.0 (d, 2C, α-C), 149.9 (d, 2C, α-C), 149.7 (d, 2C, α-C), 140.9 (d, 2C, *ipso*-C), 140.6 (u, 4C, *o*-C), 139.1 (u, 2C, *p*-C), 134.7 (d, 4C, *m*-C), 132.9 (u, 2C, β-C), 132.5 (u, 2C, β-C), 131.7 (u, 2C, β-C), 131.6 (u, 2C, β-C), 131.3 (u, 2C, β-C), 131.2 (u, 2C, β-C), 130.8 (u, 2C, β-C), 130.4 (u, 2C, β-C), 129.0 (u, 4C, py-C), 128.7 (d, 2C, py-C), 124.7 (d, 2C, *meso*-C), 111.4 (d, 2C, *meso*-C), 109.5 (d, 2C, alkynyl-C), 101.4 (d, 2C, *meso*-C), 99.3 (d, 4C, *meso*-C and alkynyl-C), 88.1 (d, 2C, alkynyl-C),

82.1 (d, 2C, alkynyl-C), 69.7 (d, 4C, O*C*H_2), 33.6 (d, 12C, *C*H_2), 33.4 (d, 6C, *C*H_2), 31.8 (d, 4C, *C*H_2), 31.7 (d, 6C, *C*H_2), 31.7 (d, 12C, *C*H_2), 29.5 (d, 4C, *C*H_2), 29.3 (d, 4C, *C*H_2), 29.2 (d, 4C, *C*H_2), 29.1 (d, 4C, *C*H_2), 28.8 (d, 4C, *C*H_2), 28.7 (d, 4C, *C*H_2), 25.2 (d, 4C, *C*H_2), 24.4 (d, 6C, *C*H_2), 24.1(d, 12C, *C*H_2), 22.8 (d, 6C, *C*H_2), 22.7 (d, 12C, *C*H_2), 22.6 (d, 4C, *C*H_2), 14.2 (u, 18C, *C*H_3), 14.1 (u, 4C, *C*H_3), 13.9 (d, 6C, *C*H_2-Si), 12.7 (d, 12C, *C*H_2-Si); *m/z* (MALDI-TOF): 3583.14 ($C_{226}H_{360}N_{10}O_4Si_6Zn_2$ requires 3580.55)

Demetallation of zinc dimer **P2py2-Zn 6** (synthesis of free-base dimer **7**, **P2py2**)

Zinc porphyrin dimer **6** (159.5 mg, 0.045 mmol, 1.0 equiv.) was dissolved in chloroform (50 mL). TFA (0.69 mL, 9.0 mmol, 200 equiv.) was added dropwise under stirring. After 10 min pyridine (6.0 mL) was added and the green mixture was directly filtered over a plug of silica eluting with chloroform. Solvents were removed from the filtrate under reduced pressure affording free-base dimer **7**, **P2py2** in 95% yield (145.3 mg).

^{1}H-NMR (400 MHz, $CDCl_3$): δ = 9.80 (t, *J* = 4.6 Hz, 4H, β-H), 9.59 (t, *J* = 4.6 Hz, 4H, β-H), 8.89 (d, *J* = 4.4 Hz, 2H, β-H), 8.81 (t, *J* = 3.4 Hz, 4H, β-H), 8.71 (d, *J* = 4.6 Hz, 2H, β-H), 8.53 (s, 4H, py-H), 8.28 (s, 4H, *o*-H), 8.02 (s, 2H, *p*-H), 4.02 (t, *J* = 6.3 Hz, 8H, OC*H*$_2$), 1.77–1.69 (m, 12H, alkyl-H), 1.57–1.26 (m, 150H, alkyl- H), 1.07–0.47 (m, 240H, alkyl-H), -1.82 (s, 4H, N*H*). ^{13}C-deptQ-NMR (125 MHz, $CDCl_3$): δ = 155.6 (d, 4C, py-C), 140.6 (u, 4C, *o*-C), 139.7 (u, 2C, *p*-C), 135.4 (d, 4C, *m*-C), 129.1 (u, 4C, py-C), 127.0 (d, 2C, py-C), 124.2 (d, 2C, *meso*-C), 111.3 (d, 2C, *meso*-C), 107.9 (d, 2C, alkynyl-C), 101.8 (d, 2C, *meso*-C), 101.5 (d, 2C, *meso*-C), 99.1 (d, 2C, alkynyl-C), 87.3 (d, 2C, alkynyl-C), 82.7 (d, 2C, alkynyl-C), 69.9 (d, 4C, O*C*H_2), 33.7 (d, 12C, *C*H_2), 33.5 (d, 6C, *C*H_2), 31.8 (d, 4C, *C*H_2), 31.8 (d, 6C, *C*H_2), 31.8 (d, 12C, *C*H_2), 29.4 (d, 4C, *C*H_2), 29.3 (d, 4C, *C*H_2), 29.2 (d, 4C, *C*H_2), 29.1 (d, 4C, *C*H_2), 29.0 (d, 4C, *C*H_2), 28.8 (d, 4C, *C*H_2), 28.7 (d, 4C, *C*H_2), 25.3 (d, 4C, *C*H_2), 24.5 (d, 6C, *C*H_2), 24.2(d, 12C, *C*H_2), 22.8 (d, 6C, *C*H_2), 22.8 (d, 12C, *C*H_2), 22.7 (d, 4C, *C*H_2), 14.3 (u, 18C, *C*H_3), 14.1 (u, 4C, *C*H_3), 13.9 (d, 6C, *C*H_2-Si), 12.8 (d, 12C, *C*H_2-Si); *m/z* (MALDI-TOF): 3455.99 ($C_{226}H_{364}N_{10}O_4Si_6$ requires 3453.73); UV/Vis: λ_{max} [nm] (ε/mol^{-1}Lcm^{-1}) (toluene) = 451 (3.35×10^5), 485 (1.47×10^5), 626 (6.45×10^4), 731 (8.77×10^4).

3.8 References

(1) McDermott, G.; Prince, S. M.; Freer, A. A.; Hawthornthwaite-Lawless, A. M.; Papiz, M. Z.; Cogdell, R. J.; Isaacs, N. W. *Nature* **1995**, *374*, 517–521.

(2) Choi, M. S.; Yamazaki, T.; Yamazaki, I.; Aida, T. *Angew. Chem.- Int. Ed.* **2004**, *43*, 150–158.

(3) Devadoss, C.; Bharathi, P.; Moore, J. S. *J. Am. Chem. Soc.* **1996**, *118*, 9635–9644.

(4) Tsuda, A.; Hu, H.; Tanaka, R.; Aida, T. *Angew. Chem.- Int. Ed.* **2005**, *44*, 4884–4888.

(5) Wilson, S. G.; Anderson, H. L. *Chem. Commun.* **1999**, 1539–1540.

(6) Aimi, J.; Nagamine, Y.; Tsuda, A.; Muranaka, A.; Uchiyama, M.; Aida, T. *Angew. Chem.- Int. Ed.* **2008**, *47*, 5153–5156.

(7) Aimi, J.; Oya, K.; Tsuda, A.; Aida, T. *Angew. Chem.- Int. Ed.* **2007**, *46*, 2031–2035.

(8) Hoffmann, M.; Wilson, C. J.; Odell, B.; Anderson, H. L. *Angew. Chem.-Int. Ed.* **2007**, *46*, 3122–3125.

(9) Hoffmann, M.; Kärnbratt, J.; Chang, M.; Herz, L. M.; Albinsson, B.; Anderson, H. L. *Angew. Chem.- Int. Ed.* **2008**, *120*, 5071–5074.

(10) O'Sullivan, M. C.; Sprafke, J. K.; Kondratuk, D. V; Rinfray, C.; Claridge, T. D. W.; Saywell, A.; Blunt, M. O.; O'Shea, J. N.; Beton, P. H.; Malfois, M.; Anderson, H. L. *Nature* **2011**, *469*, 72–75.

(11) Liu, S.; Kondratuk, D. V; Rousseaux, S. A. L.; Gil-Ramírez, G.; O'Sullivan, M. C.; Cremers, J.; Claridge, T. D. W.; Anderson, H. L. *Angew. Chem.- Int. Ed.* **2015**, *54*, 5355–5359.

(12) Job, P. *Ann. di Chim. Appl.* **1928**, *9*, 113–203.

(13) Hirose, K. *J. Incl. Phenom. Macrocycl. Chem.* **2001**, *39*, 193–209.

(14) Kondratuk, D. V; Perdigão, L. M. A.; Esmail, A. M. S.; O'Shea, J. N.; Beton, P. H.; Anderson, H. L. *Nat. Chem.* **2015**, *7*, 317–322.

(15) Parkinson, P.; Kondratuk, D. V; Menelaou, C.; Gong, J. Q.; Anderson, H. L.; Herz, L. M. *J. Phys. Chem. Lett.* **2014**, *5*, 4356–4361.

(16) Gong, J. Q.; Favereau, L.; Anderson, H. L.; Herz, L. M. *J. Phys. Chem. Lett.* **2016**, *7*, 332–338.

(17) Cogdell, R. J.; Gall, A.; Köhler, J. *Q. Rev. Biophys.* **2006**, *39*, 227–324.

(18) Parkinson, P.; Knappke, C. E. I.; Kamonsutthipaijit, N.; Sirithip, K.; Matichak, J. D.; Anderson, H. L.; Herz, L. M. *J. Am. Chem. Soc.* **2014**, *136*, 8217–8220.

(19) Forster, T. *Ann. Phys.* **1948**, *437*, 55.

(20) Beenken, W. J. D.; Pullerits, T. *J. Chem. Phys.* **2004**, *120*, 2490–2495.

(21) Parkinson, P.; Christian, M.; Stingelin, N.; Johnston, M. B.; Herz, L. M. *J. Phys. Chem. Lett.* **2010**, *1*, 2788–2792.

(22) Yang, J.; Ham, S.; Kim, T.-W.; Park, K. H.; Nakao, K.; Shimizu, H.; Iyoda, M.; Kim, D. *J. Phys. Chem. B* **2015**, *119*, 4116–4126.

(23) Tretiak, S.; Saxena, A.; Martin, R. L.; Bishop, A. R. *Phys. Rev. Lett.* **2002**, *89*, 097402/1–097402/4.

(24) Kim, W.; Sung, J.; Park, K. H.; Shimizu, H.; Imamura, M.; Han, M.; Sim, E.; Iyoda, M.; Kim, D. *J. Phys. Chem. Lett.* **2015**, *6*, 4444–4450.

(25) Camargo, F. V. A.; Anderson, H. L.; Meech, S. R.; Heisler, I. A. *J. Phys. Chem. B* **2015**, *119*, 14660–14667.

(26) Gaefke, G.; Höger, S. *Synthesis.* **2008**, *14*, 2155–2157.

(27) Kiriya, D.; Chang, H.-C.; Kitagawa, S. *J. Am. Chem. Soc.* **2008**, *130*, 5515–5522.

(28) Féau, C.; Klein, E.; Kerth, P.; Lebeau, L. *Synth. Commun.* **2010**, *40*, 3033–3045.

Chapter 4

Classical and Vernier Template-Directed Synthesis of Linear Oligomers

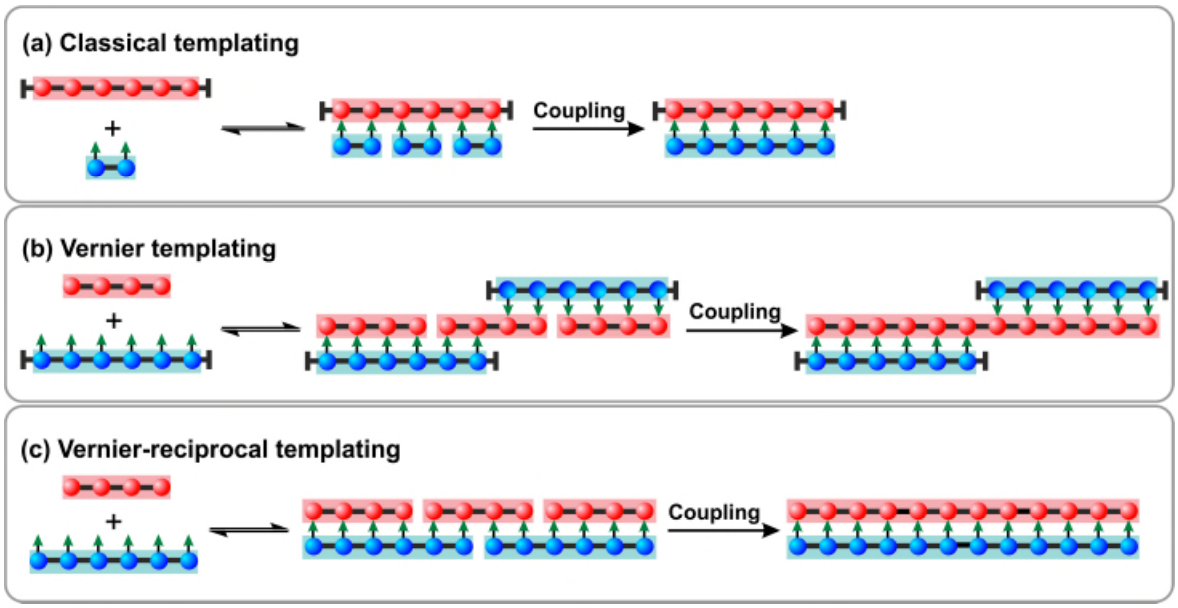

This chapter describes three different types of template-directed syntheses of linear porphyrin oligomers: classical, Vernier and Vernier-reciprocal templating. The classical templating reaction revealed strong template effects, providing good yields of desired products with the commensurate lengths of templates. The stabilities and cooperativities of related ladder structures were also investigated by UV-vis-NIR titration. After the promising results from this versatile method, it was adapted towards Vernier and Vernier-reciprocal templating reactions to produce non-commensurate length oligomer products from two simple components. The efficiency of the Vernier-reciprocal template effect is sufficient to produce two distinctive metalloporphyrin oligomers in comparable yields to cyclic Vernier templating, despite the fact that two approaches involve different intermediate structures.

4.1 Background information

Linear conjugated porphyrin oligomers with butadiyne linkages are of great interest for their potential applications in molecular electronics, photovoltaics and non-linear optics, owing to the unusual electronic and optical properties arising from their conjugated structures.[1–7] Moreover, increasing the length of porphyrin oligomers gives access to molecules with lower HOMO-LUMO gaps that are also excellent candidates for charge- and energy-transport over long distances.[5,6] However, the synthesis of long linear porphyrin oligomers requires a number of preparative steps and column chromatography. In this chapter, we first utilise classical templating to program the type and length of linear porphyrin oligomers of up to six porphyrin subunits with a template of commensurate length, via the formation of ladder complexes. This approach has limitations, since the synthesis of long templates becomes laborious. We propose a linear Vernier templating approach to overcome this problem in the synthesis of long porphyrin oligomers. The use of the Vernier principle in chemical self-assembly was first proposed in 1991; it exploits the mismatch between binding sites of two complementary components to bind each other until all binding sites are occupied.[8] The total number of binding sites in a Vernier assembly is the lowest common multiple of the number of binding sites in its components. Larger assemblies can be constructed from two simple, synthetically accessible components. This mechanism has been adopted in supramolecular chemistry, leading to the production of linear Vernier assemblies not only in non-covalent double[9] and triple strand approaches[10] but also dynamic covalent molecular ladders.[11] Synthetic DNA nanostructures were also length-programmed by Vernier assemblies.[12,13] Nevertheless, there have been no reports of subsequent ligation to connect the linearly arranged components of a Vernier complex into a covalent strand. Previous work in Oxford we demonstrated efficient cyclic Vernier templating using the non-commensurate combination of a hexapyridyl ligand template and a Zn porphyrin tetramer to synthesise a 12-unit porphyrin nanoring,[14,15] and also extended the same strategy to prepare rings of up to 50 porphyrin units.[16] Here, changing from cyclic to linear structures, we initially tested a linear Vernier templating reaction using the same number of binding sites as in the cyclic Vernier templating mentioned

above: a hexapyridyl Ni porphyrin hexamer template and a Zn tetramer substrate to produce a Zn porphyrin 12-mer. Then, Vernier-reciprocal templating was investigated using two simple substrates: Zn tetramer and hexapyridyl Ni hexamer, with no additional template, providing two different types of linear metalloporphyrin 12-mers as products.

The goal of this project is to control the synthesis of well-defined linear porphyrin oligomers by classical and Vernier templating. Our design, inspired by DNA replication, is based on the concept that the template carries the information of length and type of porphyrin and when the template is replicated into a complementary product, it passes this information on to the daughter porphyrin units.

4.2 Linear template-directed synthesis design

The templated synthesis of linear porphyrin oligomers is based on the homocoupling reaction of free acetylene functions at the ends of the substrate. Three types of linear templating reactions are highlighted in this chapter as shown in **Figure 4.1**.

a) *Classical templating:* A template binds to a complementary substrate to form a double strand complex. After coupling the porphyrin product will be commensurate with the template (**Figure 4.1a**).

b) *Vernier templating:* This templating strategy uses the mismatch between binding sites of substrate and template to direct the formation of the Vernier oligomer product with the lowest common multiple of the number of binding sites in both substrate and template (**Figure 4.1b**).

c) *Vernier-reciprocal templating:* Similar to above approach, but here we use two complementary substrates with the Vernier concept. Under the coupling condition, one strand can act as the Vernier-reciprocal template for the complementary strand to direct the Vernier product and the resulting Vernier product can then act as the template to promote the coupling of the complementary species. Finally, two types of Vernier products are obtained from both substrates (**Figure 4.1c**).

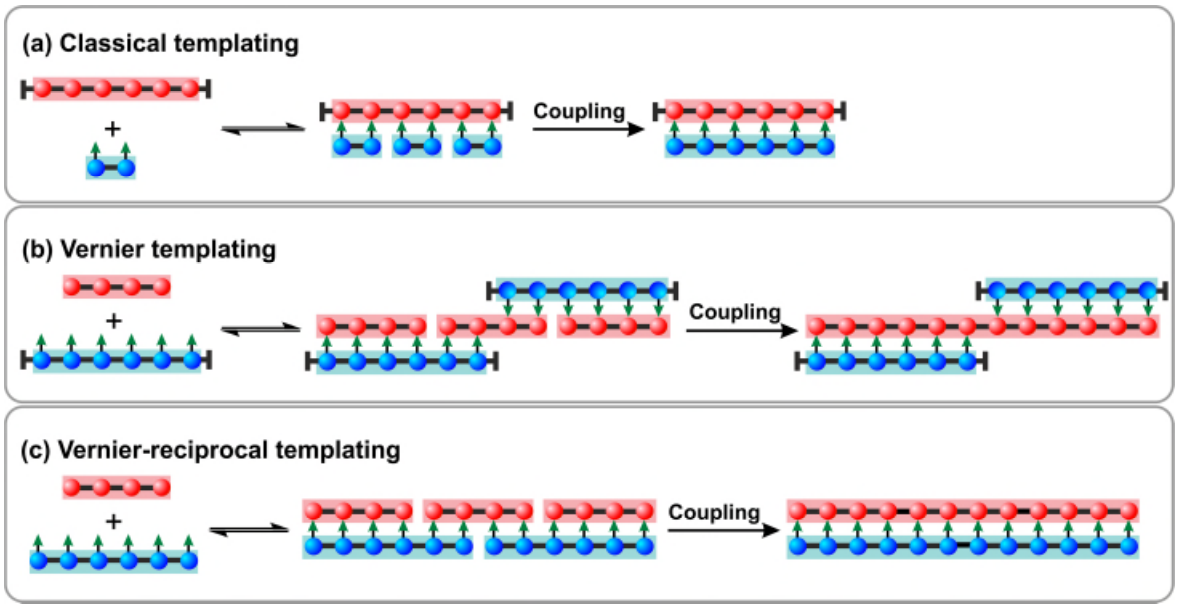

Figure 4.1 Linear template-directed syntheses of monodisperse linear porphyrin oligomers. (a) Example of the classical templating synthesis of linear oligomers which have commensurate lengths with the template. (b) Vernier templating synthesis of linear oligomers which are non-commensurate with templates. (c) Vernier-reciprocal templating synthesis of linear oligomers which are non-commensurate with two substrates.

Structural design. We used two types of complementary porphyrins as models: Zn porphyrins in which the metal can form pentacoordinate complexes on binding a nitrogen-based axial ligand such as pyridine, and for their counterpart, porphyrins bearing pyridyl substituents that can drive the self-assembly between zinc metal and pyridyl group to subsequently form ladder complexes (**Figure 4.2**). We use nickel as a blocking metal in the latter porphyrin units in order to avoid metal insertion from the coupling reagent during the coupling reaction. Tetracoordinate Ni is selected since it has a very low affinity for axial ligands.[17,18] For the template, either phenyl acetylene group (**PhA**), (3-cyanopropyl)diisopropylsilyl group (**CPDIPS**) or trihexylsilyl group (**THS**) were used as a capping group to avoid the polymerisation of the template under coupling conditions. The capping group **PhA** was used for linear tetramer templating and compared to the capping group **CPDIPS** only in the case of Zn tetramer template. **PhA** was also employed for Vernier templating synthesis. **CPDIPS** was also employed for the characterization of the ladder complexes and **THS** for linear hexamer templating synthesis. For the porphyrin substrate, a free acetylene at both ends of the porphyrin chain allows for the homocoupling of substrates within the substrate-template complexes to increase the length of the linear porphyrin oligomers.

Intermolecular reactions can also occur, but the intramolecular reaction (within a substrate-template complex) is expected to be faster because of the preorganised structure of the complex. Thus, mild reaction conditions are preferred to avoid intermolecular reactions and the formation of longer oligomers. Two different types of solubilizing groups, 3,5-bis(trihexylsilyl)phenyl and 3,5-bis(dodecyloxy)pyridyl substituents, on porphyrins were used to enhance solubility and to avoid aggregation. Details of the synthesis and characterization of these compounds are provided in the **Experimental section 4.9**.

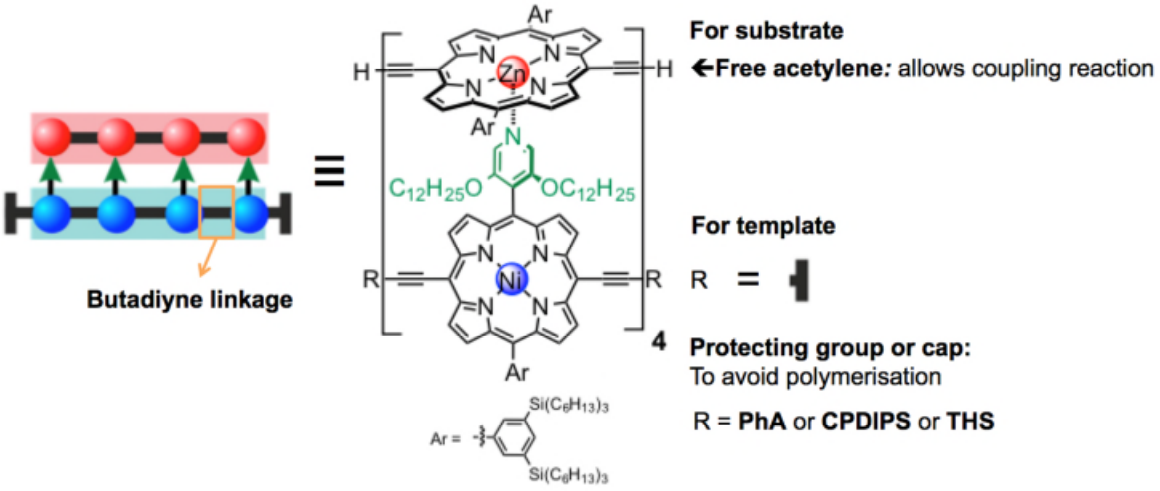

Figure 4.2 Molecular design for linear template-directed synthesis using two complementary porphyrin components. **PhA =** –C≡C–Ph, **CPDIPS** = $-Si^{i}Pr_2CH_2CH_2CH_2CN$ and **THS** = $-Si(C_6H_{13})_3$.

Coupling condition. Classical Glaser-Hay conditions employ CuCl and tetramethylethylenediamine (**TMEDA**) as coupling reagents for homocoupling reaction. The reaction proceeds in a dry air atmosphere in dry DCM at room temperature.[19–21] However, coordination of the nitrogen-containing ligand to the porphyrin could disrupt the formation of the porphyrin substrate-template complex. The UV-vis-NIR formation titration of Zn porphyrin monomer with **TMEDA** (**Figure 4.3-left**) revealed significant binding K_f (**TMEDA**) = (1.9 ± 0.2) × 10^4 M^{-1} which is almost as strong as the binding of pyridine to the Zn monomer, K_{py} = (2.8 ± 0.2) × 10^4 M^{-1} (see the binding constant of pyridine with the Zn monomer in **Section 4.4.3**). 2,2'-Bipyridine (**2,2'-BiPy**) is also known to act as a ligand in this reaction[20,21] and the titration shows it binds less strongly to zinc porphyrins, K_f (**2,2'-BiPy**) = 5.6 ± 0.3 M^{-1} because of a steric

clash between the porphyrin and the pyridyl substituent upon coordination (**Figure 4.3-right**). The use of **2,2'-BiPy** rather than **TMEDA** gives a larger template effect on coupling reactions; the CuCl and **TMEDA** reaction gives faster coupling but **TMEDA** binds to Zn-porphyrins four orders of magnitude more strongly than **2,2'BiPy**. Although the reaction is slower, the **2,2'-BiPy** ligand also facilitates coupling, and thus is chosen for this work.

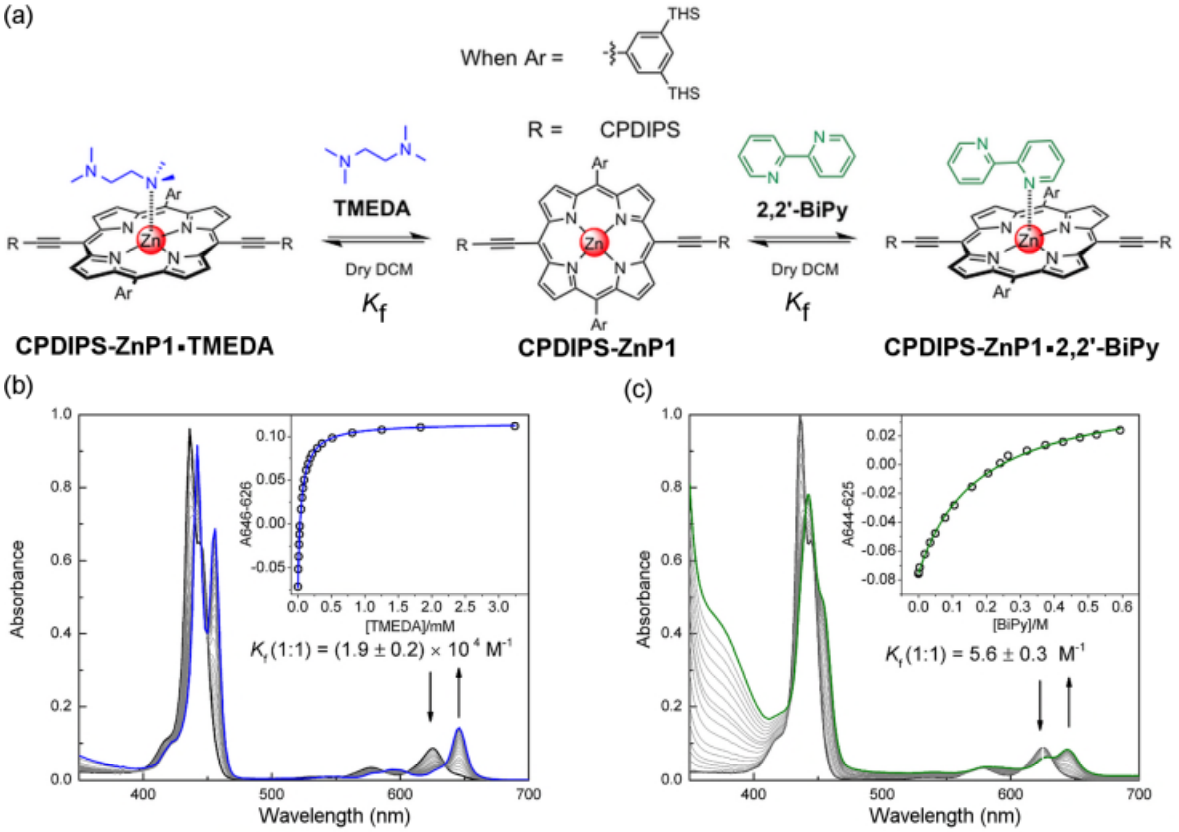

Figure 4.3 UV-vis-NIR formation titrations of **CPDIPS-ZnP1** ([**CPDIPS-ZnP1**] = 2.12 × 10^{-6} M) with two different amine bases: **TMEDA** and **2,2'-BiPy** in dry DCM at 298 K. (a) (left) Formation of **TMEDA** and Zn porphyrin monomer complex. (right) Formation of **2,2'-BiPy** and Zn porphyrin monomer complex. (b) Changes in absorption upon addition of **TMEDA**; (inset) binding isotherm (open dots) derived from the absorption data at λ = 646-626 nm and fit obtained from Origin® (blue line). R^2 = 0.9998. (c) Changes in absorption upon addition of **2,2'-BiPy**; (inset) binding isotherm (open dots) derived from the absorption data at λ = 644-625 nm and fit obtained from Origin® (green line). R^2 = 0.9987. Arrows indicate area of increasing and decreasing absorption during titration.

4.3 Classical template-directed synthesis

We demonstrated classical template-directed synthesis by using a porphyrin tetramer as a template and a porphyrin dimer as a substrate to direct the porphyrin product with commensurate length. Both Ni and Zn porphyrin tetramer templates were explored for tetramer templating

reactions. Linear templating was further investigated by extending the number of porphyrin units of the template up to six, as shown in more detail in the hexamer templating reaction.

4.3.1 Zn tetramer as the template for making Ni tetramer (2 × 2 = 4)

The **NiP2** dimer was used as a substrate, and **PhA-ZnP4** as a template. Initially, **NiP2** and **PhA-ZnP4** were mixed in a 2:1 ratio in dry DCM, and the solution was stirred at room temperature to allow the formation of the non-covalent ladder complex **$(NiP2)_2$•(PhA-ZnP4)**. UV-vis-NIR spectroscopy was used to confirm the formation of the complex (the formation of the double-strand complex was detected within 1 minute). Then the mixture was subjected to the CuCl/**2,2'-BiPy** Glaser-Hay coupling conditions. The non-templated control reaction was performed in a similar manner, but in the absence of the template (**Figure 4.4a**).

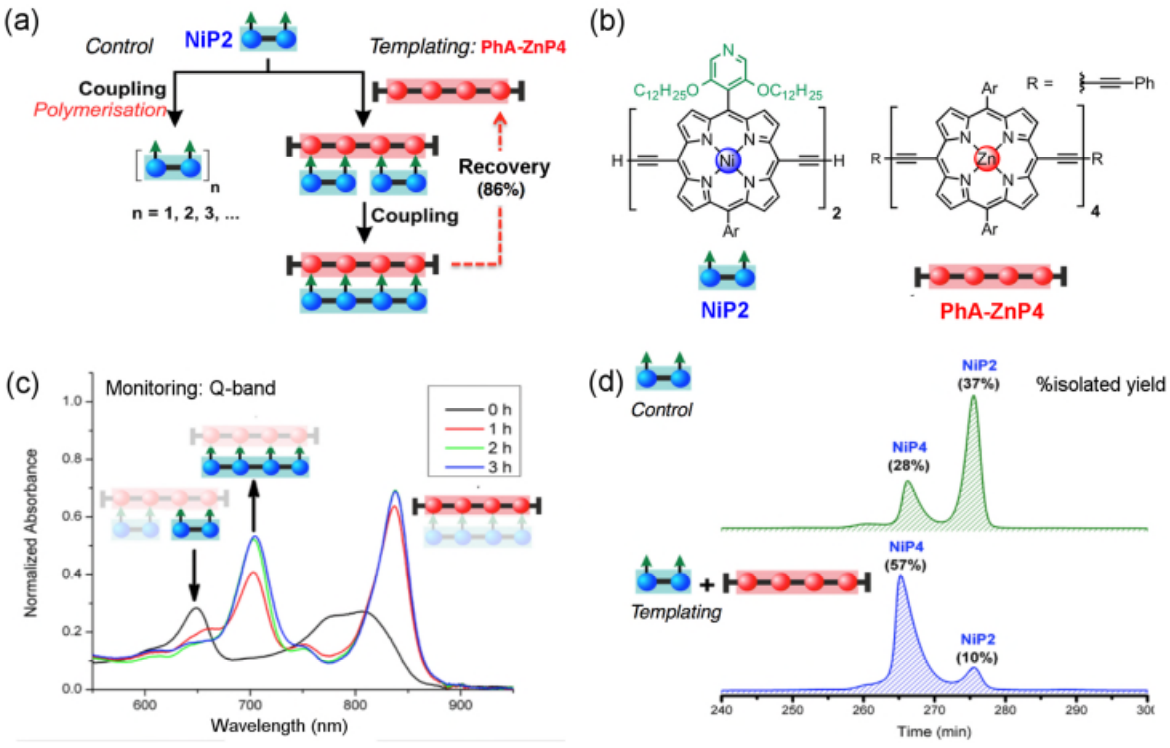

Figure 4.4 Reaction design and outcome of linear tetramer templating for the synthesis of the commensurate length product **NiP4** from **NiP2**, using **PhA-ZnP4** as a template. (a) Schematic representation of the linear tetramer templated and the non-templated syntheses of **NiP4**. (b) Chemical structures of the substrate and the template. (c) The change in UV-vis-NIR absorption spectra of the templated synthesis of **NiP4** from 0 to 3 h. (d) Recycling GPC traces (detection at 646 nm in fourth cycle, toluene/1% pyridine) of the non-templated reaction (top) and the linear templating reaction (bottom) product mixture after removal of the template **PhA-ZnP4**. Products were identified by MALDI-ToF MS and ^{1}H NMR for **NiP2** and **NiP4**.

The absorption spectra of porphyrins consist of two bands called a B-band (400-550 nm) and a Q-band (650-950 nm). The absorption spectra of Ni and Zn porphyrins are distinctive for equal oligomer length because the Q-band of Ni porphyrins occurs at shorter wavelengths, making it easy to observe changes in the course of the reaction. As shown in **Figure 4.4c**, initially, before the start of the coupling reaction, the absorption spectra show two Q-bands at the short (650 nm) and long (808 nm) wavelengths corresponding to the bound Ni dimer and the Zn template on the ladder complex, respectively. Over the course of the reaction the Q-band of **NiP2** starts to decrease and a new Q-band appears at the red-shifted wavelength of 704 nm, which indicates the formation of longer Ni porphyrin oligomers, including the desired product **NiP4.** At the same time, the Q-band of the Zn template is red-shifted and becomes sharper at 838 nm, indicating that the Zn template is held in a more rigid and conjugated conformation.[1,22] After 2 h, there is no further change in the absorption spectra. The coupling reagents and the template **PhA-ZnP4** were easily separated from the nickel-porphyrin oligomers by passing through a short silica column eluting with a gradient of 1 to 10% pyridine in chloroform. From this separation, the template was recovered in 86% isolated yield. The non-templated reaction was worked up in the same way as the templated reaction. After this first purification step, the crude mixture of **NiPn** oligomers was purified by gel permeation chromatography (GPC) in toluene/1% pyridine (**Figure 4.4d**), and was analysed by MALDI-ToF and ^{1}H NMR spectroscopy. Without the template, **NiP2** was converted to **NiP4** slowly in 28% isolated yield and the unreacted substrate was re-isolated in 37% yield. In the templated reaction, the template accelerated the coupling of **NiP2** to generate **NiP4** in 57% isolated yield; unreacted **NiP2** was re-isolated in 10% isolated yield. The template improves the yield of the desired product **NiP4** by a factor of two, since the template forces the reactive acetylene ends of the bound dimers to be brought into close proximity, resulting in a rapid intramolecular coupling.

The unreacted **NiP2** was observed in both templating and non-templating since the reaction was stopped before completion to prevent the formation of longer Ni oligomers (which would be inevitable at high extents of coupling). However, small traces of longer Ni porphyrin oligomers should have been seen in GPC traces. One possible reason for not seeing the higher molecular weight Ni oligomers in the above cases may be their low solubility under the conditions used for

GPC analysis (toluene/1% pyridine). Another possibility is that the higher molecular weight Ni oligomers were removed at the same time as the coupling reagents during chromatography on silica.

Changing the capping group from **PhA** to **CPDIPS** was also investigated in the same approach, giving similar yields. The desired product **NiP4** was formed in a range from 35% (from 39 mg of **NiP2**), 42% (from 3.0 mg of **NiP2**) to 54% (from 22.3 mg of **NiP2**) isolated yield all using the template **CPDIPS-ZnP4**.

4.3.2 Ni tetramer as the template for making Zn tetramer (2 × 2 = 4)

Zn and Ni porphyrins can swap their roles by using **ZnP2** as a substrate and **PhA-NiP4** as a template. **PhA-NiP4** was synthesised by Pd/Cu-catalysed oxidative coupling between excess phenylacetylene and fully deprotected Ni tetramer **NiP4** which was obtained from the previous Zn tetramer templating reaction (for details of the synthesis, see **Experimental section 4.9**). The linear templated and non-templated reactions were performed as seen in **Figure 4.5a**. UV-vis-NIR spectroscopy before addition of the coupling reagents showed overlapping absorptions between the substrate **ZnP2** and the template **PhA-NiP4** (**Figure 4.5c)** because the red-shift of the absorption of longer Ni-containing oligomers cause the Q-band to come in the same region as shorter Zn oligomers. After 1 h, the planarisation of the template provides a slightly red-shifted and sharper Q-band at 709 nm and a new Q-band corresponding to the longer oligomers (most likely the desired product **ZnP4**) appears at longer wavelengths (838 nm). Then at 2 h, another species appears with a far-red shifted absorption at 875 nm, possibly corresponding to longer Zn porphyrin polymers. Since the peak at 875 nm increases with longer reaction times, the reaction was stopped after 3.5 h at the first attempt. The coupling reagents were removed and template separated using a short silica column eluted with a chloroform/1-10% pyridine gradient, re-isolating the template in 71% yield. The product distribution was analysed by GPC (toluene/1% pyridine) (**Figure 4.5d**). The template accelerates the coupling reaction, consuming almost all starting material (98% conversion by GPC) and providing the desired product **ZnP4** in 23% isolated yield (22% GPC analytical yield). Besides the expected product **ZnP4,** more products with lengths in multiples of

four units from intermolecular coupling were observed (**ZnP8** and **ZnP12**) compared with other oligomers. The formation of multiple-of-four products may be attributed to the further coupling of free acetylenic end groups between the desired product **ZnP4**. With no template, the reaction yields a product distribution characteristic to statistical polymerization and shows more of the unreacted substrate left in 15% GPC yield.

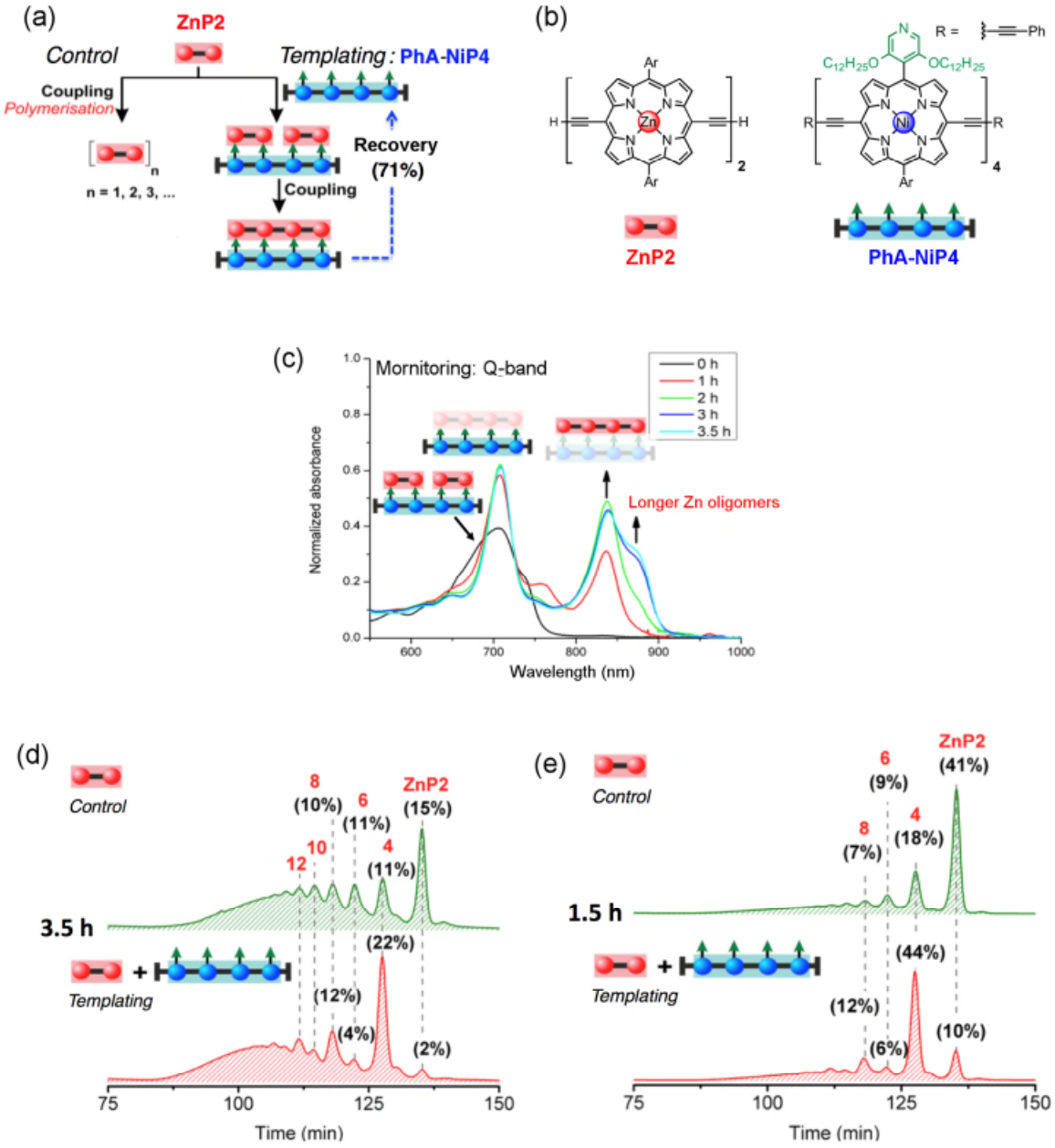

Figure 4.5 Reaction design and outcome of linear tetramer templating for the synthesis of the commensurate length product **ZnP4** from **ZnP2** using **PhA-NiP4** as a template. (a) Schematic representation of the linear tetramer templated and non-templated syntheses of **ZnP4**. (b) Chemical structures of the substrate and the template. (c) The change in UV-vis-NIR absorption spectra of the templated synthesis of **ZnP4** from 0 to 3.5 h. (d) Recycling GPC traces (detection at 591 nm in second cycle, toluene/1% pyridine) of the non-templated reaction (top) and the linear templated reaction (bottom) product mixture after removal of the template **PhA-NiP4** at 3.5 h and (e) at 1.5 h. Products were identified by analytical GPC based on calibrated retention

times, MALDI-ToF and ^{1}H-NMR for **ZnP2** and **ZnP4**. **ZnP4** was isolated in 23% and 30% yield from the reaction time at 3.5 and 1.5 h, respectively. The percentages in GPC traces represent the %GPC yields of corresponding compounds, calculated by integration of the peak areas.

We found that the formation of longer oligomeric byproducts could be reduced while increasing the yield of the desired product **ZnP4**, by reducing the reaction time from 3.5 h to 1.5 h. The GPC traces (**Figure 4.5e**) reveal that smaller amounts of long polymers were formed in both templated and non-templated reactions. With template, the coupling yielded **ZnP4** up to 30% isolated yield (44% GPC yield) and also gave more multiple-of-four products than other oligomers.

The template acts as a *positive* template in this reaction, promoting the intramolecular coupling leading to the formation of the desired tetramer from dimers. These template effects are easy to control by reducing the reaction time so as to enhance the formation of the tetramer.

Interestingly, the coupling reaction of Zn porphyrin oligomers is faster than that of Ni porphyrin oligomers despite the fact that nickel is more electron withdrawing than zinc, which could enhance the Glaser coupling reactivity as reported previously.[23,24]

4.3.3 Hexamer template-directed synthesis (2 × 3 = 6)

Encouraged by the above result, we extended the limit of linear templating by trying the longest template **THS-ZnP6** examined here to produce the commensurate length product (i.e. **NiP6**) using **NiP2** as a starting material. The templated and non-templated reactions were set up similarly to the previous experiment, with a stoichiometric ratio of **NiP2** to **THS-ZnP6** of 3:1. Under identical reaction conditions, the control reaction with no template gave negligible amounts of **NiP6** as previously shown in **Figure 4.4d**. With this longer template, we successfully isolated the desired product **NiP6** in a good yield of 56% (5 mg from 9 mg of **NiP2**) and the template was re-isolated in 86% yield (**Figure 4.6**).

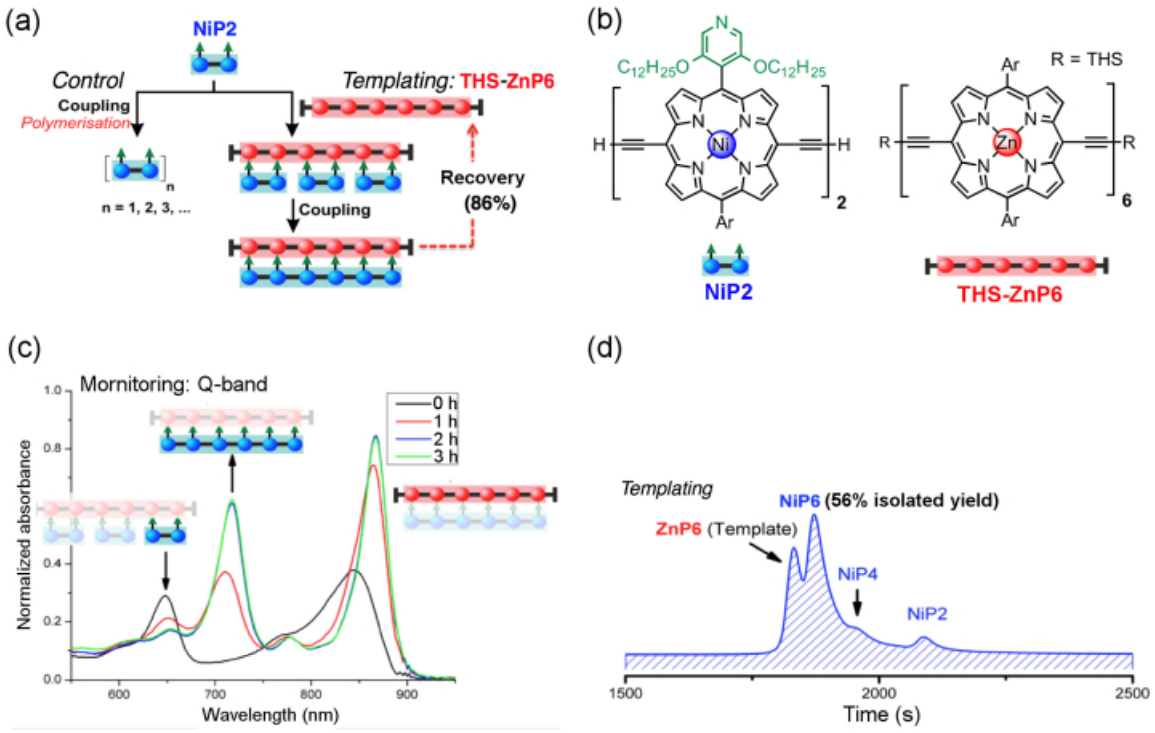

Figure 4.6 Reaction design and outcome of linear tetramer templating for the synthesis of the commensurate length product **NiP6** from **NiP2** using **THS-ZnP6** as a template. (a) Schematic representation of the linear tetramer templated and the non-templated syntheses of **NiP6**. (b) The change in UV-vis-NIR absorption spectra of the templated synthesis of **NiP6** from 0 to 3 h. (c) GPC traces (detection at 646 nm, THF) of the linear templating reaction product mixture with the template **THS-ZnP6**. Products were identified by MLALDI-ToF and ^{1}H-NMR for **NiP6**.

This reaction was scaled up to 20 mg of **NiP2** substrate and the desired product **NiP6** was isolated in 13 mg, 63% isolated yield. This is a synthetically useful route to **NiP6** that yields the starting material for the synthesis of **PhA-NiP6** in the Vernier templating **Section 4.4** and the

substrate for the Vernier-reciprocal templated reaction in **Section 4.5**. There is no reason why it should not be possible to extend the length of the templates, provided that there is no solubility problem, and that the templates are synthetically accessible.

4.4 Binding studies of molecular ladder complexes

Effective molarity (*EM*) is a key factor to determine the stability and cooperativity of ladder formation. *EM*s for both 2- and 4-rung ladder complexes were determined and compared, which require the binding constants for formation of both ladder complexes to be determined.

4.4.1 Determination of the binding constant of the 2-rung ladder complex

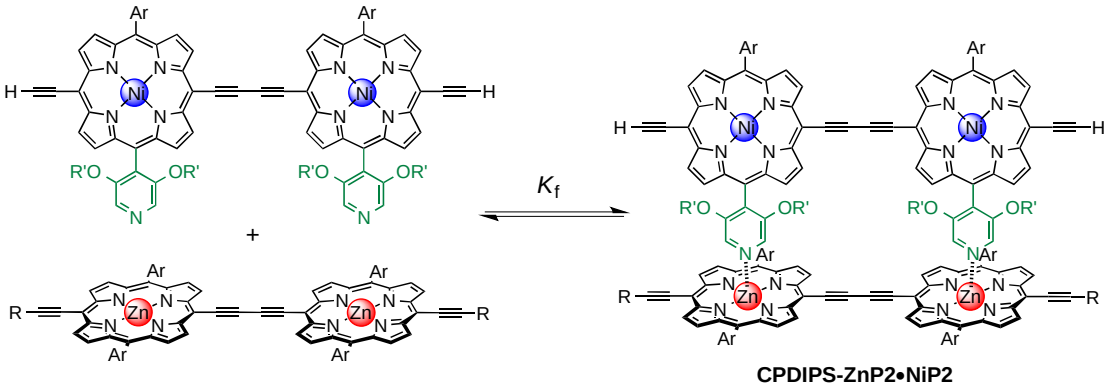

Figure 4.7 Formation of **CPDIPS-ZnP2•NiP2** complex. R = (3-Cyanopropyl)dimethylsilyl, R' = dodecyl. Ar = 3,5-bis(trihexylsilyl)phenyl.

The binding constant of the **CPDIPS-ZnP2•NiP2** complex was elucidated as a reference in comparison to the binding constant of the **CPDIPS-ZnP4•NiP4** complex. The UV-vis-NIR formation titration of **CPDIPS-ZnP2** with **NiP2** was first performed (**Figure 4.8**). The binding isotherm of dimer-dimer formation gave a sharp end point at 1:1 ratio of **NiP2** to **CPDIPS-ZnP2**, confirming the 1:1 stoichiometry of the complex (**Figure 4.8**).

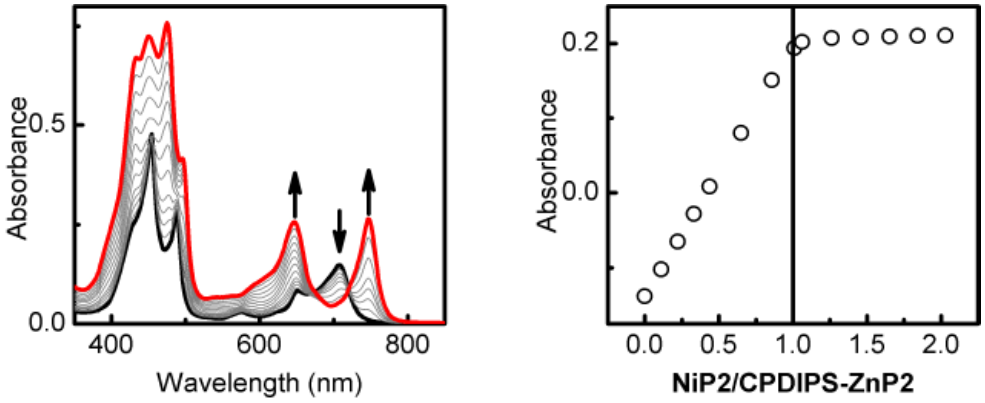

Figure 4.8. UV-vis-NIR formation titration of **CPDIPS-ZnP2** ([**CPDIPS-ZnP2**] = 1.41 × 10^{-6} M) with **NiP2** in dry DCM at 298 K. (left) Changes in absorption upon addition of **NiP2**. Arrows indicate areas of increasing and decreasing absorption during the titration; (right) Binding isotherm derived from absorption data at 747-707 nm. The vertical line indicates a 1 to 1 ratio of **NiP2** to **CPDIPS-ZnP2**.

This complex is too stable (K_f > 10^8 M^{-1}) due to the square-binding isotherm (**Figure 4.8 right**), which does not allow K_f to be determined. Thus, the formation constant, K_f can be determined indirectly via the generic thermodynamic cycle in **Figure 4.9** using the following equation:

$$K_f = \frac{K_{py}^{N}}{K_{dn}} \qquad \textbf{(eq. 4.1)}$$

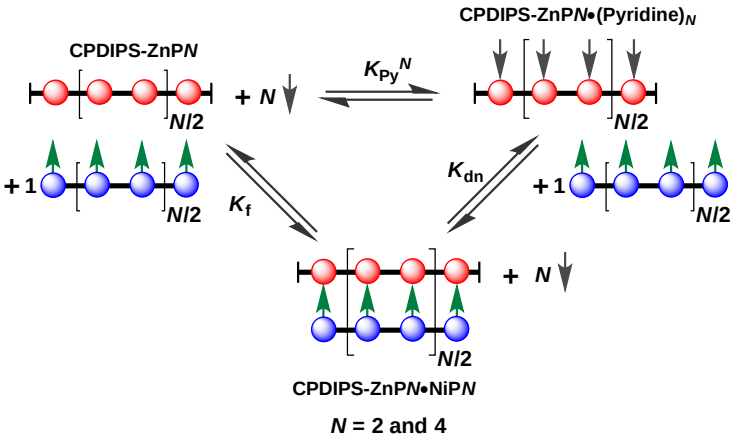

Figure 4.9 Thermodynamic cycle relating the formation constant of the template complex (K_f) to the denaturation constant (K_{dn}) and binding constant of each porphyrin unit for pyridine (K_{py}). The excess of pyridine was added to displace the multidentate ligand **NiP*N*** from **CPDIPS-ZnP*N*** to generate (**CPDIPS-ZnP*N***)•(**Pyridine**)$_N$.

According to **Figure 4.8** and **Equation 4.1**, in order to acquire K_f, the denaturation constant (K_{dn}) and the reference constant (K_{py}) are necessary. The former is determined by the denaturation titration as shown below and the latter is described in **Section 4.4.3**.

The denaturation titration of **CPDIPS-ZnP2•NiP2** with pyridine was analysed and the equilibrium can be treated as the displacement of a two-site ligand **L** from a two-site receptor **P**, with the initial concentration of **PL** being, [**P**]$_0$.

PL + 2**Py** ⇆ **PPy$_2$** + **L**

$$K_{dn} = \frac{[\mathbf{PPy_2}][\mathbf{L}]}{[\mathbf{PL}][\mathbf{Py}]^2} \qquad \textbf{(eq. 4.2)}$$

The denaturation constant, K_{dn} of **CPDIPS-ZnP2•NiP2** complex was defined by **Equation 4.2** and was evaluated by fitting the binding isotherm to **Equation 4.3**.

$$\frac{A - A_0}{A_f - A_0} = \frac{-K_{dn}[\mathbf{Py}]^N + \sqrt{K_{dn}^2[\mathbf{Py}]^{2N} + 4K_{dn}[\mathbf{Py}]^N[\mathbf{P}]_0}}{2[\mathbf{P}]_0} \qquad \textbf{(eq. 4.3)}$$

where A is the observed absorption at a specific wavelength or difference of absorption at two wavelengths; A_0 is the starting absorption at this wavelength or difference of absorption in these two wavelengths; A_f is the asymptotic final absorption at this wavelength or difference of absorption in these two wavelengths; [**Py**] is the concentration of pyridine and [**P**]$_0$ is the total concentration of **CPDIPS-ZnP2•NiP2** complex. N is the number of binding sites (N = 2).

Equation 4.3 makes the approximation that [**Py**] ≈ total pyridine concentration [**Py**]$_0$ which is valid when [**Py**]$_0$ >> [**P**]$_0$.

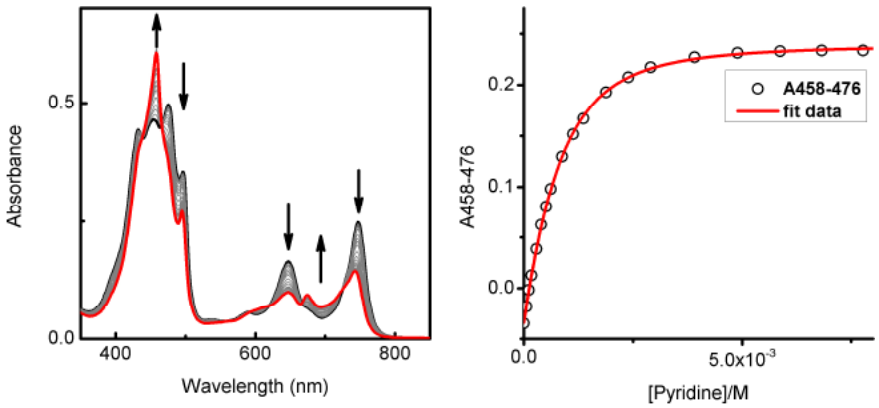

Figure 4.10. UV-vis-NIR denaturation titration of **CPDIPS-ZnP2•NiP2** ([complex] = 1.41 × 10^{-6} M) with pyridine in dry DCM at 298 K. (left) Changes in absorption upon addition of pyridine. Arrows indicate areas of increasing and decreasing absorption during the titration; (right) Binding isotherm (open dots) derived from absorption data at λ = 458 – 476 nm and fit with **Equation 4.3** obtained from Origin® (red line) (Run1: R^2 = 0.999; Run2: R^2 =0.999).

The average value of K_{dn} obtained from fitting the binding isotherms of two titrations to a 2-site binding model for the breakup of **CPDIPS-ZnP2•NiP2** is K_{dn} = 1.66 ± 0.04 M^{-1} (**Figure 4.10**). The error was estimated from two replicates.

The 1:1 formation constant, K_f for **CPDIPS-ZnP2•NiP2** was calculated from K_{dn} = 1.66 ± 0.04 M^{-1} and K_{py} = (2.88 ± 0.21) × 10^4 M^{-1} (see detail of K_{py} in determination of reference constant **Section 4.4.3**) using **Equation 4.1** with N = 2, giving K_f = (5.00 ± 0.74) × 10^8 M^{-1}. This K_f value will be used to calculate the effective molarity in **Section 4.4.4**.

4.4.2 Determination of the binding constant of the 4-rung ladder complex

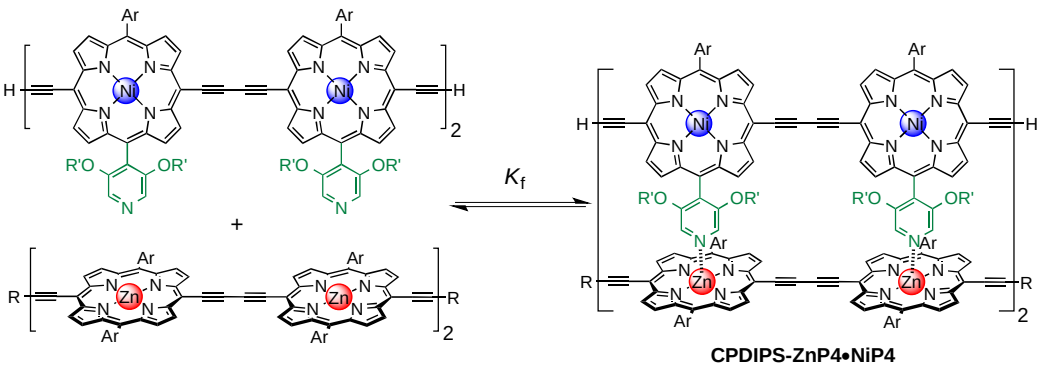

Figure 4.11. Formation of **CPDIPS-ZnP4•NiP4** complex. R = (3-Cyanopropyl)dimethylsilyl, R' = dodecyl. Ar = 3,5-bis(trihexylsilyl)phenyl.

The binding strength of the 4-rung ladder complex between **NiP4** and **CPDIPS-ZnP4** was studied to provide a measure of the stability and cooperativity of the ladder formation (**Figure 4.11**). The UV-vis-NIR formation titration was performed at a constant micromolar concentration of **CPDIPS-ZnP4** in dry DCM at 25 °C (**Figure 4.12**). Upon addition of **NiP4**, the Q-band absorption of **ZnP4** red shifts and is sharpened as a consequence of coplanarization of the porphyrin units, leading to stronger electronic coupling among the units.[1,25,26] The binding isotherm is essentially linear and reaches an abrupt end-point after addition of 1 equivalent of the ligand **NiP4**, consistent with the 1:1 stoichiometry of the ladder complex **NiP4•CPDIPS-ZnP4.** As in the previous section, the stability constant is too high to determine directly from the formation curve, but it can be evaluated indirectly by denaturation with pyridine via thermodynamic cycle (**Figure 4.9**).

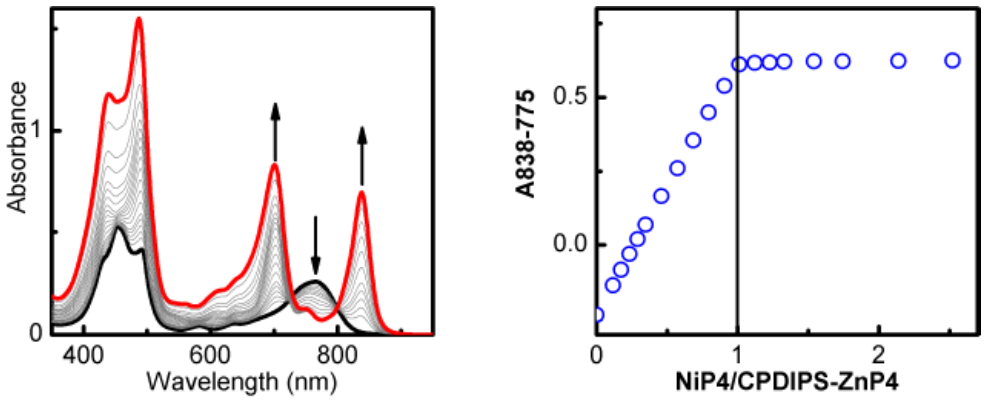

Figure 4.12 UV-vis-NIR formation titration of **CPDIPS-ZnP4** ([**CPDIPS-ZnP4**] = 1.11 × 10^{-6} M) with **NiP4** in dry DCM at 298 K. (left) Changes in absorption upon addition of **NiP4**. Arrows indicate areas of increasing and decreasing absorption during the titration; (right) Binding isotherm derived from absorption data at 838-775 nm. The vertical line indicates a 1 to 1 ratio of **NiP4** to **CPDIPS-ZnP4**.

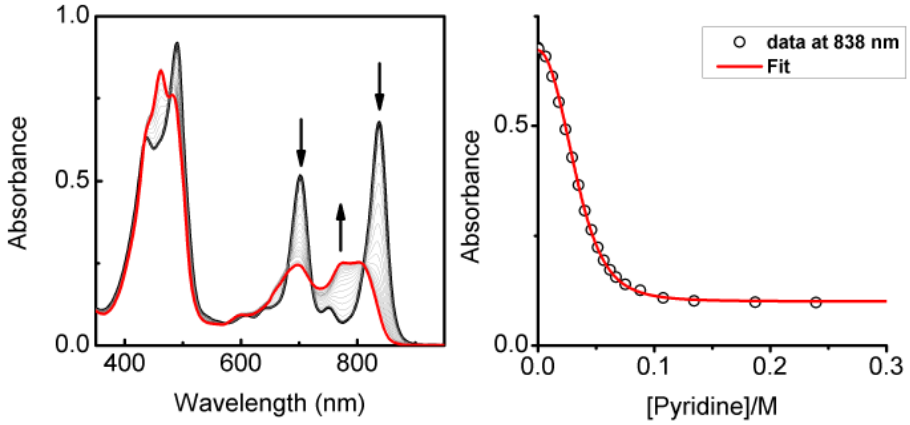

Figure 4.13 UV-vis-NIR denaturation titration of **CPDIPS-ZnP4•NiP4** ([complex] = 1.11 × 10^{-6} M) with pyridine in dry DCM at 298 K. (left) Changes in absorption upon addition of pyridine; the spectrum of the initial complex (thick black line) and the final spectra of the pyridine-saturated Zn tetramer and unbound Ni tetramer (red line). Arrows indicate areas of increasing and decreasing absorption during the titration; (right) Binding isotherm (open dots) derived from absorption data at λ = 838 nm and fit with **Equation 4.3** obtained from Origin® (red line) (Run1: R^2 = 0.9997; Run2: R^2 =0.9997).

Under the same conditions as the formation titration, a large excess of pyridine was titrated to the 4-rung ladder complex to displace the tetradentate ligand **NiP4**. The denaturation titration shows that the absorption spectra of the **NiP4•CPDIPS-ZnP4** complex are red-shifted and sharper in Q-bands compared to the pyridine bound **CPDIPS-ZnP4** at the end of titration due to the more rigid structure and coplanarization between porphyrin units in the ladder complex (**Figure 4.13**).[26,27] Observation of several isosbestic points in the denaturation titration and the sigmoidal binding isotherm indicate an all-or-nothing two-state equilibrium (i.e., that partially denatured species are not populated) (**Figure 4.13-left**).[27–30]

The binding constant, K_f of the **CPDIPS-ZnP4•NiP4** complex was determined via the denaturation titration of **CPDIPS-ZnP4•NiP4** with excess pyridine can be analysed as a two-equilibrium state, where PL is **CPDIPS-ZnP4•NiP4** and **L** is **NiP4**.

$$\mathbf{PL} + 4\mathbf{Py} \leftrightarrows \mathbf{PPy_4} + \mathbf{L}$$

$$K_{dn} = \frac{[\mathbf{PPy_4}][\mathbf{L}]}{[\mathbf{PL}][\mathbf{Py}]^4} \qquad \textbf{(eq. 4.4)}$$

The denaturation constant, K_{dn}, defined by **Equation 4.4** was determined by fitting the binding isotherm to **Equation 4.3** with N = 4.

The average value of K_{dn} obtained from fitting the binding isotherms of two titrations to a 4-site binding model for the breakup of **CPDIPS-ZnP4•NiP4** is K_{dn} = 0.39 ± 0.06 M^{-3} (**Figure 4.13-right**). The error approximated from two replicates. The 1:1 formation constant, K_f for **CPDIPS-ZnP4•NiP4** was calculated via the generic thermodynamic cycle using **Equation 4.1** with N = 4, giving K_f = (1.8 ± 0.60) × 10^{18} M^{-1}. This K_f value will be used to calculate the effective molarity in **Section 4.4.4**.

4.4.3 Determination of reference constant

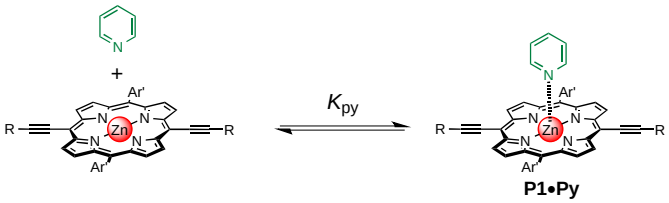

Figure 4.14 Formation of pyridine and porphyrin monomer complex (**P1•Py**). Ar' = 3,5-bis(trihexylsilyl)phenyl, R = (3-Cyanopropyl)dimethylsilyl.

The binding constant of pyridine to Zn porphyrin monomer complex (K_{py}) is needed to derive the binding constants (K_f) of the **CPDIPS-ZnP2•NiP2** and **CPDIPS-ZnP4•NiP4** complexes from the thermodynamic cycle. K_{py} was obtained by UV-vis-NIR formation titration of Zn porphyrin monomer **CPDIPS-ZnP1** with pyridine (**Figure 4.14**).

The experimental data were in excellent agreement with the theoretically derived 1:1 formation binding mode, resulting in average K_{py} = (2.88 ± 0.21) × 10^4 M^{-1} (**Figure 4.15**). The error was estimated from two replicates.

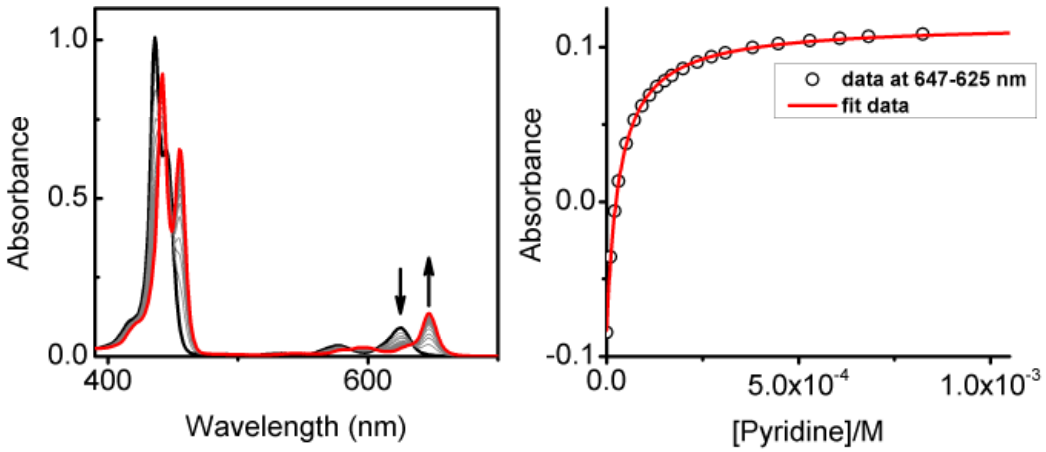

Figure 4.15 UV-vis-NIR formation titration of **CPDIPS-ZnP1** ([**CPDIPS-ZnP1**] = 2.12 × 10^{-6} M) with pyridine in dry DCM at 298 K; Average K_{py} = (2.88 ± 0.21) × 10^4 M^{-1} obtained from two runs. (left) Changes in absorption upon addition of pyridine; the spectra of the Zn monomer (thick black line) and the end spectra of the pyridine-saturated Zn monomer (red line). Arrows indicate areas of increasing and decreasing absorption during the titration; (right) Binding isotherm (black dots) derived from absorption data at λ = 647 - 625 nm and fit obtained from Origin® (red line) (Run1, R^2 = 0.9996; Run2, R^2 =0.9996).

4.4.4 Calculation of effective molarities of 2- and 4-rung ladder complexes

The complementarity between the two strands of the 4-rung ladder complex **NiP4•CPDIPS-ZnP4** can be evaluated by effective molarity, in comparison to the one for the 2-rung ladder complex **NiP2•CPDIPS-ZnP2**.[28,29] The binding strength of the 4-rung ladder complex from the previous section is very high which could lead to the strong *EM*.[30]

The effective molarities of **CPDIPS-ZnP2•NiP2** (EM_1) and **CPDIPS-ZnP4•NiP4** (EM_2) can be calculated using the equations in **Figure 4.16a** and **b**, respectively. The statistical factors for equilibria as shown in **Figure 4.16** are evaluated from symmetry numbers as explained in **Appendix**.[29] The chemical binding constant $K_{chem,1}$ was estimated by dividing the binding constant for coordination of pyridine to Zn porphyrin monomer **CPDIPS-ZnP1** K_1 by the statistical factor (K_σ = 2), providing $K_{chem,1}$ = (1.44 ± 0.11) × 10^4 M^{-1}. K_2 and K_4 were obtained from the measured binding constants of **CPDIPS-ZnP2•NiP2** (K_2 = (5.00 ± 0.74) × 10^8 M^{-1}) and **CPDIPS-ZnP4•NiP4** (K_4 = (1.79 ± 0.60) × 10^{18} M^{-1}) from denaturation titrations in **Section 4.4.1** and **4.4.2**, respectively. The chemical binding constant of **CPDIPS-ZnP2•NiP2** $K_{chem,2}$ was obtained by dividing K_2 by the statistical factor (K_σ = 8), giving $K_{chem,2}$ = (6.24 ± 0.92) × 10^7 M^{-1}). With the values of $K_{chem,1}$, $K_{chem,2}$, K_2 and K_4, the effective molarities of **CPDIPS-ZnP2•NiP2** and

CPDIPS-ZnP4•NiP4 can be given by EM_1 = 0.3 ± 0.1 M and EM_2 = 14 ± 6 M, respectively. For the 4-rung ladder complex, the average effective molarity ($\overline{EM}$) was also determined using the equation in **Figure 4.16c**, providing $\overline{EM}$ = 1.1 ± 0.2 M.

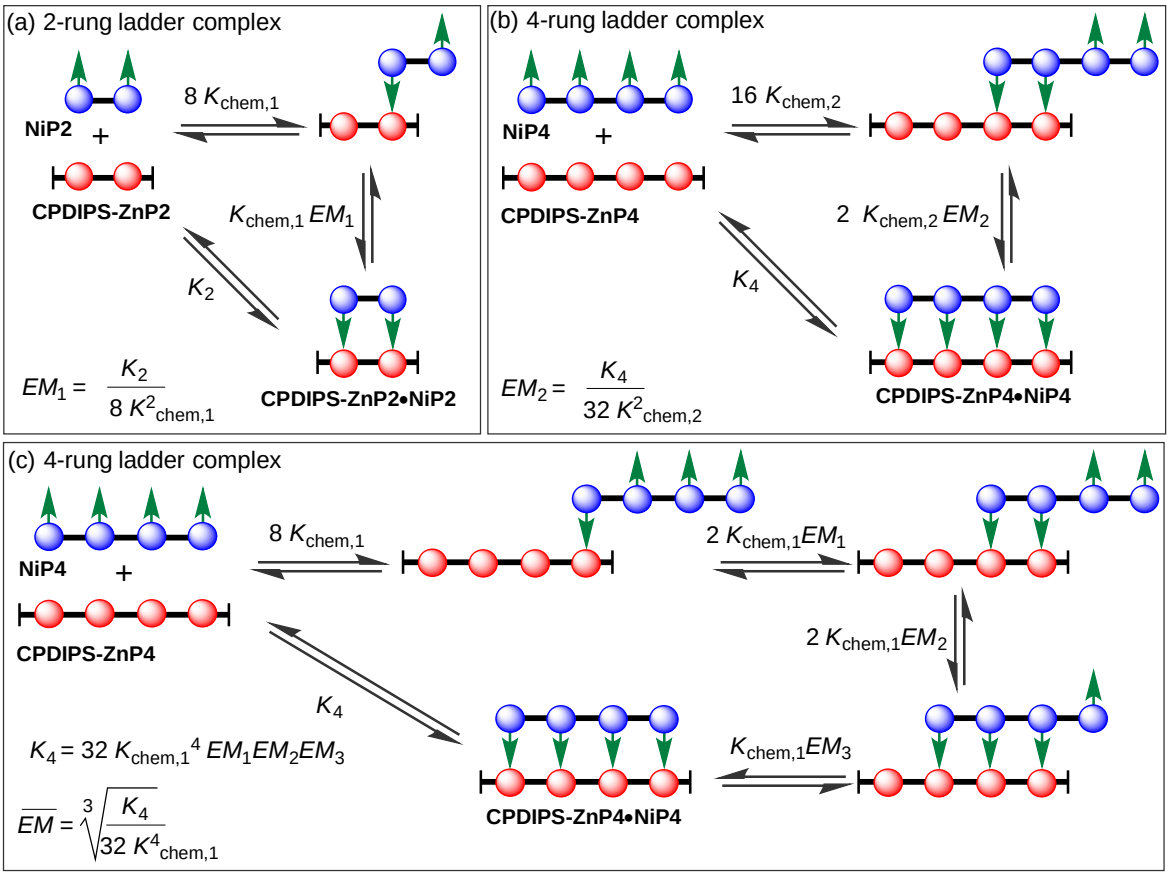

Figure 4.16 Self-assembly of (a) **CPDIPS-ZnP2•NiP2**, (b) and (c) **CPDIPS-ZnP4•NiP4** complexes.

It is remarkable that increasing the number of coordination sites within the structure by a factor of two enhances the cooperative effect by almost a factor of 50, reflecting the preorganised structure and increase in rigidification of the structure with increasing molecular size. The low *EM* in the 2-rung ladder complex also reveals the flexibility of the complex. The higher cooperativity in the 4-rung ladder complex leads to the higher yield in the template-directed synthesis of linear porphyrin tetramer.

4.5 Molecular structures of ladder complexes

4.5.1 ^{1}H NMR Characterisation

^{1}H NMR spectroscopy is one of the most useful tools for the structure determination of supramolecular assemblies. The assignments of the signals in the NMR spectra of the ladder complexes were carried out by a combination of COSY and NOE experiments. Due to the complexity of the ^{1}H NMR of the 4-rung ladder complex **CPDIPS-ZnP4•NiP4**, the 2-rung ladder complex **CPDIPS-ZnP2•NiP2** was analysed first to gain more understanding of the simplest system.

4.5.1.1 ^{1}H NMR assignment of **CPDIPS-ZnP2•NiP2**

The 2-rung ladder complex **CPDIPS-ZnP2•NiP2** was prepared by titration of **CPDIPS-ZnP2** ([**CPDIPS-ZnP2**] = 0.57 mM) with **NiP2** in $CDCl_3$ at 298 K. When a 1:1 ratio of Zn dimer to Ni dimer was reached, the signals corresponding to individual components disappeared and a new product appeared to have been formed (**Figure 4.17**).

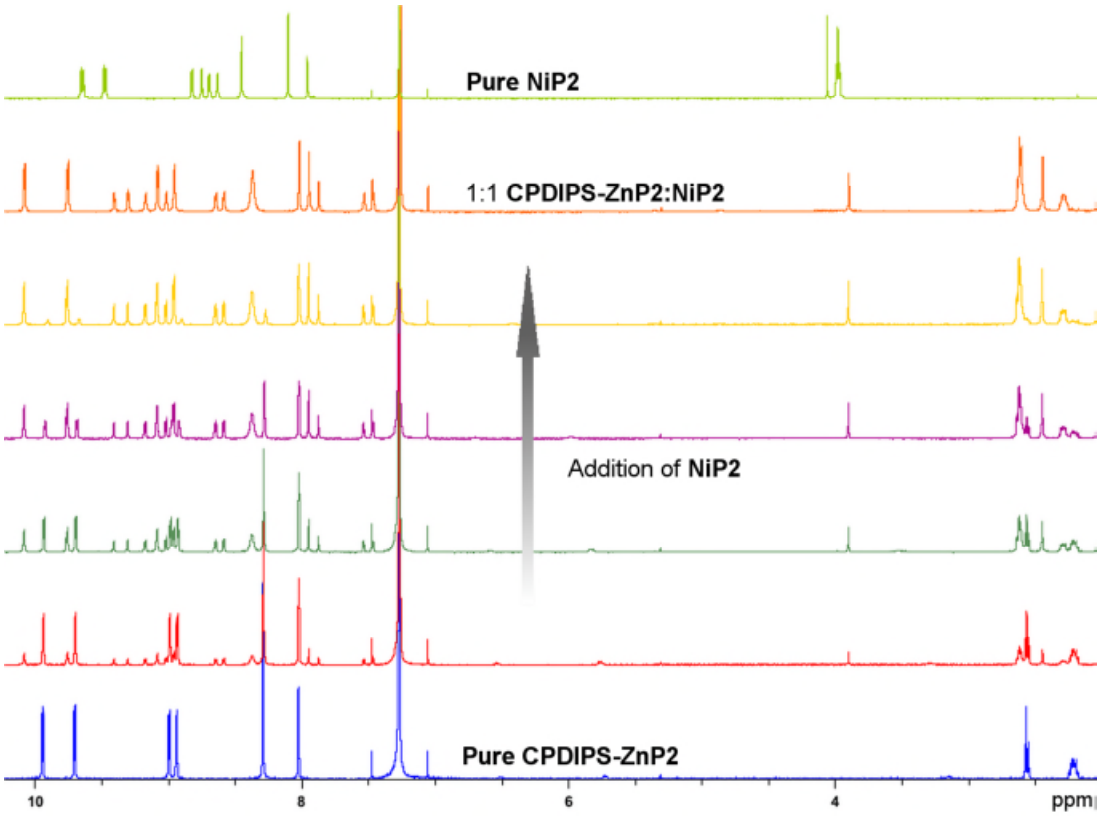

Figure 4.17 ^{1}H NMR titration of the 2-rung ladder complex of **CPDIPS-ZnP2** with **NiP2** (500 MHz, $CDCl_3$, 298 K, [**CPDIPS-ZnP2**] = 0.5 mM).

Based on the symmetry of the **CPDIPS-ZnP2•NiP2** complex, only half of the molecule needs to be considered in the interpretation of the ^{1}H NMR spectrum. The chemical structure in **Figure 4.18** represents a porphyrin unit of **CPDIPS-ZnP2** coordinating to a porphyrin unit of **NiP2**.

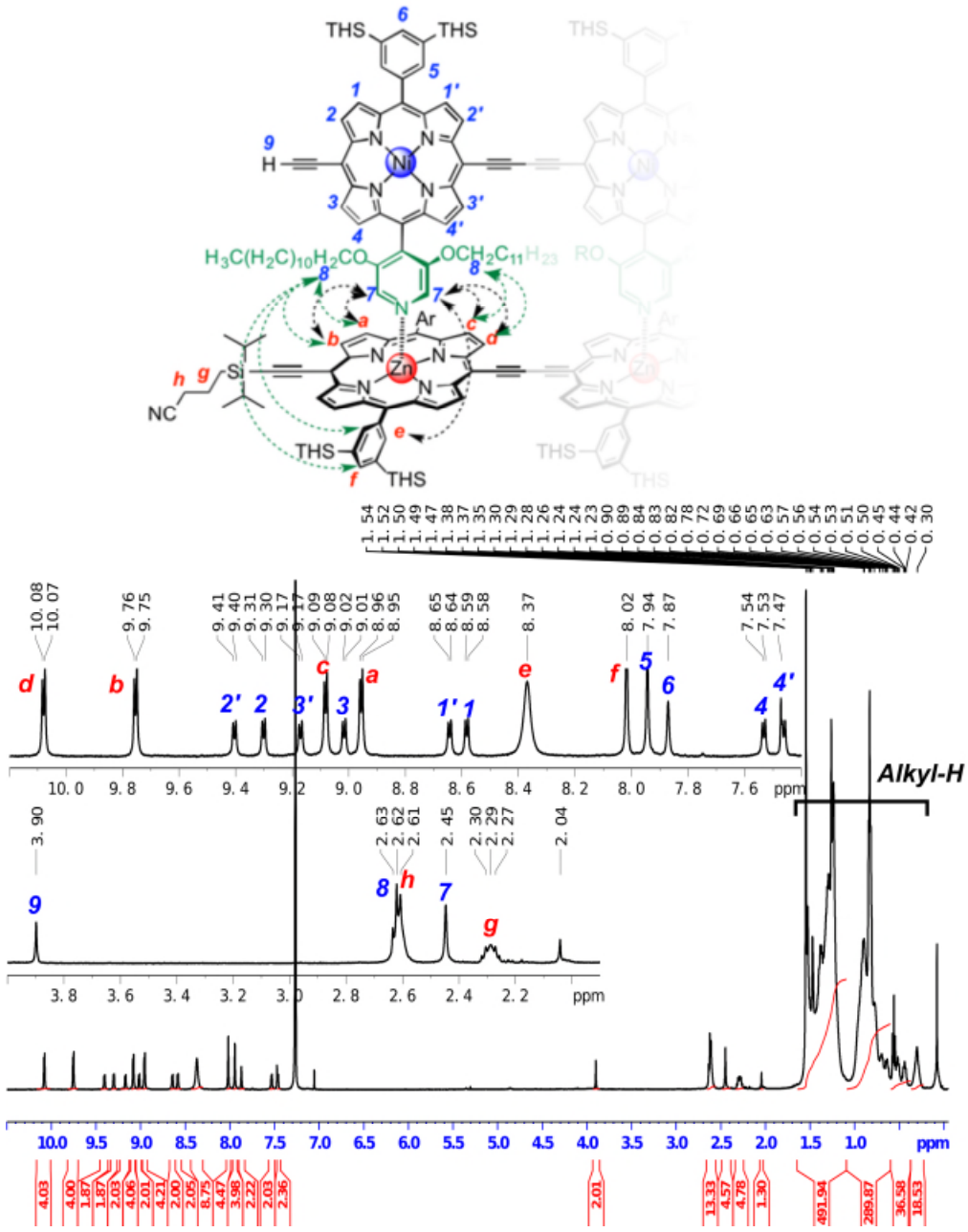

Figure 4.18 Representative half of the 2-rung ladder structure for the interpretation of the ^{1}H NMR spectrum (top, arrows for key NOEs) and ^{1}H NMR spectrum of **CPDIPS-ZnP2•NiP2** (bottom, 500 MHz, $CDCl_3$, 298 K).

Our assignment of the ^{1}H NMR spectrum starts with the β-protons from the Zn porphyrin dimer (**Figure 4.19**). Protons ***d*** and ***b*** which are adjacent to the triple bond are at the higher chemical shift than protons ***a*** and ***c***. Proton ***d*** which is inside the molecule, experiences more deshielding than proton ***b***, resulting in chemical shift of proton ***d*** higher than ***b***. There are also correlations ***a*⇔*b*** and ***c*⇔*d*** in the COSY spectrum, confirming the close proximity of these β-protons. The assignment of ***b*** is also confirmed by the observation of an NOE between ***b*⇔*g*** as shown in **Figure 4.19**.

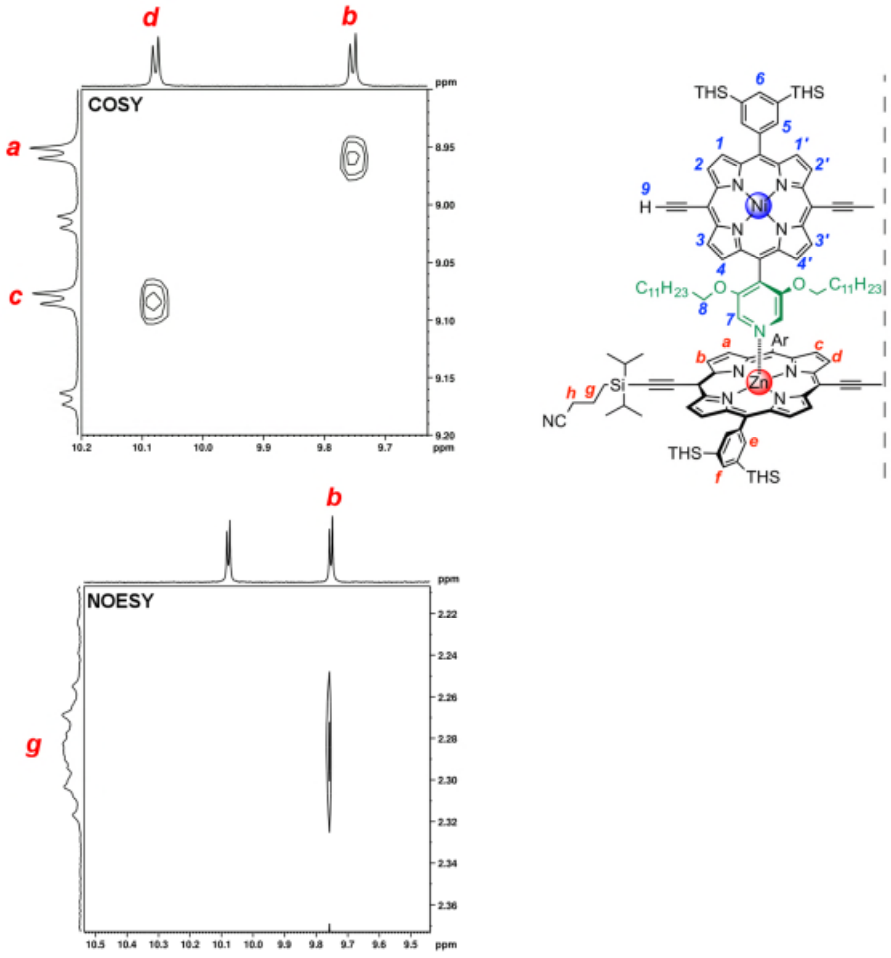

Figure 4.19 Region of the COSY and NOE spectra of **CPDIPS-ZnP2•NiP2** corresponding to **CPDIPS-ZnP2** β-protons ***a***, ***b***, ***c*** and ***d*** and protecting group protons ***g*** and β-proton ***b*** (500 MHz, $CDCl_3$, 298 K).

As shown in **Figure 4.20**, β-protons ***a*** and ***c*** show strong NOEs with aryl side-group proton ***e*** and β-protons ***b*** and ***d*** show weak NOEs with proton ***e***. Proton ***e*** also has coupling with aryl side group proton ***f*** in the COSY spectrum. All protons ***a***, ***b***, ***c***, ***d***, ***e*** and ***f*** are on the Zn porphyrin dimer. Aryl rotation of the Zn porphyrin dimer interconverts two ***e*** environments, making signal of ***e*** broad.

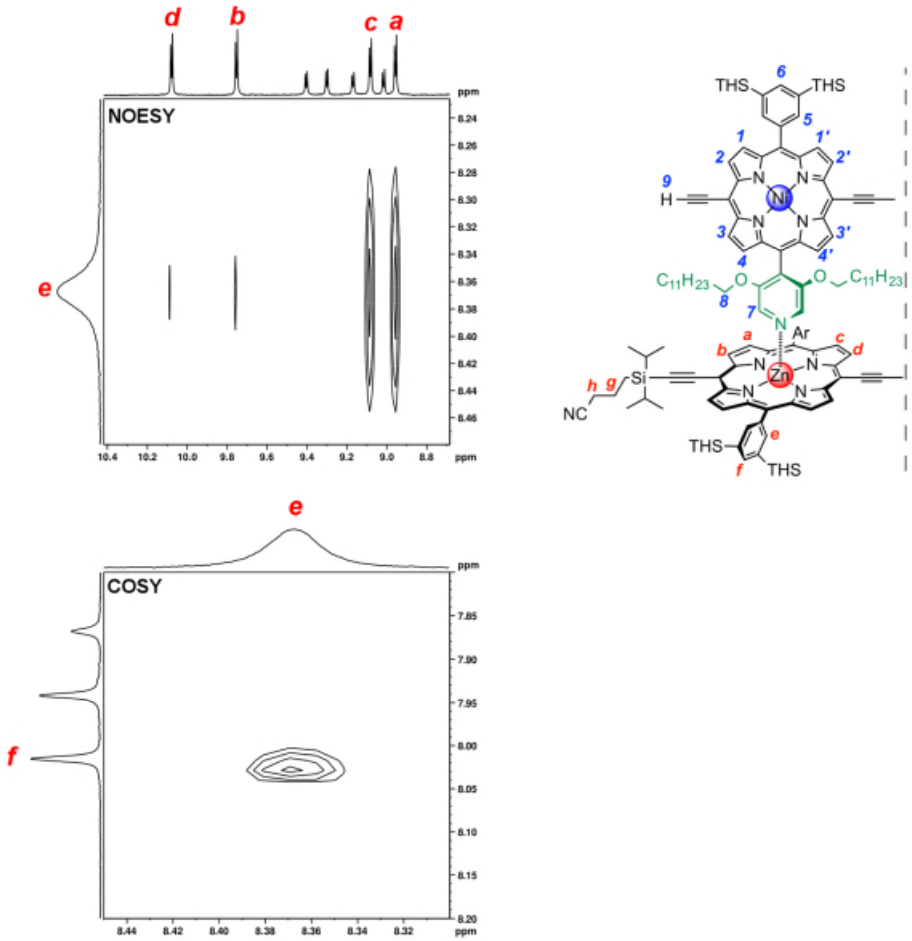

Figure 4.20 Region of the NOESY and COSY spectra of **CPDIPS-ZnP2•NiP2** corresponding to **CPDIPS-ZnP2** β-protons ***a***, ***b***, ***c*** and ***d*** and aryl side-group protons ***e*** and ***f*** (500 MHz, $CDCl_3$, 298 K).

Protecting group protons ***g*** and ***h*** on the Zn porphyrin dimer were assigned based on their correlation in the COSY spectrum (**Figure 4.21**).

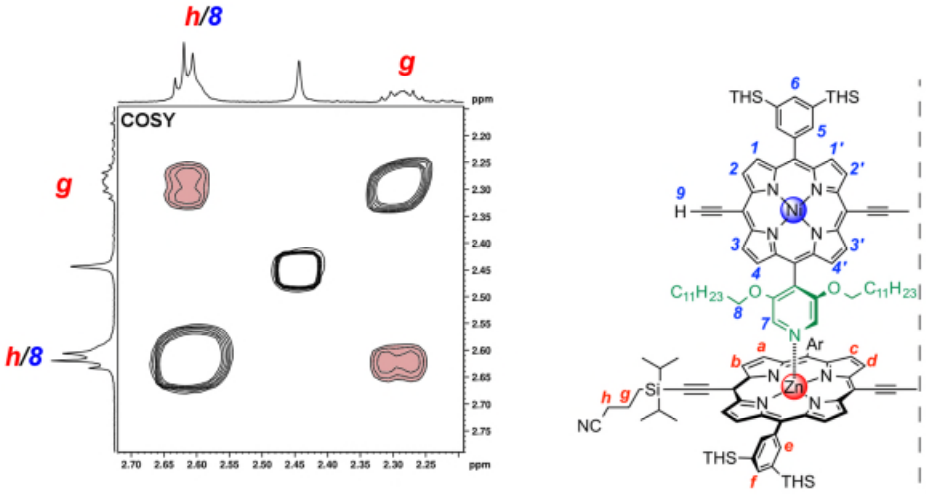

Figure 4.21 Region of the COSY spectrum of **CPDIPS-ZnP2•NiP2** corresponding to **CPDIPS-ZnP2** protecting group protons ***g*** and ***h*** (500 MHz, $CDCl_3$, 298 K). The pink colour of the peaks highlights the correlation between protons ***g*** and ***h*** in the COSY spectrum.

Due to the ring current effect, the α-proton ***7*** on pyridyl side-groups of **NiP2** is strongly shielded and appears as a singlet at 2.45 ppm. The triplet signal of alkyl side-chain proton ***8*** on the pyridyl side-groups is also shielded from the ring current effect and shifted to the up-field at 2.62 ppm which is overlapping with the proton ***h*** of **CPDIPS-ZnP2**.

In the NOESY spectrum (**Figure 4.22**), the Zn porphyrin β-protons ***a***, ***b***, ***c***, ***d*** and ***e*** show NOEs with the Ni porphyrin pyridyl proton ***7*** and alkyl side-chain proton ***8*** on the pyridyl groups and there is also a NOE between proton ***f*** and proton ***8***, confirming the proximity of **CPDIPS-ZnP2** and **NiP2**.

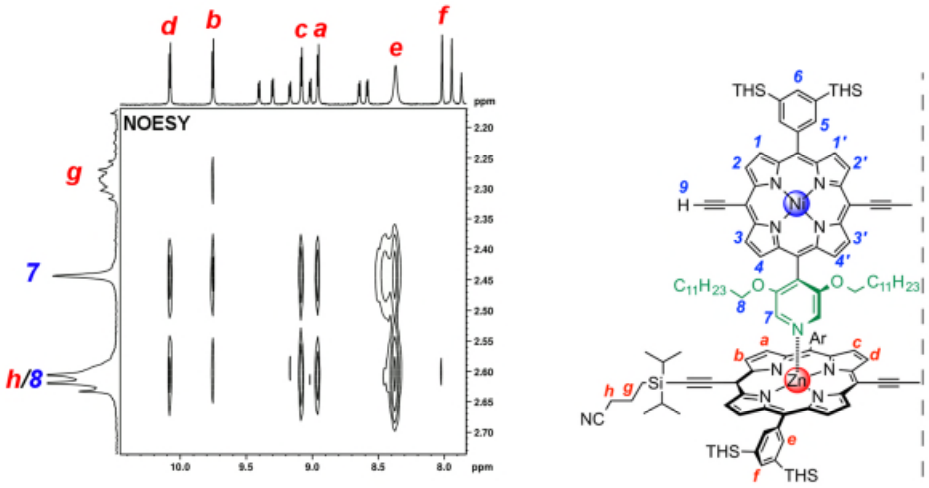

Figure 4.22 Region of the NOESY spectrum of **CPDIPS-ZnP2•NiP2** corresponding to **CPDIPS-ZnP2** protons ***a***, ***b***, ***c***, ***d***, ***e*** and ***f*** and **NiP2** protons ***7*** and ***8*** (500 MHz, $CDCl_3$, 298 K).

Of the β-protons of **NiP2**, protons ***2***, ***2'***, ***3*** and ***3'***, which are adjacent to the triple bond, are at higher chemical shift than protons ***1***, ***1'***, ***4*** and ***4'***. Inner Protons ***2'*** and ***3'*** experience a stronger deshielding effect from the second porphyrin unit in the dimer, resulting in a higher chemical shift than outer protons ***2*** and ***3***, respectively.

Additionally, β-protons ***1*** and ***1'*** show NOEs with THS aryl side-group proton ***5*** and the coupling between β-protons ***1***⇔***2*** and ***1'***⇔***2'*** are also observed in the COSY spectrum (**Figure 4.23**). Based on these couplings and NOEs, ***1***, ***1'***, ***2*** and ***2'*** are readily assigned on the upper part of the Ni strand.

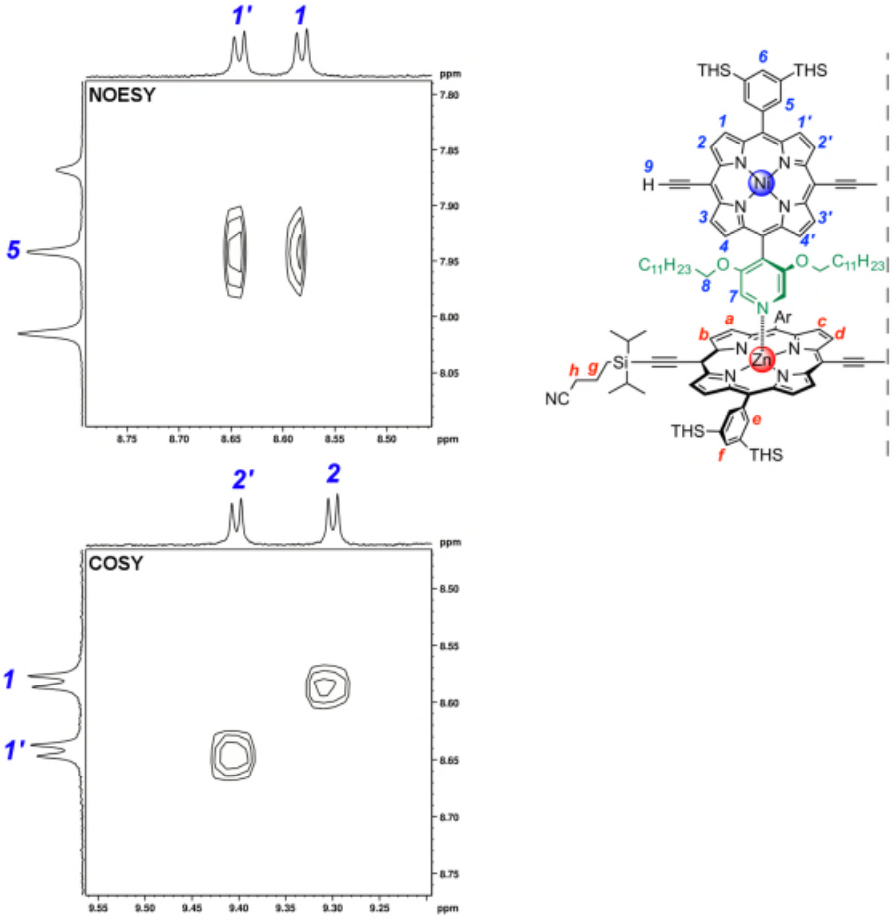

Figure 4.23 Region of NOESY and COSY spectra of **CPDIPS-ZnP2•NiP2** corresponding to **NiP2** β-protons ***1***, ***1'***, ***2*** and ***2'*** and THS aryl side-group proton ***5*** (500 MHz, $CDCl_3$, 298 K).

In the lower part of the Ni strand, β-protons ***4*** and ***4'*** are more shielded by the ring current of the Zn strand than the other β-protons ***1***, ***1'***, ***2***, ***2'***, ***3*** and ***3'*** due to the close proximity to the Zn porphyrin plane, providing the large shift at 7.54 and 7.47 ppm, respectively. Based on their NOEs with protons ***7*** and ***8***, the assignment of β-protons ***4*** and ***4'*** can be confirmed (**Figure 4.24 top**). The couplings between protons ***3'***⇔***4'*** and ***3***⇔***4*** are observed in the COSY spectrum (**Figure 4.24 bottom**). This clarifies the assignment of protons ***3*** and ***3'*** on the lower part of the Ni strand.

The acetylene proton ***9*** is slightly shifted to the up-field since the small effect of ring currents from the Zn strand.

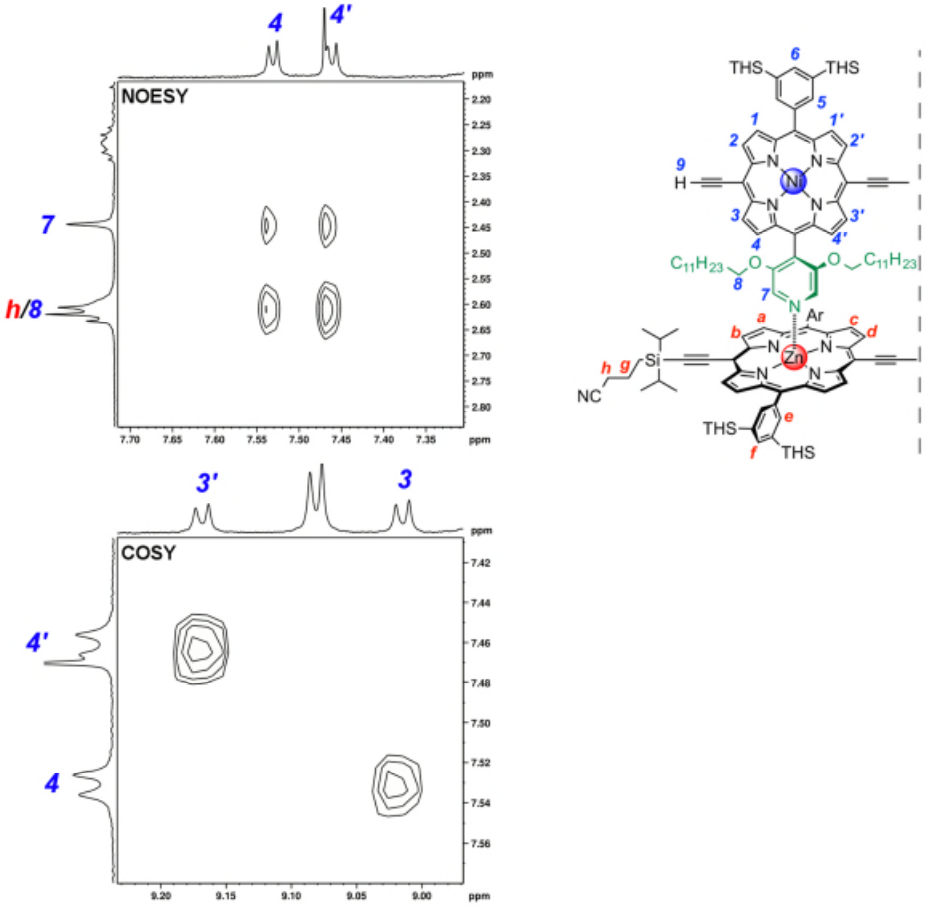

Figure 4.24 Region of the NOESY and COSY spectra of **CPDIPS-ZnP2•NiP2** corresponding to **NiP2** β-protons ***3***, ***3'***, ***4*** and ***4'*** and protons ***7*** and ***8*** (500 MHz, $CDCl_3$, 298 K).

4.5.1.2 ^{1}H NMR assignment of **CPDIPS-ZnP4•NiP4**

The 4-rung ladder complex **CPDIPS-ZnP4•NiP4** was prepared by titration of a solution of **NiP4** into **CPDIPS-ZnP4** in a similar fashion to the 2-rung ladder complex (**Figure 4.25**).

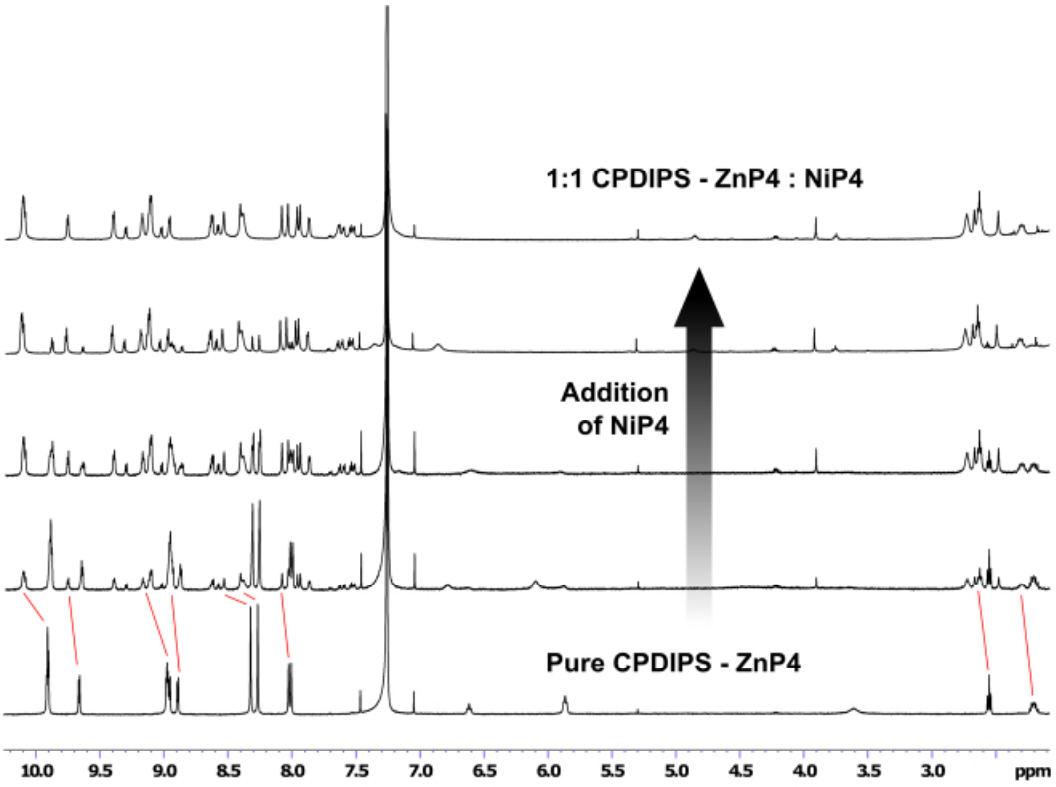

Figure 4.25 ^{1}H NMR titration of **CPDIPS-ZnP4** with **NiP4** to form the 4-rung ladder complex (500 MHz, $CDCl_3$, 298 K, [**CPDIPS-ZnP4**] = 0.22 mM).

Based on the symmetry of the **CPDIPS-ZnP4•NiP4** complex, only half of the molecule needs to be considered in the interpretation of the ^{1}H NMR spectrum. The chemical structure in **Figure 4.26** represents two porphyrin units of **CPDIPS-ZnP4** coordinating to two porphyrin units of **NiP4**.

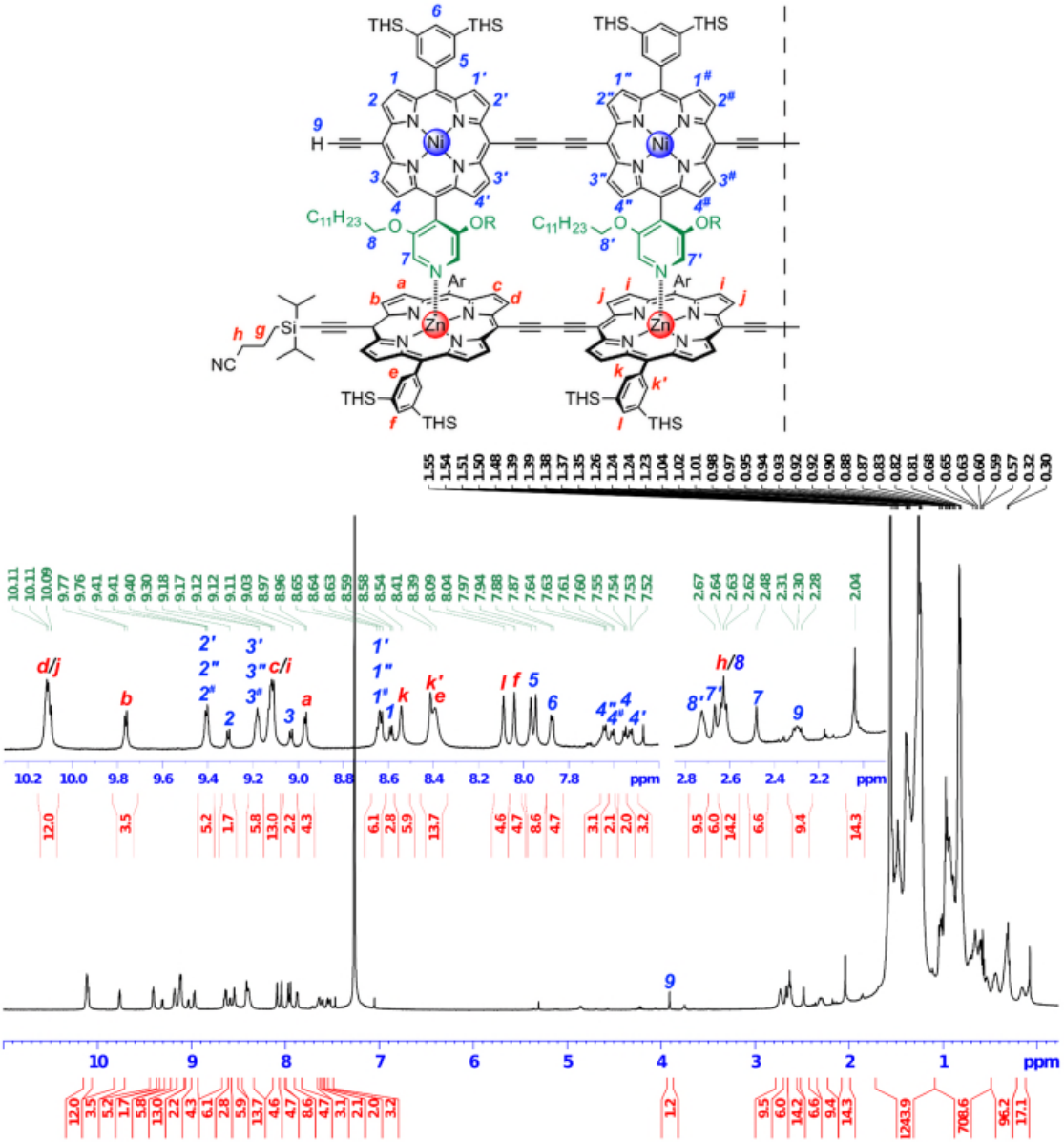

Figure 4.26 Representative half of the 4-rung ladder structure (top) and ^{1}H NMR spectrum of **CPDIPS-ZnP4•NiP4** (bottom, 500 MHz, $CDCl_3$, 298 K).

Our assignment of the ^{1}H NMR spectrum begins with the β-protons from **CPDIPS-ZnP4**. Proton ***d*** overlaps with proton ***j*** and proton ***c*** overlaps with proton ***i*** because they are in very similar environments. Protons ***b***, ***d*** and ***j***, which are adjacent to the triple bond, are at a higher chemical shift than protons ***a***, ***c*** and ***i***. Protons ***d*** and ***j***, which point towards another porphyrin unit, are more deshielded by the butadiyne bridge, resulting in a higher chemical shift for protons ***d*** and ***j*** than for ***b***. There are also correlations ***b*⇔*a***, ***d*⇔*c*** and ***j*⇔*i*** in the COSY spectrum, confirming the close proximity of these β-protons (**Figure 4.27**). The assignment of ***b*** is also confirmed by the observation of an NOE between ***b*⇔*g*** as shown in **Figure 4.30**.

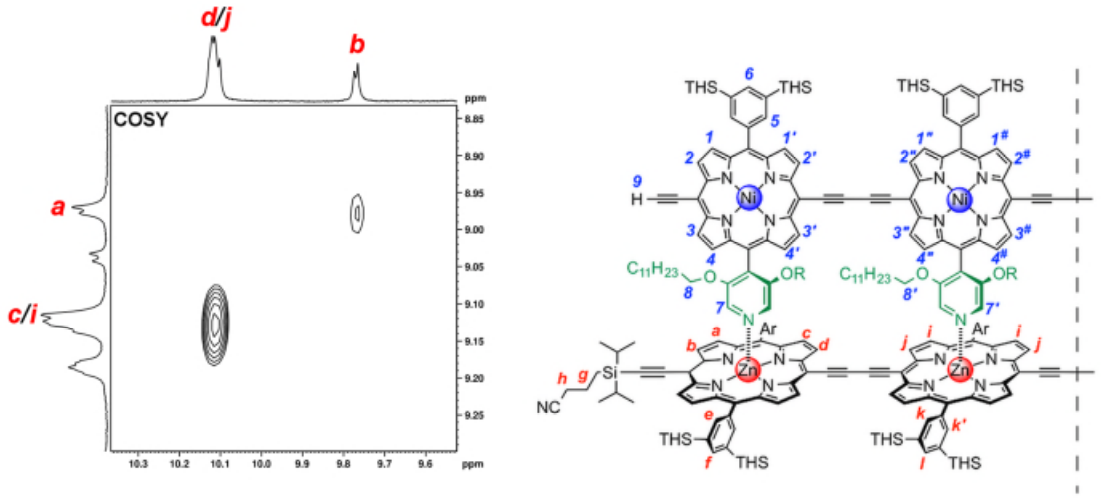

Figure 4.27 Region of the COSY spectrum of **CPDIPS-ZnP4•NiP4** corresponding to **CPDIPS-ZnP4** β-protons ***a***, ***b***, ***c***, ***d***, ***i*** and ***j*** (500 MHz, $CDCl_3$, 298 K).

β-protons ***a***, ***b***, ***c*** and ***d*** from the outer Zn porphyrin unit also show NOEs with outer aryl side-group proton ***e*** while β-protons ***i*** and ***j*** from the inner Zn porphyrin unit show NOEs with inner aryl side-group proton ***k*** and ***k'*** (**Figure 4.28**). Inner aryl side-group proton ***k*** and ***k'*** have coupling with each other as shown in **Figure 4.29**. Proton ***e*** also has coupling with aryl side-group proton ***f*** whereas proton ***k*** and ***k'*** have coupling with proton ***l*** in COSY spectrum (**Figure 4.29**).

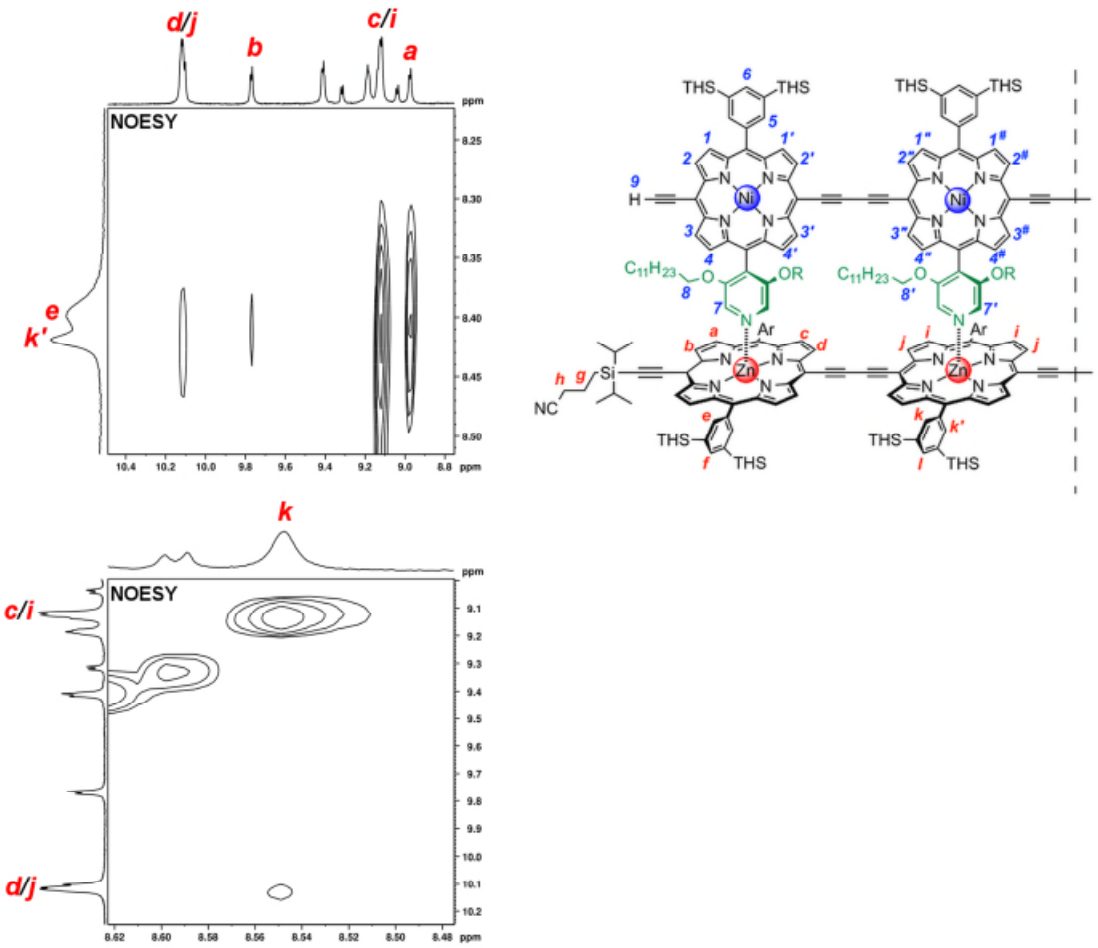

Figure 4.28 Region of the NOESY spectra of **CPDIPS-ZnP4•NiP4** corresponding to **CPDIPS-ZnP4** β-protons ***a***, ***b***, ***c***, ***d***, ***i*** and ***j*** and aryl side-group protons ***e***, ***k*** and ***k'*** (500 MHz, $CDCl_3$, 298 K).

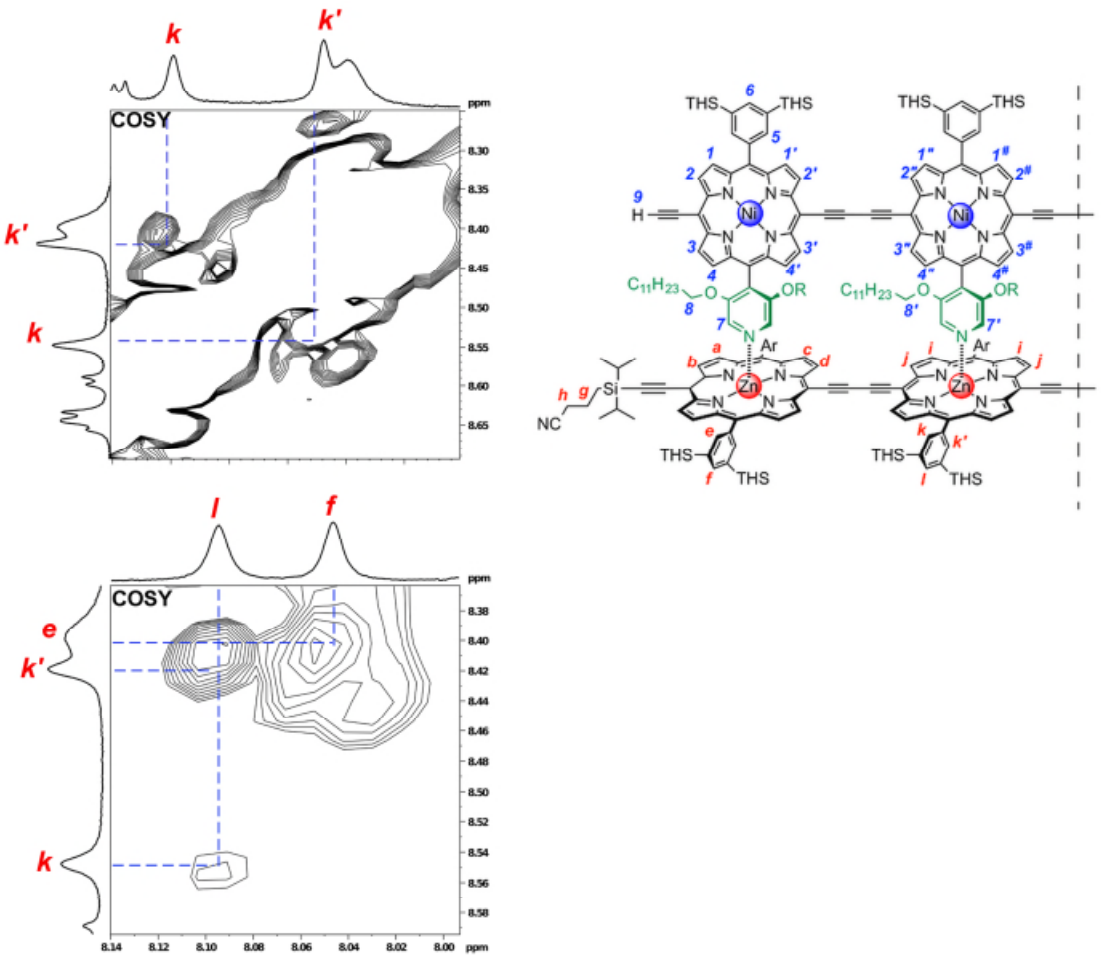

Figure 4.29 Region of the COSY spectra of **CPDIPS-ZnP4•NiP4** corresponding to **CPDIPS-ZnP4** aryl side-group protons ***e***, ***f***, ***l***, ***k*** and ***k'*** (500 MHz, $CDCl_3$, 298 K).

Protecting group protons ***g*** and ***h*** on the Zn strand were assigned based on their correlation in the COSY spectrum and the relationship of NOEs between proton ***g*** and proton ***b*** (**Figure 4.30**).

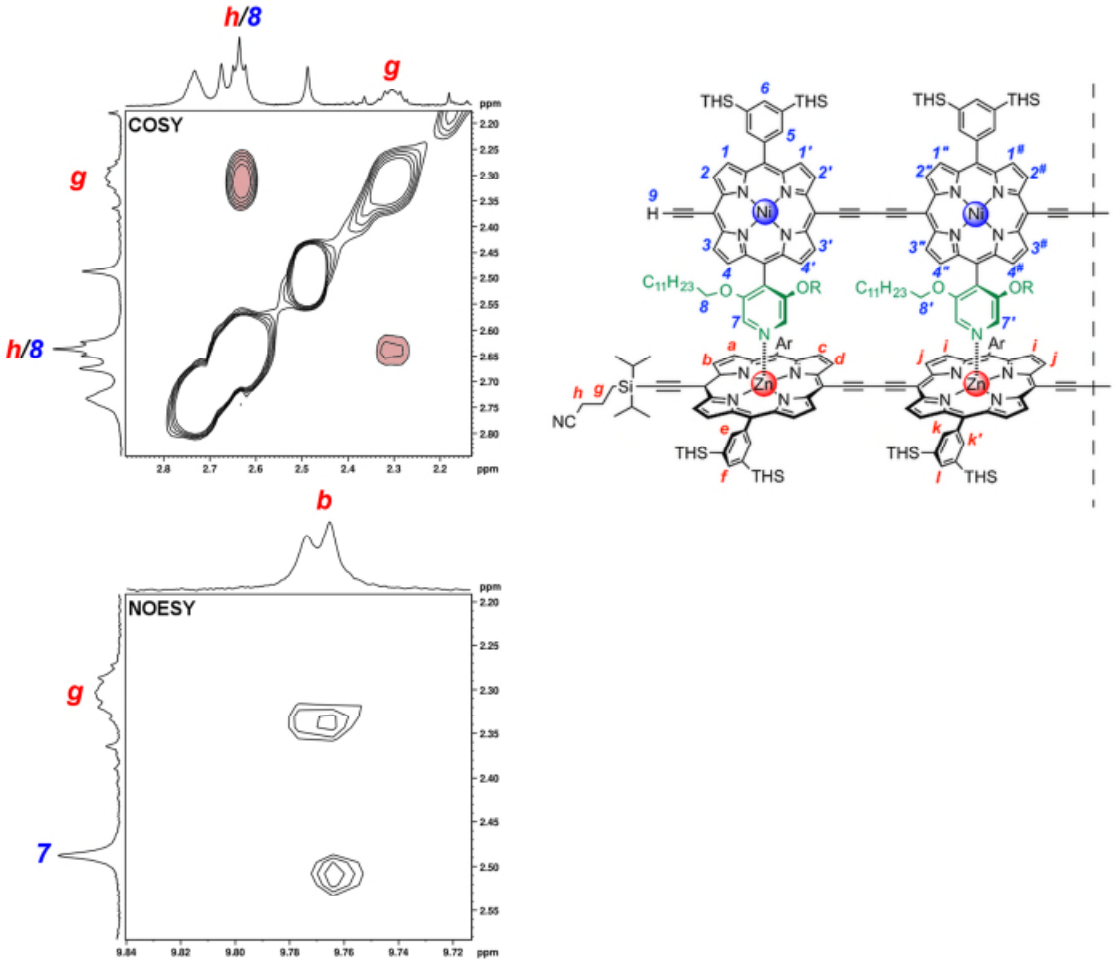

Figure 4.30 Region of the COSY and NOESY spectra of **CPDIPS-ZnP4•NiP4** corresponding to **CPDIPS-ZnP4** protecting group protons ***g*** and ***h*** and β-proton ***b*** (500 MHz, $CDCl_3$, 298 K). The pink colour of the peaks highlights the correlation between protons ***g*** and ***h*** in the COSY spectrum.

Due to the ring current effect, α-protons ***7*** (outer) and ***7'*** (inner) on pyridyl side-groups of **NiP4** are strongly shielded and appear as two singlet signals at very low chemical shifts (2.48 and 2.67 ppm, respectively). Two triplet signals of alkyl side-chain proton ***8*** (outer) and ***8'*** (inner) on the pyridyl side-groups of **NiP4** are also shielded from the ring current effect and shifted to the up-field at 2.63 and 2.73 ppm, respectively and the outer proton ***8*** is overlapping with the proton ***h*** of **CPDIPS-ZnP4**.

Furthermore, protons ***8*** and ***8'*** show a correlation with alkyl side chain protons at low chemical shifts (0.5 - 0.65 ppm) while protons ***7*** and ***7'*** do not have this correlation, confirming the assignment of ***7***, ***7'*** and ***8***, ***8'*** in the COSY spectrum (**Figure 4.31**).

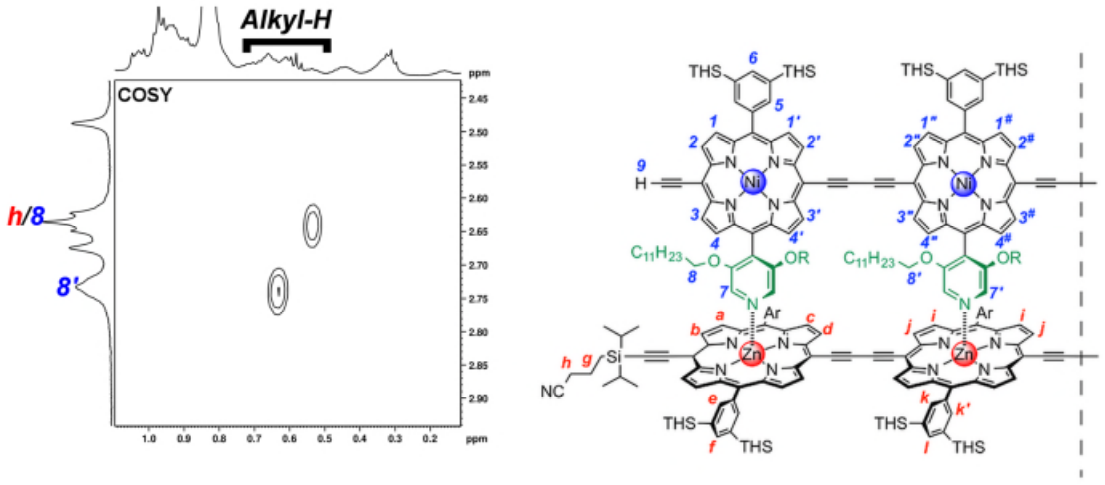

Figure 4.31 Region of the COSY spectrum of **CPDIPS-ZnP4•NiP4** corresponding to **NiP4** alkyl side-chain protons ***8*** and ***8'*** and alkyl side chain protons (500 MHz, $CDCl_3$, 298 K).

In the NOESY spectrum (**Figure 4.32**), α-pyridyl protons ***7*** and ***7'*** and alkyl side-chain proton ***8*** and ***8'*** on **NiP4** can be distinguished to be either on the outer or the inner Ni porphyrin units based on their NOEs with β-protons ***a***, ***b***, ***c***, ***d***, ***i*** and ***j***, and THS aryl side-group protons ***e*** and ***k*** on **CPDIPS-ZnP4**. α-proton ***7*** on the outer Ni porphyrin unit shows a NOE with β-protons ***a***, ***b***, ***c*** and ***d*** and THS aryl side-group proton ***e*** on outer Zn porphyrin unit whereas α-proton ***7'*** on the inner Ni porphyrin unit shows a NOE with β-protons ***i*** and ***j*** and THS aryl side-group proton ***k*** on the inner Zn porphyrin unit.

Additionally, alkyl side-chain proton ***8*** on the outer Ni porphyrin unit shows a NOE with β-proton ***a*** and THS aryl side-group proton ***e*** on the outer Zn porphyrin unit, while alkyl side-chain proton ***8'*** on the inner Ni porphyrin unit shows a NOE with β-protons ***i*** and ***j*** and THS aryl side-group proton ***k*** on the inner Zn porphyrin unit (**Figure 4.32**). NOE of protons ***7'*** and **8'** with proton ***k*** is confirmed that ***k*** is on the upper side and ***k'*** is on the lower side of the aryl group.

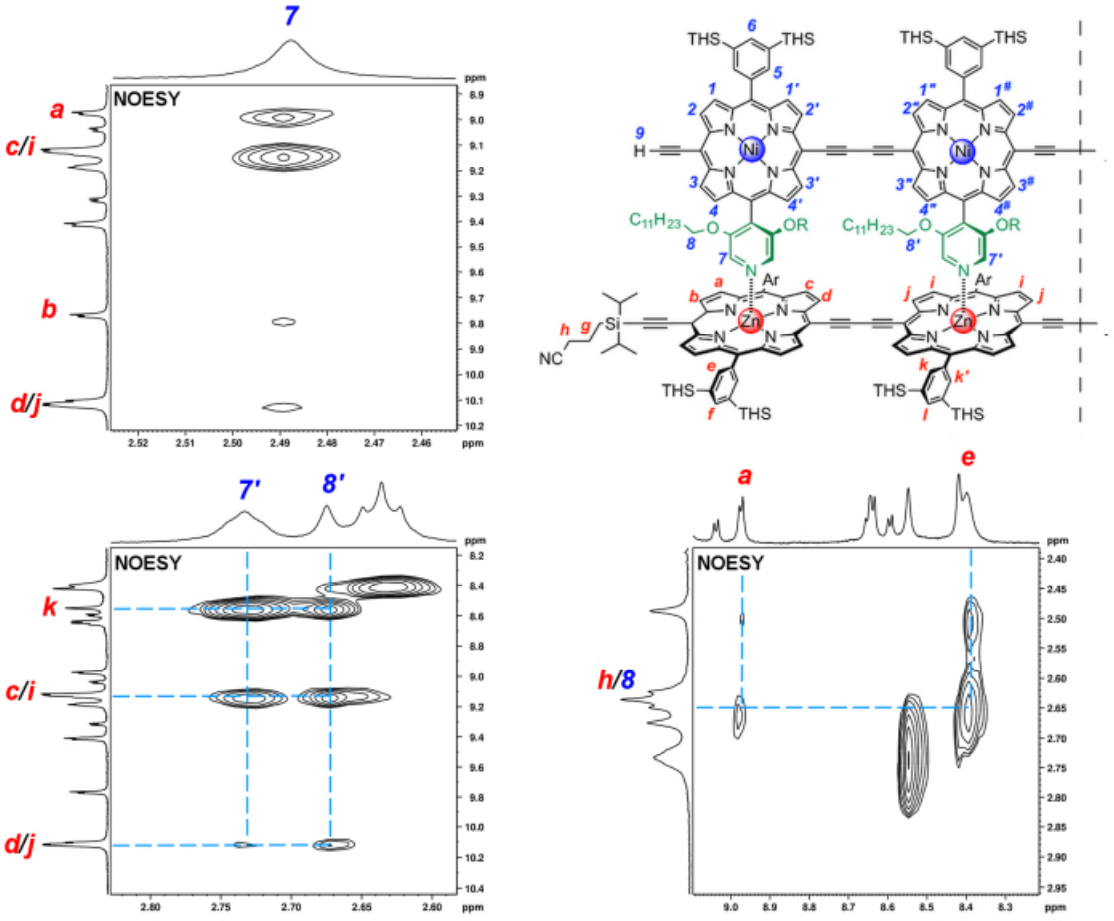

Figure 4.32 Region of the NOESY spectra of **CPDIPS-ZnP4•NiP4** corresponding to **NiP4** protons ***7***, ***7'***, ***8*** and ***8'*** and **CPDIPS-ZnP4** protons ***a***, ***b***, ***c***, ***d***, ***e***, ***i***, ***j*** and ***k*** (500 MHz, $CDCl_3$, 298 K).

Of the β-protons of **NiP4**, protons ***2***, ***2'***, ***2"***, ***2#***, ***3***, ***3'***, ***3"*** and ***3#***, which are adjacent to the triple bond, are higher chemical shift than protons ***1***, ***1'***, ***1"***, ***1#***, ***4***, ***4'***, ***4"*** and ***4#***. Protons ***2'***, ***2"***, ***2#*** and ***3'***, ***3"***, ***3#***, which point towards another porphyrin unit, have a stronger deshielding effect from the butadiyne bridge, providing higher chemical shift (9.41, 9.18 ppm, respectively) than outer protons ***2*** and ***3*** respectively (9.30, 9.03 ppm, respectively).

Apart from that, β-protons ***1***, ***1'***, ***1"*** and ***1#*** show NOEs with THS aryl side-group proton ***5*** and the coupling between β-protons ***1'***, ***1"***, ***1#***⇔***2'***, ***2"***, ***2#*** and ***1***⇔***2*** are also observed in the COSY spectrum. Based on these coupling and NOEs, ***1***, ***1'***, ***1"***, ***1#***, ***2***, ***2'***, ***2"***, and ***2#*** are readily assigned on the upper part of the Ni strand (**Figure 4.33**).

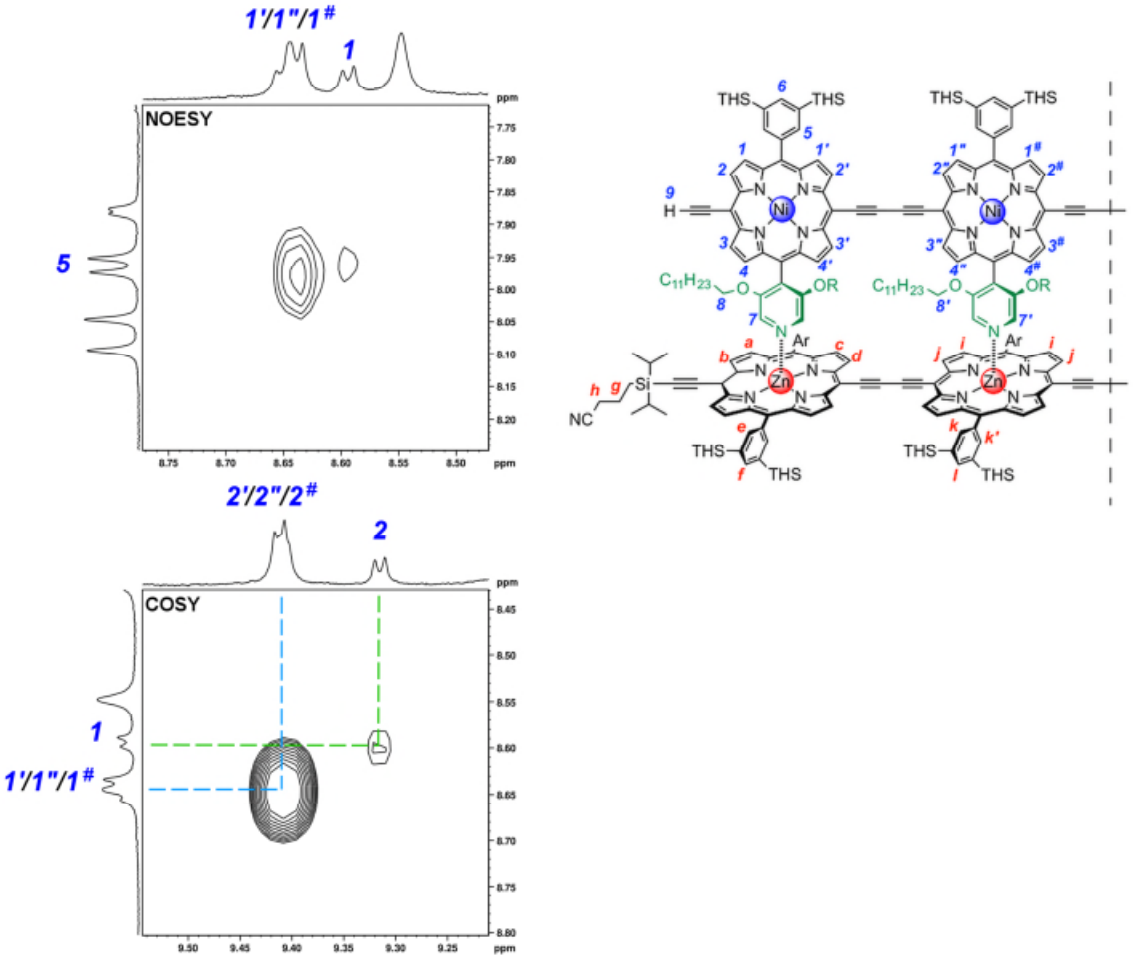

Figure 4.33 Region of the NOESY and COSY spectra of **CPDIPS-ZnP4•NiP4** corresponding to **NiP4** β-protons ***1***, ***1'***, ***1"***, ***1#***, ***2***, ***2'***, ***2"*** and ***2#*** and THS aryl side-group proton ***5*** (500 MHz, $CDCl_3$, 298 K).

In the lower part of the Ni strand, β-protons ***4***, ***4'***, ***4"*** and ***4$^{\#}$*** are more shielded due to the short distance to the ring current of the Zn strand than the other β-protons ***1***, ***1'***, ***1"***, ***1$^{\#}$***, ***2***, ***2'***, ***2"***, ***2$^{\#}$***, ***3***, ***3'***, ***3"*** and ***3$^{\#}$***, resulting in a downfield shift to 7.51-7.64 ppm.

As shown in **Figure 4.34**, β-protons ***4"*** and ***4$^{\#}$*** on the inner Ni porphyrin unit show NOE with α-pyridyl proton ***7'*** and alkyl side-chain proton ***8'*** from the same unit whereas β-protons ***4*** and ***4'*** on the outer Ni porphyrin unit show NOE with α-pyridyl proton ***7*** and alkyl side-chain proton ***8*** from the same unit. The coupling between protons ***3'***, ***3"***, ***3$^{\#}$*⇔*4'***, ***4"***, ***4$^{\#}$*** and ***3*⇔*4*** is observed in the COSY spectrum. This indicates that protons ***3***, ***3'***, ***3"*** and ***3$^{\#}$*** are also on the lower part of the Ni strand. The assignment of β-protons ***4***, ***4'***, ***4"*** and ***4$^{\#}$*** can be confirmed, based on their NOEs between protons ***7***, ***7'***, ***8*** and ***8'*** and their coupling with protons ***3***, ***3'***, ***3"*** and ***3$^{\#}$***.

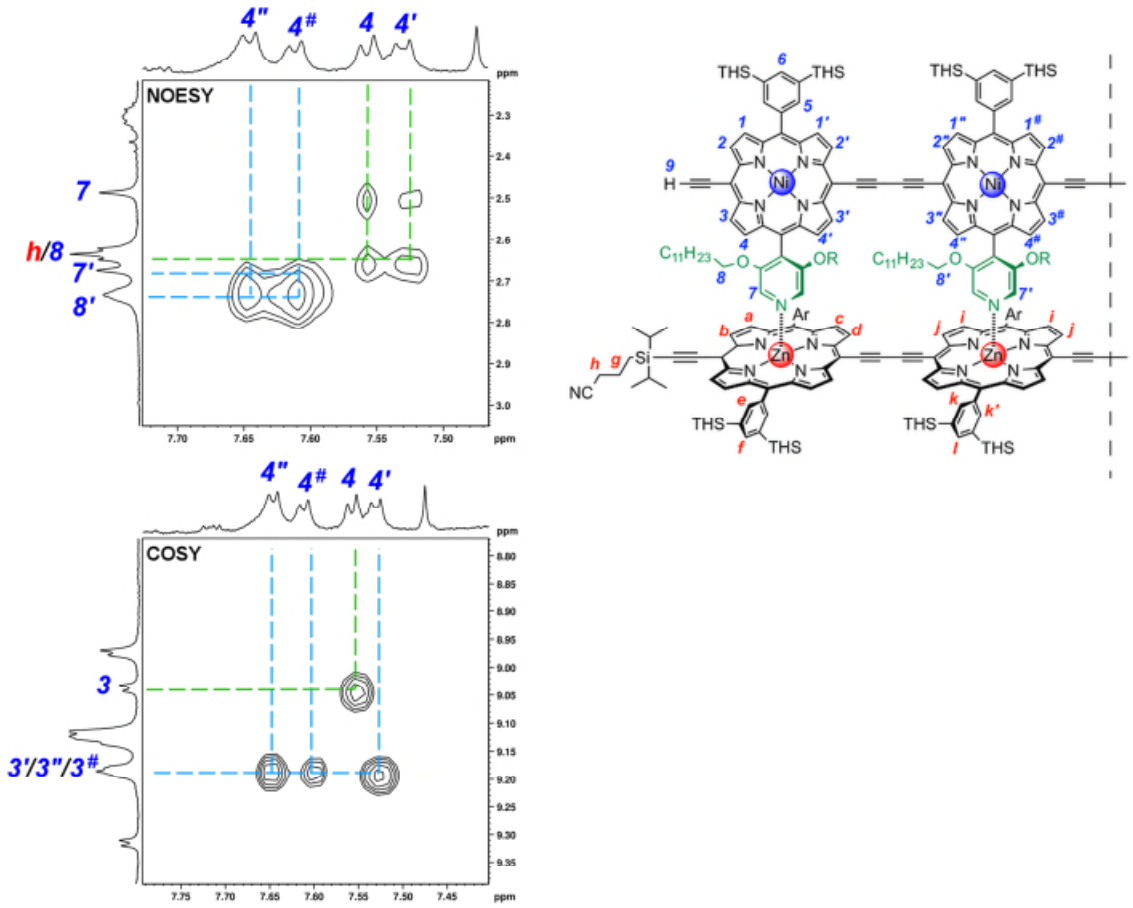

Figure 4.34 Region of the NOESY and COSY spectra of **CPDIPS-ZnP4•NiP4** corresponding to **NiP4** β-protons ***3***, ***3'***, ***3"***, ***3$^{\#}$***, ***4***, ***4'***, ***4"*** and ***4$^{\#}$*** and protons ***7***, ***7'***, ***8*** and ***8'*** (500 MHz, $CDCl_3$, 298 K).

The acetylene proton ***9*** is slightly shifted to the up-field since the small effect of ring currents from the Zn strand.

Apart from the assignment, key signals in the NOESY spectrum reveal the connection between two strands of **NiP4** and **CPDIPS-ZnP4** (**Figure 4.35**). Observation of NOEs shows the exchange correlation for both the protons of dodecyloxy group and the α-protons on the pyridyl side groups in the Ni strand with the *ortho*-protons of aryl side groups and the β-pyrrole protons of the porphyrin units in the Zn strand, confirming the close proximity of both strands.

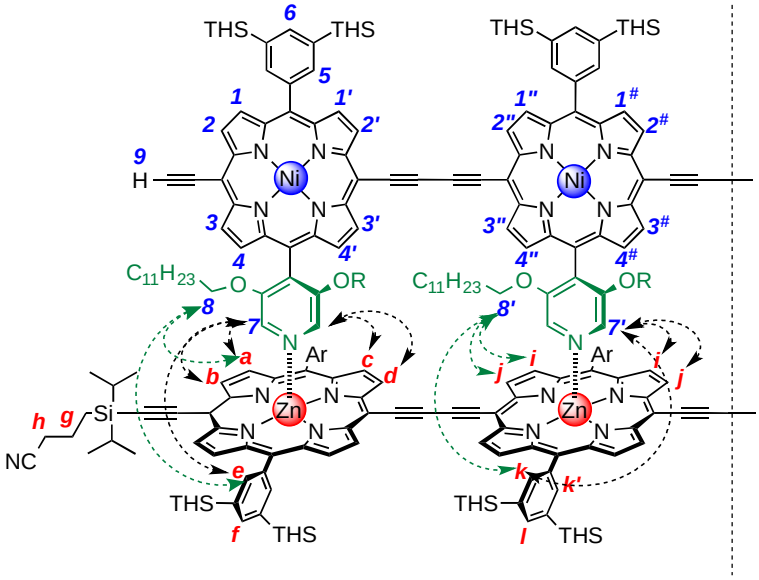

Figure 4.35 Key NOEs observed between the Ni porphyrin strand and the Zn porphyrin strand. NOEs are observed between both –OCH_2 of dodecyloxy side groups (green dotted line) and the α-protons on the pyridyl side groups (black dotted line) in the Ni strand with the *ortho*-protons of aryl side groups and the β-pyrrole protons of the porphyrin units in the Zn strand.

4.5.1.3 Changes in chemical shifts for protons in **CPDIPS-ZnP4•NiP4**

The ^{1}H NMR spectrum of the 4-rung ladder complex was also compared to that of the individual corresponding components: **NiP4** and **CPDIPS-ZnP4** (**Figure 4.36**), revealing significant differences in the aromatic region.

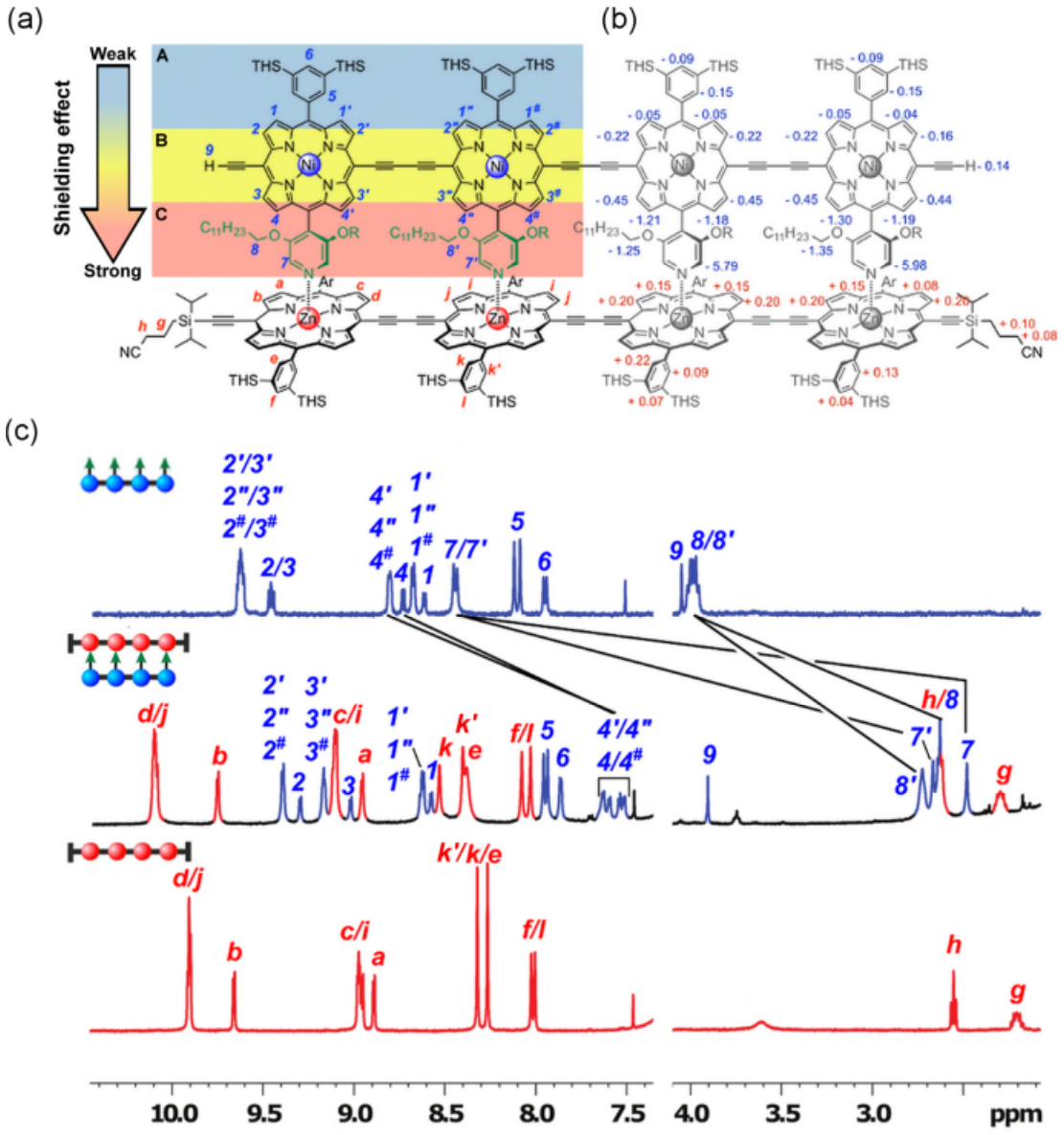

Figure 4.36 (a) The chemical structure of the 4-rung ladder complex **NiP4•CPDIPS-ZnP4** ($CDCl_3$, 500 MHz, 298 K) and signal assignment for the complex (red letters, protons on **CPDIPS-ZnP4**; blue letters, protons on **NiP4**). Three regions, A, B and C indicate the shielding effect from weak to strong based on the distance from the Zn porphyrin plane. (b) The chemical shift changes ($\Delta\delta$) induced by the shielding effects of the Zn porphyrin plane and the deshielding effect of the Ni porphyrin plane. (c) Comparison of ^{1}H NMR spectra of the 4-rung ladder complex **NiP4•CPDIPS-ZnP4** and the corresponding individual components (500 MHz, $CDCl_3$, 298 K); (bottom) red signals, ^{1}H NMR of **CPDIPS-ZnP4**; (middle) mixed-colour signals, ^{1}H NMR of **NiP4•CPDIPS-ZnP4**; (top) blue signals, ^{1}H NMR of **NiP4**. The black lines indicate the large change in chemical shift ($\Delta\delta$) between the ladder complex and free Ni strand as a consequence of the strong shielding effect of the ring-current of the Zn strand.

According to the proposed structure of the complex (**Figure 4.36a**), the Ni strand lies within the shielding region of the aromatic ring-current of the Zn strand, causing protons of the Ni strand at varying distances to experience different degrees of shielding. We roughly divide the degrees of the shielding effect depending on the distances of the protons of the Ni strands into three regions,

A, B and C from weak to strong effect (**Figure 4.36a**). The summary of the shielding effect from the Zn porphyrin plane is described by the change of chemical shifts ($\Delta\delta$) of **NiP4** protons between free form and bound form (to **CPDIPS-ZnP4**) as shown in **Figure 4.36b**. The magnitude of the shielding effect increases with decreasing distances from the Zn plane (from region A to C). Furthermore, this effect makes the overlapping signals of all protons in region B distinct from those of the free Ni strand, splitting up overlapping signals corresponding to protons ***2'***, ***2"***, ***2#***, ***3'***, ***3"***, ***3#*** to two groups of signals corresponding to protons ***2'***, ***2"***, ***2#*** and ***3'***, ***3"***, ***3#*,** and overlapping signals corresponding to protons ***2*** and ***3*** to two signals corresponding to protons ***2*** and ***3*** (**Figure 4.36c**). The strongest shielding effect is experienced by all protons in region C as a consequence of the closest distance to the Zn plane, providing the large change in chemical shift ($\Delta\delta$) for the β-pyrrole protons, ***4***, ***4'***, ***4"*** and ***4#*** at 1.17, 1.16, 1.19 and 1.27 ppm, respectively, for the α-protons on the pyridyl side groups, ***7*** and ***7'*** at 5.95 and 5.76 ppm, respectively, and for the protons of dodecyloxy group on the pyridyl side groups, ***8*** and ***8'*** at 1.34 and 1.24 ppm, respectively relative to the corresponding protons on free Ni strand (**Figure 4.36c**).

Every single proton of **NiP4** is influenced by the typical shielding effects from Zn porphyrin ring structure. The change of chemical shifts $\Delta\delta$ reflects the distances between protons of **NiP4** and the Zn porphyrin units.

4.5.2 MALDI-ToF Mass analysis of CPDIPS-ZnP4•NiP4

Additional support for the proposed structure of the 4-rung ladder complex was supplied by MALDI-ToF MS technique that proved to be a valuable tool for analyzing non-covalent complexes. As shown in **Figure 4.37**, the mass spectrum (DTCB matrix) of the complex revealed, besides the two peaks belonging to the individual components **NiP4** (*m*/*z* = 6004.6, expected 6002.3) and **CPDIPS-ZnP4** (*m*/*z* = 7174.9, expected 7175.9), the expected molecular peak of the corresponding supramolecular complex (*m*/*z* = 13,170, expected 13,178). This confirms the identity of the desired complex **CPDIPS-ZnP4•NiP4**.

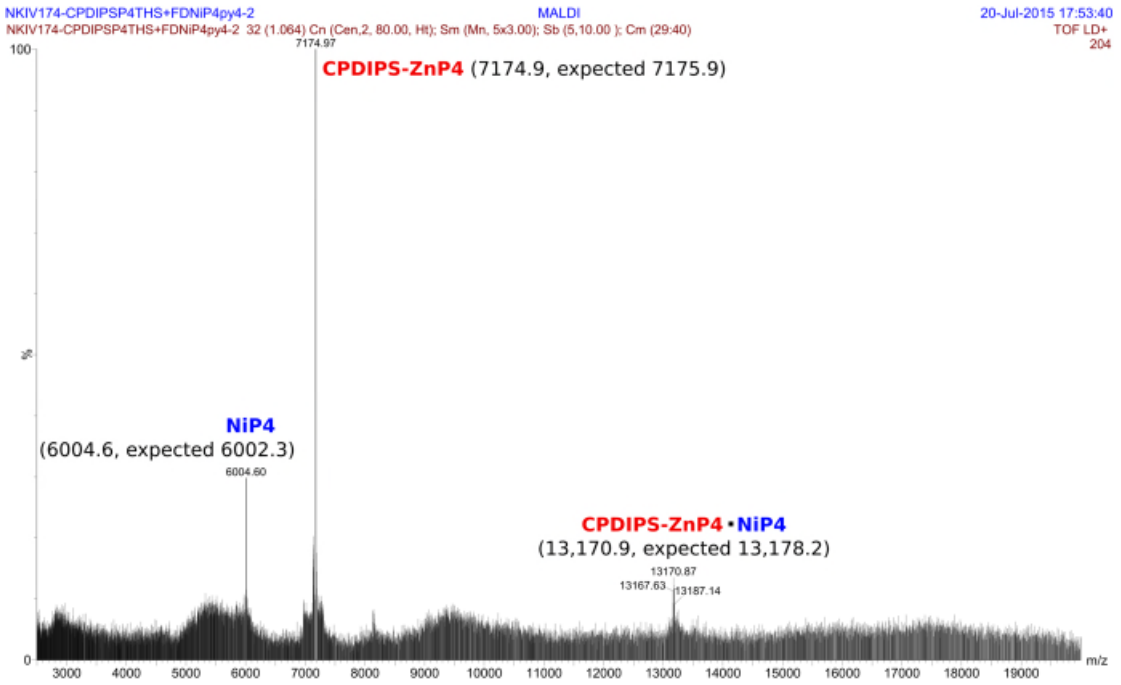

Figure 4.37 MALDI-ToF mass analysis of the **CPDIPS-ZnP4•NiP4** complex (DTCB as matrix).

4.6 Vernier template-directed synthesis (4 × 3 = 2 × 6)

To synthesise larger porphyrin oligomers by classical templating, we require the commensurate length of the templates, whose syntheses become difficult. An alternative approach we introduce here is linear Vernier templating, which is a facile approach to create a wide range in length of molecular ladders.

A trial experiment of Vernier templating was carried out using **PhA-NiP6** as a template and **ZnP4** as a substrate, to form the zinc porphyrin dodecamer **ZnP12**. This initial experiment was designed to optimise the templating conditions for the next strategy in template-directed synthesis, a Vernier-reciprocal templating which uses two substrates, **ZnP4** and **NiP6**, with no *real* template as will be described later in **Section 4.7**. The template **PhA-NiP6** was synthesised by Pd/Cu catalysed oxidative coupling between excess phenylacetylene **PhA** and fully deprotected Ni hexamer **NiP6** (see details of the synthesis of **PhA-NiP6** in **Experimental Section 4.9**). The templated reaction was set up similarly to the previous experiment; the substrate **ZnP4** and the template **PhA-NiP6** were mixed in a 3:2 stoichiometric ratio in dry DCM and stirred for 30 minutes (the complex was detected by UV-vis-NIR spectroscopy within 1 minute). Then the

coupling reagents CuCl and **2,2'-BiPy** was added into the reaction mixture. The control reaction with no template is identical to the Zn control which will be described in the next **Section 4.7**. The reaction was monitored by UV-vis-NIR spectroscopy every 30 min until there was insignificant change in the absorption spectrum from 3 to 4 h (**Figure 4.38c**), implying slower coupling reaction after 3 h. After removal of the coupling reagents and template, the reaction products were identified by analytical GPC (toluene/1% pyridine) based on calibrated retention times.[16] The analytical yields were calculated by peak fitting of resolved GPC peak areas from the absorption at 591 nm where all Zn species have the same extinction coefficient per porphyrin unit (**Figure 4.38d**).

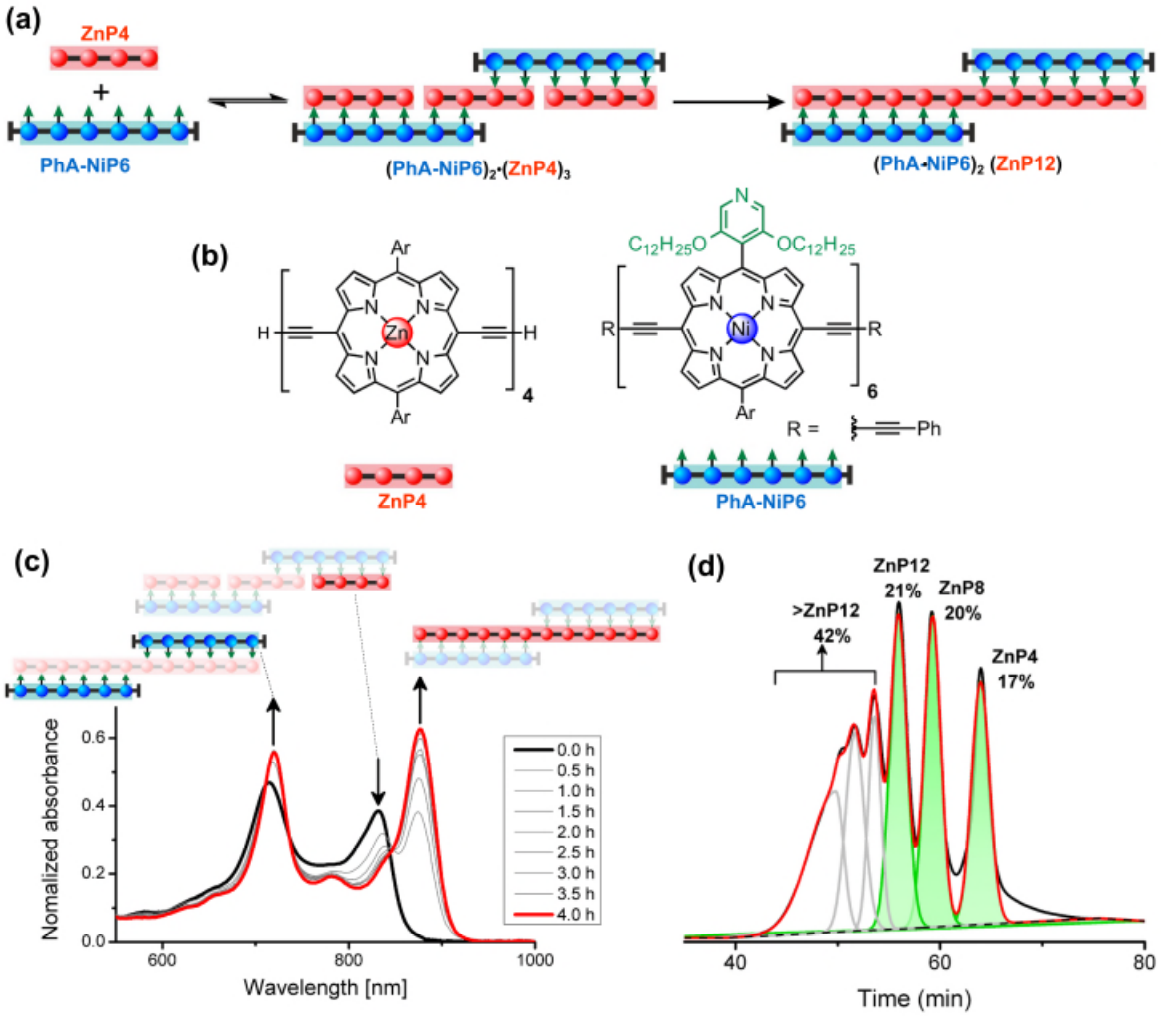

Figure 4.38 Reaction design and outcome of linear Vernier templating for the synthesis of the non-commensurate length product **ZnP12** from **ZnP4** using **PhA-NiP6** as a template. (a) Schematic representation of the linear Vernier templated synthesis of **ZnP12**. (b) Chemical structure of the substrate **ZnP4** and the template **PhA-NiP6**. Ar =3,5-bis(trihexylsilyl)phenyl. (c) The change in Q band of UV-vis-NIR absorption spectra of the templated synthesis of **ZnP12** from 0 h (black solid line) to 4 h (red solid line). (d) Recycling GPC traces (detection at 591 nm in first cycle, toluene/ 1% pyridine) of the linear templated

reaction product mixture after removal of the template **PhA-NiP6** at 4 h. Products were identified by analytical GPC based on calibrated retention times. The percentages in GPC traces represent the %GPC yields of corresponding compounds, calculated by integration of the peak areas.

As seen in **Figure 4.38d**, the substrate **ZnP4** was converted to two major products; the intermediate Vernier product **ZnP8** in 20% analytical yield and the desired product **ZnP12** in 21% analytical yield. The unreacted substrate **ZnP4** was observed in 17% analytical yield, indicating the slower coupling in the Vernier templating reaction than the classical templating reaction. It appears that template-directed formation of **ZnP8** is faster than subsequent coupling to form **ZnP12**. The GPC result shows that **ZnP12** can be synthesised by the linear Vernier templating reaction under this condition. Monitoring the formation of the desired product **ZnP12** by UV-vis-NIR spectroscopy is difficult for the Vernier templating reaction since Q-bands of longer Zn oligomers rise up at the same wavelength as **ZnP12**, as we see polymers appearing in 42% analytical yield. The yield of the desired product **ZnP12** could potentially be further improved by increasing the amount of the coupling reagent and reaction time, and changing the monitor to GPC rather than the UV-vis-NIR absorption.

4.7 Vernier-reciprocal template-directed synthesis ($4 \times 3 = 2 \times 6$)

4.7.1 Binding study of the Vernier assembly

In order to test the validity of the Vernier templating approach for the synthesis of larger porphyrin oligomers, we investigated the ability of Zn and Ni porphyrin oligomers to form Vernier complexes by studying the stability of the 2:3 complex between a Ni hexamer and a Zn tetramer, (**NiP6**)$_2$•(**ZnP4**)$_3$ (**Figure 4.39**).

The Vernier assembly could be characterised using UV-vis-NIR formation titration. The titration of **ZnP4** with **NiP6** was performed at a constant concentration of **ZnP4** (approximately 10^{-6} M) in dry DCM at 25 °C. When increasing amounts of the **NiP6** were added, the intensity of the Q-band absorption of free **ZnP4** at 764 nm decreased, and two new sharper Q-bands appeared at the blue- and red-shifted wavelengths of 712 nm and 836 nm corresponding to two bound porphyrin species, i.e. **NiP6** at 712 nm and **ZnP4** at 836 nm. Observation of three subsequent

isosbestic points at 0.5, 0.7 and 1.0 equivalents of **NiP6** indicates formation of a series of self-assembled complexes with **NiP6**:**ZnP4** complexes of 1:2, 2:3 and 1:1 stoichiometries as illustrated in **Figure 4.39** and **4.40a**. The titration data were analysed by SPECFIT in term of five coloured species, **ZnP4**, **NiP6**, 1:2, 2:3 and 1:1 complexes. The experimental data give an excellent fit to this model, yielding a binding constant of each species as shown in **Figure 4.40b** and listed in **Table 4.1**. Theses overall binding constants can be used to calculate the concentration at 50% bound (C_{50}) as shown in **Table 4.1**, resulting in C_{50} in order of (1:1) < (1:2) < (2:3). The calculation of C_{50} is shown in **Appendix**. This confirms that the 1:1, 1:2 and 2:3 assembly are present under micromolar concentration in this titration. The corresponding speciation profile (**Figure 4.40c**) shows that the intermediate 1:2 assembly appears before the 2:3 assembly becomes the major species (up to 80%) present at the appropriate stoichiometry, and then dissociation of the Vernier complex by excess **NiP6** occurs**.** The binding study suggests that the double strand approach provides the successful construction of the Vernier assembly with enough stability at the appropriate stoichiometry in DCM, suggesting the new approach for the synthesis of larger oligomers by linear Vernier templating is valid.

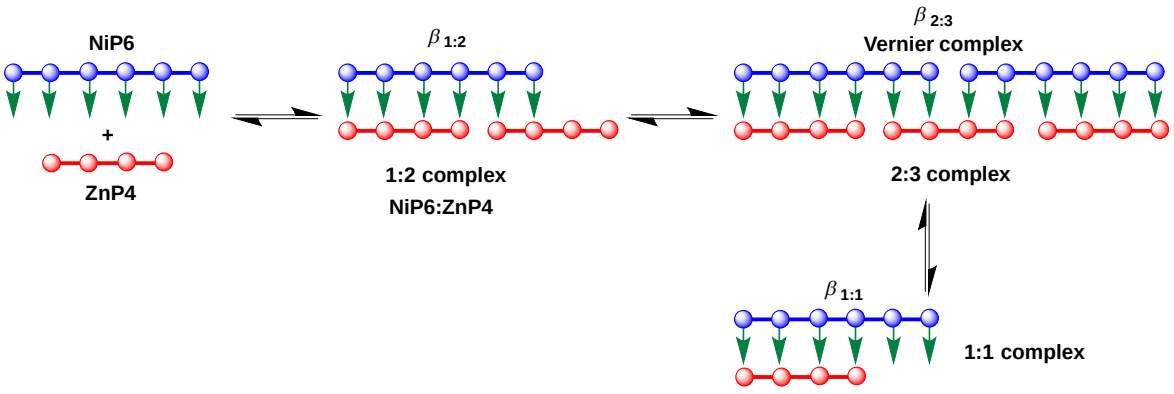

Figure 4.39 Complex formed between **ZnP4** and **NiP6**. The overall stability constants for the formation of each complex are provided in terms of $\beta_{1:2}$, $\beta_{2:3}$ and $\beta_{1:1}$.

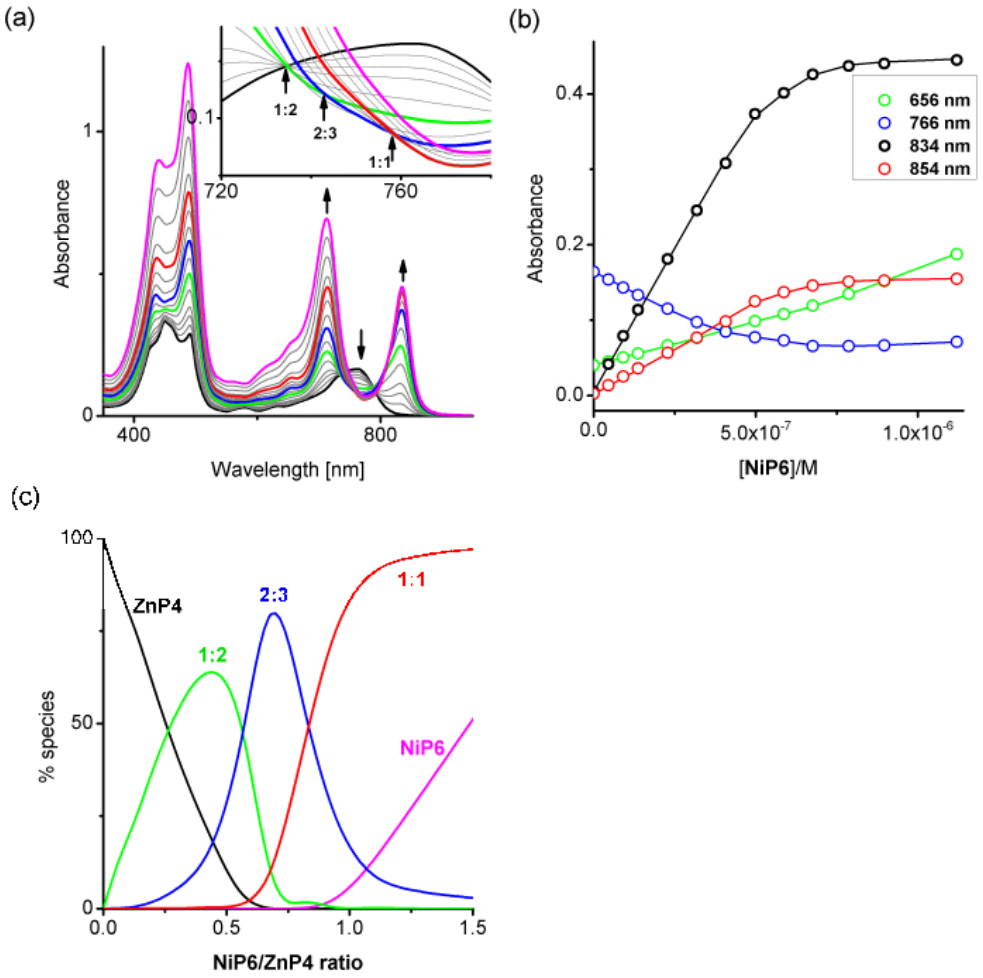

Figure 4.40 (a) UV-vis-NIR formation titration of **ZnP4** ([**ZnP4**] = 7.27 × 10^{-7} M) with **NiP6** in dry DCM at 298 K. Arrows indicate increasing or decreasing absorption (black, free **ZnP4**; green, 1:2 complex; blue, 2:3 complex, red, 1:1 complex and magenta, the end spectra of the **NiP6**-saturated-**ZnP4**). Inset: zoom-in of the change of isosbestic points in the absorption spectra. Arrows point out three subsequent isosbestic points at 0.5, 0.7 and 1.0 equivalents of **NiP6**, which is consistent with **NiP6**:**ZnP4** complexes of 1:2, 2:3 and 1:1 stoichiometries, respectively. (b) Binding isotherm (open dots) derived from absorption data at various wavelengths and fit obtained from global analysis with SPECFIT (solid lines). (c) The speciation plots as a function of the ratio [**NiP6**]/[**ZnP4**] (black, free **ZnP4**; green, 1:1 complex; blue, 2:3 complex, red, 1:1 complex and magenta, free **NiP6**).

Table 4.1 Overall stability constants (β) and concentration at 50% bound (C_{50}) of 1:2, 2:3 and 1:1 complexes from UV-vis-NIR formation titration.

Complex	log β			C_{50} (M)
	Run1	Run2	Average	
1:1	12.8 ± 0.51	12.6 ± 0.59	12.7 ± 0.39	(3.99 ± 1.03) × 10^{-13}
1:2	21.6 ± 0.63	21.9 ± 0.79	21.8 ± 0.51	(1.26 ± 0.47) × 10^{-11}
2:3	42.3 ± 0.88	41.7 ± 0.98	42.0 ± 0.66	(1.96 ± 0.79) × 10^{-11}

4.7.2 Vernier-reciprocal templating reaction

The result from the trial Vernier templating reaction in **Section 4.6** and the binding study of the Vernier complex in **Section 4.7.1** encouraged us to try the Vernier-reciprocal templating synthesis of two different types of linear metalloporphyrin 12-mers using two non-commensurate substrates **ZnP4** and **NiP6**. When both substrates form the Vernier ladder complex, under coupling conditions the Zn and Ni strand can serve as templates for each other in order to direct the construction of **ZnP12** and **NiP12** as expected from the lowest common multiple of the number of binding units of **ZnP4** and **NiP6** (**Figure 4.41**). It is not necessary for both strands to couple at the same time because after one strand couples, the Vernier product can act as a template for the other strand.

Similarly to the previous experiment, **ZnP4** and **NiP6** were mixed in a 3:2 stoichiometric ratio in dry DCM and the complex was detected by UV-vis-NIR spectroscopy within 1 min. Then the coupling reagent CuCl/**2,2'-BiPy** was added into the reaction mixture every three hours so as to maintain the coupling reaction since we observed slower coupling after 3 h in the trial Vernier templating reaction (**Section 4.6**). The reaction was monitored by taking aliquots and analysing them by GPC (eluting with 1% pyridine/THF) at 1, 3, 4, 6, 7 and 8 h. After 8 h, the reaction was further analysed by MALDI-ToF mass spectrometry.

Three control reactions were set up as follows (**Figure 4.41**):

- *Zn control*: This control was prepared in a similar approach to the Vernier-reciprocal templating reaction but in the absence of **NiP6** so that we can see the statistical homocoupling of **ZnP4** on its own.
- *Ni control*: This control was prepared similarly to the Vernier-reciprocal templating reaction but in the absence of **ZnP4** in order to understand the statistical homocoupling of **NiP6** with no template-like effect.
- *Pyridine control*: This control was set up in identical condition to the Vernier- reciprocal templating reaction but in the presence of 10% pyridine so that pyridine can inhibit the formation of the Vernier complex $(\mathbf{ZnP4})_3\bullet(\mathbf{NiP6})_2$. As a result, the coupling reaction

between **ZnP4** and **NiP6** would randomly produce the homocoupling product from Ni and Zn species and heterocoupling between Ni and Zn species in the presence of pyridine.

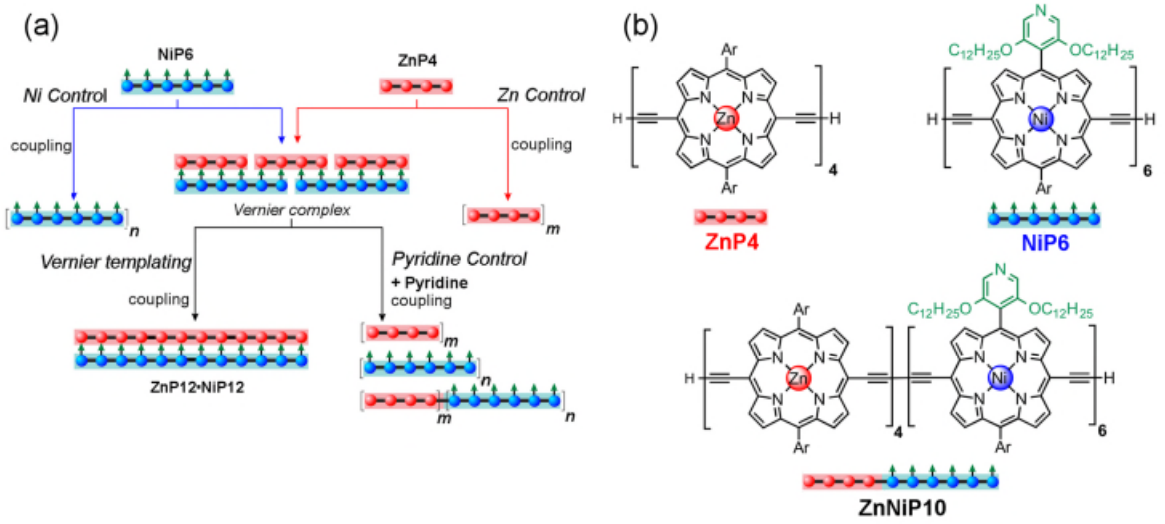

Figure 4.41 (a) The Vernier-reciprocal templating and three control reactions for the synthesis of **NiP12** and **ZnP12**. *m* and *n* are the number of the repeat units. (b) Chemical structures of two types of substrates **ZnP4** and **NiP6** and an example of heterocoupling product **ZnNiP10**.

The results from all reactions are presented in 2D-plots of the retention times versus Q-band absorption spectra, deconvoluted GPC traces and 1D-plots of analytical concentrations that were calculated by peak fitting of resolved GPC peak areas, and MALDI-ToF mass analysis, respectively, as follows.

2D-Plots. Interestingly, the 2D-plots of the retention times versus Q-band absorption spectra (**Figure 4.42c**) allow the identification of the type of metalloporphyrins by the characteristic absorptions of Ni porphyrins at shorter wavelength than Zn porphyrins, even when the Ni and Zn porphyrin oligomers give unresolved overlapping peaks in the 1D GPC traces. In addition, we can see the growing formation of the products by monitoring the change in the Q-bands of corresponding compounds, yielding consistent results with the trends from the deconvoluted GPC traces to be discussed later.

The Vernier products in the beginning of the templating reaction show the relatively weak Q-band for **ZnP12** whereas **ZnP8** and **NiP12** are quite intense, but at the end the three products have almost the same intensity (**Figure 4.42c**–*Vernier-reciprocal templating*). Although the

retention times of **NiP12** and **ZnP12** are very close, their corresponding Q-bands can still be deconvoluted from the shorter and longer absorption wavelengths.

The Q-bands in the Zn control are more red-shifted in shorter retention times with increasing reaction time, reflecting the formation of longer Zn oligomers (**Figure 4.42c**-*Zn control*) while the Q-bands in the Ni control show up at shorter wavelengths and are mostly unchanged, indicating slow conversion from **NiP6** to **NiP12** and small amount of polymers at shorter retention times (**Figure 4.42c**-*Ni control*).

Strikingly, in the pyridine control, in addition to the expected distinctive absorptions from Ni and Zn porphyrin oligomers, we can see the Q-band absorption in regions where both species absorb, confirming the formation of the product **ZnNiP10** of heterocoupling between **ZnP4** and **NiP6** (**Figure 4.42c**-*Pyridine control*).

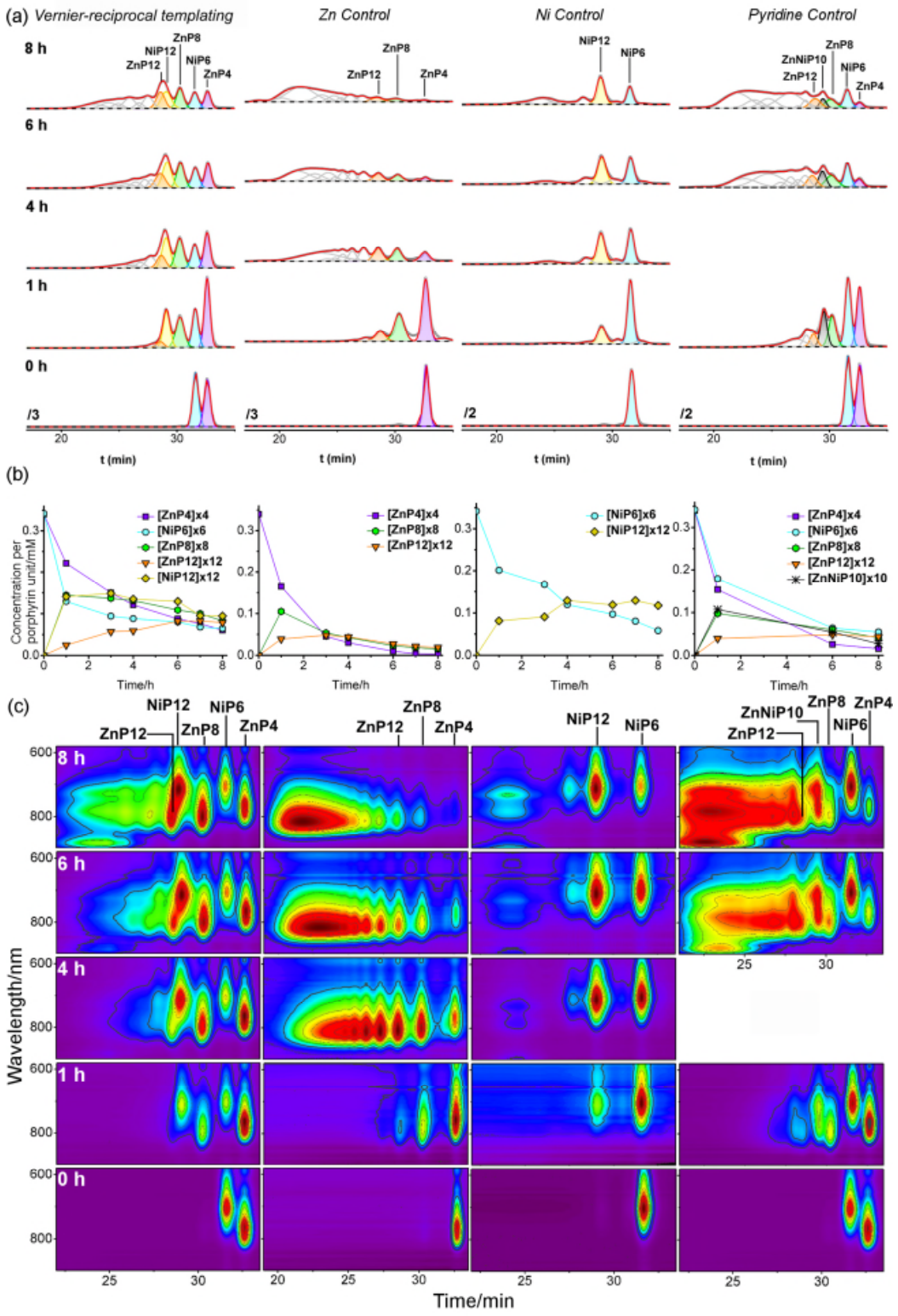

Figure 4.42 The outcome of the Vernier-reciprocal templating and three control reactions of the synthesis of **NiP12** and **ZnP12**. (a) The selected deconvoluted GPC traces fitted by Origin® at 0, 1, 4, 6 and 8 h, respectively (THF/ 1% pyridine, detection at 479 nm where all species have essentially the same extinction coefficient per porphyrin unit). (b) The plots of analytical yields that were calculated by peak fitting of resolved GPC peak areas. (c) The selected 2D-plots at 0, 1, 4, 6 and 8 h, respectively. The intensity was normalised by rainbow colours from purple (lowest) to red (highest). The retention times of all components were calibrated from known compounds, and their identification was based on the calibrated retention time in GPC.

Deconvoluted GPC traces and 1D-plots. Figure 4.42a shows deconvoluted GPC traces of the Vernier-reciprocal templated and three control syntheses of **ZnP12** and **NiP12** from the absorption at 479 nm where all species have essentially the same extinction coefficient per porphyrin unit (see the extinction coefficient spectra in **Experimental section 4.9**). All components were assigned based on their retention times, using a calibration scale based on the retention times of known compounds (see the detail of analytical GPC calibration in **Experimental section 4.9**). Analytical yields were calculated by peak fitting of resolved GPC peak areas (**Figure 4.42a** and **b**).

In the beginning of linear Vernier-reciprocal templating (at 1 h), the Zn strand accelerates the coupling reaction of **NiP6** yielding **NiP12** in 41% whereas **ZnP12** forms only in 7% yield, and partial coupling from **ZnP4** to **ZnP8** (42%) was observed at the same yield as **NiP12**. It can be seen that the Zn strand speeds up the coupling reaction of the Ni strand as **NiP6** is consumed faster than in the Ni control (**Figure 4.42a,b**-*Vernier-reciprocal templating* compared to *Ni control*). Surprisingly, the Ni strand appears to slow down the coupling of the Zn strand compared to the corresponding control (**Figure 4.42a,b**-*Vernier-reciprocal templating* compared to *Zn control*). Then while **ZnP8** is gradually converted to **ZnP12**, **NiP12** can further couple to form longer oligomers due to the absence of protecting groups at the acetylenic ends. After 8 h, the yields of the three products **ZnP8** (24%), **ZnP12** (23%) and **NiP12** (28%) became almost equivalent (**Figure 4.42a,b**-*Vernier-reciprocal templating*). Both desired products **NiP12** and **ZnP12** could convert to their corresponding longer oligomer as far as the coupling reagent is still active, providing traces of high-mass oligomers as seen in the GPC traces at longer reaction times (**Figure 4.42a**-*Vernier- reciprocal templating*). If we had stopped the Vernier templating reaction at the right time (i. e. 6 h), the best yields of the desired Vernier products would have been achieved (38% for **NiP12** and 24% for **ZnP12**).

As expected, the Zn control reaction led to the increasing statistical coupling of the Zn oligomer products as time proceeded, yielding polymers as the major products at the end of the reaction time (at 8 h). In the beginning at 1 h, the unreacted substrate **ZnP4** was dominant at 48% and **ZnP8** and **ZnP12** were also observed in 31% and 11% yield respectively. With increasing time

from 3 to 8 h, the polymers become the major products and yields of **ZnP8** (from 16% to 4%) and **ZnP12** (from 14% to 6%) become identical and very low. The highest yield of **ZnP12** (14%) is still much lower than from Vernier-reciprocal templating (24%) (**Figure 4.42a,b**-*Zn control*).

On the other hand, the Ni control reaction gradually produced **NiP12** and a small trace of polymers due to the slow coupling rate of the Ni porphyrins, however without template effect, the yield of **NiP12** in the beginning (24% at 1 h) is almost two times lower than from the Vernier templating (41%) and then increases to 34% at 8 h (**Figure 4.42a,b**-*Ni control*).

In the pyridine control (**Figure 4.42a,b**-*Pyridine control*), homocoupling products **ZnP8** (from 28% to 12%) and **ZnP12** (from 12% to 13%) were statistically produced at almost the same rate as in the Zn control from 1 to 8 h. **NiP12** is not clearly observed in the GPC traces while the new species of the product of heterocoupling between **ZnP4** and **NiP6** was obviously observed as anticipated, yielding the 10-porphyrin unit oligomer **ZnNiP10** in 29% and reducing to 7% yield from 1 to 8 h. At the end in 8 h, the polymers become the main products.

Since the retention time of **ZnP12** and **NiP12** are very close at 28.55 and 29.05 min in the Vernier-reciprocal templated reaction, there is uncertainty in the fitting area of the corresponding deconvoluted peaks. Thus, to confirm the reliability in the fitting results, yields of the product mixtures at 779 nm where only Zn species absorb were determined and compared indirectly by the product-to-substrate ratios of **ZnP12**/**ZnP4** and **ZnP8**/**ZnP4** to those at 479 nm, resulting in a good agreement of the values in both wavelengths as shown in **Figure 4.43**.

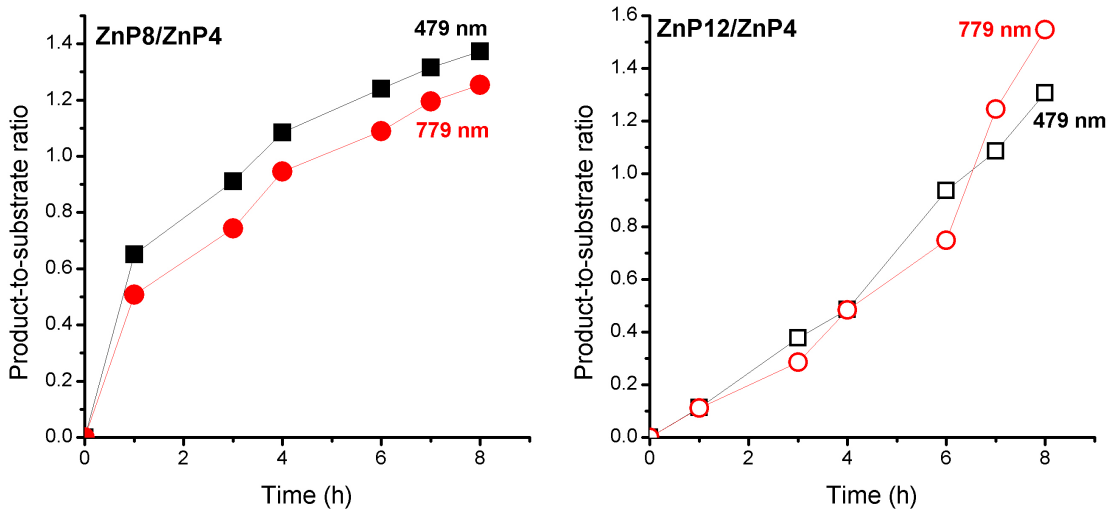

Figure 4.43 Comparison of the product-to-substrate ratios from the Vernier templating reaction, calculated at different wavelengths. (Left) The product-to-substrate ratios of **ZnP8**/**ZnP4** calculated from the GPC traces at 479 (black solid squares) and 779 nm (red solid circles). (Right) The product-to-substrate ratios of **ZnP12**/**ZnP4** calculated from the GPC traces at 479 (black open squares) and 779 nm (red open circles). The solid lines are a guide to the eye.

MALDI-ToF mass analysis. To support the analyses by the calibrated GPC retention time, the product species in the Vernier-reciprocal templating and the control reactions were also analysed by the MALDI-ToF mass spectrometry (**Figure 4.44-4.47**). Mass peaks are quite broad due to the low resolution of the detector for high-molecular weight molecules, but it is still sufficient to identify the peaks since all predicted products have a mass difference of at least 2000 Da.

The summary of mass analysis is shown in **Table 4.2**. In the Vernier-reciprocal templating reaction, the mass spectrum reveals the presence of all substrates **ZnP4** and **NiP6**, the intermediate **ZnP8** and desired products **ZnP12** and **NiP12**. No cross-coupling product **ZnNiP10** was detected from the Vernier-reciprocal templating, confirming the strong template effects. Statistical homocoupling species were observed as expected in both Zn and Ni controls, whereas the pyridine control provided not only both homocoupling products from Zn and Ni species but also heterocoupling products such as **ZnNiP10** as expected.

The mass data are also in good agreement with the assignment of all species in GPC traces as discussed above.

Table 4.2 The summary of mass data in the Vernier-reciprocal templating and three control reactions

Compound	MW (g/mol) (calculation)	*m*/*z* (g/mol) (observed)			
		Vernier-reciprocal	Zn control	Ni control	Pyridine control
ZnP4	6811.2	7026.5	7134.6		7176.1
ZnP8	13620.4	14174.7	14308.7		14379.4
ZnP12	20429.6	21302.4	21364.2		21406.5
ZnP16	27238.8		28519.4		
NiP6	9002.4	9689.3		9684.1	9820.2
NiP12	18002.9	19086.8		19238.3	
NiP18	27003.3			28780.9	
ZnNiP10	15813.6				16888.1
ZnNiP14	22622.8				24124.6

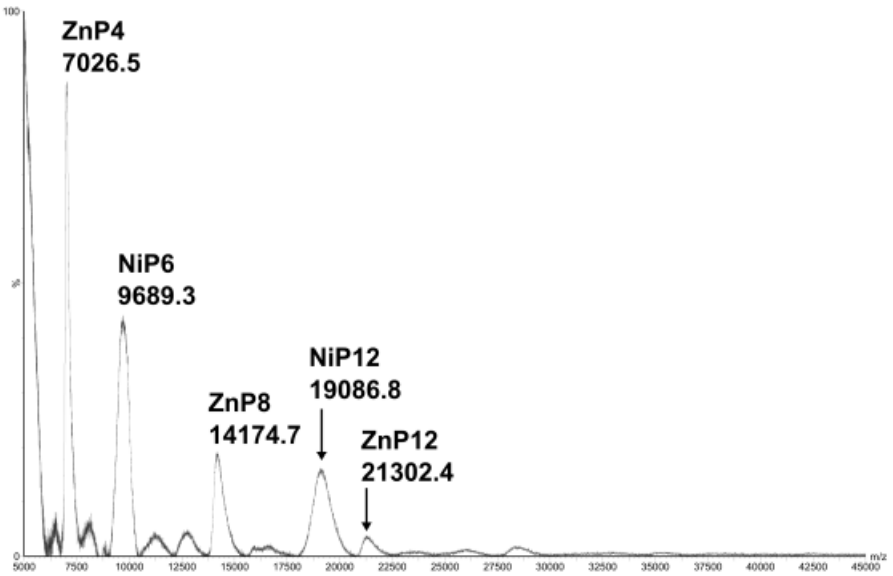

Figure 4.44 MALDI-ToF mass analysis of the product mixture of the Vernier-reciprocal templating reaction (flight mode: linear, matrix: DTCB).

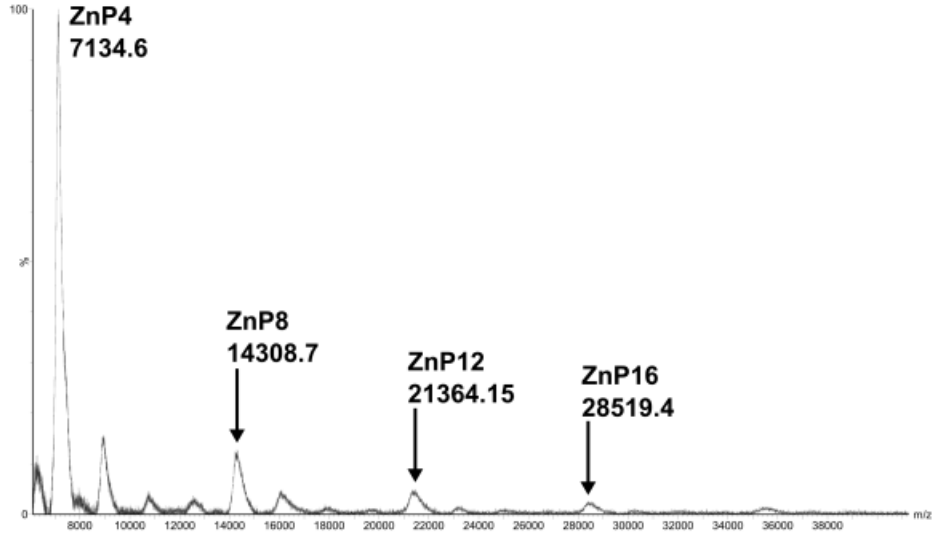

Figure 4.45 MALDI-ToF mass analysis of the product mixture of the Zn control reaction (flight mode: linear, matrix: DTCB).

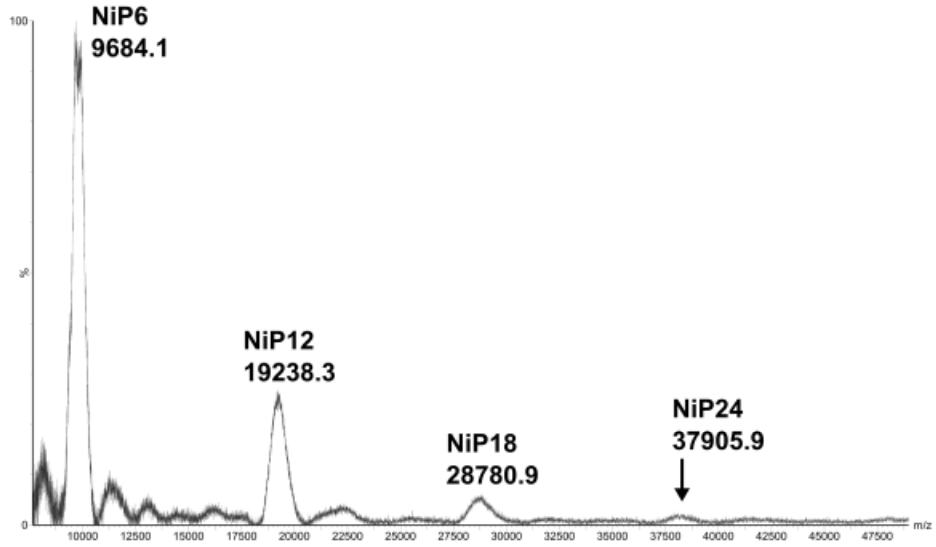

Figure 4.46 MALDI-ToF mass analysis of the product mixture of the Ni control reaction (flight mode: linear, matrix: DTCB).

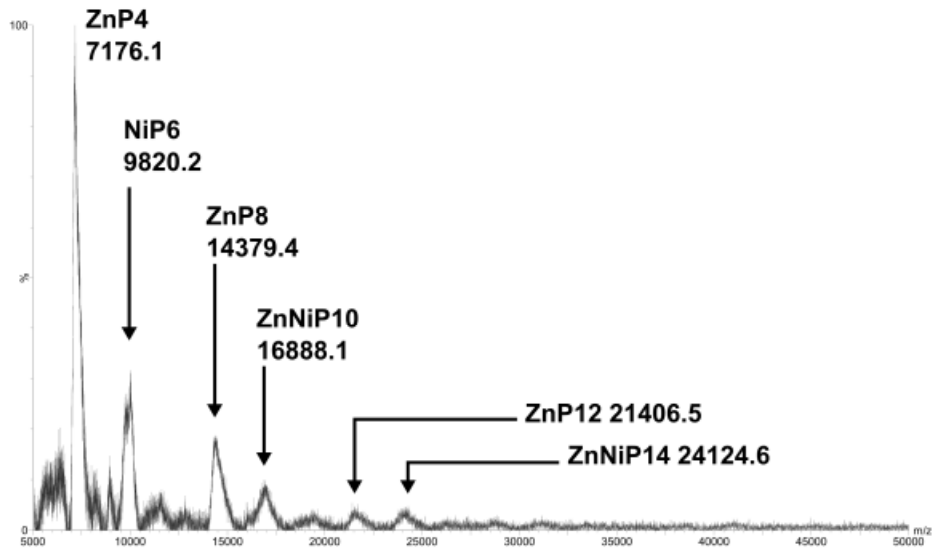

Figure 4.47 MALDI-ToF mass analysis of the product mixture of the pyridine control reaction (flight mode: linear, matrix: DTCB).

4.7.3 Comparison to cyclic Vernier templating synthesis

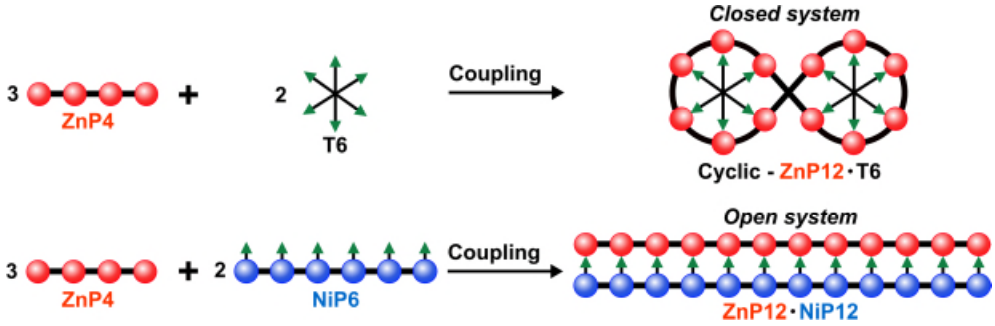

Figure 4.48 Comparison between cyclic Vernier and linear Vernier-reciprocal templating reactions.

In comparison to the cyclic Vernier templating synthesis of cyclic 12-porphyrin nanoring using the Zn porphyrin tetramer substrate and radial hexapyridyl ligand template (**T6**) as published,[14,15] the linear Vernier-reciprocal templating approach here shows that two distinctive species **NiP12** and **ZnP12** can be synthesised without a *real* template, rather than one species (**Figure 4.48**). Despite the fact that the unprotected end groups of the products **NiP12** and **ZnP12** can react further to produce polymeric mixtures in the linear route (a problem that does not arise in the case of the closed structure of the cyclic templates), the efficiency of the two methods are comparable in term of the range of yields (38% for **NiP12** and 24% for **ZnP12** compared to 39% for cyclic 12-mer[14]). In fact, using non-covalent metal ligand coordination to assemble the Vernier complex rather than

dynamic covalent bonding for the linear route is beneficial because the misaligned Vernier complex can be rearranged to reach the equilibrium faster, leading to higher yields of the coupling products[11] if the reaction is stopped at the right time.

4.8 Summary

Linear porphyrin oligomers of up to six porphyrin units were successfully synthesised by the classical templating approach using complementary templates and substrates with commensurate lengths under oxidative-coupling conditions, in a manner reminiscent of DNA replication. The porphyrin templates in the conventional approach can be recovered in a very high yield, up to 85%, making this method efficient for creating large amounts of desired products without the need to synthesise more template for every production cycle. However, classical templating is not suitable for the synthesis of larger linear oligomers due to the challenge in the synthesis of large templates. To solve this problem, we exploited the linear Vernier-reciprocal template-directed synthesis to demonstrate the construction of two complementary supramolecular oligomers with well-defined length via the Vernier assembly of two different types of small substrates. The Vernier-reciprocal templating gives much higher yields of the Vernier products than in the controls, proving the effectiveness of the template effects. This approach can be used as another toolbox for supramolecular syntheses of nanoscopic materials with photophysical properties of interest from simple components.

4.9 Experimental section

4.9.1 General methods

All chemicals were purchased from commercial suppliers and used without further purification unless otherwise stated. CuCl was freshly prepared.[31] Dry CH_2Cl_2 was obtained by passing through a column of activated alumina under nitrogen pressure. Diisopropylamine (DIPA) was dried over calcium hydride, distilled and stored under nitrogen over molecular sieves. "Petrol ether" (PE) always refers to 40/60 petrol ether. NMR data were recorded at 500 MHz using a Bruker AVII500 (with cryoprobe) or DRX500, or at 400 MHz using a Bruker AVII400 or AVIII400, or at 700 MHz using a Bruker AVIII700 (with cryoprobe) at 298 K. Chemical shifts are quoted as parts per million (ppm) relative to residual $CHCl_3$ (δ_H 7.27 ppm for ^{1}H NMR and at δ_C 77.2 ppm for ^{13}C NMR) and coupling constants (*J*) are reported in Hertz. MALDI-TOF-MS was measured with a Waters MALDI Micro MX spectrometer. *Trans*-2-[3-(4-*tert*-butylphenyl)-2-methyl-2-propenylidene]malononitrile (DTCB) was used as a matrix for all MALDI-TOF measurements. All UV-vis-NIR spectra were recorded at 25 °C on Perkin-Elmer Lambda 20 photospectrometer using quartz 1 cm cuvettes. UV-vis-NIR titrations were analyzed by calculating the difference in absorptions and plotted using Origin® software or fitted with predicted models using SPECFIT software. Size exclusion chromatography (SEC) was carried out using Bio-Beads S-X1, 200– 400 mesh (Bio Rad). Analytical and semi-preparative GPC were carried out on Shimadzu Recycling GPC system equipped with LC-20 AD pump, SPD-M20A UV detector and a set of JAIGEL 3H (20 × 600 mm) and JAIGEL 4H (20 × 600 mm) columns in toluene/1% pyridine as eluent with a flow rate of 3.5 mL/min or carried out on VWR Hitachi Lachrom Elite (pump L-2130, Autosampler L-2200, Diode Array Detector L-2450, Column oven L-2350) and a set of JAIGEL 3H-A (8 × 500 mm) and JAIGEL 4H-A (8 × 500 mm) columns in THF/1% pyridine as eluent with a flow rate of 1.0 mL/min.

4.9.2 Synthetic procedures

4.9.2.1. Synthesis of known compounds

Fully protected Zn porphyrin monomer **CPDIPS-ZnP1**,[32] Fully protected and fully deprotected Zn porphyrin dimer **THS-ZnP2**[6] and **ZnP2**,[6] Fully protected and fully deprotected Zn porphyrin tetramer **THS-ZnP4**,[6] **CPDIPS-ZnP4**[32] and **ZnP4**,[32] Zn porphyrin pentamer **THS-ZnP5**[6], Zn porphyrin hexamer **THS-ZnP6**[6] and Freebase-pyridyl porphyrin dimer **THS-H2P2py**[32] were synthesised by previously published procedures.

4.9.2.2. Synthesis of Novel compounds

Fully deprotected Ni pyridyl porphyrin dimer **NiP2**

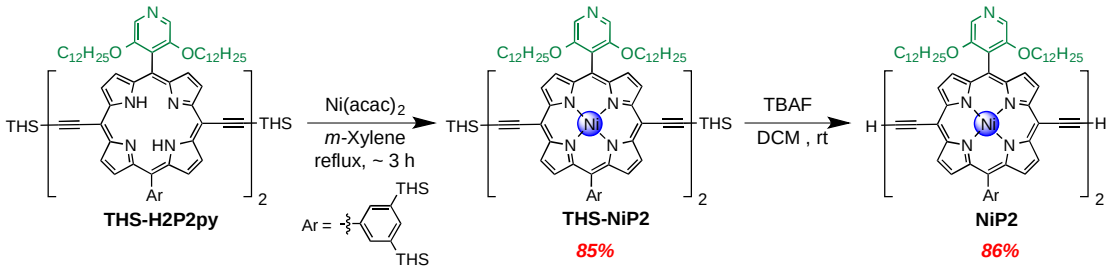

Fully protected Ni pyridyl porphyrin dimer, THS-NiP2: Freebase porphyrin dimer (50.0 mg, 0.014 mmol, 1.0 equiv.) was dissolved in *m*-xylene (10 mL). $Ni(acac)_2$ (108 mg, 0.420 mmol, 30.0 equiv.) was added. The mixture was heated to reflux under nitrogen for 3 h. After cooling the mixture was passed through a short silica plug eluting with chloroform/1% pyridine. The solvent was removed from the green filtrate and dried in vacuum, providing the desired product (44.0 mg, 85%) in form of a green solid.

THS-NiP2: ^{1}H NMR (400 MHz, $CDCl_3$): δ_H 9.63 (m, 4H, β-H), 9.46 (m, 4H, β-H), 8.80 (d, J = 4.0 Hz, 2H, β-H), 8.72 (d, J = 4.0 Hz, 2H, β-H), 8.68 (d, J = 4.0 Hz, 2H, β-H), 8.61 (d, J = 4.0 Hz, 2H, β-H), 8.45 (s, 4H, py-H), 8.10 (s, 4H, *o*-H), 7.95 (s, 2H, *p*-H), 3.98 (t, J = 4.0 Hz, 8H, OCH_2), 1.72–1.68 (m, 12H, alkyl-H), 1.56–1.30 (m, 150H, alkyl-H), 1.17–0.52 (m, 230H, alkyl-H). ***m/z* (MALDI-TOF)**: 3565.92 ($C_{226}H_{360}N_{10}Ni_2O_4Si_6$ requires 3562.56).

Fully deprotected Ni pyridyl porphyrin dimer, NiP2: Ni-dimer (32.7 mg, 0.009 mmol, 1.0 equiv.) was dissolved in chloroform (5 mL). TBAF-solution (1 M in THF, 5.0 µL, 0.005 mmol, 0.5 equiv.) was added and the mixture was stirred for 30 min at rt. Methanol was layered and precipitation was completed in the fridge overnight. The green precipitate was filtered to remove all solution and washed with methanol and dried in vacuum, affording the desired product in 28.1 mg, 86% yield.

NiP2: ^{1}H NMR (400 MHz, $CDCl_3$): δ_H 9.63 (m, 4H, β-H), 9.46 (m, 4H, β-H), 8.81 (d, J = 4.0 Hz, 2H, β-H), 8.74 (d, J = 4.0 Hz, 2H, β-H), 8.68 (d, J = 4.0 Hz, 2H, β-H), 8.62 (d, J = 4.0 Hz, 2H, β-H), 8.43 (s, 4H, py-H), 8.08 (s, 4H, *o*-H), 7.94 (s, 2H, *p*-H), 4.07 (s, 2H, ethinyl-H), 3.96 (t, J = 4.0 Hz, 8H, OCH_2), 1.45–0.52 (m, 248H, alkyl-H). **^{13}C-deptQ-NMR** (125 MHz, $CDCl_3$): δ_C 155.3 (d, 4C, py-C), 145.9 (d, 2C, α-C), 145.7 (d, 2C, α-C), 145.3 (d, 2C, α-C), 145.1 (d, 2C, α-C), 143.4 (d, 2C, α-C), 143.2 (d, 2C, α-C), 143.0 (d, 2C, α-C), 142.8 (d, 2C, α-C), 139.9 (d, 2C, *ipso*-C), 139.6 (u, 4C, *o*-C), 138.5 (u, 2C, *p*-C), 135.6 (d, 4C, *m*-C), 133.6 (u, 2C, β-C), 133.3 (u, 2C, β-C), 132.6 (u, 2C, β-C), 132.4 (u, 2C, β-C), 132.3 (u, 2C, β-C), 132.1 (u, 2C, β-C), 131.6 (u, 2C, β-C), 131.4 (u, 2C, β-C), 129.1 (u, 4C, py-C), 126.2 (d, 2C, py-C), 122.7 (d, 2C, *meso*-C), 110.6 (d, 2C, *meso*-C), 99.3 (d, 2C, alkynyl-C), 98.7 (d, 2C, *meso*-C), 85.1 (d, 4C, *meso*-C and alkynyl-C), 84.7 (d, 2C, alkynyl-C), 82.5 (d, 2C, alkynyl-C), 69.9 (d, 4C, OCH_2), 33.7-22.7 (d, 108C, CH_2), 14.3 (u, 18C, CH_3), 14.2 (u, 4C, CH_3), 12.7 (d, 12C, CH_2-Si). ***m/z* (MALDI-TOF)**: 3001.23 ($C_{190}H_{284}N_{10}O_4Si_4Ni_2$ requires 3001.02). **λ_{max} (CH_2Cl_2)/ nm (log ε)**: 450 (5.28), 476 (5.24), 562 (4.34), 648 (4.76).

Phenylacetylene Zn porphyrin tetramer **PhA-ZnP4**

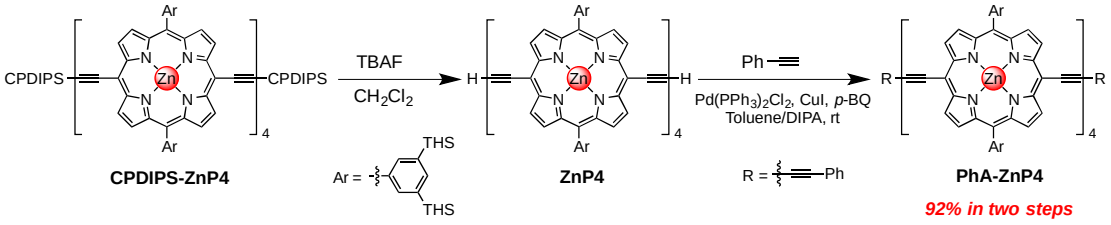

CPDIPS-ZnP4 (7.0 mg, 0.98 µmol, 1.0 equiv.) was dissolved in dry DCM and then added TBAF solution (1.0 M in THF; 3.0 µL, 2.44 µmol, 2.5 equiv.). After stirring for 2h, the reaction

was completed. The crude mixture was passed through a small silica plug eluting with $CHCl_3$ to remove TBAF. The solvent was removed and dried under high vacuum. Then the crude product **ZnP4**, phenylacetlyene (2.1 μL, 19.5 μmol, 20.0 equiv.), $Pd(PPh_3)_2Cl_2$ (1.0 mg, 2.0 μmol, 2.0 equiv.), copper(I) iodide (1.0 mg, 6.0 μmol, 6.0 equiv.) and 1,4-benzoquinone (1.0 mg, 10.0 μmol, 10.0 equiv.) were dissolved in dry toluene (1.00 mL), followed by dry DIPA (0.25 mL). The reaction was stirred at room temperature for 30 min and then added 25.0 μL (0.306 mmol, 312 equiv.) of phenylacetylene again to make sure that all terminal acetylenes were coupled. The reaction mixture was stirred further for another 1 h. The reaction mixture was passed through a short alumina plug eluting with chloroform/1% pyridine and then removed all solvent and redissolved in toluene to pass through a SEC-column to remove 1,4-benzoquinone and excess diphenylacetylene. The desired product was reprecipitated by bilayers of chloroform/MeOH, affording **PhA-ZnP4** in 6.5 mg, 92% yield in two steps.

PhA-ZnP4: ^{1}H NMR (400 MHz, $CDCl_3$): δ_H 9.92 (m, 12H, β-H), 9.69 (d, J = 4.0 Hz, 4H, β-H), 8.98 (m, 12H, β-H), 8.91 (d, J = 4.0 Hz, 4H, β-H), 8.33 (s, 8H, *o*-H), 8.29 (s, 8H, *o*-H), 8.04 (s, 4H, *p*-H), 8.02 (s, 4H, *p*-H), 7.75 (m, 4H, Ph-H), 7.45 (m, 6H, Ph-H), 1.55–1.20 (m, 384H, CH_2), 0.99–0.82 (m, 240H, CH_2 and CH_3). **^{13}C-NMR** (125 MHz, $CDCl_3$): δ_C 153.2, 153.1, 153.0, 150.8, 150.7, 143.7, 140.9, 140.3, 139.4, 135.3, 133.5, 132.8, 131.2, 128.7, 125.1, 125.0, 122.6, 122.4, 100.8, 53.6, 33.7, 31.8, 24.2, 22.8, 14.3, 12.8. ***m/z* (MALDI-TOF)**: 7004.9 ($C_{448}H_{690}N_{16}Si_{16}Zn_4$ requires 7011.4).

Phenylacetylene Ni porphyrin tetramer **PhA-NiP4**

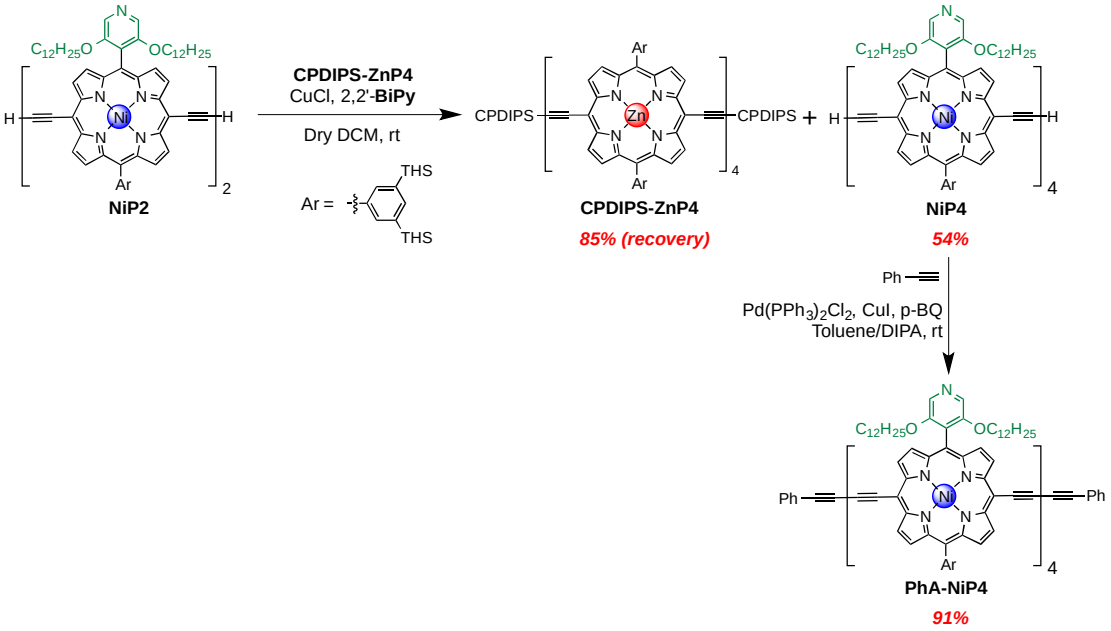

Firstly, **NiP4** was synthesised by linear templating with template **CPDIPS-ZnP4**. **NiP2** (22.3 mg, 7.43 μmol, 1.0 equiv.) was dissolved in dry DCM (74.3 mL) using a 1-L-flask. Template **CPDIPS-ZnP4** (26.7 mg, 3.71 μmol, 0.5 equiv.) was added and the mixture was stirred for 20 min, monitoring by UV-vis-NIR spectrocopy. CuCl (103 mg, 1.04 mmol, 140 equiv.) was added, followed by **2,2'-BiPy** (162 mg, 1.04 mmol, 140 equiv.). The reaction was vigorously stirred in the large flask with a lot of air. The reaction was followed carefully by UV-vis-NIR spectroscopy, and after 3 h had gone to completion. To the reaction mixture, 7 mL of pyridine was added. Then crude product was subjected into a short silica column eluting with gradient 1%-10% pyridine/chloroform to separate the template and elute the Ni-porphyrin products. Then the crude Ni-product was passed through the small SEC-column. The solvent was removed and dried over vacuum. The crude product was dissolved in toluene/1% pyridine and filtered by microfilter. The product distribution was analysed and separated by recycling GPC eluting with toluene/1% pyridine, affording the desired **NiP4** in 12.3 mg, 54% yield. The template was recovered in 22.6 mg, 85% recovered yield. Characterization data are shown in **Section 4.9.3.2**-the classical templated synthesis of **NiP4**.

Then **NiP4** (14.7 mg, 2.40 μmol, 1.0 equiv.), phenylacetlyene (5.4 μL, 49.0 μmol, 20.0 equiv.), $Pd(PPh_3)_2Cl_2$ (1.0 mg, 2.00 μmol, 0.8 equiv.), copper(I) iodide (1.0 mg, 6.0 μmol, 2.5 equiv.) and

1,4-benzoquinone (1.0 mg, 10.0 μmol, 4.2 equiv.) were dissolved in dry toluene (4.0 mL), followed by dry DIPA (1 mL). The reaction was stirred at rt for 30 min and then added 25.0 μL (0.306 mmol, 312 equiv.) of phenylacetylene again to make sure that all terminal acetylenes were coupled. The reaction mixture was stirred further for another 1 h. The reaction mixture was passed through a short alumina plug eluting with chloroform/1% pyridine and then removed all solvent and redissolved in toluene to pass through a SEC-column to remove 1,4-benzoquinone and excess diphenylacetylene. The desired product was reprecipitated by bilayers of chloroform/MeOH, affording **PhA-NiP4** in 13.5 mg, 91% yield.

PhA-NiP4: ^{1}H NMR (400 MHz, $CDCl_3$): δ_H =9.64 (m, 12H, β-H), 9.47 (m, 4H, β-H), 8.82 (m, 6H, β-H), 8.76 (d, J = 8.0 Hz, 2H, β-H), 8.69 (m, 6H, β-H), 8.64 (d, J = 4.0 Hz, 2H, β-H), 8.48 (s, 4H, py-H), 8.46 (s, 4H, py-H), 8.14 (s, 4H, *o*-H), 8.11 (s, 4H, *o*-H), 7.98 (s, 2H, *p*-H), 7.97 (s, 2H, *p*-H), 7.70 (m, 4H, Ph-H), 7.45 (m, 6H, Ph-H), 3.98 (m, 16H, OCH_2), 1.47–0.56 (m, 496H, alkyl-H). **^{13}C NMR** (125 MHz, $CDCl_3$): δ_C 155.5, 146.0, 145.8, 145.8, 143.2, 143.0, 140.0, 139.7, 138.4, 135.7, 133.7, 132.8, 132.2, 131.5, 129.5, 129.1, 128.7, 126.1, 125.2, 123.2, 123.1, 122.1, 111.2, 111.0, 99.2, 99.1, 99.1, 85.3, 84.3, 82.8, 82.7, 82.3, 81.8, 70.0, 69.9, 33.7, 31.9, 31.9, 31.8, 29.5, 29.5, 29.4, 29.3, 29.3, 29.2, 29.1, 28.8, 25.4, 24.2, 22.8, 22.7, 22.7, 14.3, 14.2, 14.1, 12.8. ***m/z* (MALDI-TOF)**: 6197.43 ($C_{396}H_{574}N_{20}Ni_4O_8Si_8$ requires 6202.08).

Phenylacetylene Ni porphyrin hexamer **PhA-NiP6**

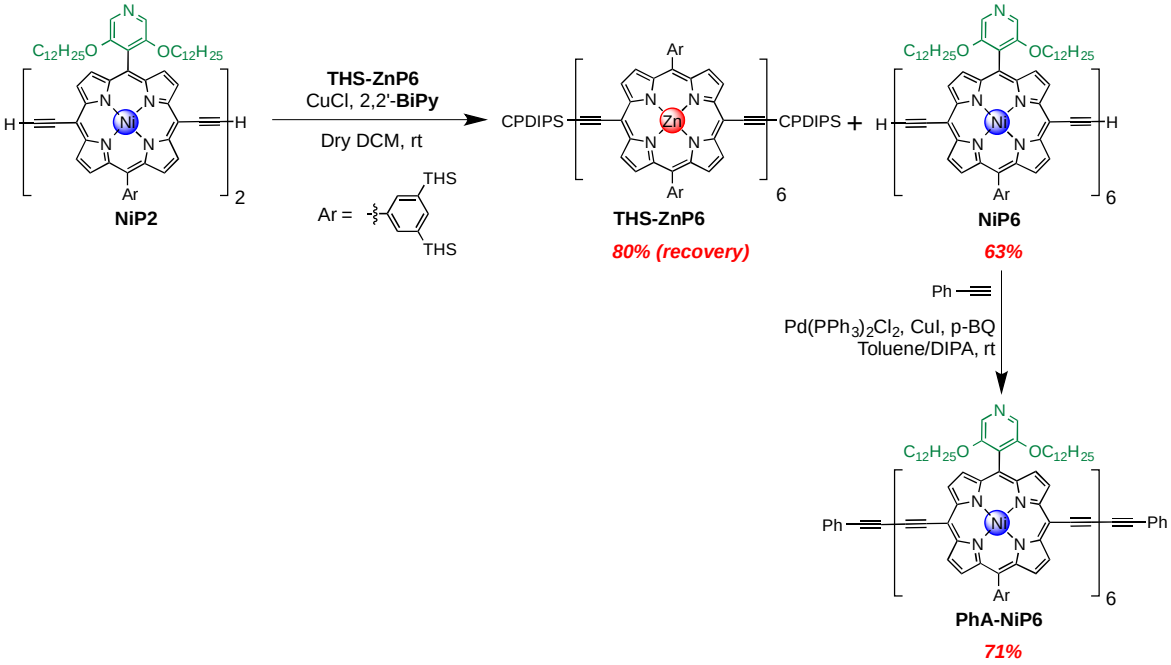

Firstly, **NiP6** was synthesised by linear templating with template **THS-ZnP6**. **NiP2** (20 mg, 6.6 μmol, 1.0 equiv.) and template **THS-ZnP6** (24 mg, 2.2 μmol, 0.33 equiv.) were dissolved in dry DCM (74 mL) using a 1-L-flask. The mixture was stirred for 20 min, monitoring by UV-vis-NIR spectrocopy. CuCl (92 mg, 0.93 mmol, 140 equiv.) was added, followed by **2,2'-BiPy** (145 mg, 0.93 mmol, 140 equiv.). The reaction was vigorously stirred in the large flask with a lot of air. The reaction was followed carefully by UV-vis-NIR spectroscopy, and after 3 h had gone to completion. To the reaction mixture, 7 mL of pyridine was added. Then crude product was subjected into a short silica column eluting with gradient chloroform/1% - 10% pyridine to remove all the coupling reagents, separate the template and elute the Ni-porphyrin products. The solvent was removed from the crude Ni product and dried over vacuum. The crude product was dissolved in toluene/1% pyridine and filtered by microfilter. The product distribution was separated by recycling GPC eluting with toluene/1% pyridine, affording the desired **NiP6** in 12.6 mg, 63% yield. The template was recovered in 19 mg, 80% recovered yield. Characterization data are shown in **Section 4.9.3.3**-the classical templated synthesis of **NiP6**.

Then **NiP6** (5.0 mg, 0.56 μmol, 1.0 equiv.), phenylacetlyene (25.0 μL, 227.7 μmol, 406.6 equiv.), $Pd(PPh_3)_2Cl_2$ (1.0 mg, 2.00 μmol, 3.57 equiv.), copper(I) iodide (1.0 mg, 6.0 μmol,

10.7 equiv.) and 1,4-benzoquinone (1.0 mg, 10.0 μmol, 17.8 equiv.) were dissolved in dry DCM (1.60 mL) and pyridine (0.05 mL), followed by dry DIPA (0.40 mL). The reaction was stirred at room temperature for 30 min and then added 25.0 μL of phenylacetylene again to make sure that all terminal acetylenes were coupled. The reaction mixture was stirred further for another 4 h. The reaction mixture was passed through a short silica plug eluting with chloroform/1% - 10% pyridine and then removed all solvent and redissolved in toluene to pass through a SEC-column to remove 1,4-benzoquinone and excess diphenylacetylene. The desired product was reprecipitated by bilayers of hexane/chloroform/MeOH and then hexane/MeOH, affording **PhA-NiP6** in 3.5 mg, 71% yield.

PhA-NiP6: ^{1}H NMR (500 MHz, $CDCl_3$): δ_H 9.64 (m, 20H, β-H), 9.47 (m, 4H, β-H), 8.82 (m, 10H, β-H), 8.75 (d, J = 5.0 Hz, 2H, β-H), 8.70 (m, 10H, β-H), 8.63 (d, J = 5.0 Hz, 2H, β-H), 8.47 (broad s, 12H, py-H), 8.14 (s, 8H, *o*-H), 8.11 (s, 4H, *o*-H), 7.98 (s, 4H, *p*-H), 7.96 (s, 2H, *p*-H), 7.70 (m, 4H, Ph-H), 7.44 (m, 6H, Ph-H), 4.02 (m, 24H, OCH_2), 1.47–0.54 (m, 744H, alkyl-H). **^{13}C NMR** (125 MHz, $CDCl_3$): δ_C 145.9, 145.7, 143.2, 143.0, 139.9, 139.7, 138.4, 135.7, 133.7, 132.8, 132.2, 131.5, 129.1, 128.9,128.7, 125.1, 123.2, 99.2, 69.9, 69.9, 38.9, 33.7, 32.3, 32.1, 31.9, 31.8, 31.8, 29.8, 29.5, 29.4, 29.3, 29.3, 29.2, 29.1, 28.8, 26.5, 25.4, 24.2, 23.9, 23.6, 23.1, 22.8, 22.7, 22.6, 14.3, 14.2, 14.1, 12.7. ***m/z* (MALDI-TOF)**: 9202.7 ($C_{586}H_{856}N_{30}Ni_6O_{12}Si_{12}$ requires 9202.08)

Fully THS protected Zn porphyrin heptamer **THS-ZnP7**, octamer **THS-ZnP8** and dodecamer **THS-ZnP12**

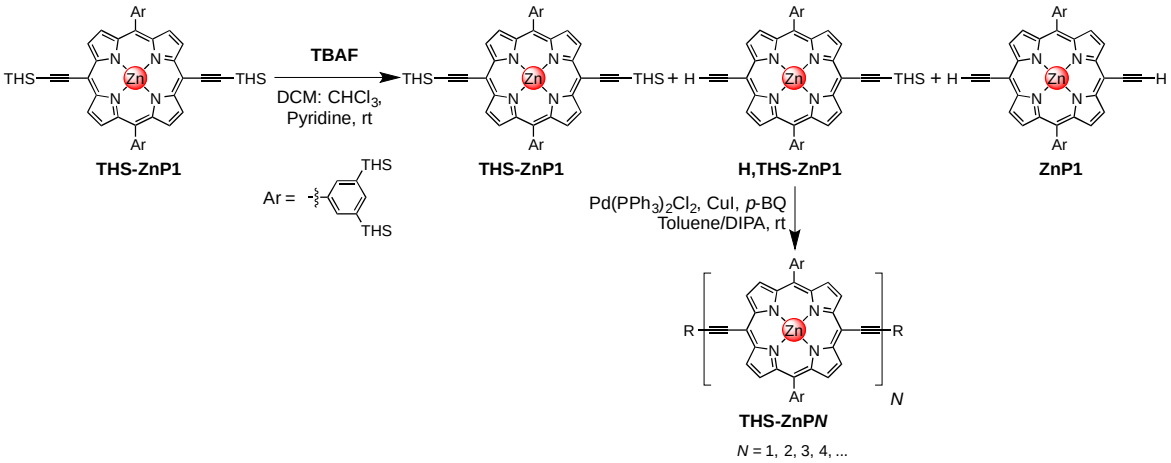

THS-ZnP1 (790 mg, 0.35 mmol, 1.0 equiv.) was dissolved in DCM (52 mL), chloroform (26

mL) and pyridine (7.0 mL). The solution was cooled in a water-ice bath and TBAF (520 μL, 1.0 M in THF) was added. The mixture was stirred and frequently monitored by TLC (petrol/toluene 98:2). As soon as the preferred ratio of deprotection was reached the reaction was quenched with acetic acid (few drops) and the mixture of **THS-ZnP1**, **H,THS-ZnP1** and **ZnP1** was filtered through a short column of silica gel (DCM/ 1% pyridine).

The crude mixture was used without further purification for the statistical coupling reaction. The crude mixture was dissolved in dry toluene (40 mL). $PdCl_2(PPh_3)_2$ (122 mg, 174 μmol, 0.5 equivalent), copper(I) iodide (684 mg, 4.9 mmol, 14 equivalent), 1,4-benzoquinone (677 mg, 6.3 mmol, 18 equivalent) and dry *i*Pr2NH (10 mL) were finally added. The reaction was monitored by TLC. After one and a half hour, all **H,THS-ZnP1** and **ZnP1** had gone. The volume was reduced and the mixture was filtered through a short column of silica gel (Petrol ether/DCM/ 1 % pyridine). The mixture was passed through a SEC column (toluene/ 1% pyridine) to remove **THS-ZnP1** and 1,4-benzoquinone. The crude porphyrin oligomers were further purified by GPC eluting with toluene/1% pyridine. The forth cycle of GPC traces is shown below:

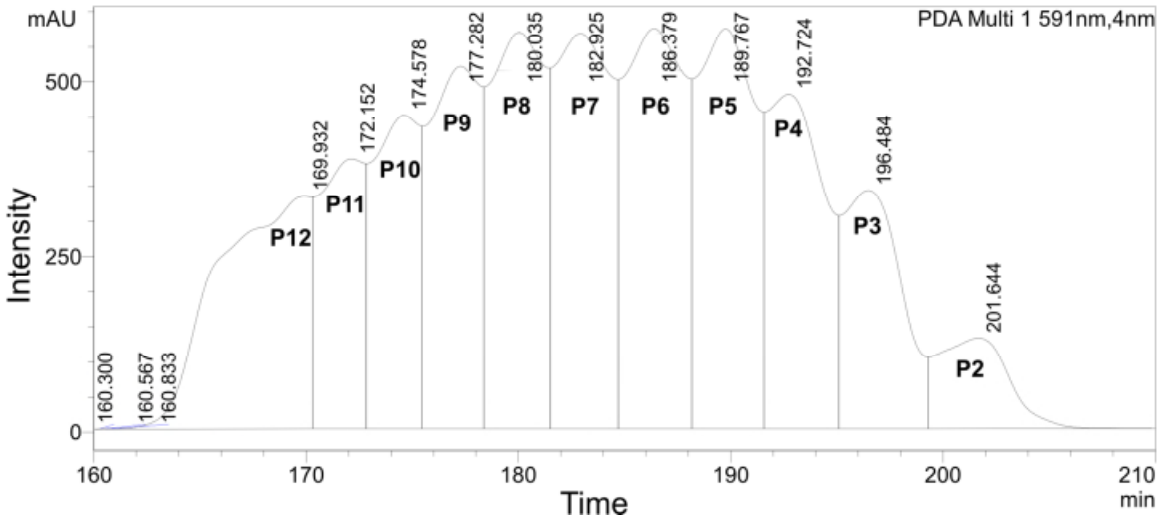

THS-ZnP2 (2%), **THS-ZnP4** (5%), **THS-ZnP5** (6%), **THS-ZnP6** (6%), **THS-ZnP7** (6%), **THS-ZnP8** (5%) and **THS-ZnP12** (3%) were isolated by recycling GPC to be used as references for making analytical GPC calibration curve for the THF/1% pyridine GPC column as see detail in **Section 4.9.4**.

THS-ZnP2, **THS-ZnP4**, **THS-ZnP5** and **THS-ZnP6** were characterised as literature.[6]

THS-ZnP7: ^{1}H NMR (400 MHz, $CDCl_3$): δ_H 9.90 (m, 24H, β-H), 9.61 (d, J = 4.0 Hz, 4H, β-H), 8.96 (m, 24H, β-H), 8.86 (d, J = 4.0 Hz, 4H, β-H), 8.32 (s, 20H, *o*-H), 8.26 (s, 8H, *o*-H), 8.02 (s, 10H, *p*-H), 8.00 (s, 4H, *p*-H), 1.55–0.89 (m, 1170H, CH_2 and CH_3). ***m/z* (MALDI-TOF)**: 12637.4 ($C_{792}H_{1268}N_{28}Si_{30}Zn_7$ requires 12460.8).

THS-ZnP8: ^{1}H NMR (400 MHz, $CDCl_3$): δ_H 9.91 (m, 28H, β-H), 9.68 (d, J = 4.0 Hz, 4H, β-H), 8.96 (m, 28H, β-H), 8.86 (d, J = 4.0 Hz, 4H, β-H), 8.33 (s, 24H, *o*-H), 8.27 (s, 8H, *o*-H), 8.03 (s, 12H, *p*-H), 8.00 (s, 4H, *p*-H), 1.56-0.89 (m, 1326H, CH_2 and CH_3). ***m/z* (MALDI-TOF)**: 13993.6 ($C_{900}H_{1438}N_{32}Si_{34}Zn_8$ requires 14160.0).

THS-ZnP12: ^{1}H NMR (400 MHz, $CDCl_3$): δ_H 9.91 (m, 44H, β-H), 9.67 (d, J = 4.0 Hz, 4H, β-H), 8.95 (m, 44H, β-H), 8.86 (d, J = 4.0 Hz, 4H, β-H), 8.33 (s, 40H, *o*-H), 8.27 (s, 8H, *o*-H), 8.03 (s, 20H, *p*-H), 8.00 (s, 4H, *p*-H), 1.56-0.89 (m, 1950H, CH_2 and CH_3). ***m/z* (MALDI-TOF)**: 21441.3 ($C_{1332}H_{2118}N_{48}Si_{50}Zn_{12}$ requires 20956.7).

Fully deprotected Zn porphyrin dodecamer **ZnP12**

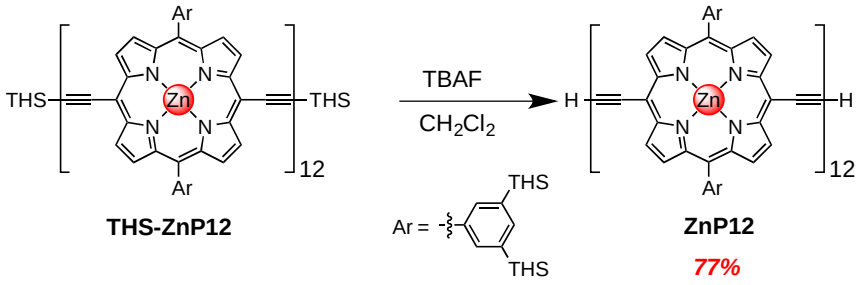

THS-ZnP12 (5.0 mg, 0.24 μmol, 1.0 equiv.) was dissolved in DCM (1.0 mL), chloroform (1.0 mL) and pyridine (20 μL) and then added TBAF solution (1.0 M in THF; 2.4 μL, 2.4 μmol, 2.5 equiv.). After stirring for 10 minutes, the reaction was completed. The crude mixture was passed through a small silica plug eluting with $CHCl_3$ to remove TBAF. The solvent was removed and dried under high vacuum, providing **ZnP12** in 3.8 mg, 77% yield.

ZnP12: ^{1}H NMR (400 MHz, $CDCl_3$): δ_H 9.99 (m, 44H, β-H), 9.76 (d, J = 4.0 Hz, 4H, β-H), 9.06 (m, 44H, β-H), 8.97 (d, J = 4.0 Hz, 4H, β-H), 8.38 (s, 40H, *o*-H), 8.32 (s, 8H, *o*-H), 8.07 (s, 20H, *p*-H), 8.04 (s, 4H, *p*-H), 4.22 (s, 2H, ethinyl-H), 1.56-0.89 (m, 1872H, CH_2 and CH_3).

***m/z* (MALDI-TOF)**: 20847.2 ($C_{1296}H_{2042}N_{48}Si_{48}Zn_{12}$ requires 20392.17).

4.9.3 Linear template-directed synthesis

*4.9.3.1 Classical templated synthesis of **NiP4** with **PhA-ZnP4***

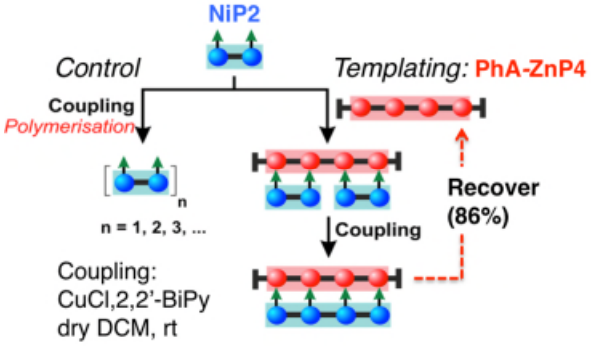

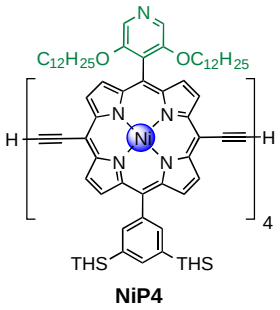

NiP4

NiP2 (6.20 mg, 2.24 μmol, 1.0 equiv.) was dissolved in dry DCM (20.7 mL) and 10 mL of this solution was aliquoted into a 50-mL-flask. Template **PhA-ZnP4** (3.40 mg, 0.53 μmol, 0.5 equiv.) was added and the mixture was stirred for 20 min, monitoring by UV-vis-NIR spectroscopy. CuCl (13.9 mg, 0.14 mmol, 140 equiv.) was added, followed by **2,2'-BiPy** (21.9 mg, 0.14 mmol, 140 equiv.). A second reaction was set up, similar with respect to the above, but in the absence of **PhA-ZnP4**. The reactions were followed carefully by UV-vis-NIR spectroscopy, and after 3 h had gone to completion. To each of the reaction mixtures, 0.1 mL of pyridine was added. Then crude product was subjected into a short silica column eluting with gradient 1%-10% pyridine/chloroform to separate the Zn template and elute the Ni-porphyrin products. The Zn template can be recovered in 2.9 mg, 86% yield. Then the crude Ni-product was passed through the small SEC-column eluting with toluene/1% pyridine. The solvent was removed and dried over vacuum. The crude product was dissolved in toluene/1% pyridine and filtered by microfilter. The product distribution was analysed and separated by recycling GPC eluting with toluene/1% pyridine. The desired product **NiP4** was obtained in 1.7 mg, 57% isolated yield and the unreacted substrate was left in 0.3 mg, 10% yield.

The reaction was set up again but changed the template **PhA-ZnP4** to **CPDIPS-ZnP4**, providing the desired product **NiP4** in 13.7 mg, 30% yield from 39 mg of **NiP2**, in 1.26 mg, 42% yield from 3.0 mg of **NiP2** and in 11.9 mg, 54% yield from 22 mg of **NiP2**.

NiP4: **^{1}H NMR** (400 MHz, $CDCl_3$): δ_H =9.65 (m, 12H, β-H), 9.48 (dd, *J* = 4.8, 5.2 Hz, 4H, β-H), 8.83 (m, 6H, β-H), 8.76 (d, *J* = 4.8 Hz, 2H, β-H), 8.70 (m, 6H, β-H), 8.64 (d, *J* = 5.2 Hz, 2H, β-H), 8.46 (d, *J* = 7.6 Hz, 8H, py-H), 8.13 (d, 8H, *o*-H), 7.97 (d, 4H, *p*-H), 4.07 (s, 1H, ethinyl-H), 4.01 (m, 16H, OCH_2), 1.47–0.55 (m, 496H, alkyl-H). **^{13}C NMR** (125 MHz, $CDCl_3$): δ_C 175.5, 155.3, 145.9, 143.0, 139.9, 135.7, 132.4, 130.2, 129.9, 129.1, 70.0, 69.9, 36.0, 33.7, 32.1, 31.9, 31.9, 31.8, 29.9, 29.8, 29.7, 29.5, 29.4, 29.4, 29.4, 29.3, 29.3, 29.2, 29.1, 29.1, 28.7, 27.4, 27.3, 25.7, 25.4, 25.4, 24.2, 22.8, 22.7, 22.7, 14.3, 14.2, 14.1, 12.7. ***m/z*** **(MALDI-TOF)**: 5997.73 ($C_{380}H_{566}N_{20}Ni_4O_8Si_8$ requires 6001.01). **λ_{max} (CH_2Cl_2)/ nm (log *ε*)**: 445 (5.56), 485 (5.61), 561 (4.69), 683 (5.30).

NiP2: as described in **Section 4.9.2.2**

4.9.3.2. Classical templated synthesis of **ZnP4** *with* **PhA-NiP4**

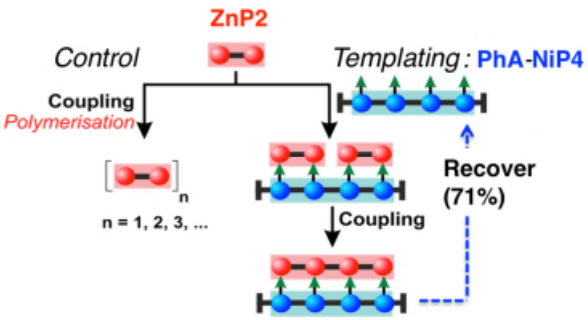

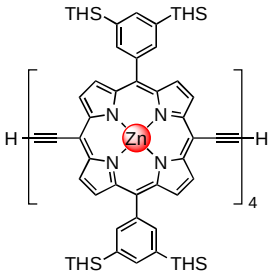

ZnP4

ZnP2 (7.0 mg, 2.05 μmol, 1.0 equiv.) was dissolved in dry DCM (20.5 mL) and 10 mL of this solution was aliquoted into a 50-mL-flask. Template **PhA-NiP4** (3.10 mg, 0.50 μmol, 0.5 equiv.) was added and the mixture was stirred for 20 min, monitoring by UV-vis-NIR spectroscopy. CuCl (13.9 mg, 0.14 mmol, 140 equiv.) was added, followed by **2,2'-BiPy** (21.9 mg, 0.14 mmol, 140 equiv.). A second reaction was set up, similar with respect to the above, but in the absence of **PhA-NiP4**. The reactions were followed carefully by UV-vis-NIR spectroscopy, and after 3.5 h had gone to completion. To each of the reaction mixtures, 0.1 mL of pyridine was added. Then crude product was subjected into a short silica column eluting with gradient 1%-10% pyridine/chloroform to separate the Zn-porphyrin products and elute the Ni template. The Ni template was recovered in 2.2 mg, 71% yield. Then the crude Zn-products were passed through the

small SEC-column eluting with toluene/1% pyridine. The solvent was removed and dried over vacuum. The crude product was dissolved in toluene/1% pyridine and filtered by microfilter. The product distribution was analysed and separated by recycling GPC eluting with toluene/1% pyridine. The desired product **ZnP4** was yield in 0.78 mg, 23% yield.

The reaction was set up again but reduced the reaction time to 1.5 h, providing the desired product in 1.02 mg, 30% yield.

ZnP4: ^{1}H NMR (400 MHz, $CDCl_3$): δ_H =9.65 (m, 12H, β-H), 9.48 (dd, *J* = 4.8, 5.2 Hz, 4H, β-H), 8.83 (m, 6H, β-H), 8.76 (d, *J* = 4.8 Hz, 2H, β-H), 8.70 (m, 6H, β-H), 8.64 (d, *J* = 5.2 Hz, 2H, β-H), 8.46 (d, *J* = 7.6 Hz, 8H, py-H), 8.13 (d, 8H, *o*-H), 7.97 (d, 4H, *p*-H), 4.07 (s, 1H, ethinyl-H), 4.01 (m, 16H, OCH_2), 1.47–0.55 (m, 496H, alkyl-H). ***m/z* (MALDI-TOF)**: 5997.73 ($C_{380}H_{566}N_{20}Ni_4O_8Si_8$ requires 6001.01).

These data match previous literature reports.[32]

*4.9.3.3. Classical templated synthesis of **NiP6** with **THS-ZnP6***

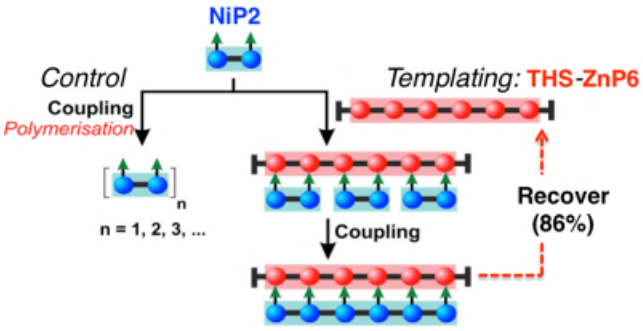

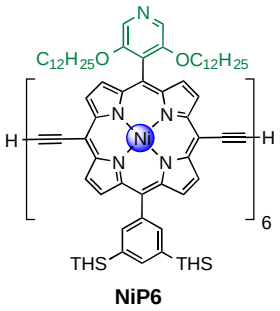

NiP6

NiP2 (9.0 mg, 3.0 μmol, 1.0 equiv.) was dissolved in dry DCM (33.3 mL) into a 1000-mL-flask. Template **THS-ZnP6** (10.7 mg, 1.0 μmol, 0.33 equiv.) was added and the mixture was stirred for 20 min, monitoring by UV-vis-NIR spectroscopy. CuCl (41.5 mg, 0.42 mmol, 140 equiv.) was added, followed by **2,2'-BiPy** (65.0 mg, 0.42 mmol, 140 equiv.). The non-templated reaction was prepared similarly as the templated reaction but in the absence of template **THS-ZnP6**. The reaction was followed carefully by UV-vis-NIR spectroscopy, and after 3 h had gone to completion. 0.3 mL of pyridine was added. Then crude product was subjected into a short silica column eluting with 20% pyridine/chloroform to remove the coupling reagent. Then the crude

mixture was passed through the small SEC-column eluting with toluene/1% pyridine. The solvent was removed and dried over vacuum. The crude product was dissolved in toluene/1% pyridine and filtered by microfilter. The product distribution was analysed and separated by recycling GPC eluting with toluene/1% pyridine. The template **THS-ZnP6** was separated and recovered in 9.2 mg, 86%yield. The desired product **NiP6** was separated in 5.1 mg, 56% yield.

NiP6: ^{1}H NMR (400 MHz, $CDCl_3$): δ_H 9.64 (m, 20H, β-H), 9.47 (m, 4H, β-H), 8.82 (d, J = 4.0 Hz, 10H, β-H), 8.75 (d, J = 4.0 Hz, 2H, β-H), 8.70 (d, J = 8.0 Hz, 10H, β-H), 8.63 (d, J = 4.0 Hz, 2H, β-H), 8.47 (s, 8H, py-H), 8.45 (s, 4H, py-H), 8.13 (s, 8H, *o*-H), 8.10 (s, 4H, *o*-H), 7.97 (s, 4H, *p*-H), 7.95 (s, 2H, *p*-H), 4.05 (s, 2H, ethinyl-H), 3.96 (m, 24H, OCH_2), 1.47–0.55 (m, 744H, alkyl-H). **^{13}C NMR** (125 MHz, $CDCl_3$): δ_C 175.5, 155.3, 145.9, 145.7, 143.2, 143.0, 139.9, 139.7, 138.4, 135.7, 133.7, 132.8, 132.2, 131.5, 129.1, 128.9, 128.7, 125.1, 123.2, 99.2, 69.9, 69.9, 38.9, 33.7, 32.3, 32.1, 31.9, 31.8, 31.8, 29.8, 29.5, 29.4, 29.3, 29.3, 29.2, 29.1, 28.8, 26.5, 25.4, 24.2, 23.9, 23.6, 23.1, 22.8, 22.7, 14.3, 14.2, 14.1, 12.7. ***m/z* (MALDI-TOF)**: 8996.17 ($C_{570}H_{848}N_{30}Ni_6O_{12}Si_{12}$ requires 9002.01). **λ_{max} (CH_2Cl_2)/ nm (log ε)**: 448 (5.67), 485 (5.78), 562 (4.83), 708 (5.5).

By-product **NiP12** from **NiP6**

After pure **NiP6** was obtained from the templating reaction, it was kept in the freezer at - 20 °C for two weeks. The Glaser coupling reaction of **NiP6** gradually occurred, providing the by-products. The crude mixture was injected into GPC (THF/1% pyridine). The by-product was isolated and identified by ^{1}H NMR and MALDI-ToF mass analysis, confirming **NiP12**. This compound can be used as a reference for the Vernier-reciprocal templating reaction.

NiP12: ^{1}H NMR (500 MHz, $CDCl_3$): δ_H 9.63 (m, 44H, β-H), 9.46 (m, 4H, β-H), 8.81 (m, 20H, β-H), 8.74 (d, J = 5.0 Hz, 2H, β-H), 8.68 (m, 20H, β-H), 8.62 (d, J = 5.0 Hz, 2H, β-H), 8.46 (s, 20H, py-H), 8.43 (s, 4H, py-H), 8.12 (s, 20H, *o*-H), 8.09 (s, 4H, *o*-H), 7.96 (s, 10H, *p*-H), 7.94 (s, 2H, *p*-H), 4.04 (s, 2H, ethinyl-H), 3.96 (m, 48H, OCH_2), 1.47–0.62 (m, 1488H, alkyl-H).

***m/z* (MALDI-TOF)**: 18106.9 ($C_{1140}H_{1696}N_{60}Ni_{12}O_{24}Si_{24}$ requires 18002.9).

*4.9.3.4. Vernier templated synthesis of **ZnP12** with **PhA-NiP6***

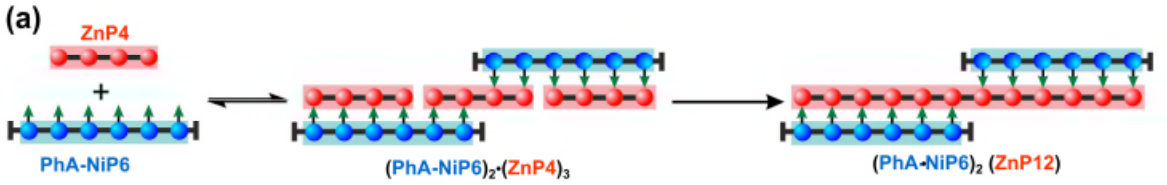

ZnP4 (3.5 mg, 0.51 μmol, 1.0 equiv.) was dissolved in dry DCM (3.0 mL) into a 25-mL-flask. Template **PhA-NiP6** (3.2 mg, 0.30 μmol, 0.60 equiv.) was dissolved in dry DCM (3.0 mL) and then added into the Zn porphyrin solution. The mixture was stirred for 20 min, monitoring by UV-vis-NIR spectroscopy. CuCl (7.1 mg, 0.07 mmol, 140 equiv.) was added, followed by **2,2'-BiPy** (11 mg, 0.07 mmol, 140 equiv.). The reactions were followed carefully by UV-vis-NIR spectroscopy, and after 4 h, there was insignificant change in absorption spectrum. To the reaction mixture, 0.6 mL of pyridine was added. Then crude product was subjected into a short silica column eluting with gradient chloroform/1%-10% pyridine to separate the Zn-porphyrin products and elute the Ni template. Then the crude Zn-products were passed through the small SEC-column eluting with toluene/1% pyridine. The solvent was removed and dried over vacuum. The crude product was dissolved in toluene/1% pyridine and filtered by microfilter. The product distribution was analysed by recycling GPC eluting with toluene/1% pyridine based on the GPC calibration curve as published.[16] The desired product **ZnP12** was analysed by fitting peak area in 21% yield.

*4.9.3.5. Vernier-reciprocal template-directed synthesis of **NiP12** and **ZnP12** with **NiP6** and **ZnP4***

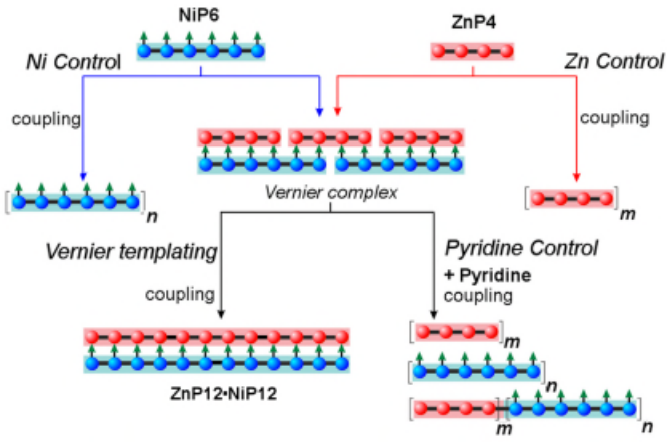

NiP6 (5.0 mg, 0.56 μmol, 1.0 equiv.) was dissolved in dry DCM (3.3 mL) (Ni-stock solution). **ZnP4** (5.38 mg, 0.79 μmol, 1.5 equiv.) was dissolved in dry DCM (9.0 mL) (Zn-stock solution). 1.0 mL of each stock solution was aliquoted into a 100-mL-flask. The mixture was further diluted with 1.0 mL of dry DCM. The mixture was stirred for 20 min. CuCl (2.36 mg, 24.0 μmol, 140 equiv.) was added, followed by **2,2'-BiPy** (3.72 mg, 24.0 μmol, 140 equiv.) 3 times at 0, 3 and 6 h. The Ni-control reaction was set up similarly with respect to the above but added dry DCM (1.0 mL) instead of the Zn-stock solution. The Zn-control reaction was set up similarly with the previous reaction but added dry DCM (1.0 mL) instead of the Ni-stock solution. The pyridine-control reaction was set up similarly with the first reaction but also added pyridine (0.3 mL). The reaction mixtures were stirred vigorously with the dry tube at room temperature. 20 μL of the linear Vernier templating reaction was aliquoted at 1, 3, 4, 6, 7 and 8 h and passed through a short silica plug eluting with DCM/10% pyridine. Then all solvents were removed before injecting to GPC (THF/1% pyridine) to monitor the starting material consuming by time. All reactions were stopped after 8 h and then passed through a short silica plug eluting with DCM/10% pyridine. The crude product mixture was analysed by GPC eluting with THF/1% pyridine and MALDI-ToF MS.

4.9.4 Analytical GPC calibration curve

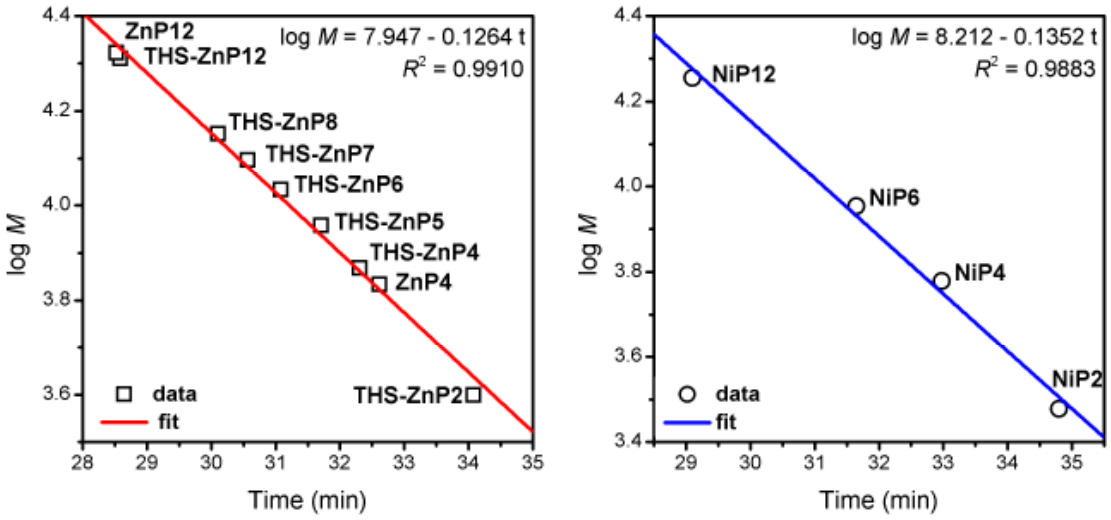

Figure 4.49 GPC retention times of linear Zn (left) and Ni (right) porphyrin oligomers plotted against log molecular weight. Squares and circles indicate Zn and Ni oligomers, respectively. All data were recorded in THF containing 1% pyridine. The points are fitted to solid lines (red, Zn oligomers; blue, Ni oligomers), according to linear equation (log M = a – bt).[16]

Analytical GPC was carried out on a series of linear Zn porphyrin oligomers and a series of linear Ni porphyrin oligomers to confirm the purities of these compounds for analytical GPC calibration (**Figure 4.48**). Analytical GPC traces of all Zn and Ni species were measured at 591 and 450 nm, respectively eluting with THF/1% pyridine. The intensities of all GPC peaks were normalised.

4.9.5 Extinction coefficients of Zn and Ni oligomers per porphyrin unit

Figure 4.49 shows the overlay of extinction coefficients per porphyrin unit of **NiP4**, **NiP6**, **THS-ZnP4** and **THS-ZnP6**. The green vertical line points out the absorption at 479 nm where all species assumably have the same extinction coefficient per porphyrin unit. Thus, we can calculate analytical yield of all species directly from the absorption at this wavelength in the GPC traces. The blue vertical line indicates the absorption at 779 nm where only Zn porphyrin species absorb dominantly. This is the alternative wavelength to observe yields of Zn porphyrin oligomer products.

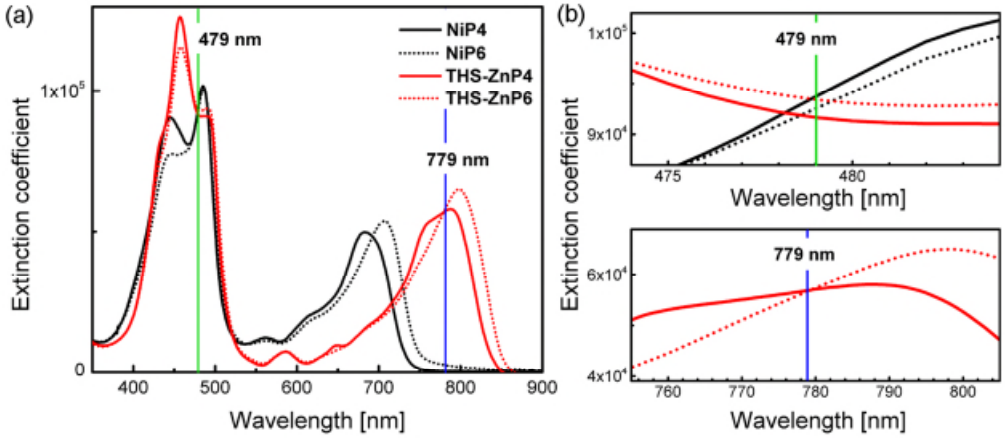

Figure 4.50 Extinction coefficients per porphyrin unit of **NiP4** (black solid line), **NiP6** (black dot line), **THS-ZnP4** (red solid line) and **THS-ZnP6** (red dot line). (a) Full range spectra. (b) Zoom in at 479 nm (top) and 779 nm (bottom).

4.10 References

(1) Anderson, H. L. *Inorg. Chem.* **1994**, *33*, 972–981.

(2) Anderson, H. L. *Chem. Commun.* **1999**, 2323–2330.

(3) Drobizhev, M.; Stepanenko, Y.; Dzenis, Y.; Karotki, A.; Rebane, A.; Taylor, P. N.; Anderson, H. L. *J. Am. Chem. Soc.* **2004**, *126*, 15352–15353.

(4) Drobizhev, M.; Stepanenko, Y.; Dzenis, Y.; Karotki, A.; Rebane, A.; Taylor, P. N.; Anderson, H. L. *J. Phys. Chem. B* **2005**, *109*, 7223–7236.

(5) Albinsson, B. *Chem. Soc. Rev.* **2015**, *44*, 845–862.

(6) Tait, C. E.; Neuhaus, P.; Peeks, M. D.; Anderson, H. L.; Timmel, C. R. *J. Am. Chem. Soc.* **2015**, *137*, 8284–8293.

(7) Tanaka, T.; Osuka, A. *Chem. Soc. Rev.* **2015**, *44*, 943–969.

(8) Lindsey, J. S. *New J. Chem* **1991**, *15*, 153–180.

(9) Kelly, T. R.; Xie, R. L.; Weinreb, C. K.; Bregant, T. *Tetrahedron Lett.* **1998**, *39*, 3675–3678.

(10) Hunter, C. A.; Tomas, S. *J. Am. Chem. Soc.* **2006**, *128*, 8975–8979.

(11) Wei, T.; Jung, J. H.; Scott, T. F. *J. Am. Chem. Soc.* **2015**, *137*, 16196–16202.

(12) Greschner, A. A.; Bujold, K. E.; Sleiman, H. F. *Biomacromolecules* **2014**, *15*, 3002–3008.

(13) Li, X.; Hao, C.; Tian, C.; Wang, P.; Mao, C. *Chem. Commun.* **2014**, *50*, 6361–6363.

(14) Kondratuk, D. V; Sprafke, J. K.; O'Sullivan, M. C.; Perdigao, L. M. A.; Saywell, A.; Malfois, M.; O'Shea, J. N.; Beton, P. H.; Thompson, A. L.; Anderson, H. L. *Chem. Eur. J.* **2014**, *20*, 12826–12834.

(15) O'Sullivan, M. C.; Sprafke, J. K.; Kondratuk, D. V; Rinfray, C.; Claridge, T. D. W.; Saywell, A.; Blunt, M. O.; O'Shea, J. N.; Beton, P. H.; Malfois, M.; Anderson, H. L. *Nature* **2011**, *469*, 72–75.

(16) Kondratuk, D. V; Perdigão, L. M. A.; Esmail, A. M. S.; O'Shea, J. N.; Beton, P. H.; Anderson, H. L. *Nat. Chem.* **2015**, *7*, 317–322.

(17) Jia, S.; Jentzen, W.; Shang, M.; Song, X.; Ma, J.; Scheidt, W. R.; Shelnutt, J. A.; Dame, N.; Dame, N.; March, R. V. *Inorg. Chem.* **1998**, *37*, 4402–4412.

(18) Cole, S. J.; Curthoys, G. C.; Magnusson, E. A.; Phillips, J. N. *Inorg. Chem.* **1972**, *11*, 1024–1028.

(19) Hay, A. S. *J. Org. Chem.* **1962**, *27*, 3320–3321.

(20) Anderson, S.; Anderson, H. L.; Sanders, J. K. M. *J. Chem. Soc. Perkin Trans. 1* **1995**, *18*, 2255–2267.

(21) Anderson, S.; Anderson, H. L.; Sanders, J. K. M. *J. Chem. Soc. Perkin Trans. 1* **1995**, *18*, 2247–2254.

(22) Peeks, M. D.; Neuhaus, P.; Anderson, H. L. *Phys. Chem. Chem. Phys.* **2016**, *18*, 5264–

5274.

(23) Bohlmann, F.; Schonowsky, H.; Inhoffen, E.; Gra, G. *Chem. Ber.* **1964**, *97*, 794–800.

(24) Siemsen, P.; Livingston, R. C.; Diederich, F. *Angew. Chem. - Int. Ed.* **2000**, *39*, 2632–2657.

(25) Wilson, G. S.; Anderson, H. L. *Chem. Commun.* **1999**, 1539–1540.

(26) Taylor, P. N.; Anderson, H. L. *J. Am. Chem. Soc.* **1999**, *121*, 11538–11545.

(27) Sprafke, J. K.; Odell, B.; Claridge, T. D. W.; Anderson, H. L. *Angew. Chem. - Int. Ed.* **2011**, *50*, 5572–5575.

(28) Ercolani, G.; Schiaffino, L. *Angew. Chem. - Int. Ed.* **2011**, *50*, 1762–1768.

(29) Hunter, C. A.; Anderson, H. L. *Angew. Chem. - Int. Ed.* **2009**, *48*, 7488–7499.

(30) Hogben, H. J.; Sprafke, J. K.; Hoffmann, M.; Pawlicki, M.; Anderson, H. L. *J. Am. Chem. Soc.* **2011**, *133*, 20962–20969.

(31) Keller, R. N.; Wycoff, H. D. *Inorg. Synth.* **1946**, *2*, 1–4.

(32) Parkinson, P.; Knappke, C. E. I.; Kamonsutthipaijit, N.; Sirithip, K.; Matichak, J. D.; Anderson, H. L.; Herz, L. M. *J. Am. Chem. Soc.* **2014**, *136*, 8217–8220.

Appendix

A.1 Equation of 1:1 binding isotherm model

For the formation of a 1:1 complex between a porphyrin *n*-mer (P) and an *n*-dentate ligand (L):

$$\mathrm{P} + \mathrm{L} \underset{}{\overset{K_\mathrm{f}}{\rightleftharpoons}} \mathrm{PL}$$

$$K_\mathrm{f} = \frac{[\mathrm{PL}]}{[\mathrm{P}][\mathrm{L}]} \quad \textbf{(eq. A.1)}$$

$$K_\mathrm{f}\,[\mathrm{P}][\mathrm{L}] - [\mathrm{PL}] = 0 \quad \textbf{(eq. A.2)}$$

As there is no consumption in the titration, it is true that:

$$[\mathrm{P}] = [\mathrm{P}]_0 - [\mathrm{PL}] \quad \textbf{(eq. A.3)}$$

$$[\mathrm{L}] = [\mathrm{L}]_0 - [\mathrm{PL}] \quad \textbf{(eq. A.4)}$$

where $[\mathrm{L}]_0$ and $[\mathrm{P}]_0$ are the total concentration of the guest ligand and the porphyrin host in the system and they are known in the titrations.

Substituting **eq. A.3** and **A.4** into **eq. A.2** gives:

$$K_\mathrm{f}[\mathrm{PL}]^2 - (K_\mathrm{f}([\mathrm{P}]_0 + [\mathrm{L}]_0) + 1)[\mathrm{PL}] + K_\mathrm{f}[\mathrm{P}]_0[\mathrm{L}]_0 = 0 \quad \textbf{(eq. A.5)}$$

Solving the quadratic equation gives the required solutions

$$[\mathrm{PL}] = \frac{(K_\mathrm{f}([\mathrm{P}]_0 + [\mathrm{L}]_0) + 1) \pm \sqrt{(K_\mathrm{f}([\mathrm{P}]_0 + [\mathrm{L}]_0) + 1)^2 - 4{K_\mathrm{f}}^2[\mathrm{P}]_0[\mathrm{L}]_0}}{2K_\mathrm{f}} \quad \textbf{(eq. A.6)}$$

$$\frac{[\mathrm{PL}]}{[\mathrm{P}]_0} = \frac{(K_\mathrm{f}([\mathrm{P}]_0 + [\mathrm{L}]_0) + 1) \pm \sqrt{(K_\mathrm{f}([\mathrm{P}]_0 + [\mathrm{L}]_0) + 1)^2 - 4{K_\mathrm{f}}^2[\mathrm{P}]_0[\mathrm{L}]_0}}{2K_\mathrm{f}[\mathrm{P}]_0} \quad \textbf{(eq. A.7)}$$

At the initial state of titration, all porphyrin species are unbound. At a specific wavelength, the absorption A_0 can be calculated as:

$$A_0 = \varepsilon_\mathrm{P}[\mathrm{P}]_0 l \quad \textbf{(eq. A.8)}$$

where ε_P is the extinction coefficient of unbound P at a specific wavelength, l is the path length of the cuvette.

At the final state of titration, all porphyrin species are bound. At the same wavelength as described in **eq. A.8**, the absorption A_f can be calculated as:

$$A_\mathrm{f} = \varepsilon_\mathrm{PL}[\mathrm{P}]_0 l \qquad \textbf{(eq. A.9)}$$

Then, the absorption A can be calculated as:

$$A = \varepsilon_\mathrm{P}[\mathrm{P}]l + \varepsilon_\mathrm{PL}[\mathrm{PL}]l = \varepsilon_\mathrm{P}([\mathrm{P}]_0 - [\mathrm{PL}])l + \varepsilon_\mathrm{PL}[\mathrm{PL}]l \qquad \textbf{(eq. A.10)}$$

Substituting **eq. A.8** and **A.9** into **eq. A.10** and then rearrangement of these gives:

$$\frac{A - A_0}{A_\mathrm{f} - A_0} = \frac{[\mathrm{PL}]}{[\mathrm{P}]_0} \qquad \textbf{(eq. A.11)}$$

As a result,

$$\frac{A - A_0}{A_\mathrm{f} - A_0} = \frac{(K_\mathrm{f}([\mathrm{P}]_0 + [\mathrm{L}]_0) + 1) \pm \sqrt{(K_\mathrm{f}([\mathrm{P}]_0 + [\mathrm{L}]_0) + 1)^2 - 4{K_\mathrm{f}}^2[\mathrm{P}]_0[\mathrm{L}]_0}}{2K_\mathrm{f}[\mathrm{P}]_0} \qquad \textbf{(eq. A.12)}$$

Trial of both equations in **eq. A.12** in the states ($\frac{A-A_0}{A_\mathrm{f}-A_0}$ = 0 – 1) of the titration indicates the right one, which is the 1:1 binding isotherm model:

$$\frac{A - A_0}{A_\mathrm{f} - A_0} = \frac{(K_\mathrm{f}([\mathrm{P}]_0 + [\mathrm{L}]_0) + 1) - \sqrt{(K_\mathrm{f}([\mathrm{P}]_0 + [\mathrm{L}]_0) + 1)^2 - 4{K_\mathrm{f}}^2[\mathrm{P}]_0[\mathrm{L}]_0}}{2K_\mathrm{f}[\mathrm{P}]_0} \qquad \textbf{(eq. A.13)}$$

where A_0 can be approximated to the first point of the titration and A_f to the final asymptote of the titration curve. Both A_0 and A_f can be set as variables in the Origin software. The absorption chosen in the data processing procedure can be the difference between two or even more wavelengths which give the greatest increase and decrease in absorption during each titration. This can eliminate effects that might cause variation in the baseline.

A.2 Equation of general n-dentate denaturation model

For the denaturation of a general *n*-dentate ligand-porphyrin oligomer (PL) complex with pyridine (Py):

$$\mathrm{PL} + n\ \mathrm{Py} \overset{K_\mathrm{dn}}{\rightleftharpoons} \mathrm{PPy}_n + \mathrm{L}$$

$$K_\mathrm{dn} = \frac{[\mathrm{PPy}_n][\mathrm{L}]}{[\mathrm{PL}][\mathrm{Py}]^n} \qquad \textbf{(eq. A.14)}$$

$$K_{\mathrm{dn}}\,[\mathrm{PL}][\mathrm{Py}]^{n} - [\mathrm{PPy}_{n}][\mathrm{L}] = 0 \qquad \textbf{(eq. A.15)}$$

As there is no reaction of the components it is also true that:

$$[\mathrm{PPy}_{n}] = [\mathrm{L}] \qquad \textbf{(eq. A.16)}$$

and

$$[\mathrm{PL}] = [\mathrm{P}]_{0} - [\mathrm{PPy}_{n}] \qquad \textbf{(eq. A.17)}$$

As a massive excess of pyridine (Py) is required compared to the complex (PL) in order to compete with the ligands (L), it can be assumed that:

$$[\mathrm{Py}] = [\mathrm{Py}]_{0} - [\mathrm{PPy}_{n}] \approx [\mathrm{Py}]_{0} \qquad \textbf{(eq. A.18)}$$

Substituting **eq. A.16**, **A.17** and **A.18** into **eq. A.15** and rearrangement give:

$$[\mathrm{PPy}_{n}]^{2} + K_{\mathrm{dn}}[\mathrm{Py}]^{n}[\mathrm{PPy}_{n}] - K_{\mathrm{dn}}[\mathrm{Py}]^{n}[\mathrm{P}]_{0} = 0 \qquad \textbf{(eq. A.19)}$$

Solving the quadratic equation gives:

$$[\mathrm{PPy}_{n}] = \frac{-K_{\mathrm{dn}}[\mathrm{Py}]_{0}{}^{n} \pm \sqrt{K_{\mathrm{dn}}^{2}[\mathrm{Py}]_{0}{}^{2n} + 4K_{\mathrm{dn}}[\mathrm{Py}]_{0}{}^{n}[\mathrm{P}]_{0}}}{2} \qquad \textbf{(eq. A.20)}$$

As before:

$$\frac{A - A_{0}}{A_{\mathrm{f}} - A_{0}} = \frac{-K_{\mathrm{dn}}[\mathrm{Py}]_{0}{}^{n} \pm \sqrt{K_{\mathrm{dn}}^{2}[\mathrm{Py}]_{0}{}^{2n} + 4K_{\mathrm{dn}}[\mathrm{Py}]_{0}{}^{n}[\mathrm{P}]_{0}}}{2[\mathrm{P}]_{0}} \qquad \textbf{(eq. A.21)}$$

Trial of both equations in **eq. A.21** in the states ($\frac{A-A_0}{A_f-A_0}$ = 0 – 1) of the titration indicates the right one, which is the *n*-dentate denaturation isotherm model:

$$\frac{A - A_{0}}{A_{\mathrm{f}} - A_{0}} = \frac{-K_{\mathrm{dn}}[\mathrm{Py}]_{0}{}^{n} + \sqrt{K_{\mathrm{dn}}^{2}[\mathrm{Py}]_{0}{}^{2n} + 4K_{\mathrm{dn}}[\mathrm{Py}]_{0}{}^{n}[\mathrm{P}]_{0}}}{2[\mathrm{P}]_{0}} \qquad \textbf{(eq. A.22)}$$

A.3 Calculation of concentration at 50% bound (C_{50})

For the formation of *m*:*n* complex between porphyrin oligomer (P) and an ligand (L):

$$m\,\mathrm{P} + n\,\mathrm{L} \underset{}{\overset{K_{\mathrm{m:n}}}{\rightleftharpoons}} \mathrm{P}_{m}\mathrm{L}_{n}$$

$$K_{m:n} = \frac{[\mathrm{P}_m\mathrm{L}_n]}{[\mathrm{P}]^m[\mathrm{L}]^n} \quad \textbf{(eq. A.23)}$$

At 50% bound, then

$$\frac{[\mathrm{P}]}{m} = \frac{[\mathrm{L}]}{n} = [\mathrm{P}_m\mathrm{L}_n] = \frac{C_{50}}{2} \quad \textbf{(eq. A.24)}$$

where c_{50} is the concentration in which complex is bound only 50%.

Substituting **eq. A.24** into **eq. A.23** and rearrangement give:

$$C_{50} = \frac{2}{\sqrt[(m+n-1)]{m^m\, n^n\, K_{m:n}}} \quad \textbf{(eq. A.25)}$$

A.4 Statistical factors

In the equilibrium of reactants A and B to give products C and D:

$$\mathrm{A} + \mathrm{B} \underset{}{\overset{K}{\rightleftharpoons}} \mathrm{C} + \mathrm{D}$$

The observed equilibrium constant (K) can be expressed in terms of the partition functions (Q_i) of each species:

$$K = \frac{Q_\mathrm{C} Q_\mathrm{D}}{Q_\mathrm{A} Q_\mathrm{B}} \quad \textbf{(eq. A.26)}$$

The partition function of each species i contained a contribution from its symmetry. It can be removed by dividing Q_i by symmetry number:

$$K = \frac{Q'_\mathrm{C} Q'_\mathrm{D}}{Q'_\mathrm{A} Q'_\mathrm{B}} \cdot \frac{\sigma_\mathrm{A}\sigma_\mathrm{B}}{\sigma_\mathrm{C}\sigma_\mathrm{D}} = K_\mathrm{chem} \cdot K_\sigma \quad \text{where} \quad K_\sigma = \frac{\sigma_\mathrm{A}\sigma_\mathrm{B}}{\sigma_\mathrm{C}\sigma_\mathrm{D}} \quad \textbf{(eq. A.27)}$$

and

$$\sigma = \sigma_\mathrm{int} \cdot \sigma_\mathrm{ext} \quad \textbf{(eq. A.28)}$$

The measured binding constant (K) can be factorised into the intrinsic equilibrium constant for the process (K_chem) and the symmetry factor for the equilibrium (K_σ) which is calculated through the symmetry numbers (σ) of the species involved in the process.[1-3] The symmetry number (σ) is the product of an internal symmetry number (σ_int), which is calculated from the number of degenerate internal rotors, and an external symmetry number (σ_ext), which is deduced from the point group of the molecule.

Table A.1 Relating external symmetry number (σ_{ext}) to point group.

Point group	σ_{ext}
C_1, C_i, C_s, $C_{\infty v}$	1
C_n, C_{nv}, C_{nh}, S_{2n}	n
$D_{\infty h}$	2
D_n, D_{nd}, D_{nh}	$2n$
T_d	12
O_d	24
I_h	60

The calculation of statistical factors in **Figure 4.16** as shown below:

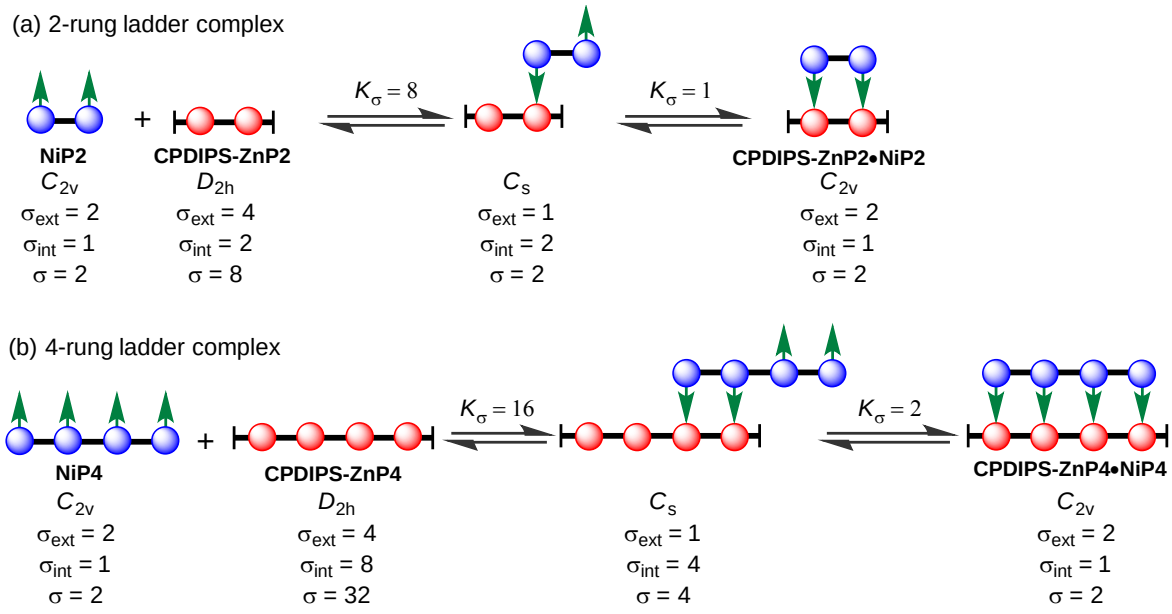

Figure A.1 The analyses of the statistical factors in **Figure 4.16a** and **b**.

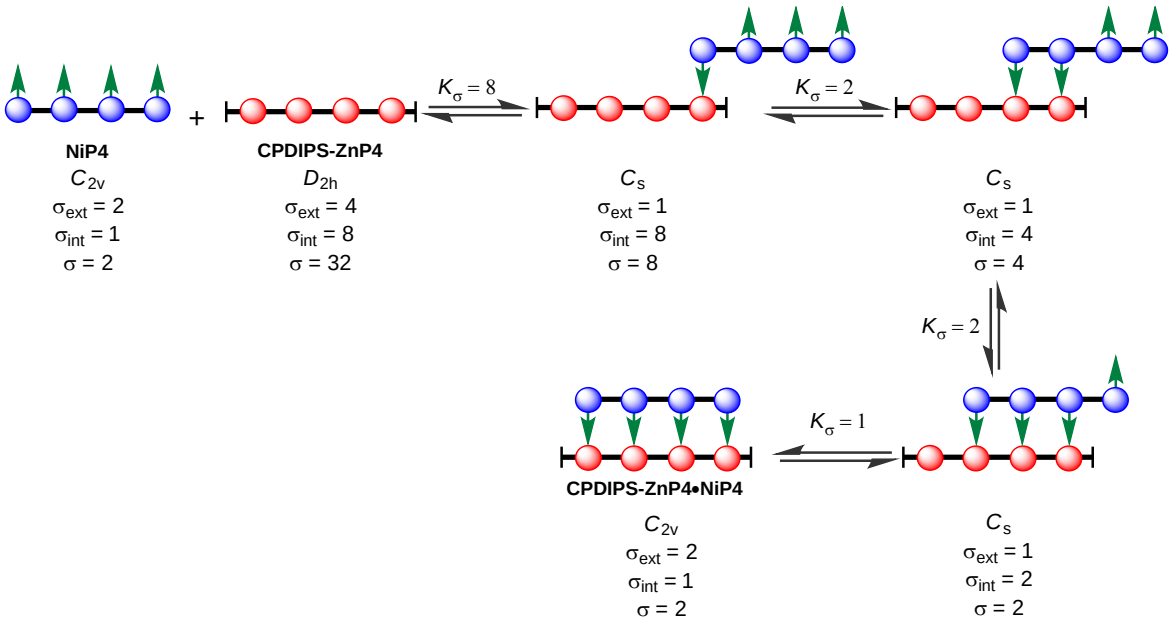

Figure A.2 The analysis of the statistical factors in **Figure 4.16c**.

A.5 References

(1) Hunter, C. A.; Anderson, H. L. *Angew. Chem. Int. Ed.* **2009**, *48*, 7488–7499.

(2) Benson, S. W. *J. Am. Chem. Soc.* **1958**, *80*, 5151–5154.

(3) Bailey, W. F.; Monahan, A. S. *J. Chem. Educ*. **1978**, *55*, 489–493.